Biomolecules at interfaces: understanding the dynamics of proteins and nanoparticles with biomimetic membranes under nitric oxide-induced stress

Inaugural dissertation

zur

Erlangung des akademischen Grades eines

Doktors der Naturwissenschaften

(Dr. rer. nat.)

der

Mathematisch-Naturwissenschaftlichen Fakultät

der

Universität Greifswald

vorgelegt von
Sanjai Karanth

Greifswald, November 2020

Dekan: Prof. Dr. Gerald Kerth

1. Gutacher: Prof. Dr. Mihaela Delcea
2. Gutacher: Prof. Dr. José Luis Toca-Herrera

Tag der Promotion: 30 March 2021

Table of Contents

Eigenständigkeitserklärung

Acknowledgements

I would like to thank and commend all the people involved through these years for the development of this thesis, without whom it would not have been a success.

Special accolades to Prof. Dr. Mihaela Delcea, who not only supervised during this tenure but also mentored me in taking critical decisions essential for career development. Her constant drive to get the best out of me is something, which I will always cherish.

This uphill task would not have been complete without the support of my colleagues, who were instrumental throughout this learning curve. Special thanks to Dr. Peter Nestler, Dr. Brahmaiah Meesaragandla, Dr. Huong Hguyen, Una Janke and other members of the team.

Additionally, I am very grateful to Prof. Dr. C.A. Helm and her colleagues, Florian Gellert, Amir Azinfar and others who supported me during my visit to their lab and assisted me during experimentation when needed. A special thank you to all of them.

I also thank Yesaswini, Karuppasamy, Dr. Oliver Otto and his group and RTG 1947/BiOx members for providing a comfortable environment during this current period.

I acknowledge the DFG for the financial support and I thank Anett Stolte and Astrid Kempcke for the adminstrative support.

Finally, I am grateful to all my family members, relatives and friends whose care is what made me here today. While the list is long, special mentioning about my father, Late A. G. Karanth, mother Shankari, brother Ajai, cousin sisters Annapurna Shastri and Priya Shanbhag who constantly provided me with moral support to pursue my goals.

Abbreviations

µL	Microliter
µm	Micrometer
µM	Micromoles
$^1O_2$	Singlet oxygen
AFM	Atomic force microscopy
AuNPs	Gold nanoparticles
eNOS	endothelial nitric oxide synthase
Fe	Iron
H_2O_2	Hydrogen peroxide
HOBr	Hypobromous acid
HOCl	Hypochlorous acid
iNOS	inducible nitric oxide synthase
kDa	kilo Daltons
MHz	Megahertz
min	Minute
mV	Millivolts
Mw	Molecular weight
nm	Nanometer
nNOS	neuronal nitric oxide synthase
$NO^{\cdot}$	Nitric oxide
$^{-}NO_2$	Nitrite
NOC-5	1-Hydroxy-2-oxo-3-(3-aminopropyl)-3-isopropyl-1-triazene
NOS	Nitric oxide synthase

Abbreviations

NPs	Nanoparticles
O_2	Molecular oxygen
O^{2-}	Superoxide ion
OH-	Hydroxyl radical
$ONOO^-$	Peroxynitrate
PDB	Protein database
pH	Potential of hydrogen
QCM-D	Quartz crystal microbalance with dissipation
RGD	Arginine-Glycine-Aspartate
RNS	Reactive nitrogen species
ROS	Reactive oxygen species
RSNOs	Nitrosothiols
SiO_2	Silicon dioxide
TEM	Transmission electron microscopy
UV	Ultraviolet
α-helix	Alpha helix
ß-structure	Beta structure

1. Introduction

Nature can be considered as an abstract art which intrigues us when explored in great detail. Every living organism is a piece of this art puzzle, which when fitted right, outlays its hidden meaning. Piecing the puzzle together began in 1665 when Robert Hooke reported the presence of small pores on cork tree, invisible to naked eye in his book *Micrographia;* to the concept of cell theory proposed by the great minds of Anton Van Leeuwenhoek, Matthias Schleiden, Theodor Schwann and Rudolf Virchow [1]. Their findings formed the foundation of our current research that all living beings, irrespective of their origin, have cells as their basic building blocks. Knowledge of the cell, its components and their abilities to communicate with each other have turned out to be essential and helpful, thereby providing insights into the understanding of modern-time diseases.

1.1 Cell membrane

Independent of the type of organism under consideration i.e. prokaryotes, eukaryotes or archaea, the cell of each of these organisms contain few common components, which are essential for their survival. Cell membrane, also called as plasma membrane, is one such critical component [2]. Cell membrane is the outermost, semi-permeable barrier surrounding the cell, which allows selective travel of molecules through it. Along with selective transport, the barrier is responsible to maintain cell integrity and functionality [3], [4]. The principal components governing this 4-5 nm thick barrier include lipids, membrane proteins, membrane carbohydrates, sphingolipids and cholesterol (Figure 1) [5]. A predominant class of lipids found in the cell membrane is represented by phospholipids. The structural rearrangement and localization of phospholipids, along with other components at the nano-level, not only determines the functionality, but also the efficacy of a particular cellular function [6]–[8]. These findings highlight the diversity of phospholipids in the membrane, which needs to be considered. One can categorize the lipids either based on their chemical structure (i.e. saturated, unsaturated, long chain, short chain) or based on their composition (i.e. between different organelles or cell types). Whilst chemical changes give specific characteristic to the lipid structure, compositional changes give rise to associated changes in lipid actions [9]–[11].

This PhD thesis aims to explore a combination of both these approaches. Phospholipids act as docking centers for proteins to hold their positions in the cell membrane. To simply quantify, it is estimated that the ratio of phospholipids to protein is 40:1 [12], however this

number depends on the cell type. The lipids surrounding and incorporating the protein also support its function. In homeostatic conditions, the action of these lipids translate into respective cellular signaling and any offset or down-regulation may lead to diseases [13]–[15].

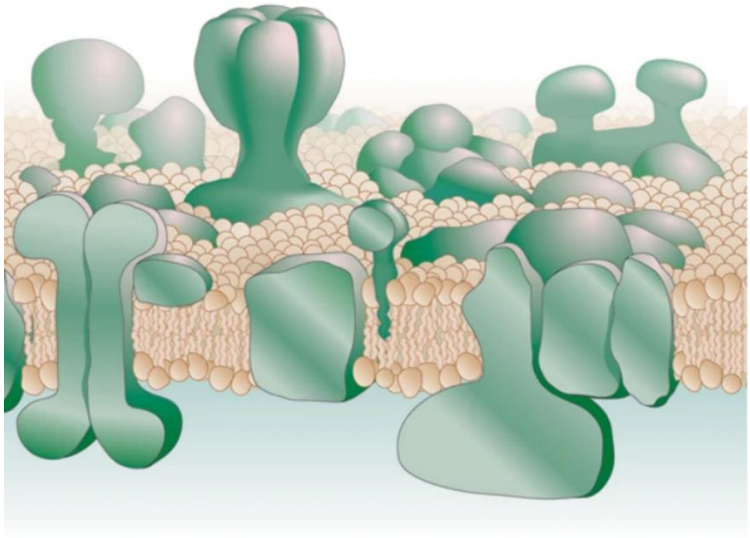

Figure 1. Fluid mosaic model of a typical cell membrane. The updated and currently accepted model of cell membrane initially proposed by Singer-Nicholson in 1972. The membrane is understood as an association of phospholipids with proteins, glycoproteins and carbohydrates dispersed between them. Adapted from Engelman [16].

1.2 Cell membrane damage: cause and effect

Exposure of cell membrane to potential lethal substances or agents creates imbalances to the membrane equilibrium. Unlike prokaryotic cell membrane, which is covered by an additional cell wall, absence of such protection in eukaryotic cell membrane increases its vulnerability to a multitude of physical (e.g. temperature, radiation and osmotic stress), chemical (e.g. ionic strength, pH and trace elements) and biological (e.g. toxins, infections, vascular injury) agents [17]–[20] able to induce significant physico-chemical change to the membrane structure and function. Therefore, a detailed elucidation of such outcomes is beneficial, e.g. in development of drugs. Whereas each of these agents has a different mode of action, human body tends to respond to these intrusions through the immune system. Once the immune system is activated, an interconnected defense network comprising of mast cells, macrophages and platelets among others, starts to counter the intrusion. One of the hallmark indicators of such counteraction is the inflammation [21]–[23]. Inflammation

can be defined as response to triggered defense mechanism by body to drive away the harmful agents and maintain hemostasis.

1.3 Free radicals and the inflammation paradox

Before knowing and understanding the inflammation paradox, we need to first look into the concept of free radicals. A chemist would define a free radical (also known as reactive species) as any molecule which contains one or more free electron in its outer single orbit. This reactive species can interact with other molecules (which could be reactive or not) forming a stable product. The action of such reactive species is dependent on its concentration, site of generation and its reactivity with other compounds. Primarily, oxygen and nitrogen based reactive species are generated in cells. At low concentrations, free radicals destroy the pathogens as part of the defense mechanism [24], [25]. Apart from these, they also act as messengers in cell signaling and related physiological roles [26]–[28]. However, when these are produced in excess, the accumulation of free radicals leads to oxidative or nitrosative stress. This imbalance is driven when radical scavengers are defeated by the high radical concentration [29]. The induced oxidative or nitrosative stress causes detrimental effects on the cell membrane affecting proteins, lipids and lipoproteins leading eventually to cell death [30]. Free radicals, when released as a result of infection, also cause inflammation. If the inflammation persists for a short period (lasting from few minutes to days) until cell repair, it is referred as acute inflammation. However, if the reversal of this inflammation to normal condition does not occur, then such continuous release of radicals leads to chronic inflammation. Such recurrent inflammation is characteristic for diseases such as cancer, type 2 diabetes, asthma, Alzheimer's, etc. [23].

1.4 Reactive oxygen and nitrogen species

Reactive species, based on their reactivity can be classified into radicals and non-radicals. With oxygen as the central element responsible for partial reduction or oxidation (hence reactive oxygen species (ROS)), a plethora of oxygen dependent reactive species are available i.e. hydroxyl (OH-), superoxide (O^{2-}), hydrogen peroxide (H_2O_2), hypochlorous acid (HOCl), hypobromous acid (HOBr), singlet oxygen ($^1O_2$) etc. [31], [32]. Among these, the most commonly studied are superoxide and hydrogen peroxide because they are largely released during cell metabolism. Hydroxyl formation occurs as per Fenton's reaction during decomposition of hydrogen peroxide [33]–[35]. Similarly, with nitrogen as central

element (hereafter reactive nitrogen species (RNS)), nitric oxide ($NO^{\cdot}$), peroxynitrate ($ONOO^{-}$), nitrosothiols (RSNOs) are commonly released in the cell [36], [37].

1.4.1 Nitric oxide

Among different available types of reactive oxygen or nitrogen species, nitric oxide ($NO^{\cdot}$) is considered to be the least reactive and stable radical with a very short half-life [38]. While its presence is known from a very long time, its action on membrane always was doubtful. Its distinct chemical and physical properties make it a very unique radical for study. Chemically, it contains an unpaired electron, hence its reaction with other radicals is very rapid. The micro-environment surrounding the $NO^{\cdot}$ [39], [40] is always a deciding factor for its role as a positive or a negative molecule.

In presence of transition metal (e.g. protein containing heme group such as in cytochrome P450 [40]), $NO^{\cdot}$ reacts to form stable metal nitrosyl complex i.e.

$$\mathrm{Fe_{aq}(II)} + \mathrm{NO^{\cdot}} \rightarrow \mathrm{Fe_{aq}(II) - NO}$$

However, the interesting aspect in our case is the auto-oxidation and nitrosation of $NO^{\cdot}$ in the lipid membranes. With $NO^{\cdot}$ and molecular oxygen having similar partition coefficients into the hydrophobic spaces of membrane [41], [42], their cross-reaction is crucial in the detrimental effect on phospholipids as shown below:

$$4\mathrm{NO^{\cdot}} + \mathrm{O_2} + 2\mathrm{H_2O} \rightarrow 4\mathrm{H^+} + 4\mathrm{NO_2^-}$$

The formed nitrite ($^{-}NO_2$) is a major nitrosating agent in biological systems [43]–[45]. Along with $NO^{\cdot}$ lipophilicity, the rapid diffusion of $NO^{\cdot}$ makes it a unique radical. With a diffusion coefficient of 3300 $\mu m^2/s$ [46], [47], $NO^{\cdot}$ can diffuse away from the generation source and travel a distance of 100-200 µm, depending on the point of origin. Combining the above physical and chemical aspects, it is clear that only short half-life of $NO^{\cdot}$ *in vivo* is not a limiting factor for its role on cell membranes.

1.4.2 Nitric oxide: key in inflammation paradox

In biological system, an enzyme called nitric oxide synthase (NOS) is responsible for the generation of nitric oxide. Its generation and concentration are dependent on the location of the enzyme complex. In response to a toxic agent or stimuli, inducible NOS (iNOS) releases $NO^{\cdot}$ (e.g. from macrophages) in large concentrations to neutralize the toxicity. The $NO^{\cdot}$ released by endothelial NOS (eNOS) is very regulatory in nature. While it is designed

to cause vasodilation of smooth muscle cells, in case of vascular injury, eNOS prevents the formation of blood clot. NO· from neuronal NOS (nNOS) works as a neurotransmitter or synaptic plasticity depending on its location in the nervous system [48]. In pathological conditions where chronic inflammation exists, there is a simultaneous and continuous release of NO· from eNOS and iNOS (Figure 2). The concentration of released NO· is so high that along with destruction of harmful cells, nearby healthy cells can also be destroyed (e.g. patients suffering from type 2 diabetes have around 50 µM of NO· related products in the blood plasma [49]). Increasing evidences of NO· being pro-inflammatory highlight its dual ability of membrane penetration and subsequent negative effect on the composition of cell membrane [50]–[54]. With limited literature on nitric oxide (and its products) action on phospholipid composition and membrane proteins, our work focused on exploring few of these open questions.

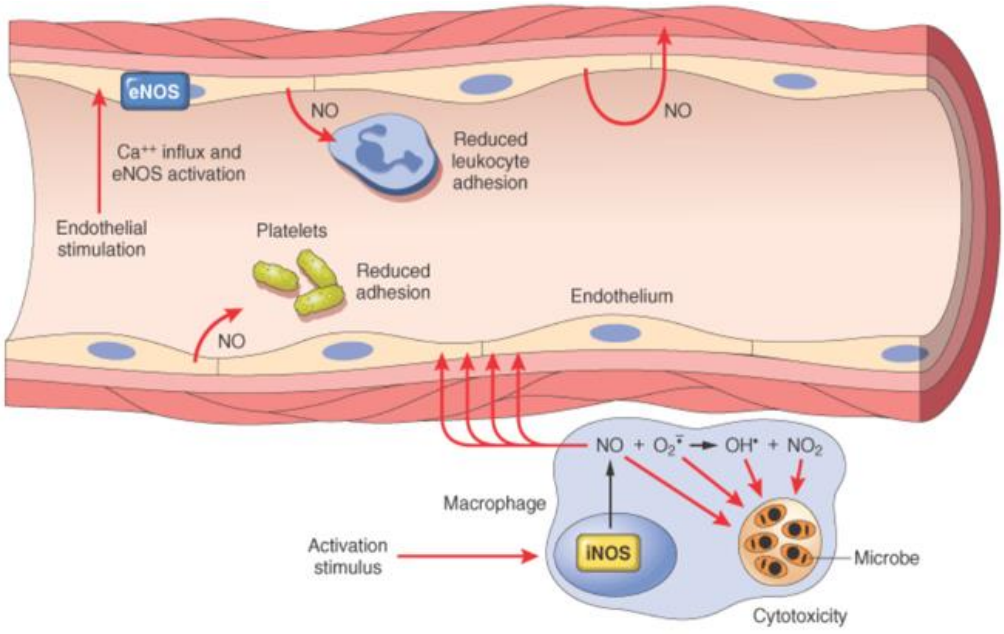

Figure 2. Release of nitric oxide from different locations upon stimulus activation. Nitric oxide synthases (NOS) are enzymes responsible for release of nitric oxide. Upon inflammation along with endothelial NOS (eNOS), inducer NOS (iNOS) is also activated. This increases the total concentration of nitric oxide in the blood stream making it toxic. Adapted from [55].

1.5 Platelets as a biological mechanosensor

Cells (e.g. neutrophils, macrophages, granulocytes, thrombocytes) which are directed to combat an intrusion and restore hemostasis, circulate in the blood and travel to the infection site post-stimulus response. Unlike the conventional understanding that most of the inter-

and intra-cell signaling and communication occurs *via* a series of biochemical pathways, cells in the blood also rely on mechanical transduction [56]. The conversion of a physical driver (e.g. force, tension, shear stress, etc.) into a biochemical signal is the principal component in these cells. These mechanosensors interact with surrounding endothelial cells, extracellular matrix to generate the required response. Studies have pointed that the dynamics of lipid bilayer [57] and the transmembrane proteins act as transducing elements by generating small magnitude forces, thereby significantly contributing to the mechanobiology of cell [58]. In this work, we attempt to deduce and quantify the responses of these transducing elements by developing model lipid systems with phospholipid composition mimicking the cell membrane of platelets.

Platelets (also called thrombocytes) are anucleated cells with diameter ranging between 2-4 µm. They have a life-span of 5-7 days when circulating in blood and are mainly responsible for thrombus formation [59], [60]. Platelets contain series of proteins called integrins embedded in their phospholipid bilayers, which act as focal adhesion points for the extra cellular matrix in signaling. The phospholipids present in the platelet cell membrane regulate its functionality i.e. adhesion, aggregation and coagulation [61]–[65], (Figure 3). Thus, elucidating the influence of phospholipid composition on the dynamics of platelet function is critical. Also, recent studies have highlighted that, unlike earlier understanding, platelets are equally responsible for pro-inflammatory roles and induce significant pathophysiological consequences [66]–[71]. Under hemodynamic shear stress, nitric oxide and reactive oxygen species are generated, which trigger the inflammatory response [72]. This cross-talk of platelets through its focal adhesion centers needs examination and a mechanistic approach can provide some awareness to its role.

Among different transmembrane proteins present, integrin αiibβ3 is of particular interest because of its copy number (80,000) per platelet cell [73]. This protein can bind effectively to multiple ligands (e.g. fibrinogen, von Wilebrand factor) and induce a structural change leading to platelet aggregation. However, its influence under redox condition has been under-reported. Because it is a transmembrane protein, part of the integrin αiibβ3 structure is embedded inside the lipid bilayer. Hence, we first investigate whether the nitric oxide can influence the dynamics of lipid bilayer with changing phospholipid chemistry and composition (**Article I**). Later, we explored by single molecule force spectroscopy the

structural changes of integrin αiibβ3 transducer reconstituted into lipid bilayers as described in **Article II**.

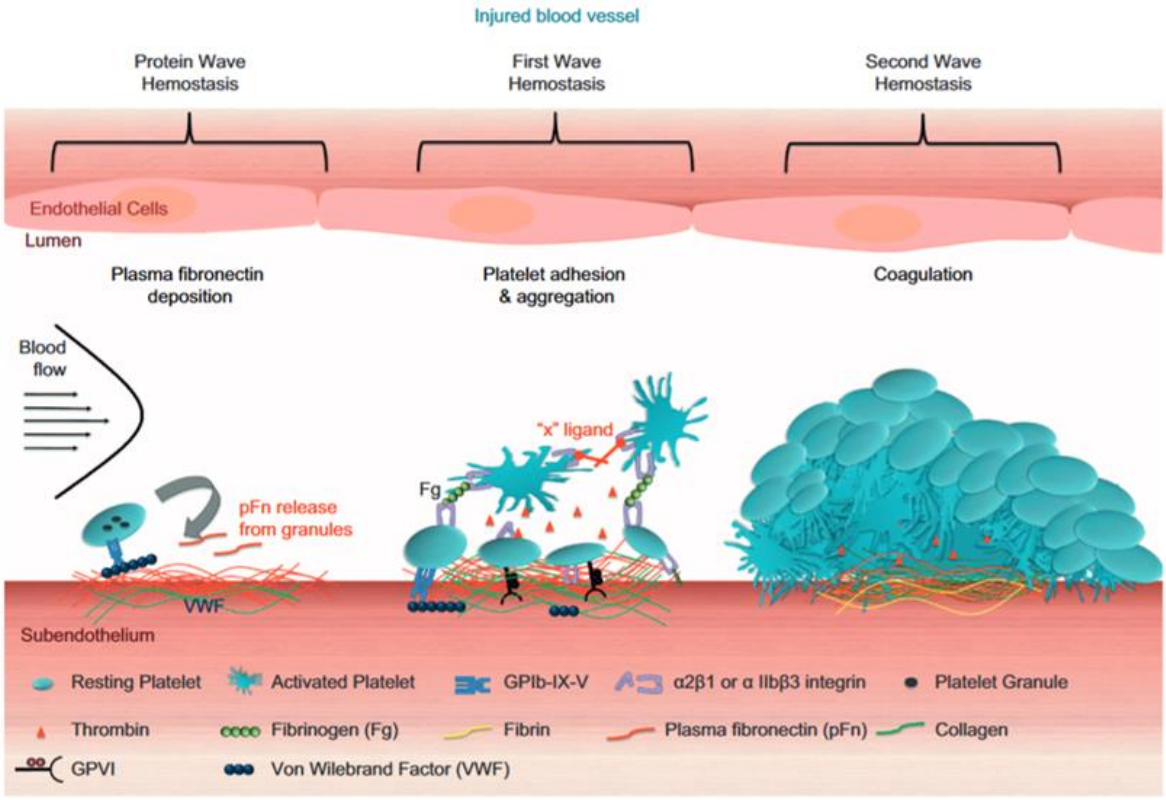

Figure 3. Overview of the process of platelet aggregation. Upon injury, the receptors or surface proteins on platelets bind to ligands, such as von Wilebrand factor (VWF) and collagen, activating integrin αiibβ3. This activation leads to binding of fibrinogen and subsequent platelet aggregation. Thrombin is generated on the negatively charged platelet surface and activates other platelets to undergo coagulation. This grows into formation of a hemostatic plug repairing the injured cell wall or region. This multifactorial process involves changes in interface dynamics of platelets, endothelial cells and other receptors. Adapted from [74].

Lipidomic analyses have shown that human platelets contain three major types of phospholipids i.e. phosphatidylcholine (40%), phosphatidylethanolamine (28%), sphingomyelin (18%) and less percentage of phosphatidylserine (9%) and phosphatidylinositol (3-5%). The ratio of cholesterol per phospholipid molecule was found to be 0.6 [61], [75], [76]. Among phosphatidylcholines, the ratio of saturated (S) phosphatidylcholines to unsaturated (U) phosphatidylcholines was found to be 0.71 (S/U). The exact distribution of the type of lipids and their chemical composition is shown in Table 1. Because platelets majorily contain phosphatidylcholine in their membranes, we considered it as our main phospholipid for developing biomimetic systems along with combination of sphingomyelin, cholesterol, phosphatidylserine and phosphoryl glycerol.

Fatty acid	Choline			Ethanolamine			Serine	Inositol
	Total	Diacyl	Plasmalogen	Total	Diacyl	Plasmalogen		
16:0	23.8 ± 1.2	27.7 ± 2.5	8.3 ± 0.3	8.5 ± 0.7	5.8 ± 0.2	1.0 ± 0.2		1.7
16:2 } 17:0 }	+		2.3 ± 0.7					
18:0	16.0 ± 0.8	15.0 ± 0.9	12.9 ± 0.3	17.2 ± 1.3	24.8 ± 1.7	0.5 ± 0.3	45.0	42.3
18:1	20.6 ± 1.8	24.8 ± 1.0	9.1 ± 2.0	6.7 ± 0.2	12.2 ± 1.3	2.2 ± 0.1	21.9	15.9
18:2	11.5 ± 0.5	11.8 ± 0.9	3.2 ± 0.4	1.9 ± 0.2	4.1 ± 0.5	1.1 ± 0.1	3.2	2.5
18:3 } * 20:0 }	1.5 ± 0.1	1.1 ± 0.1	3.3 ± 0.7		0.9 ± 0.1		0.9	
20:1	2.2 ± 0.4	2.0 ± 0.1	1.3 ± 0.8	2.0 ± 0.6	2.4 ± 0.3	0.5 ± 0.1	2.2	1.1
20:3	2.5 ± 0.1	1.9 ± 0.2	3.8 ± 0.4	1.1 ± 0.2	1.4 ± 0.3		1.9	0.9
20:4	14.7 ± 0.9	14.1 ± 2.0	12.8 ± 3.2	37.2 ± 1.1	31.1 ± 2.2	65.6 ± 1.0	16.8	32.5
20:un			1.1 ± 0.7					
20:5	2.2 ± 0.2	1.6 ± 0.2	9.5 ± 0.7	3.6 ± 0.3	3.0 ± 0.9	4.7 ± 0.9	3.8	1.8
20:un	0.8 ± 0.5		7.2 ± 0.8	2.3 ± 0.4	2.2 ± 0.7			
22:4†	0.3 ± 0.2			5.3 ± 0.8	2.3 ± 0.2	9.6 ± 1.0	4.3	1.3
22:5†	3.0 ± 1.5		16.8 ± 1.3	6.5 ± 0.9	4.6 ± 1.5	2.1 ± 0.1		
22:5†	0.9 ± 0.5		4.7 ± 0.7	4.3 ± 0.8	2.4 ± 0.4	7.3 ± 0.1		
22:6†			3.7 ± 1.3	3.4 ± 0.3	2.8 ± 0.6	5.4 ± 0.2		

Table 1. Distribution of phospholipid composition in human platelets. The different classes of phospholipids (e.g. cholines, ethanolamine, serine and inositols) are shown in terms of percentage of fatty acid content in diacyl and plasmalogen fractions. The values represent mean and standard deviation obtained from thin layer chromatography experiments. Adapted from [76]. + indicates trace amounts, *refers to lipids having same retention time, † indicates tentative identification.

2. Analysis of membrane interactions: modification and reorganization

The use of physical principles to a biological system dates back to 1848, when Du Bois Reymond measured the flow of electrical charges across the skeletal muscles [77]. With increase in the advancement of microscopy techniques, biological physics has taken center stage and is able to accurately determine changes in the membrane structure at nanometer resolution.

Atomic force microscopy (AFM) is a type of scanning probe microscope (Figure 4) developed by Binnig et al [78], which has the ability to obtain information at atomic resolution and gain sample mechanical properties like interaction force, elasticity etc. Also, its ability to provide information about morphological changes significantly enhances its utilization in single molecule studies. In this PhD thesis, AFM was used to obtain biomolecular interaction forces and sample topography.

In biomolecular interactions, apart from determining mechanistic changes, obtaining information on the loss of phospholipids from the cell membrane is another important property. This is observed in scenarios where inflammation leads to apoptosis

(programmed cell death), where the distribution of lipids in the cell membrane is modified, which acts as a trigger for immune cells to kill the infected cell [79].

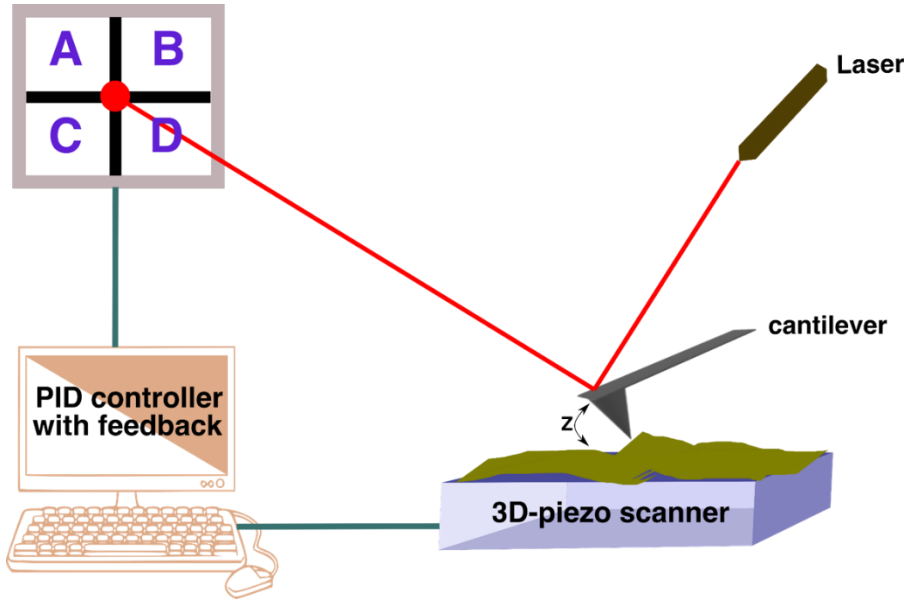

Figure 4. Schematic of an atomic force microscopy (AFM) setup. AFM consists of a controller, a piezo-scanner, a flexible cantilever onto which a probe of interest is mounted and a laser is illuminated on top of it. The movement (deflection) of the cantilever over the sample due to interaction forces is recorded by the quadrant photodiode detector.

Similarly, ruptures or pore formation to the cell membrane is also an indicator. Formation of blebs (removing part of cell membrane) from apoptotic cell are few biological examples of phospholipid loss induced during cell signaling [80]–[83]. Hence, detection of loss of phospholipids can be helpful in characterizing the type of cellular interactions.

One technique used to investigate the lipid loss from the membranes under $NO^{\cdot}$ stress is quartz crystal microbalance (QCM), a sensitive weighing scale which detect masses in the range of nanograms. The detection occurs on an oscillating quartz crystal which generates acoustic waves at its resonant frequency (5 MHz). Upon mass deposition, the frequency of the oscillation changes and is detected by the electrodes attached to the crystal on application of alternative current (AC) voltage (Figure 5). Such minute detection is possible due to the piezoelectric nature of quartz crystal. For biological samples, adsorption also depends on the rheological properties like hydration etc. which can influence the overall mass deposition. Therefore, to quantify such changes, along with frequency, detection of energy loss i.e. dissipation is also carried out. This is achieved by using quartz crystal microbalance with dissipation (QCM-D) detection. We use this technique [84], [85] to

observe the phospholipid loss. In this PhD thesis, molecular interactions of lipid bilayers were measured on SiO_2-coated quartz crystals as mentioned in **Article III**.

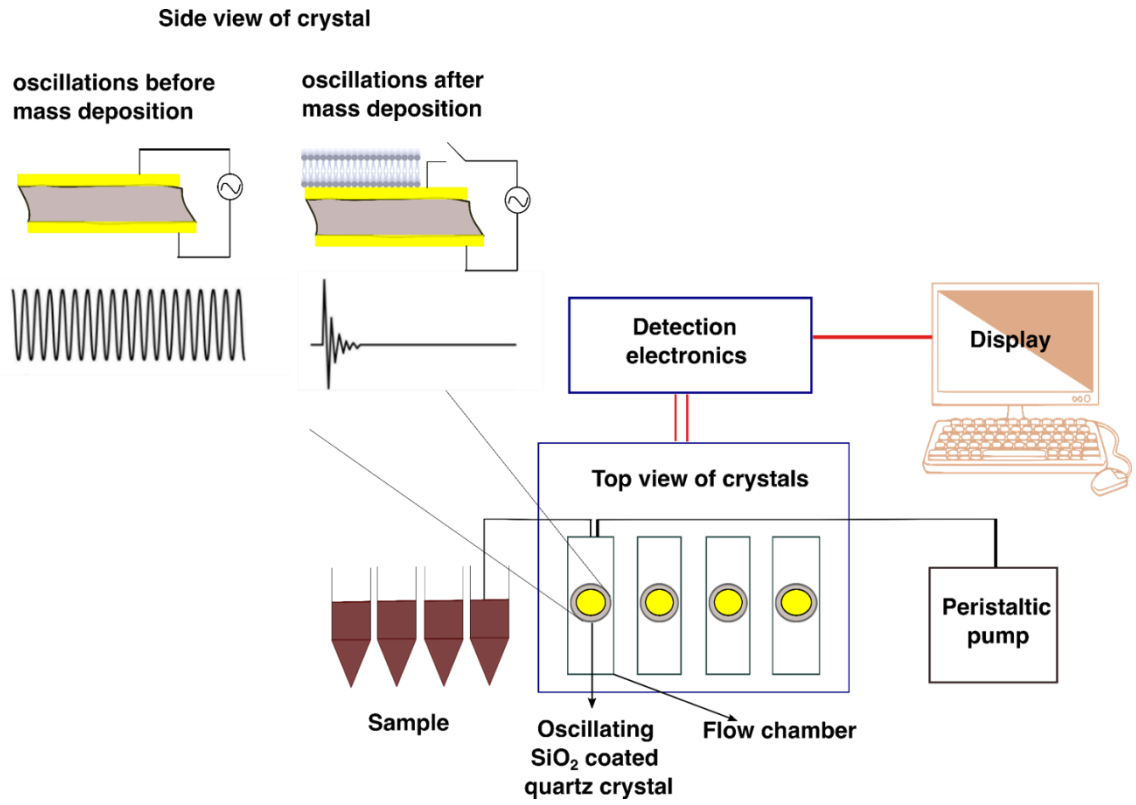

Figure 5. Schematic of quartz crystal microbalance with dissipation (QCM-D) setup. Four temperature-controlled flow chambers, each containing SiO_2-coated quartz crystal, are available. Electrodes are attached on the front and back of the crystal which measures frequency and dissipation values using detection electronics. The sample is flown through each of the crystal using a peristaltic pump for mass deposition. Upon mass deposition, dampening of the frequency occurs (as shown in the 'Side view of crystal'), which is used to gain information about the molecular interactions. Schematic adapted from *Biolin Scientific/Q-Sense* (*www.biolinscientific.com/measurements/qcm-d*) and *Nanoscience instruments (www.nanoscience.com/techniques/quartz-crystal-microbalance/) as accessed on 14 Nov 2020*.

2.1 Monitoring lipid membrane permeability and physico-chemical modifications

Nitric oxide ($NO^{\cdot}$) can act, depending on its concentration, either as a signaling molecule or a reactive species [45]. As the site of $NO^{\cdot}$ generation and its action are usually far away, $NO^{\cdot}$ has to cross through multiple lipid barriers. The translocation effectively depends on membrane hydrophobicity and composition through which it has to permeate [86]. Because, it is a relatively unstable radical, its conversion to $NO^{\cdot}$-related products can have indirect effects on the surrounding biomolecules because aerobic conditions are more prevalent [87]. Very few evidences on the influence of phospholipid composition on $NO^{\cdot}$ diffusion and respective membrane modifications are available. Presence of cholesterol is

known to reduce the diffusion of $NO^{\cdot}$ by ~20-40% [88]–[90], thereby increasing its time in the center of the hydrophobic spaces and affecting lipid membrane fluidity. The maximal steady state concentration of $NO^{\cdot}$ found on the surface of cell membrane is estimated to not exceed 5 µM [46] and $NO^{\cdot}$ starts to disappear rapidly mainly through autoxidation in water. This is an indication of the short half-life of $NO^{\cdot}$. To detect whether $NO^{\cdot}$ behaves like a pro-oxidant and causes physico-chemical changes to the phospholipids, molecular characterization was carried out on supported lipid bilayers (SLBs) with distinct phospholipid composition.

In the study highlighted in **Article I** we used a combination of saturated lipids (phosphatidylcholine (14:0) and phosphoryl glycerol (14:0)), monounsaturated lipids (phosphatidylcholine (16:0-18:1) and phosphatidylserine (16:0-18:1)) and lipid rafts containing monounsaturated phosphatidylcholine (16:0-18:1), sphingomyelin and cholesterol [91]. Each of these lipidic systems were subjected to different $NO^{\cdot}$ concentrations (not exceeding steady state concentration of 5 µM) using a donor molecule (1-Hydroxy-2-oxo-3-(3-aminopropyl)-3-isopropyl-1-triazene, abbreviated as NOC-5) and lipid membrane characteristics were investigated. Using atomic force microscopy, we determined the height profiles of lipid bilayer and membrane permeability. For permeability studies, adhesive forces i.e. AFM tip pull-off forces of the membrane were measured. Normally, when phospholipids are subjected to radical attack, they undergo peroxidation. Lipid peroxidation involves three steps i.e. formation of a lipid radical (*initiation*) followed by formation of peroxyl radical (*propagation*) until an antioxidant stops the propagation (*termination*) [92], [93]. In case of strong radicals like hydroxyl, the propagation step is very long and causes formation of reactive oxidized products like aldehydes, ketones, alkanes, etc. [94]. These formed reactive products serve as markers for peroxidation. Malondialdehyde is one such reactive aldehyde. We also studied whether these reactive aldehydes are formed upon reaction with $NO^{\cdot}$ (as it is a less reactive radical when compared to hydroxyl). Saturated lipid bilayers showed little to no effect on treatment with low concentrations of $NO^{\cdot}$. The lipid membrane permeability and bilayer thickness remained unaltered [91]. At high concentration, a slight decrease in membrane permeability was observed. This perturbation is believed to be mainly due to penetration of $NO^{\cdot}$ deep into the hydrophobic core altering the movement of lipid chains [95]. At low $NO^{\cdot}$

concentrations, unsaturated lipid bilayers showed a significant reduction in the bilayer thickness, but its permeability was unchanged [91]. The decrease in bilayer thickness caused tighter packing of phospholipid molecules trying to maintain membrane integrity [96], [97]. This, effectively reduces the diffusion of $NO^{\cdot}$ molecule out of the hydrophobic space and correlates with the unaltered membrane permeability. However, at high $NO^{\cdot}$ concentrations, complete disruption of unsaturated lipid bilayer occurred [91]. In case of lipid rafts, along with $NO^{\cdot}$, we also modulated the concentration of sphingomyelin and observed its effect on maintaining membrane integrity. At equal concentrations of sphingomyelin and cholesterol, $NO^{\cdot}$ had no influence on the membrane characteristics [91]. This was prevalent at both low and high $NO^{\cdot}$ concentrations. When concentration of sphingomyelin was increased (with cholesterol concentration fixed throughout), $NO^{\cdot}$ acted like a pro-oxidant reducing the membrane thickness and increasing the membrane permeability [91]. In lipid rafts, where sphingomyelin was absent and cholesterol was present, $NO^{\cdot}$ caused decrease in membrane permeability and thickness at both $NO^{\cdot}$ concentrations. Generally, proton flux is increased and water permeability is decreased in sphingomyelin- and cholesterol-rich bilayers [98]. However, presence of $NO^{\cdot}$ can alter this equilibrium. The oxidation of lipid molecules by $NO^{\cdot}$ was confirmed by the formation of malondialdehyde [91] highlighting the regulatory role of sphingomyelin along with $NO^{\cdot}$ in lipid rafts. The cross-talk of $NO^{\cdot}$ and sphingomyelin has previously been observed inside cell's sphingolipid metabolic pathways leading to inflammation and enhancing the iNOS activity [99], [100], but its continued action on membrane's sphingomyelin underlines its increased role post-sphingolipid formation.

2.2 Detecting changes in the integrin αiibβ3-RGD ligand interactions

Biological membranes are not only composed of phospholipid molecules; they also comprise of proteins which can either traverse through them (transmembrane) or attach to lipid surface. As mentioned before, the lipid-to-protein ratio is estimated to be 40:1 [12] in eukaryotic system. Such composite structures make all the components of cell membrane equally susceptible to $NO^{\cdot}$ radical attack. Proteins which contain reactive amino acids (e.g. cysteine, methionine, histidine, tyrosine, tryptophan and phenylalanine) can undergo modifications in response to radical [101]. These modifications can lead to either structural instability (e.g. protein misfolding) or loss of functionality (Figure 6). Cysteine and

methionine, sulphur-containing amino acids are highly sensitive to radicals [102], [103] when compared to other amino acids.

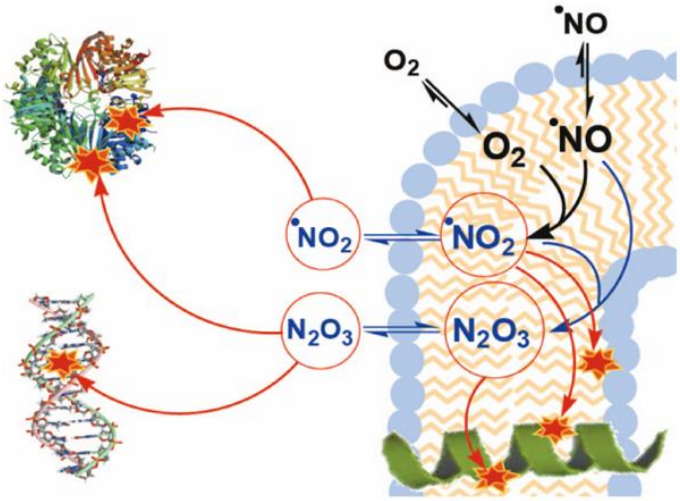

Figure 6. Direct and indirect effects of nitric oxide at the membrane interface. $NO^{\cdot}$ can directly interact with the lipid membrane or react with oxygen (indirectly) forming NO_2 or N_2O_3. These nitric oxide products can oxidize, nitrosate and nitrate lipids and proteins in the lipid membrane. The formation of NO_2 or N_2O_3 is predominant due to higher solubility of $NO^{\cdot}$ and oxygen into the hydrophobic spaces. However, the products can diffuse into the aqueous phase attacking the biomolecules at the interface depending on the location. Adapted from [42].

Integrin αiibβ3, a transmembrane protein present on the platelet cell surface is a mechanosensor responsible for platelet aggregation and its dynamics can be modulated in presence of a free radical. Every transmembrane protein has three distinct regions i.e. an external part (called as ectodomain) facing the hydrophilic/extra-cellular interface, transmembrane domain embedded inside the bilayer and internal domain facing the cytoplasm. Several crystal structure studies are available in the protein database (PDB), but the complete structure (consisting of all domains) of integrin αiibβ3 has not yet been elucidated [104]. From the available structural sequence, it is known that integrin αiibβ3 (consisting of two subunits α and β) contains multiple cysteine residues (18 in α-subunit and 56 in β-subunit) [105]. While most of them are denoted to maintain the structural integrity, 7 cysteine residues are present in the ectodomain of integrin αiibβ3 [106] and contribute to protein functionality. These residues in the ectodomain can easily undergo $NO^{\cdot}$ attack leading to protein modification. While reduced platelet adhesion and chemical modification (i.e. S-nitrosylation) of integrin αiibβ3 by $NO^{\cdot}$ is described [107], [108], little is known about possible protein changes in the lipid bilayer. To determine this, single

protein studies were carried out. For this purpose, integrin αiibβ3 was reconstituted into specialized lipid membrane systems called nanodiscs [105]. An advantage was the fact that we were able to incorporate (reconstitute) one integrin molecule per lipid bilayer (called proteonanodiscs). The controlled regulation on the size of nanodiscs and number of proteins per nanodisc proved advantageous for single molecule force spectroscopy analysis. The study has been described in **Article II**.

In normal circulating blood, integrin is in an inactive conformation and is activated in presence of ligands [109]. These ligands contain peptide sequence RGD (Arginine-Glycine-Aspartate) which binds to the ectodomain of the integrin protein. Hence, determining the interaction force (rupture force) between RGD peptide and the integrin protein under $NO^{\cdot}$ influence will clarify the possible protein-membrane characteristics. High rupture forces between the ligand and integrin αiibβ3 indicate strong interactions between them and *vice-versa*.

To detect the rupture forces, only by the protein and not due to any other interfering biomolecules, protein reconstitution was done in a saturated lipid system as described in **Article I**. Also, the $NO^{\cdot}$ concentrations were limited to 1 µM, as these showed stability of the lipid membranes as seen in **Article I**. For integrin αiibβ3-RGD ligand interaction studies, the bent state of integrin αiibβ3 was exposed to $NO^{\cdot}$ and RGD ligand was allowed to interact. It was found that at low $NO^{\cdot}$ concentrations, the rupture forces generated were similar to those forces characteristic for the bent state of integrin αiibβ3 [105]. Increasing $NO^{\cdot}$ concentrations, generated higher rupture forces. Initially, these results highlighted that addition of $NO^{\cdot}$ changed the conformation of integrin αiibβ3 from inactive (bent) to active state [105]. When AFM imaging was carried out, it was seen that integrin αiibβ3 proteins were released from respective proteonanodiscs (i.e. nanodiscs containing integrin) and aggregated. The high rupture forces detected by the RGD ligand were due to the interaction with these integrin αiibβ3 aggregates [105]. The morphological observation suggested that although the structural integrity of integrin αiibβ3 is disturbed, its functionality may not be affected. The aggregation behavior was, however, concentration-dependent i.e. a critical concentration of 0.5 µM $NO^{\cdot}$ was observed over which all the integrin αiibβ3 was completely removed from proteonanodiscs as described in **Article II**. This observation was also confirmed by dynamic light scattering measurements, which showed that the hydrodynamic diameters of proteonanodiscs started to reduce with $NO^{\cdot}$ addition, indicating

loss of integrin αiibβ3 [105]. To overrule the chances of protein destabilization due to lipid modification, height profiles of empty nanodiscs under different $NO^{\cdot}$ concentrations were determined and the membrane thickness was found to be intact throughout. This confirmed that the loss of integrin αiibβ3 structure is mainly due to protein-radical interaction. When compared, the thickness of empty nanodiscs and the proteonanodiscs which released integrin αiibβ3 had a difference of 1 nm [105]. This difference in height is explained by two possibilities; i) it shows the space occupied by single integrin molecule when present inside the lipid bilayer, and ii) during the release of integrin from the lipid bilayer, few of the phospholipids attached to the transmembrane domain of integrin αiibβ3 were also released thereby reducing the thickness. If the second scenario prevails, then this action is similar to the release of microparticles from platelet cell membrane in response to an inflammation during apoptosis [110]–[113]. These released platelet microparticles have constituents of cell membrane (usually phospholipids and integrin proteins) and function as signaling molecules. To check for any amino acid modification in integrin αiibβ3, UV-visible spectroscopy analysis was performed and the amide bond peaks at 202 nm which correspond to cysteine residues were diminished post $NO^{\cdot}$-treatment [105] indicating cysteine modification by $NO^{\cdot}$. Because $NO^{\cdot}$ is an unstable radical with high reactivity, products of $NO^{\cdot}$ autoxidation were also measured. Direct $NO^{\cdot}$ concentration was measured using an amperometric sensor and the nitrites formed were detected using the Greiss assay, an absorbance-based method. High concentrations of nitrite and low $NO^{\cdot}$ concentrations were detected [105].

2.3 Encountering the cell membrane damage: Nanoparticles

During inflammation, the cell lines in the vicinity of the inflamed region are common targets of unprovoked damage (e.g. in chronic inflammation related diseases). The unprovoked damage interrupts normal functioning of the surrounding healthy cell, which might trigger unrelated and persistent cascade effects. Also, in biological system, $NO^{\cdot}$ is produced by nitric oxide synthase enzyme (NOS). As mentioned before, eNOS and nNOS are membrane bound enzymes found in epithelial and neuronal cells, while iNOS is activated in response to inflammation [48]. Generally, actions of eNOS and nNOS are positive for the cell, but are regulated to toxicity in presence of iNOS [114]–[116]. For successful functionality of platelets, endothelial cells must interact with the focal adhesion

points i.e. integrins of platelets and regulate the blood clotting mechanism [117] through the extracellular matrix (as platelet aggregation is a multifactorial physiological process). However, any disturbance of its activity will lead to dysfunction as reported in **Article II** where structure and function of integrin protein are lost. Also, damage to the endothelial cell barrier cannot be neglected (observed in diseases where $NO^{\cdot}$ imbalance is predominant [118]–[120]). In such a contradicting scenario, either the inflammation region must be targeted (i.e. iNOS activity should be controlled) without causing unwarranted action (i.e. only eNOS/iNOS should be present) to the neighboring cells. Another alternative is providing assisted approach, that can help in retaining the biological activity of platelets. Such a targeted approach with relevant surface modifications can be answered by the use of nanoparticles as an exogenous delivery method to encounter the membrane damage [121].

Nanoparticles (NPs) are materials with size smaller than 100 nm and can be engineered to target a specific response [122]. The unique features of nanoparticles are its high surface-to-mass ratio, ability to adsorb different compounds on its surface (i.e. proteins, lipids, carbohydrates, polymers, etc.), biocompatibility and faster development making them best candidate [123]. NPs can be composed of different materials which can be either of biological (e.g. phospholipids, lipids biopolymers, etc.) or non-biological (e.g. metals) origin [124]. Gold nanoparticles (AuNPs) due to their distinct physical, chemical and optoelectronic properties along with excellent biocompatibility and low toxicity makes them ideal source for preparation of NPs [125]–[127]. Naturally occurring polymers (also called biopolymers) from living organisms can easily be attached onto the surface of AuNPs providing the required therapeutic application. The main advantage of biopolymers is its biodegradability [128]. A well-established and understood biopolymer with a significant implication in the blood clotting management is chitosan, which is a linear polysaccharide derived from marine animals and found abundantly in nature [129]. Chitosan is structurally similar to cellulose except the presence of nitrogen moiety in C-2 instead of hydroxyl group (as seen in cellulose) [130]–[132]. Along with application in wound management, chitosan also has anti-microbial activity. In situations as presented in **Article II**, chitosan can act as a therapeutic agent assisting platelet activity without damaging the surrounding environment (i.e. the membrane integrity of endothelial cells and platelet cells should remain intact in presence of chitosan, but its action with the

extracellular matrix and other surface proteins for blood clotting should continue). To answer few of these questions, AuNPs were coated with chitosan and their action on lipid membranes was studied as described in **Article III**.

Because the inflammation region is surrounded by $NO^{\cdot}$ imbalance, the efficacy of chitosan (Mw ~600 kDa) coated AuNPs under the influence of $NO^{\cdot}$ was also studied. For this study, saturated phosphatidylcholines (14:0) was selected as model lipids as phosphatidylcholines are the highest fraction of phospholipids found in both platelets and endothelial cells [133]–[135]. This study was conducted in near physiological conditions to mimic the behavior of circulating blood i.e. at 37 °C, pH 7.4 with AuNPs flowing at rate of 100 µL/min. These flowing AuNPs were allowed to interact with supported lipid bilayer and the interactions were studied using QCM-D and *in-situ* AFM imaging.

Post characterization of chitosan-coated AuNPs (in terms of size, shape and charge), the NPs were allowed to come in contact with the lipid bilayer and immediate removal of phosphatidylcholine molecules on interaction were detected from QCM-D measurements [136]. The loss of phospholipid molecules corroborated with reduced thickness of bilayer and increased membrane surface heterogeneity as observed in AFM images [136]. Due to the fact that chitosan is an aminoglycan, its interaction with the headgroup of phospholipid is possible. The disruption of membrane is believed to be due to electrostatic and hydrogen bonding between the chitosan and lipid molecules [136]. The changes in the viscoelastic properties were not significant enough when dissipation data was observed qualitatively in QCM measuerements. As the chitosan-coated AuNPs were under constant flow, the amount of lipid loss was restricted to the upper leaflet of the membrane. Formation of deep pockets or holes were not visible, but membrane reorganization was expected [136]. The minimalistic disruption of lipid bilayer with chitosan-coated AuNPs was similar to that of pure chitosan reported earlier [137]–[139]. To check if $NO^{\cdot}$ imbalance influences the AuNPs-membrane interactions, chitosan-coated AuNPs treated with $NO^{\cdot}$ were allowed to interact with lipid bilayer. Initially, the zeta-potential (i.e. surface charge) of chitosan-coated AuNPs reduced from 30 mV to 23.1 mV indicating a modification of the amino group present on the chitosan molecule with $NO^{\cdot}$ [136], but its functionality on the lipid bilayer appeared less perturbed, i.e. a gradual (instead of immediate) removal of phospholipids from the bilayer was observed. AFM imaging revealed that the stability of

chitosan-coated AuNPs was reduced significantly and chitosan molecules were released from the gold surface and formed aggregates [136].

Dextran biopolymer, on the other hand is a branched polysaccharide derived from bacteria and is known as an anti-coagulant i.e. it reduces platelet aggregation [140]–[142]. Its ability to reduce inflammatory response is also well known [143]. The branching nature of polysaccharides is theorized to be the reason for its above responses [144]. We tested its interaction with the lipid bilayer in comparison with chitosan-coated AuNPs. In this study, as highlighted in **Article III**, we used dextran (Mw ~10 kDa) coated AuNPs and found that these NPs started to interact with the lipid bilayer after 5 min and followed a continuous removal of lipid bilayer from the supported surface [136]. AFM imaging revealed that dextran-coated AuNPs disrupted the complete bilayer (upper and lower leaflet) leading to a total loss of phospholipids. This kind of disruption significantly changed the viscoelastic properties of lipid bilayer as observed from the dissipation data of QCM-D [136]. Structurally, dextran contains hydroxyl groups which will form H-bonds with the phospholipids. Also, steric hindrances will not be observed by dextran-coated AuNPs (unlike in case of chitosan). An interaction model has been proposed explaining the removal of phospholipids by chitosan- and dextran-coated AuNPs. The model takes into consideration, the chitosan deacetylation, molecular weight, flow conditions and possible chemical interactions. In terms of size, the engineered NPs (hydrodynamic diameters of ~55 nm for chitosan coated AuNPs and ~37 nm for dextran coated AuNPs) are similar to the size of particle aggregates available in the cell (i.e. lipoprotein particles, protein assemblies, exosomes and vesicles). In cells, these biological particles are consumed by pinocytosis [145], [146]. Formation of holes, which occurs during internalization, was visible for dextran-coated AuNPs treatment [136]. Adhesion of engineered AuNPs on bilayers (for either of biopolymer coating) was not observed, most probably due to the continuous flow of AuNPs. When dextran-coated AuNPs were treated with $NO^{\cdot}$, the interaction was found only to be delayed, but its action was not influenced. It also led to the disruption of lipid membranes. Unlike chitosan-coated AuNPs, dextran-coated AuNPs did not show any loss of ligand from the gold surface [136]. The surface charge of the dextran-coated AuNPs was found to be increased. We believe that modification of the hydroxyl groups of dextran is not expected because these are secondary alcohol groups and under the defined experimental conditions, a catalyst would be needed for chemical

modifications [136]. Combining these results, it was observed that the action of engineered AuNPs was localized on the cell membrane surface. Chitosan-coated AuNPs can assist in platelet activity [147] even under $NO^{\cdot}$ radical environment without disrupting the phosphatidylcholines organization significantly, however dextran-coated AuNPs are efficient in complete disruption of lipid bilayer.

2.4 Multifunctional roles of nanoparticles in circulating environment

$NO^{\cdot}$-induced protein misfolding or aggregate formation as presented in **Article II** arises the possible diversifications of similar structural and physical changes by other proteins containing reactive amino acids such as cysteine, tyrosine, etc. [54], [148], [149]. Presence of such aggregates can contribute to significant restriction to the blood flow. These aggregates are typically insoluble and are referred to as amyloidogenic proteins [150], [151] or amyloids with characteristic ß-structure [152] which enhances their toxicity. Among amyloids circulating in blood, insulin-derived amyloids are triggered by increased iNOS activity [153]–[156]. The increased inflammation also causes resistance to the release of insulin normally in human body (i.e. by the pancreatic beta cells in diabetes patients). The iNOS induced changes are capable of reducing the pH of local environment, which causes attachment of these amyloid proteins on to the surface of cell membrane and further enhance the attachment of misfolded proteins [157], [158]. Such adhesions to the lipid bilayer are shown to permeabilize the membrane, cause pore formation by interacting with the acyl chains of lipids and increase cytotoxicity depending on the lipid composition [159]–[161], similar to behaviours described in **Article I**. Amyloid formation is a multistep method where the initial misfolded protein monomers aggregate to form oligomers containing ß-structures (*nucleation* phase). These oligomers undergo structural rearrangments to form long strands called protofibrils (*elongation* phase), which on saturation form mature amyloid fibrils (*saturation* phase) [162]. We explored whether the action of such polysaccharide-coated AuNPs can be extrapolated to other misfolded protein scenarios [163]–[167] such that pathological response could be reduced (i.e. reduction in damage to cell membrane if adsorped as seen in **Article III**) or whether the kinetics of the fibril formation can be controlled. This multifaceted study is described in **Article IV**.

In this study, two variants of AuNPs coated with linear and branched polysaccharides were used and the kinetics of human insulin fibril growth was investigated. Dextrin- and

chitosan-coated AuNPs (linear polysaccharide) and Dextran-10 and Dextran-40 (both differing in molecular weights) coated AuNPs (branched polysaccharide) were allowed to interact with insulin fibrils prepared *in-vitro* [168]. AFM imaging showed that upon interaction with Dextran-10 and Dextran-40 coated AuNPs, insulin fibrils became slightly less thick and shorter in length. However, a significant number of oligomer formation were detected [168]–[170]. A drawback here was that, transmission electron microscopy (TEM) analysis showed extensive aggregation of these coated AuNPs on the surface of insulin fibrils, which is believed to reduce their action. Dextrin-coated AuNPs rather showed a different behavior i.e. the insulin fibrils rather than being long, were very short and thick (in comparison with Dextran-10 and Dextran-40 coated AuNPs). The oligomers detected were also very thick, but less concentrated in comparison to branched polysaccharide-coated AuNPs. [168]. Chitosan-coated AuNPs on the other hand, caused extreme thinning of insulin fibrils and hardly any oligomers were detected.

The change in the physical characteristics of insulin fibrils were confirmed with circular dichroism spectroscopy, a technique which detects the secondary structure of proteins. It was found that while all biopolymers suppressed the transition of protein secondary structure from α-helix to ß-sheets, dextrin and chitosan coated AuNPs inhibited it completely and the inhibition depended on the concentration of AuNPs [168]. A proposed mechanism of inhibition based on electrostatic repulsion and hydrogen bonding between insulin fibrils and biopolymer-coated AuNPs, which might be responsible for thinning and shortening of fibrils, has been shown. While the coated AuNPs were effective, investigating their cytotoxicity was crucial for their use in drug-delivery applications. For this purpose, their influence on the viability of pancreatic (PaTu-T and PaTu-S) cell lines was investigated. Pure insulin fibrils added to the above cell lines decreased the cell viability rapidly, while addition of biopolymer-coated AuNPs induced a higher cell viability. In comparison to the different types of biopolymer-coated AuNPs, chitosan- and dextrin-coated AuNPs showed increased viability compared to dextran-10 and dextran-40 coated AuNPs [168]. It was observed that chitosan-coated AuNPs can inhibit the growth of insulin fibril formation as reported in **Article IV** without causing significant disruption to the phospholipids (as described in **Article III)** even under $NO^{\cdot}$ environment.

3. Summary and Outlook

The cell membrane is a complex biological network with multiple variables and parameters. In this PhD thesis, we aimed to understand from a biophysical point of view how the membrane equilibrium is disturbed in response to nitric oxide radical. We focused on answering some specific questions:

1) How the cell membrane permeability and bilayer thickness would be influenced by the nitric oxide radical when different compositions of phospholipids are present?
2) How (in a more complex system) a transmembrane protein incorporated into the bilayer interacts with the nitric oxide radical?
3) How can we overcome any negative effects encountered by the phospholipids and proteins present in the lipid bilayer?

Nitric oxide is a least reactive radical whose action is concentration-dependent. At low concentrations, it works as a signaling molecule and assists in cell metabolism and other important pathways. Increased concentration of nitric oxide converts it into a pro-oxidant and toxic molecule which can cause significant damage to the cells. This is observed in diseases linked to chronic inflammation.

Due to its higher partition coefficient into the membranes, we first investigated how toxicity of nitric oxide influences the normal functioning of lipid membranes. We studied the action of nitric oxide on three different compositions of phospholipids i.e. saturated, unsaturated and lipid rafts as described in **Article I** [91]. We found that saturated lipids have the very least impact of nitric oxide on its membrane permeability. At concentrations detected on the surface of cell membrane, the bilayer thickness and permeability were unaltered. Unsaturated phospholipids had a linear change with nitric oxide toxicity. Lipid bilayer underwent gradual disruption causing loss of membrane permeability and alteration of its thickness. However, an unexpected phenomenon was observed in case of lipid rafts. The concentration of sphingomyelin influenced the action of nitric oxide on the bilayer. When sphingomyelin and cholesterol were in equal ratios, the membrane was not perturbed even at higher nitric oxide concentration and its membrane permeability and thickness remained the same. If sphingomyelin concentration was greater than cholesterol, then sphingomyelin along with nitric oxide caused an increase in membrane permeability and reduction in the

thickness of lipid bilayer. Both of these components combine to show pro-oxidant nature causing damage to the membranes.

After understanding phospholipid-nitric oxide radical interactions, we inspected protein-nitric oxide radical interactions. For this purpose, we have chosen the transmembrane protein integrin αiibβ3 reconstituted in nanodiscs, lipidic systems mimmicking platelets. In **Article II** [105], we observed that with increase in concentration of nitric oxide, integrin αiibβ3 reconstituted in a lipid membrane underwent significant structural modifications, which led to its release from the lipid bilayer and its aggregation. Modification of the cysteine residues present in integrin αiibβ3 was observed upon treatment with nitric oxide. Also, we found that along with nitric oxide, high concentrations of nitrite were detected.

To encounter the loss of platelet functionality due to structural damage to integrin αiibβ3, naturally occurring polymers (biopolymers) were considered as solution. Chitosan is a linear polysaccharide which is known to enhance and assist in platelet aggregation. We investigated its efficacy in a redox environment and the impact on lipid membrane interface as described in **Article III** [136]. Chitosan-coated gold nanoparticles interacting with lipid bilayers made of saturated phosphatidylcholines caused localized disruption and removal of phospholipids from the bilayer. The removal of lipid mass was limited only to the upper leaflet of the membrane. This caused a slight reduction in the thickness of lipid bilayer and increased lipid packing, but the membrane appeared intact due to some kind of thermodynamic equilibrium. This behavior was unaltered even in presence of nitric oxide radical, except the stability of coated nanoparticles were reduced but the functionality of chitosan was not affected. This was not observed in dextran-10 coated gold nanoparticles which caused complete disruption of lipid bilayer and caused formation of holes.

We further explored whether the nanoparticles can be potentially used in a multifunctional role and treat other pathophysiological conditions arising due to chronic inflammation and increased nitric oxide concentration. In **Article IV** [168], different polysaccharide-coated gold nanoparticles interacted with insulin amyloid fibrils, which can undergo adhesion with cell membrane and increase toxicity and, at same time, cause restriction to the blood flow. Polysaccharides from dextran family i.e. dextrin, dextran-10 and dextran-40 and chitosan-coated gold nanoparticles were incubated with insulin fibrils and it was found that each of these biopolymers were able to reduce the thickness of the fibrils and reduce their growth

to oligomers. However, dextrin- and chitosan-coated gold nanoparticles were found to be most effective, not only in reducing the thickness of the insulin fibrils, but themselves did not undergo aggregation. Also, they showed reduced cytotoxicity in comparison to other nanoparticles and inhibited the transition of protein structure from α-helices to ß-sheets.

Combining all the different carried studies, we investigated the nitric oxide-induced toxicity to lipids and proteins and assessed the consequences in an elementary fashion. The sequential methodology followed here helped us to understand what kind of combinatorial approach needs to be determined when nitric oxide radical is present in the surrounding environment. We then moved from identification of the problem to solving it by using biopolymer-coated nanoparticles. Such biopolymer-coated nanoparticles can be applied as potential solution to other similar proteins facing similar consequences.

This fundamental research gives an insight into the multi-dimensional biological questions which can be answered using biomimetic systems. With experimental conditions prevalent closer to physiological conditions, a small effort was made in this dissertation to answer some of the common prevailing clinical questions related to nitric oxide's pro-inflammatory role in chronic inflammation related diseases. Biophysical and bioanalytical elucidations under a given set of conditions can be used as a blueprint for a specific cellular function.

Further attempts and research is needed to increase the complexity of the biomimetic system by moving from supported lipid bilayers to vesicles (representing cell size) and understanding the membrane mechanics. As cell-cell interactions are key to any cellular activity, development of asymmetric synthetic systems (as phospholipid distribution is heterogenous in cell membrane) with required cellular components (at interface and cytosol) in a bottom-up approach method will help in mapping the complete mechanism of any protein functionality under investigation.

4. References

[1] P. Mazzarello, “A unifying concept: the history of cell theory,” *Nat Cell Biol*, vol. 1, no. 1, pp. E13–E15, May 1999, doi: 10.1038/8964.

[2] I. Ellinger and A. Ellinger, “Smallest Unit of Life: Cell Biology,” in *Comparative Medicine*, E. Jensen-Jarolim, Ed. Vienna: Springer Vienna, 2014, pp. 19–33.

[3] N. E. Ziółkowska, R. Christiano, and T. C. Walther, “Organized living: formation mechanisms and functions of plasma membrane domains in yeast,” *Trends in Cell Biology*, vol. 22, no. 3, pp. 151–158, Mar. 2012, doi: 10.1016/j.tcb.2011.12.002.

[4] R. R. W. Wayne Albers, “Cell Membrane Structures and Functions,” in *Basic Neurochemistry*, Elsevier, 2012, pp. 26–39.

[5] G. Li and H. Wang, Eds., *Membrane Biophysics: New Insights and Methods*, 1st ed. 2018. Singapore: Springer Singapore : Imprint: Springer, 2018.

[6] R. Nussinov, “The spatial structure of cell signaling systems,” *Phys. Biol.*, vol. 10, no. 4, p. 045004, Aug. 2013, doi: 10.1088/1478-3975/10/4/045004.

[7] M. F. Garcia-Parajo, A. Cambi, J. A. Torreno-Pina, N. Thompson, and K. Jacobson, “Nanoclustering as a dominant feature of plasma membrane organization,” *Journal of Cell Science*, vol. 127, no. 23, pp. 4995–5005, Dec. 2014, doi: 10.1242/jcs.146340.

[8] M. Cebecauer, M. Spitaler, A. Serge, and A. I. Magee, “Signalling complexes and clusters: functional advantages and methodological hurdles,” *Journal of Cell Science*, vol. 123, no. 3, pp. 309–320, Feb. 2010, doi: 10.1242/jcs.061739.

[9] T. Harayama *et al.*, “Lysophospholipid Acyltransferases Mediate Phosphatidylcholine Diversification to Achieve the Physical Properties Required In Vivo,” *Cell Metabolism*, vol. 20, no. 2, pp. 295–305, Aug. 2014, doi: 10.1016/j.cmet.2014.05.019.

[10] B. Antonny, S. Vanni, H. Shindou, and T. Ferreira, “From zero to six double bonds: phospholipid unsaturation and organelle function,” *Trends in Cell Biology*, vol. 25, no. 7, pp. 427–436, Jul. 2015, doi: 10.1016/j.tcb.2015.03.004.

[11] S. Grösch, S. Schiffmann, and G. Geisslinger, “Chain length-specific properties of ceramides,” *Progress in Lipid Research*, vol. 51, no. 1, pp. 50–62, Jan. 2012, doi: 10.1016/j.plipres.2011.11.001.

[12] L. Di *et al.*, “Evidence-based approach to assess passive diffusion and carrier-mediated drug transport,” *Drug Discovery Today*, vol. 17, no. 15–16, pp. 905–912, Aug. 2012, doi: 10.1016/j.drudis.2012.03.015.

[13] C. A. Hubner, “Ion channel diseases,” *Human Molecular Genetics*, vol. 11, no. 20, pp. 2435–2445, Oct. 2002, doi: 10.1093/hmg/11.20.2435.

[14] F. R. Maxfield and I. Tabas, “Role of cholesterol and lipid organization in disease,” *Nature*, vol. 438, no. 7068, pp. 612–621, Dec. 2005, doi: 10.1038/nature04399.

[15] J. T. Marinko, H. Huang, W. D. Penn, J. A. Capra, J. P. Schlebach, and C. R. Sanders, “Folding and Misfolding of Human Membrane Proteins in Health and Disease: From Single Molecules to Cellular Proteostasis,” *Chem. Rev.*, vol. 119, no. 9, pp. 5537–5606, May 2019, doi: 10.1021/acs.chemrev.8b00532.

[16] D. M. Engelman, “Membranes are more mosaic than fluid,” *Nature*, vol. 438, no. 7068, pp. 578–580, Dec. 2005, doi: 10.1038/nature04394.

[17] R. C. Petersen, “Free-radicals and advanced chemistries involved in cell membrane organization influence oxygen diffusion and pathology treatment,” *AIMS biophysics*, vol. 4, no. 2, pp. 240–283, 2017, doi: 10.3934/biophy.2017.2.240.

[18] C. A. Pasternak, G. M. Alder, C. L. Bashford, Y. E. Korchev, C. Pederzolli, and T. K. Rostovtseva, “Membrane damage: common mechanisms of induction and

prevention," *FEMS Microbiol Immunol*, vol. 5, no. 1–3, pp. 83–92, Sep. 1992, doi: 10.1111/j.1574-6968.1992.tb05890.x.

[19] R. T. Dean, "Free radicals, membrane damage and cell-mediated cytolysis," *Br. J. Cancer Suppl.*, vol. 8, pp. 39–45, Jun. 1987.

[20] S. T. Cooper and P. L. McNeil, "Membrane Repair: Mechanisms and Pathophysiology," *Physiol. Rev.*, vol. 95, no. 4, pp. 1205–1240, Oct. 2015, doi: 10.1152/physrev.00037.2014.

[21] J. Parkin and B. Cohen, "An overview of the immune system," *The Lancet*, vol. 357, no. 9270, pp. 1777–1789, Jun. 2001, doi: 10.1016/S0140-6736(00)04904-7.

[22] R. H. McCusker and K. W. Kelley, "Immune-neural connections: how the immune system's response to infectious agents influences behavior," *J. Exp. Biol.*, vol. 216, no. Pt 1, pp. 84–98, Jan. 2013, doi: 10.1242/jeb.073411.

[23] A. U. Ahmed, "An overview of inflammation: mechanism and consequences," *Front. Biol.*, vol. 6, no. 4, p. 274, Aug. 2011, doi: 10.1007/s11515-011-1123-9.

[24] I. S. Young and J. V. Woodside, "Antioxidants in health and disease," *J. Clin. Pathol.*, vol. 54, no. 3, pp. 176–186, Mar. 2001, doi: 10.1136/jcp.54.3.176.

[25] W. Dröge, "Free radicals in the physiological control of cell function," *Physiol. Rev.*, vol. 82, no. 1, pp. 47–95, Jan. 2002, doi: 10.1152/physrev.00018.2001.

[26] M. Genestra, "Oxyl radicals, redox-sensitive signalling cascades and antioxidants," *Cell. Signal.*, vol. 19, no. 9, pp. 1807–1819, Sep. 2007, doi: 10.1016/j.cellsig.2007.04.009.

[27] B. Halliwell, "Biochemistry of oxidative stress," *Biochem. Soc. Trans.*, vol. 35, no. Pt 5, pp. 1147–1150, Nov. 2007, doi: 10.1042/BST0351147.

[28] P. Pacher, J. S. Beckman, and L. Liaudet, "Nitric oxide and peroxynitrite in health and disease," *Physiol. Rev.*, vol. 87, no. 1, pp. 315–424, Jan. 2007, doi: 10.1152/physrev.00029.2006.

[29] V. Dhawan, "Reactive Oxygen and Nitrogen Species: General Considerations," in *Studies on Respiratory Disorders*, N. K. Ganguly, S. K. Jindal, S. Biswal, P. J. Barnes, and R. Pawankar, Eds. New York, NY: Springer New York, 2014, pp. 27–47.

[30] M. O. Eze, "Membrane fluidity, reactive oxygen species, and cell-mediated immunity: implications in nutrition and disease," *Med. Hypotheses*, vol. 37, no. 4, pp. 220–224, Apr. 1992, doi: 10.1016/0306-9877(92)90191-e.

[31] B. Halliwell, "Free radicals and antioxidants: a personal view," *Nutr. Rev.*, vol. 52, no. 8 Pt 1, pp. 253–265, Aug. 1994, doi: 10.1111/j.1753-4887.1994.tb01453.x.

[32] K. Krumova and G. Cosa, "Chapter 1. Overview of Reactive Oxygen Species," in *Comprehensive Series in Photochemical & Photobiological Sciences*, vol. 1, S. Nonell and C. Flors, Eds. Cambridge: Royal Society of Chemistry, 2016, pp. 1–21.

[33] H. Sies, "Role of metabolic H2O2 generation: redox signaling and oxidative stress," *J. Biol. Chem.*, vol. 289, no. 13, pp. 8735–8741, Mar. 2014, doi: 10.1074/jbc.R113.544635.

[34] B. Halliwell and J. M. Gutteridge, "The importance of free radicals and catalytic metal ions in human diseases," *Mol. Aspects Med.*, vol. 8, no. 2, pp. 89–193, 1985, doi: 10.1016/0098-2997(85)90001-9.

[35] S. Lenzen, "Chemistry and biology of reactive species with special reference to the antioxidative defence status in pancreatic β-cells," *Biochim Biophys Acta Gen Subj*, vol. 1861, no. 8, pp. 1929–1942, Aug. 2017, doi: 10.1016/j.bbagen.2017.05.013.

[36] S. Di Meo, T. T. Reed, P. Venditti, and V. M. Victor, "Role of ROS and RNS Sources in Physiological and Pathological Conditions," *Oxid Med Cell Longev*, vol. 2016, p. 1245049, 2016, doi: 10.1155/2016/1245049.

[37] K. K. Griendling *et al.*, "Measurement of Reactive Oxygen Species, Reactive Nitrogen Species, and Redox-Dependent Signaling in the Cardiovascular System: A Scientific Statement From the American Heart Association," *Circ. Res.*, vol. 119, no. 5, pp. e39-75, Aug. 2016, doi: 10.1161/RES.0000000000000110.

[38] J. R. Lancaster, "Nitric oxide: a brief overview of chemical and physical properties relevant to therapeutic applications," *Future science OA*, vol. 1, no. 1, p. FSO59, Aug. 2015, doi: 10.4155/fso.15.59.

[39] J. M. Rifkind, E. Nagababu, and S. Ramasamy, "Nitric oxide redox reactions and red cell biology," *Antioxid. Redox Signal.*, vol. 8, no. 7–8, pp. 1193–1203, Aug. 2006, doi: 10.1089/ars.2006.8.1193.

[40] D. A. Wink and J. B. Mitchell, "Chemical biology of nitric oxide: Insights into regulatory, cytotoxic, and cytoprotective mechanisms of nitric oxide," *Free Radic. Biol. Med.*, vol. 25, no. 4–5, pp. 434–456, Sep. 1998, doi: 10.1016/s0891-5849(98)00092-6.

[41] M. Möller, H. Botti, C. Batthyany, H. Rubbo, R. Radi, and A. Denicola, "Direct measurement of nitric oxide and oxygen partitioning into liposomes and low density lipoprotein," *J. Biol. Chem.*, vol. 280, no. 10, pp. 8850–8854, Mar. 2005, doi: 10.1074/jbc.M413699200.

[42] M. N. Möller, Q. Li, J. R. Lancaster, and A. Denicola, "Acceleration of nitric oxide autoxidation and nitrosation by membranes," *IUBMB Life*, vol. 59, no. 4–5, pp. 243–248, May 2007, doi: 10.1080/15216540701311147.

[43] L. J. Ignarro, J. M. Fukuto, J. M. Griscavage, N. E. Rogers, and R. E. Byrns, "Oxidation of nitric oxide in aqueous solution to nitrite but not nitrate: comparison with enzymatically formed nitric oxide from L-arginine," *Proc. Natl. Acad. Sci. U.S.A.*, vol. 90, no. 17, pp. 8103–8107, Sep. 1993, doi: 10.1073/pnas.90.17.8103.

[44] H. J. Forman, J. M. Fukuto, and M. Torres, "Redox signaling: thiol chemistry defines which reactive oxygen and nitrogen species can act as second messengers," *Am. J. Physiol., Cell Physiol.*, vol. 287, no. 2, pp. C246-256, Aug. 2004, doi: 10.1152/ajpcell.00516.2003.

[45] N. Hogg and B. Kalyanaraman, "Nitric oxide and lipid peroxidation," *Biochim. Biophys. Acta*, vol. 1411, no. 2–3, pp. 378–384, May 1999, doi: 10.1016/s0005-2728(99)00027-4.

[46] J. R. Lancaster, "A tutorial on the diffusibility and reactivity of free nitric oxide," *Nitric Oxide*, vol. 1, no. 1, pp. 18–30, Feb. 1997, doi: 10.1006/niox.1996.0112.

[47] T. Malinski, Z. Taha, S. Grunfeld, S. Patton, M. Kapturczak, and P. Tomboulian, "Diffusion of nitric oxide in the aorta wall monitored in situ by porphyrinic microsensors," *Biochem. Biophys. Res. Commun.*, vol. 193, no. 3, pp. 1076–1082, Jun. 1993, doi: 10.1006/bbrc.1993.1735.

[48] U. Förstermann and W. C. Sessa, "Nitric oxide synthases: regulation and function," *Eur. Heart J.*, vol. 33, no. 7, pp. 829–837, 837a–837d, Apr. 2012, doi: 10.1093/eurheartj/ehr304.

[49] K. Maejima *et al.*, "Increased basal levels of plasma nitric oxide in Type 2 diabetic subjects. Relationship to microvascular complications," *J. Diabetes Complicat.*, vol. 15, no. 3, pp. 135–143, Jun. 2001, doi: 10.1016/s1056-8727(01)00144-1.

[50] J. N. Sharma, A. Al-Omran, and S. S. Parvathy, "Role of nitric oxide in inflammatory diseases," *Inflammopharmacology*, vol. 15, no. 6, pp. 252–259, Dec. 2007, doi: 10.1007/s10787-007-0013-x.

[51] G. Yilmaz, P. Esser, N. Kociok, P. Aydin, K. Heimann, and N. Kociek, "Elevated vitreous nitric oxide levels in patients with proliferative diabetic retinopathy," *Am. J. Ophthalmol.*, vol. 130, no. 1, pp. 87–90, Jul. 2000, doi: 10.1016/s0002-9394(00)00398-6.

[52] W. Ratajczak-Wrona, E. Jablonska, B. Antonowicz, D. Dziemianczyk, and S. Z. Grabowska, "Levels of biological markers of nitric oxide in serum of patients with squamous cell carcinoma of the oral cavity," *Int J Oral Sci*, vol. 5, no. 3, pp. 141–145, Sep. 2013, doi: 10.1038/ijos.2013.59.

[53] X. Liu, Q. Yan, K. L. Baskerville, and J. L. Zweier, "Estimation of nitric oxide concentration in blood for different rates of generation. Evidence that intravascular nitric oxide levels are too low to exert physiological effects," *J. Biol. Chem.*, vol. 282, no. 12, pp. 8831–8836, Mar. 2007, doi: 10.1074/jbc.M611684200.

[54] R. B. Mikkelsen and P. Wardman, "Biological chemistry of reactive oxygen and nitrogen and radiation-induced signal transduction mechanisms," *Oncogene*, vol. 22, no. 37, pp. 5734–5754, Sep. 2003, doi: 10.1038/sj.onc.1206663.

[55] V. Kumar, A. K. Abbas, N. Fausto, S. L. Robbins, and R. S. Cotran, *Robbins and Cotran pathologic basis of disease*. Philadelphia: Elsevier/Saunders, 2005.

[56] A. W. Orr, B. P. Helmke, B. R. Blackman, and M. A. Schwartz, "Mechanisms of Mechanotransduction," *Developmental Cell*, vol. 10, no. 1, pp. 11–20, Jan. 2006, doi: 10.1016/j.devcel.2005.12.006.

[57] A.-L. Le Roux, X. Quiroga, N. Walani, M. Arroyo, and P. Roca-Cusachs, "The plasma membrane as a mechanochemical transducer," *Philosophical Transactions of the Royal Society of London. Series B, Biological Sciences*, vol. 374, no. 1779, p. 20180221, 19 2019, doi: 10.1098/rstb.2018.0221.

[58] J. Kim *et al.*, "Topological Adaptation of Transmembrane Domains to the Force-Modulated Lipid Bilayer Is a Basis of Sensing Mechanical Force," *Current biology: CB*, vol. 30, no. 9, pp. 1614-1625.e5, May 2020, doi: 10.1016/j.cub.2020.02.028.

[59] M. Holinstat, "Normal platelet function," *Cancer Metastasis Reviews*, vol. 36, no. 2, pp. 195–198, 2017, doi: 10.1007/s10555-017-9677-x.

[60] P. E. J. van der Meijden and J. W. M. Heemskerk, "Platelet biology and functions: new concepts and clinical perspectives," *Nature Reviews. Cardiology*, vol. 16, no. 3, pp. 166–179, 2019, doi: 10.1038/s41569-018-0110-0.

[61] V. B. O'Donnell, R. C. Murphy, and S. P. Watson, "Platelet lipidomics: modern day perspective on lipid discovery and characterization in platelets," *Circulation Research*, vol. 114, no. 7, pp. 1185–1203, Mar. 2014, doi: 10.1161/CIRCRESAHA.114.301597.

[62] H. Xiao, R. A. Siddiqui, M. H. Al-Hassani, D. Sliva, and R. J. Kovacs, "Phospholipids released from activated platelets improve platelet aggregation and endothelial cell migration," *Platelets*, vol. 12, no. 3, pp. 163–170, May 2001, doi: 10.1080/09537100120039389.

[63] R. J. Morin, "The role of phospholipids in platelet function," *Annals of Clinical and Laboratory Science*, vol. 10, no. 6, pp. 463–473, Dec. 1980.

[64] S. Koseoglu *et al.*, "Analytical characterization of the role of phospholipids in platelet adhesion and secretion," *Analytical Chemistry*, vol. 87, no. 1, pp. 413–421, Jan. 2015, doi: 10.1021/ac502293p.

[65] B. Peng *et al.*, "Identification of key lipids critical for platelet activation by comprehensive analysis of the platelet lipidome," *Blood*, vol. 132, no. 5, pp. e1–e12, 02 2018, doi: 10.1182/blood-2017-12-822890.

[66] K. Y. Stokes and D. N. Granger, "Platelets: a critical link between inflammation and microvascular dysfunction," *The Journal of Physiology*, vol. 590, no. 5, pp. 1023–1034, Mar. 2012, doi: 10.1113/jphysiol.2011.225417.

[67] C. N. Morrell, A. A. Aggrey, L. M. Chapman, and K. L. Modjeski, "Emerging roles for platelets as immune and inflammatory cells," *Blood*, vol. 123, no. 18, pp. 2759–2767, May 2014, doi: 10.1182/blood-2013-11-462432.

[68] A. Gros, V. Ollivier, and B. Ho-Tin-Noé, "Platelets in inflammation: regulation of leukocyte activities and vascular repair," *Frontiers in Immunology*, vol. 5, p. 678, 2014, doi: 10.3389/fimmu.2014.00678.

[69] M. Mezger *et al.*, "Platelets and Immune Responses During Thromboinflammation," *Frontiers in Immunology*, vol. 10, p. 1731, 2019, doi: 10.3389/fimmu.2019.01731.

[70] G. Caligiuri, "Mechanotransduction, immunoregulation, and metabolic functions of CD31 in cardiovascular pathophysiology," *Cardiovascular Research*, vol. 115, no. 9, pp. 1425–1434, 01 2019, doi: 10.1093/cvr/cvz132.

[71] G. A. Ramirez, A. A. Manfredi, and N. Maugeri, "Misunderstandings Between Platelets and Neutrophils Build in Chronic Inflammation," *Frontiers in Immunology*, vol. 10, p. 2491, 2019, doi: 10.3389/fimmu.2019.02491.

[72] H.-J. Hsieh, C.-A. Liu, B. Huang, A. H. Tseng, and D. L. Wang, "Shear-induced endothelial mechanotransduction: the interplay between reactive oxygen species (ROS) and nitric oxide (NO) and the pathophysiological implications," *Journal of Biomedical Science*, vol. 21, p. 3, Jan. 2014, doi: 10.1186/1423-0127-21-3.

[73] D. Varga-Szabo, I. Pleines, and B. Nieswandt, "Cell adhesion mechanisms in platelets," *Arteriosclerosis, Thrombosis, and Vascular Biology*, vol. 28, no. 3, pp. 403–412, Mar. 2008, doi: 10.1161/ATVBAHA.107.150474.

[74] Y. Hou, N. Carrim, Y. Wang, R. C. Gallant, A. Marshall, and H. Ni, "Platelets in hemostasis and thrombosis: Novel mechanisms of fibrinogen-independent platelet aggregation and fibronectinmediated protein wave of hemostasis," *J Biomed Res*, Nov. 2015, doi: 10.7555/JBR.29.20150121.

[75] J. S. Owen, R. A. Hutton, R. C. Day, K. R. Bruckdorfer, and N. McIntyre, "Platelet lipid composition and platelet aggregation in human liver disease," *Journal of Lipid Research*, vol. 22, no. 3, pp. 423–430, Mar. 1981.

[76] P. Cohen and A. Derksen, "Comparison of phospholipid and fatty acid composition of human erythrocytes and platelets," *British Journal of Haematology*, vol. 17, no. 4, pp. 359–371, Oct. 1969, doi: 10.1111/j.1365-2141.1969.tb01382.x.

[77] J. Lombard, "Once upon a time the cell membranes: 175 years of cell boundary research," *Biology Direct*, vol. 9, p. 32, Dec. 2014, doi: 10.1186/s13062-014-0032-7.

[78] null Binnig, null Quate, and null Gerber, "Atomic force microscope," *Physical Review Letters*, vol. 56, no. 9, pp. 930–933, Mar. 1986, doi: 10.1103/PhysRevLett.56.930.

[79] R. A. Chaurio, C. Janko, L. E. Muñoz, B. Frey, M. Herrmann, and U. S. Gaipl, "Phospholipids: key players in apoptosis and immune regulation," *Molecules (Basel, Switzerland)*, vol. 14, no. 12, pp. 4892–4914, Nov. 2009, doi: 10.3390/molecules14124892.

[80] Y. Zhang, X. Chen, C. Gueydan, and J. Han, "Plasma membrane changes during programmed cell deaths," *Cell Research*, vol. 28, no. 1, pp. 9–21, 2018, doi: 10.1038/cr.2017.133.

[81] A. A. Baxter, M. D. Hulett, and I. K. H. Poon, "The phospholipid code: a key component of dying cell recognition, tumor progression and host-microbe interactions," *Cell Death and Differentiation*, vol. 22, no. 12, pp. 1893–1905, Dec. 2015, doi: 10.1038/cdd.2015.122.

[82] A. P. Demchenko, "The change of cellular membranes on apoptosis: fluorescence detection," *Experimental Oncology*, vol. 34, no. 3, pp. 263–268, Oct. 2012.

[83] M. L. Coleman, E. A. Sahai, M. Yeo, M. Bosch, A. Dewar, and M. F. Olson, "Membrane blebbing during apoptosis results from caspase-mediated activation of ROCK I," *Nature Cell Biology*, vol. 3, no. 4, pp. 339–345, Apr. 2001, doi: 10.1038/35070009.

[84] M. C. Dixon, "Quartz crystal microbalance with dissipation monitoring: enabling real-time characterization of biological materials and their interactions," *Journal of biomolecular techniques: JBT*, vol. 19, no. 3, pp. 151–158, Jul. 2008.

[85] C. A. Keller and B. Kasemo, "Surface specific kinetics of lipid vesicle adsorption measured with a quartz crystal microbalance," *Biophysical Journal*, vol. 75, no. 3, pp. 1397–1402, Sep. 1998, doi: 10.1016/S0006-3495(98)74057-3.

[86] M. N. Möller and A. Denicola, "Diffusion of nitric oxide and oxygen in lipoproteins and membranes studied by pyrene fluorescence quenching," *Free Radical Biology & Medicine*, vol. 128, pp. 137–143, 20 2018, doi: 10.1016/j.freeradbiomed.2018.04.553.

[87] D. A. Wink, M. B. Grisham, J. B. Mitchell, and P. C. Ford, "Direct and indirect effects of nitric oxide in chemical reactions relevant to biology," *Methods in Enzymology*, vol. 268, pp. 12–31, 1996, doi: 10.1016/s0076-6879(96)68006-9.

[88] S. Miersch *et al.*, "Plasma membrane cholesterol content affects nitric oxide diffusion dynamics and signaling," *The Journal of Biological Chemistry*, vol. 283, no. 27, pp. 18513–18521, Jul. 2008, doi: 10.1074/jbc.M800440200.

[89] W. K. Subczynski, M. Lomnicka, and J. S. Hyde, "Permeability of nitric oxide through lipid bilayer membranes," *Free Radical Research*, vol. 24, no. 5, pp. 343–349, May 1996, doi: 10.3109/10715769609088032.

[90] A. Denicola, J. M. Souza, R. Radi, and E. Lissi, "Nitric oxide diffusion in membranes determined by fluorescence quenching," *Archives of Biochemistry and Biophysics*, vol. 328, no. 1, pp. 208–212, Apr. 1996, doi: 10.1006/abbi.1996.0162.

[91] S. Karanth, A. Azinfar, C. A. Helm, and M. Delcea, "Identification of a critical lipid ratio in lipid rafts exposed to nitric oxide: An AFM study."

[92] H. Yin, L. Xu, and N. A. Porter, "Free radical lipid peroxidation: mechanisms and analysis," *Chemical Reviews*, vol. 111, no. 10, pp. 5944–5972, Oct. 2011, doi: 10.1021/cr200084z.

[93] A. Ayala, M. F. Muñoz, and S. Argüelles, "Lipid peroxidation: production, metabolism, and signaling mechanisms of malondialdehyde and 4-hydroxy-2-nonenal," *Oxidative Medicine and Cellular Longevity*, vol. 2014, p. 360438, 2014, doi: 10.1155/2014/360438.

[94] R. Saxena, "Arthritis as a Disease of Aging and Changes in Antioxidant Status," in *Aging*, Elsevier, 2014, pp. 49–59.

[95] S. Nedeianu, T. Páli, and D. Marsh, "Membrane penetration of nitric oxide and its donor S-nitroso-N-acetylpenicillamine: a spin-label electron paramagnetic resonance

spectroscopic study," *Biochimica Et Biophysica Acta*, vol. 1661, no. 2, pp. 135–143, Mar. 2004, doi: 10.1016/j.bbamem.2003.12.008.

[96] G. Weber *et al.*, "Lipid oxidation induces structural changes in biomimetic membranes," *Soft Matter*, vol. 10, no. 24, pp. 4241–4247, Jun. 2014, doi: 10.1039/c3sm52740a.

[97] D. J. Suchyta and M. H. Schoenfisch, "Controlled release of nitric oxide from liposomes," *ACS biomaterials science & engineering*, vol. 3, no. 9, pp. 2136–2143, Sep. 2017, doi: 10.1021/acsbiomaterials.7b00255.

[98] R. H. Gensure, M. L. Zeidel, and W. G. Hill, "Lipid raft components cholesterol and sphingomyelin increase H+/OH- permeability of phosphatidylcholine membranes," *The Biochemical Journal*, vol. 398, no. 3, pp. 485–495, Sep. 2006, doi: 10.1042/BJ20051620.

[99] E. Clementi, N. Borgese, and J. Meldolesi, "Interactions between nitric oxide and sphingolipids and the potential consequences in physiology and pathology," *Trends in Pharmacological Sciences*, vol. 24, no. 10, pp. 518–523, Oct. 2003, doi: 10.1016/j.tips.2003.08.008.

[100] C. Perrotta, C. De Palma, and E. Clementi, "Nitric oxide and sphingolipids: mechanisms of interaction and role in cellular pathophysiology," *Biological Chemistry*, vol. 389, no. 11, pp. 1391–1397, Nov. 2008, doi: 10.1515/BC.2008.155.

[101] A. Berrill, J. Biddlecombe, and D. Bracewell, "Product Quality During Manufacture and Supply," in *Peptide and Protein Delivery*, Elsevier, 2011, pp. 313–339.

[102] M. J. Davies, "Protein oxidation and peroxidation," *The Biochemical Journal*, vol. 473, no. 7, pp. 805–825, Apr. 2016, doi: 10.1042/BJ20151227.

[103] P. Bin, R. Huang, and X. Zhou, "Oxidation Resistance of the Sulfur Amino Acids: Methionine and Cysteine," *BioMed Research International*, vol. 2017, p. 9584932, 2017, doi: 10.1155/2017/9584932.

[104] B. S. Coller, "αIIbβ3: structure and function," *Journal of thrombosis and haemostasis: JTH*, vol. 13 Suppl 1, pp. S17-25, Jun. 2015, doi: 10.1111/jth.12915.

[105] S. Karanth and M. Delcea, "Nitrosative stress affects the interaction of integrin alphaIIbbeta3 with its ligands," *Biochimica Et Biophysica Acta. Biomembranes*, vol. 1862, no. 5, p. 183198, 01 2020, doi: 10.1016/j.bbamem.2020.183198.

[106] R. Mor-Cohen, "Disulfide Bonds as Regulators of Integrin Function in Thrombosis and Hemostasis," *Antioxidants & Redox Signaling*, vol. 24, no. 1, pp. 16–31, Jan. 2016, doi: 10.1089/ars.2014.6149.

[107] G. M. Walsh *et al.*, "S-Nitrosylation of platelet alphaIIbbeta3 as revealed by Raman spectroscopy," *Biochemistry*, vol. 46, no. 21, pp. 6429–6436, May 2007, doi: 10.1021/bi0620712.

[108] N. G. Oberprieler, W. Roberts, R. Riba, A. M. Graham, S. Homer-Vanniasinkam, and K. M. Naseem, "cGMP-independent inhibition of integrin alphaIIbbeta3-mediated platelet adhesion and outside-in signalling by nitric oxide," *FEBS letters*, vol. 581, no. 7, pp. 1529–1534, Apr. 2007, doi: 10.1016/j.febslet.2007.02.072.

[109] J. S. Bennett, "Structure and function of the platelet integrin alphaIIbbeta3," *The Journal of Clinical Investigation*, vol. 115, no. 12, pp. 3363–3369, Dec. 2005, doi: 10.1172/JCI26989.

[110] L. Badimon, R. Suades, E. Fuentes, I. Palomo, and T. Padró, "Role of Platelet-Derived Microvesicles As Crosstalk Mediators in Atherothrombosis and Future Pharmacology Targets: A Link between Inflammation, Atherosclerosis, and

Thrombosis," *Frontiers in Pharmacology*, vol. 7, p. 293, 2016, doi: 10.3389/fphar.2016.00293.

[111] D. Varon and E. Shai, "Platelets and their microparticles as key players in pathophysiological responses," *Journal of thrombosis and haemostasis: JTH*, vol. 13 Suppl 1, pp. S40-46, Jun. 2015, doi: 10.1111/jth.12976.

[112] J. E. Italiano, A. T. A. Mairuhu, and R. Flaumenhaft, "Clinical relevance of microparticles from platelets and megakaryocytes," *Current Opinion in Hematology*, vol. 17, no. 6, pp. 578–584, Nov. 2010, doi: 10.1097/MOH.0b013e32833e77ee.

[113] M. C. Martínez, A. Tesse, F. Zobairi, and R. Andriantsitohaina, "Shed membrane microparticles from circulating and vascular cells in regulating vascular function," *American Journal of Physiology. Heart and Circulatory Physiology*, vol. 288, no. 3, pp. H1004-1009, Mar. 2005, doi: 10.1152/ajpheart.00842.2004.

[114] P. M. Vanhoutte, "Nitric Oxide: From Good to Bad," *Annals of Vascular Diseases*, vol. 11, no. 1, pp. 41–51, Mar. 2018, doi: 10.3400/avd.ra.17-00134.

[115] M. Lind *et al.*, "Inducible nitric oxide synthase: Good or bad?," *Biomedicine & Pharmacotherapy = Biomedecine & Pharmacotherapie*, vol. 93, pp. 370–375, Sep. 2017, doi: 10.1016/j.biopha.2017.06.036.

[116] F. Gao *et al.*, "Reduction of Endothelial Nitric Oxide Increases the Adhesiveness of Constitutive Endothelial Membrane ICAM-1 through Src-Mediated Phosphorylation," *Frontiers in Physiology*, vol. 8, p. 1124, 2017, doi: 10.3389/fphys.2017.01124.

[117] D. B. Cines *et al.*, "Endothelial cells in physiology and in the pathophysiology of vascular disorders," *Blood*, vol. 91, no. 10, pp. 3527–3561, May 1998.

[118] B. L. Chung *et al.*, "Nanomedicines for Endothelial Disorders," *Nano Today*, vol. 10, no. 6, pp. 759–776, Dec. 2015, doi: 10.1016/j.nantod.2015.11.009.

[119] X. Castellon and V. Bogdanova, "Chronic Inflammatory Diseases and Endothelial Dysfunction," *Aging and Disease*, vol. 7, no. 1, pp. 81–89, Jan. 2016, doi: 10.14336/AD.2015.0803.

[120] P. Rajendran *et al.*, "The vascular endothelium and human diseases," *International Journal of Biological Sciences*, vol. 9, no. 10, pp. 1057–1069, 2013, doi: 10.7150/ijbs.7502.

[121] J. K. Patra *et al.*, "Nano based drug delivery systems: recent developments and future prospects," *Journal of Nanobiotechnology*, vol. 16, no. 1, p. 71, Sep. 2018, doi: 10.1186/s12951-018-0392-8.

[122] D. M. Bowman, "More than a Decade On: Mapping Today's Regulatory and Policy Landscapes Following the Publication of Nanoscience and Nanotechnologies: Opportunities and Uncertainties," *Nanoethics*, vol. 11, no. 2, pp. 169–186, Aug. 2017, doi: 10.1007/s11569-017-0281-x.

[123] W. H. De Jong and P. J. A. Borm, "Drug delivery and nanoparticles:applications and hazards," *International Journal of Nanomedicine*, vol. 3, no. 2, pp. 133–149, 2008, doi: 10.2147/ijn.s596.

[124] P. R. Leroueil, S. Hong, A. Mecke, J. R. Baker, B. G. Orr, and M. M. Banaszak Holl, "Nanoparticle interaction with biological membranes: does nanotechnology present a Janus face?," *Accounts of Chemical Research*, vol. 40, no. 5, pp. 335–342, May 2007, doi: 10.1021/ar600012y.

[125] X. Ye, Y. Gao, J. Chen, D. C. Reifsnyder, C. Zheng, and C. B. Murray, "Seeded growth of monodisperse gold nanorods using bromide-free surfactant mixtures," *Nano Letters*, vol. 13, no. 5, pp. 2163–2171, May 2013, doi: 10.1021/nl400653s.

[126] Y.-C. Yeh, B. Creran, and V. M. Rotello, "Gold nanoparticles: preparation, properties, and applications in bionanotechnology," *Nanoscale*, vol. 4, no. 6, pp. 1871–1880, 2012, doi: 10.1039/C1NR11188D.

[127] Z. Yang *et al.*, "Controllable Biosynthesis and Properties of Gold Nanoplates Using Yeast Extract," *Nano-Micro Letters*, vol. 9, no. 1, p. 5, 2017, doi: 10.1007/s40820-016-0102-8.

[128] M. D. Fahmy, H. E. Jazayeri, M. Razavi, R. Masri, and L. Tayebi, "Three-Dimensional Bioprinting Materials with Potential Application in Preprosthetic Surgery," *Journal of Prosthodontics: Official Journal of the American College of Prosthodontists*, vol. 25, no. 4, pp. 310–318, Jun. 2016, doi: 10.1111/jopr.12431.

[129] P. Morganti and M.-B. Coltelli, "A New Carrier for Advanced Cosmeceuticals," *Cosmetics*, vol. 6, no. 1, p. 10, Feb. 2019, doi: 10.3390/cosmetics6010010.

[130] M. N. V. Ravi Kumar, "A review of chitin and chitosan applications," *Reactive and Functional Polymers*, vol. 46, no. 1, pp. 1–27, Nov. 2000, doi: 10.1016/S1381-5148(00)00038-9.

[131] A. Moeini, P. Pedram, P. Makvandi, M. Malinconico, and G. Gomez d'Ayala, "Wound healing and antimicrobial effect of active secondary metabolites in chitosan-based wound dressings: A review," *Carbohydr Polym*, vol. 233, p. 115839, Apr. 2020, doi: 10.1016/j.carbpol.2020.115839.

[132] I. Bano, M. Arshad, T. Yasin, M. A. Ghauri, and M. Younus, "Chitosan: A potential biopolymer for wound management," *Int J Biol Macromol*, vol. 102, pp. 380–383, Sep. 2017, doi: 10.1016/j.ijbiomac.2017.04.047.

[133] B. K. Rastogi and A. Nordøy, "Lipid composition of cultured human endothelial cells," *Thrombosis Research*, vol. 18, no. 5, pp. 629–641, Jun. 1980, doi: 10.1016/0049-3848(80)90218-2.

[134] M. Cansell, J. P. Gouygou, J. Jozefonvicz, and D. Letourneur, "Lipid composition of cultured endothelial cells in relation to their growth," *Lipids*, vol. 32, no. 1, pp. 39–44, Jan. 1997, doi: 10.1007/s11745-997-0006-3.

[135] S. Colombo *et al.*, "Phospholipidome of endothelial cells shows a different adaptation response upon oxidative, glycative and lipoxidative stress," *Sci Rep*, vol. 8, no. 1, p. 12365, 17 2018, doi: 10.1038/s41598-018-30695-0.

[136] S. Karanth, B. Meesaragandla, and M. Delcea, "Changing surface properties of artificial lipid membranes at the interface with biopolymer coated gold nanoparticles under normal and redox conditions," *Biophys Chem*, vol. 267, p. 106465, Sep. 2020, doi: 10.1016/j.bpc.2020.106465.

[137] F. J. Pavinatto *et al.*, "Probing chitosan and phospholipid interactions using Langmuir and Langmuir-Blodgett films as cell membrane models," *Langmuir*, vol. 23, no. 14, pp. 7666–7671, Jul. 2007, doi: 10.1021/la700856a.

[138] F. J. Pavinatto *et al.*, "Interaction of chitosan with cell membrane models at the air-water interface," *Biomacromolecules*, vol. 8, no. 5, pp. 1633–1640, May 2007, doi: 10.1021/bm0701550.

[139] N. Fang, V. Chan, H. Q. Mao, and K. W. Leong, "Interactions of phospholipid bilayer with chitosan: effect of molecular weight and pH," *Biomacromolecules*, vol. 2, no. 4, pp. 1161–1168, 2001, doi: 10.1021/bm015548s.

[140] P. Robless, D. Okonko, D. P. Mikhailidis, and G. Stansby, "Dextran 40 reduces in vitro platelet aggregation in peripheral arterial disease," *Platelets*, vol. 15, no. 4, pp. 215–222, Jun. 2004, doi: 10.1080/09537100410001682814.

[141] D. I. Booi, "Perioperative fluid overload increases anastomosis thrombosis in the free TRAM flap used for breast reconstruction," *Eur J Plast Surg*, vol. 34, no. 2, pp. 81–86, Apr. 2011, doi: 10.1007/s00238-010-0466-9.

[142] M. Askari, C. Fisher, F. G. Weniger, S. Bidic, and W. P. A. Lee, "Anticoagulation therapy in microsurgery: a review," *J Hand Surg Am*, vol. 31, no. 5, pp. 836–846, Jun. 2006, doi: 10.1016/j.jhsa.2006.02.023.

[143] G. Sun and J. J. Mao, "Engineering dextran-based scaffolds for drug delivery and tissue repair," *Nanomedicine (Lond)*, vol. 7, no. 11, pp. 1771–1784, Nov. 2012, doi: 10.2217/nnm.12.149.

[144] J. Emery and T. Falcone, "Complications of Hysteroscopic Surgery," in *Hysteroscopy*, Elsevier, 2009, pp. 241–250.

[145] H. S. Kruth, "Receptor-independent fluid-phase pinocytosis mechanisms for induction of foam cell formation with native low-density lipoprotein particles," *Curr Opin Lipidol*, vol. 22, no. 5, pp. 386–393, Oct. 2011, doi: 10.1097/MOL.0b013e32834adadb.

[146] L. Shang, K. Nienhaus, and G. U. Nienhaus, "Engineered nanoparticles interacting with cells: size matters," *J Nanobiotechnology*, vol. 12, p. 5, Feb. 2014, doi: 10.1186/1477-3155-12-5.

[147] T.-C. Chou, E. Fu, C.-J. Wu, and J.-H. Yeh, "Chitosan enhances platelet adhesion and aggregation," *Biochem Biophys Res Commun*, vol. 302, no. 3, pp. 480–483, Mar. 2003, doi: 10.1016/s0006-291x(03)00173-6.

[148] I. Kovacs and C. Lindermayr, "Nitric oxide-based protein modification: formation and site-specificity of protein S-nitrosylation," *Front Plant Sci*, vol. 4, p. 137, 2013, doi: 10.3389/fpls.2013.00137.

[149] R. Radi, "Nitric oxide, oxidants, and protein tyrosine nitration," *Proc Natl Acad Sci U S A*, vol. 101, no. 12, pp. 4003–4008, Mar. 2004, doi: 10.1073/pnas.0307446101.

[150] A. Relini, N. Marano, and A. Gliozzi, "Misfolding of amyloidogenic proteins and their interactions with membranes," *Biomolecules*, vol. 4, no. 1, pp. 20–55, Dec. 2013, doi: 10.3390/biom4010020.

[151] D. Eisenberg and M. Jucker, "The amyloid state of proteins in human diseases," *Cell*, vol. 148, no. 6, pp. 1188–1203, Mar. 2012, doi: 10.1016/j.cell.2012.02.022.

[152] G.-F. Chen *et al.*, "Amyloid beta: structure, biology and structure-based therapeutic development," *Acta Pharmacol Sin*, vol. 38, no. 9, pp. 1205–1235, Sep. 2017, doi: 10.1038/aps.2017.28.

[153] Y. Gupta, G. Singla, and R. Singla, "Insulin-derived amyloidosis," *Indian J Endocrinol Metab*, vol. 19, no. 1, pp. 174–177, Feb. 2015, doi: 10.4103/2230-8210.146879.

[154] J. L. Evans and I. D. Goldfine, "Aging and insulin resistance: just say iNOS," *Diabetes*, vol. 62, no. 2, pp. 346–348, Feb. 2013, doi: 10.2337/db12-1239.

[155] S. Saito *et al.*, "Effect of nitric oxide in amyloid fibril formation on transthyretin-related amyloidosis," *Biochemistry*, vol. 44, no. 33, pp. 11122–11129, Aug. 2005, doi: 10.1021/bi050327i.

[156] A. Höhn, T. Jung, and T. Grune, "Pathophysiological importance of aggregated damaged proteins," *Free Radic Biol Med*, vol. 71, pp. 70–89, Jun. 2014, doi: 10.1016/j.freeradbiomed.2014.02.028.

[157] P. KJ Kinnunen, "Amyloid formation on lipid membrane surfaces.," *The Open Biology Journal*, no. 2, pp. 163–175, 2009, doi: 10.2174/1874196700902010163.

[158] C. Aisenbrey *et al.*, "How is protein aggregation in amyloidogenic diseases modulated by biological membranes?," *Eur Biophys J*, vol. 37, no. 3, pp. 247–255, Mar. 2008, doi: 10.1007/s00249-007-0237-0.

[159] E. Kachooei, A. A. Moosavi-Movahedi, F. Khodagholi, H. Ramshini, F. Shaerzadeh, and N. Sheibani, "Oligomeric forms of insulin amyloid aggregation disrupt outgrowth and complexity of neuron-like PC12 cells," *PLoS One*, vol. 7, no. 7, p. e41344, 2012, doi: 10.1371/journal.pone.0041344.

[160] H. A. Lashuel, "Membrane permeabilization: a common mechanism in protein-misfolding diseases," *Sci Aging Knowledge Environ*, vol. 2005, no. 38, p. pe28, Sep. 2005, doi: 10.1126/sageke.2005.38.pe28.

[161] B. N. Ratha, M. Kim, B. Sahoo, K. Garai, D. Lee, and A. Bhunia, "Insulin-eukaryotic model membrane interaction: Mechanistic insight of insulin fibrillation and membrane disruption," *Biochim Biophys Acta Biomembr*, Feb. 2018, doi: 10.1016/j.bbamem.2018.02.008.

[162] A. A. Kulikova, A. A. Makarov, and S. A. Kozin, "[The role of zinc ions and structural polymorphism of β-amyloid in the Alzheimer's disease initiation]," *Mol Biol (Mosk)*, vol. 49, no. 2, pp. 249–263, Apr. 2015.

[163] A. Sukhanova *et al.*, "Nanoparticles With a Specific Size and Surface Charge Promote Disruption of the Secondary Structure and Amyloid-Like Fibrillation of Human Insulin Under Physiological Conditions," *Front Chem*, vol. 7, p. 480, 2019, doi: 10.3389/fchem.2019.00480.

[164] S. Hsieh, C. Chang, and H. Chou, "Gold nanoparticles as amyloid-like fibrillogenesis inhibitors," *Colloids Surf B Biointerfaces*, vol. 112, pp. 525–529, Dec. 2013, doi: 10.1016/j.colsurfb.2013.08.029.

[165] Y. Ma, R. Huang, W. Qi, R. Su, and Z. He, "Fluorescent silicon nanoparticles inhibit the amyloid fibrillation of insulin," *J Mater Chem B*, vol. 7, no. 9, pp. 1397–1403, 07 2019, doi: 10.1039/c8tb02964d.

[166] K. Siposova *et al.*, "The molecular mass of dextran used to modify magnetite nanoparticles affects insulin amyloid aggregation," *Journal of Magnetism and Magnetic Materials*, vol. 427, pp. 48–53, Apr. 2017, doi: 10.1016/j.jmmm.2016.10.083.

[167] Y.-H. Liao, Y.-J. Chang, Y. Yoshiike, Y.-C. Chang, and Y.-R. Chen, "Negatively charged gold nanoparticles inhibit Alzheimer's amyloid-β fibrillization, induce fibril dissociation, and mitigate neurotoxicity," *Small*, vol. 8, no. 23, pp. 3631–3639, Dec. 2012, doi: 10.1002/smll.201201068.

[168] B. Meesaragandla, S. Karanth, U. Janke, and M. Delcea, "Biopolymer-coated gold nanoparticles inhibit human insulin amyloid fibrillation," *Sci Rep*, vol. 10, no. 1, p. 7862, 12 2020, doi: 10.1038/s41598-020-64010-7.

[169] F. S. Ruggeri, F. Benedetti, T. P. J. Knowles, H. A. Lashuel, S. Sekatskii, and G. Dietler, "Identification and nanomechanical characterization of the fundamental single-strand protofilaments of amyloid α-synuclein fibrils," *Proc Natl Acad Sci U S A*, vol. 115, no. 28, pp. 7230–7235, 10 2018, doi: 10.1073/pnas.1721220115.

[170] R. Khurana *et al.*, "A general model for amyloid fibril assembly based on morphological studies using atomic force microscopy," *Biophys J*, vol. 85, no. 2, pp. 1135–1144, Aug. 2003, doi: 10.1016/S0006-3495(03)74550-0.

5. Publication list and author contributions

Publications accepted in peer-reviewed journals

1. **Karanth, S**. and Delcea, M., (2020). Nitrosative stress affects the interaction of integrin alphaIIbbeta3 with its ligands. *Biochimica et Biophysica Acta (BBA)-Biomembranes*, 1862(5), 183198.

   Author contributions:
   SK and MD are responsible for conceptualization and design of the manuscript. SK conducted all the experiments and interpreted the data. SK wrote the manuscript. MD is responsible for critical evaluation and manuscript review.

2. **Karanth, S**., Meesaragandla, B. and Delcea, M., (2020). Changing surface properties of artificial lipid membranes at the interface with biopolymer coated gold nanoparticles under normal and redox conditions. *Biophysical Chemistry*, *267*, *106465*.

   Author contributions:
   SK is responsible for design and conceptualization of the manuscript. SK conducted all the experiments and data interpretation. SK wrote the manuscript. BM provided the biopolymer nanoparticles. SK, BM and MD are responsible for critical evaluation and reviewing the manuscript.

3. Meesaragandla, B., **Karanth, S**., Janke, U. and Delcea, M., (2020). Biopolymer-coated gold nanoparticles inhibit human insulin amyloid fibrillation. *Scientific Reports*, 10(1),1-14.

   Author contributions:
   BM is responsible for conceptualization and performed most of the experiments. SK conducted AFM measurements, analysis and preparation of AFM figures. and data interpretation the data. U.J. performed ELISA and cytotoxicity experiments, related data analysis and figures. BM, SK, UJ and MD are responsible for critical evaluation and reviewing the manuscript.

Manuscripts submitted

4. **Karanth, S**., Azinfar, A., Helm, C.A., and Delcea, M., (2020). Identification of a critical lipid ratio in lipid rafts exposed to nitric oxide: An AFM study

   Author contributions:
   SK and MD are responsible for conceptualization and design of manuscript. SK performed force-spectroscopy measurements, data analysis and preparation of figures. AA performed AFM imaging. SK and AA jointly analyzed imaging data and finalized the figures. SK wrote the manuscript. SK, AA, CAH and MD are responsible for evaluation and reviewing the manuscript. SK and AA are co-authors.

6. Articles

I. Identification of a critical lipid ratio in lipid rafts exposed to nitric oxide: An AFM study

Sanjai Karanth, Amir Azinfar, Christiane A. Helm and Mihaela Delcea

Biophysical Journal, *Under Review*

Manuscript Number: 2020BIOPHYSJ312350

Identification of a critical lipid ratio in lipid rafts exposed to nitric oxide: An AFM study

SK, AA, CAH and MD

Running Title: Permeability of NO-treated lipid rafts

Abstract

Lipid rafts are discrete, heterogeneous domains of phospholipids, sphingolipids and sterols which are present in the cell membrane. They are responsible for conducting cell signaling and maintaining lipid-protein functionality. Redox-stress induced modifications to any of their components can severely alter the mechanics and dynamics of the membrane causing impairment to the lipid-protein functionality. Here, we report on the effect of sphingomyelin (SM) in controlling membrane permeability and its role as a regulatory lipid in the presence of nitric oxide (NO) radical. Force spectroscopy and atomic force microscopy (AFM) imaging of 1-palmitoyl-2-oleoyl-glycero-3-phosphocholine (POPC): sphingomyelin (SM): cholesterol (CH) bilayers (at three different ratios) showed that the adhesion forces to pull the AFM tip out of the membrane increase with rising SM concentration, indicating a decreased membrane permeability. However, in the presence of NO radical (1µM and 5µM), the adhesion forces decreased depending on SM concentration. The lipid membrane was found to be stable at the ratio POPC:SM:CH (2:1:1) even when exposed to 1µM NO. We believe that this is a critical ratio needed by the lipid rafts to maintain homeostasis under stress conditions. The stability could be due to an interplay between SM and cholesterol. However, at 5µM NO, membrane deteriorations were detected. For POPC:SM:CH (2:2:1) ratio, NO displayed a pro-oxidant behavior and damaged the membrane at both radical concentrations. These changes were reflected by the differences in the height profiles of the rafts observed by AFM imaging. Malondialdehyde (a peroxidation product) detection suggests that lipids may have undergone lipid nitroxidation. The changes were instantaneous and independent of radical concentration and incubation time. Our study underlines the need for identifying appropriate ratios in the lipid rafts of the cell membranes to withstand redox imbalances caused by radicals such as NO.

Keywords: lipid rafts, nitric oxide, peroxidation, force spectroscopy, AFM imaging

Statement of Significance: Modifications in lipid rafts can alter membrane functionality, especially under stress conditions. Here, we identified by AFM imaging and force spectroscopy a critical lipid ratio (2:1:1) in POPC:sphingomyelin:cholesterol lipid rafts at which lipid membrane integrity under nitric oxide radical exposure is maintained. This study is essential for understanding cell membrane modifications in response to a redox environment.

Introduction

Cell membrane can be understood as a specialized dynamic bilayer primarily composed of phospholipids, which can undergo various physical modulations in response to a biological process. The induced physical changes for example due to protein function (1, 2) are reflected by changes in the mechanical properties of the cell membrane. Along with phospholipids, proteins and carbohydrates are important components of cell membrane (3) and form a frontline barrier in maintaining cell integrity. However, in a redox environment, phospholipids are highly susceptible and can undergo modifications (from a localized change to complete membrane disruption). Generally, an exogenous or endogenous free radical attack on the phospholipids causes lipid peroxidation, a process which consists of three steps: (i) initiation, which includes formation of lipid peroxyl radicals (4), (ii) propagation of peroxyl radicals and (iii) its termination. Each of these steps can cause significant changes to the chemical structure of phospholipids; wherein membrane functionality can either be impaired or lost. The propensity with which the lipids are modified depends highly on the type of radical used. Such modifications of the phospholipids can be elucidated by detecting changes in the membrane forces (rupture or adhesion) as a parameter, among many others available (5-7). Such quantifications can help to understand properties such as membrane permeability (not to be confused with passive diffusion of molecules across a lipid bilayer) and instability (which can be measured with tip-membrane pull-off force), possible lateral movement of phospholipids, etc. An increase in the pull-off force indicates an increase in membrane rigidity and a decrease in membrane permeability.

Nitric oxide (NO) is one of the most intriguing radical due to its ability to promote and inhibit lipid peroxidation (8). Although NO is not a strong oxidant and has a very short half-life, its action cannot be undermined, especially under aqueous conditions. Its lipophilic nature makes it an interesting molecule for its action on lipid bilayers. Of special interest is its effect on lipid rafts (LRs) bilayers. LRs, also called as micro-domains are specialized regions in a cell membrane with distinct composition. They consist of a unique combination of phospholipids, sterols (e.g. cholesterol, CH) and sphingolipids (9, 10) which has been found to locally change the physical properties of a cell membrane. Unlike general phospholipid membranes, which are known to be ‘liquid-disordered’ in their arrangement above transition temperature, presence of cholesterol makes the membrane ‘liquid-ordered’ (11-14). This change effectively reduces the lateral diffusion of biomolecules (e.g. proteins) in the bilayer, suggesting its crucial role (e.g. in fibrin clot retraction by integrin protein αiibβ3 mediated platelet aggregation (15) or as therapeutic targets (16)). With many studies focused on understanding the effect of CH

concentration on membrane properties under redox conditions (17-20), little is known about the impact of sphingomyelin (SM) (21).

Here we combine force spectroscopy and AFM imaging to investigate the action of NO on lipid rafts (POPC:SM:CH) bilayers. Although the phospholipid composition varies with each cell type, the outer leaflet of any cell membrane in eukaryotes mainly consists of phosphatidylcholine (22, 23). For this reason, we have selected for this study the unsaturated phosphatidylcholine POPC lipid, which mimics the mammalian cell composition. We have characterized the membrane properties at varying SM concentrations and under NO addition. In addition, a biochemical assay which detects malondialdehyde, an important stress biomarker, has been used.

Materials and Methods

Formation of small unilamellar vesicles (SUVs)

Small unilamellar vesicles (SUVs) were prepared using phospholipids 1-palmitoyl-2-oleoyl-glycero-3-phosphocholine (POPC), egg sphingomyelin (SM) and natural cholesterol (CH) (Avanti Polar Lipids Inc., USA). Lipids were first solubilized in a solution containing chloroform, mixed and dried under a stream of nitrogen and kept under vacuum overnight. Then, the dried lipid film was resuspended in Phosphate Buffered Saline (PBS) buffer (Biowest, France) at pH 7.4 containing 1 mM $CaCl_2$ (Sigma, Germany). The lipid solution was then sonicated (SoniPrep 150 Plus, MSE centrifuges, UK) with a probe tip sonicator until the color of the solution turned from milky to clear (~ 5 min for the change in color). This solution was later centrifuged at 13000 g for 15 min to remove any titanium particles from the probe and the supernatant was collected. The lipid composition in the SUVs were varied: i.e. POPC:SM:CH in ratios of 2:0:1 (0.75 mM: 0 mM: 0.375 mM), 2:1:1 (0.75 mM: 0.375 mM: 0.375 mM) and 2:2:1 (0.75 mM: 0.75 mM: 0.375 mM). 100 µl of the preformed SUVs from each ratio were then diluted into 100 µL of PBS buffer. To prepare lipid rafts (LRs) from the above solution, 70 µL were taken and incubated onto freshly cleaved mica (area of 0.5cm^2) sheet for 40 min at room temperature (RT) (which is above the lipid transition temperature) to form bilayers. The excess solution containing unbound vesicles were removed and fresh PBS buffer was added onto mica sheet for further experimentation.

Nitric oxide action on lipid bilayers

The effect of nitric oxide (NO) on the bilayers was observed using the NO donor molecule: 1-Hydroxy-2-oxo-3-(3-aminopropyl)-3-isopropyl-1-triazene called as NOC-5 (Dojindo, Germany). NOC-5 was added to the pre-formed lipid bilayers and allowed to interact for 15

min at RT. The time period was selected based on our previous findings (24), where this time period was sufficient to observe a detectable physical change. Post-incubation, the NOC-5 solution was aspirated and fresh PBS buffer was added. The NO-treated bilayers were later subjected to AFM imaging and force spectroscopy. NOC-5 is a molecule which instantly releases NO when it comes in contact with H^+ ions in solution. Hence, it was prepared in 10 mM NaOH to reduce this instant release. However, as OH^- ions can impact the pH of the micro-environment, as per company suggestions, NOC-5 was added such that volume ratio does not exceed 1/50 of the total sample volume. This retained the overall pH of sample in solution. NOC-5 solution was freshly prepared for every measurement.

Force spectroscopy

Force spectroscopy measurements were carried in aqueous solution at RT to determine the forces of lipid bilayers in PBS buffer using JPK NanoWizard 3 (Berlin, Germany). Cantilevers (OBL-10, nominal spring constant of ~6 pN nm^{-1} and nominal tip radius of 30 nm from Bruker, Germany) were UV-ozone treated (Pro Cleaner Plus, Bioforce Nanoscience, USA) for 30 min and calibrated using thermal method. The calibration was first done in air against mica and then in PBS buffer. The calibration software provided in the JPK instrument recorded the new spring constant and deflection sensitivity which was used further. A deviation of 10-20% from the company mentioned spring constant was observed. The force curves obtained (approach speed of 1 µm/s) were processed using JPK Data Processing software (version 5.0.91) and analyzed using a home-written MATLAB script. To determine the peak adhesive forces, a histogram of the forces obtained was plotted and Kernel density estimation (KDE) method (non-parametric method for multivariate distribution analysis) was applied (with Gaussian kernel) to determine the peak position.

AFM imaging and data analysis

AFM imaging in liquid was carried out in Bioscope Resolve machine (Bruker, Germany) using FESP-V2 cantilevers (Bruker, Germany). Images of control and NO-treated samples were captured. The height profile of each of the samples were determined and analyzed using Nanoscope Analysis software v2.0 (Bruker, Germany). During analysis, only flatly adsorbed bilayers were considered. The roughness of both the substrate, i.e. mica, was determined.

Malondialdehyde assay

Malondialdehyde (MDA) is an organic compound formed when phospholipids undergo lipid peroxidation. In this colorimetric assay (Biorbyt, Germany), SUVs were treated initially with NO for 15 min at RT which were later allowed to react with thiobarbituric acid (TBA) molecule which forms MDA-TBA adduct (indication of oxidation-based products). Absorbance of the

formed adducts was determined at 532 nm. The quantification of MDA (nM) molecules was carried out as described in the kit's manual.

Results and Discussion

Changes in the membrane permeability (referred as tip-membrane permeability in future text) by varying SM concentration and respective action by NO were investigated by measuring the membrane forces (referred as pull-out force). Figure 1 shows an overview of the experimental setup to capture the force data.

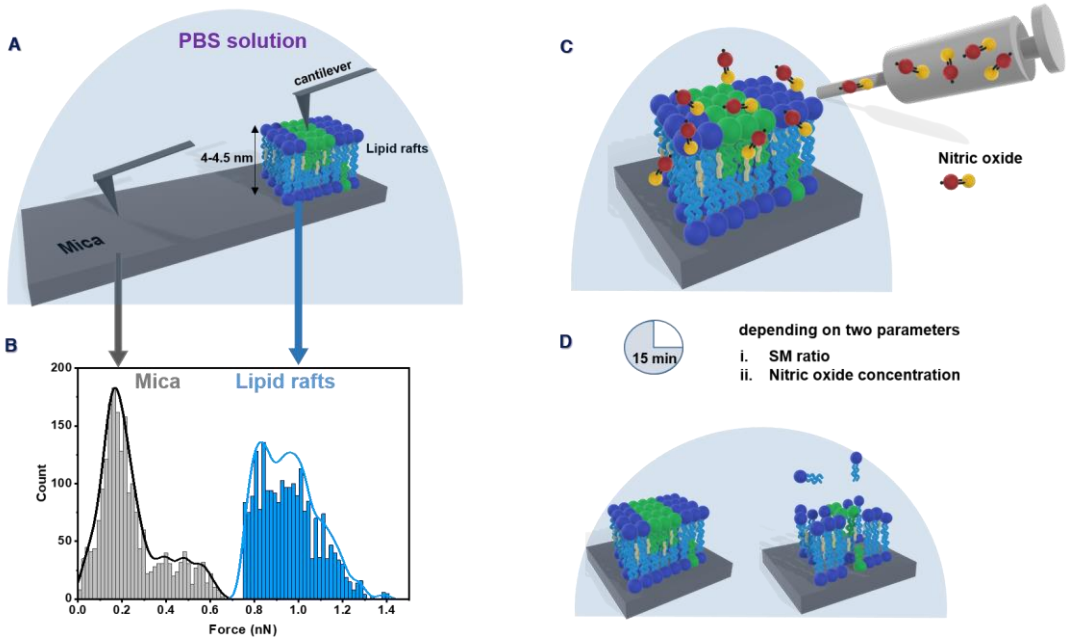

Figure 1. Overview of the experimental setup and determination of threshold forces. Prior to tip-membrane force measurements, forces due to non-specific interactions (i.e. tip-mica surface) were determined (A). The tip-mica surface generated adhesive forces ranging between 0.02 - 0.65 nN (B) with a maximum at ~ 0.2 nN. Based on the obtained values, 0.75 nN was set as threshold force above which adhesive forces were attributed to the pull-out force of the AFM tip from the lipid bilayer. Control and lipid rafts samples (with changing sphingomyelin concentration) were then treated with nitric oxide for 15 min (C) and analysed using force spectroscopy and AFM imaging (D). The histogram shown in (B) is plotted from the adhesion data of untreated POPC:SM:CH (2:0:1) bilayers. The straight lines are Kernel Density Estimates (KDE).

Figure 2 displays the schematic representation of a force curve obtained from a SMFS experiment. As the AFM tip approaches and detects the lipid bilayer, an initial repulsive force is followed by a kink in the approach curve (Figure 2, point '1') indicating the penetration of the AFM tip into lipid bilayer. Complete break-through is observed at point '2' (Figure 2) (25). When the tip is pulled out from the bilayer (retract curve), an adhesive force is observed. The width (D) obtained in each force curve represents the thickness of the bilayer. Prior experiments, baseline forces were determined to avoid non-specific interactions i.e. background noise attributed by the equipment and tip-mica interactions (due to incomplete

coverage of lipid bilayer on the mica, Figure 1A). Figure 1B shows the observed adhesive forces. A background noise of 0.02 nN was fixed and the tip-mica surface interactions yielded a distribution of adhesive forces ranging between 0.02-0.65 nN with maximum at ~ 0.2 nN (Figure 1B, *grey histogram* and Supplementary Figure S1). Based on the obtained values, an upper limit of 0.75 nN was set as threshold, above which adhesive forces were attributed to pull-out forces of tip from the lipid bilayer. From the total force curves recorded, events for tip-bilayer interactions constituted less than 5%.

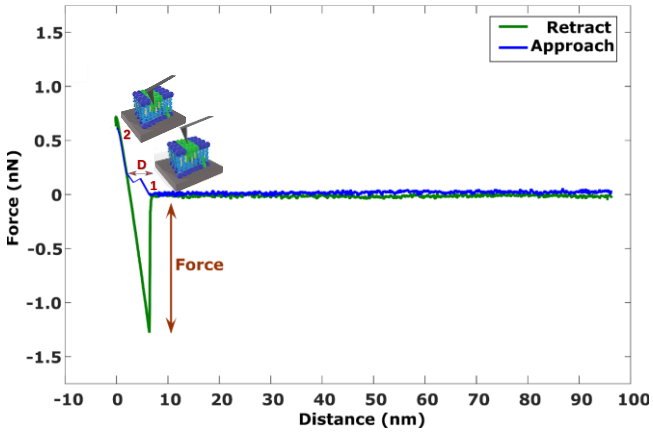

Figure 2. Schematic representation of acquisition of a force curve and respective events on the bilayer. Initially, the tip starts moving in the solution from a large distance towards the lipid bilayer (approach curve) until it comes in contact with it (indicated in the diagram as point 1). Then, the tip penetrates into the bilayer and constant compliance occurs (point 2). When the tip is pulled out of the lipid bilayer, it generates an adhesive force, detected as pull-out force (retract curve). The depth of tip penetration on approach (D), corresponds to the height of bilayer. As a typical example, a force curve for untreated POPC:SM:CH (2:0:1) bilayers is shown.

Sphingomyelin influences pull-out forces in LRs

We first analysed how sphingomyelin impacts the pull-out forces after AFM tip penetration, which entails on tip-membrane permeability. Three different ratios were used for LRs (i.e. POPC:SM:CH in ratios of 2:0:1, 2:1:1 and 2:2:1). We report for LRs with 2:0:1 ratio (i.e. in the absence of SM) two maxima of the pull-off forces at 0.83 nN and 1.0 nN with forces ranging between 0.75 - 1.38 nN (Figure 3A, *left*). The maxima of the forces were determined using KDE analysis. The data points which determined the maxima of the forces are those which had a probability density greater than 0.2 during analysis (representing significant events). With addition of SM, i.e. at 2:1:1 ratio, the pull-off force range was found to be similar to that of 2:0:1 ratio with two distinct maxima at 0.81 nN and at 1.02 nN (Figure 3B, *left*), respectively. Upon increasing SM further, i.e. at 2:2:1 ratio, there was an increase in the maximum of the pull-off force to 2.04 nN (Figure 3C, *left*). Another important observation was that, unlike previous ratios where the pull-off force spectrum was broad, most of the forces for 2:2:1 ratio were localized at around 2 nN. The increase in the pull-off forces with increased SM

concentration indicates an increase in membrane rigidity and reduction in the tip-membrane permeability.

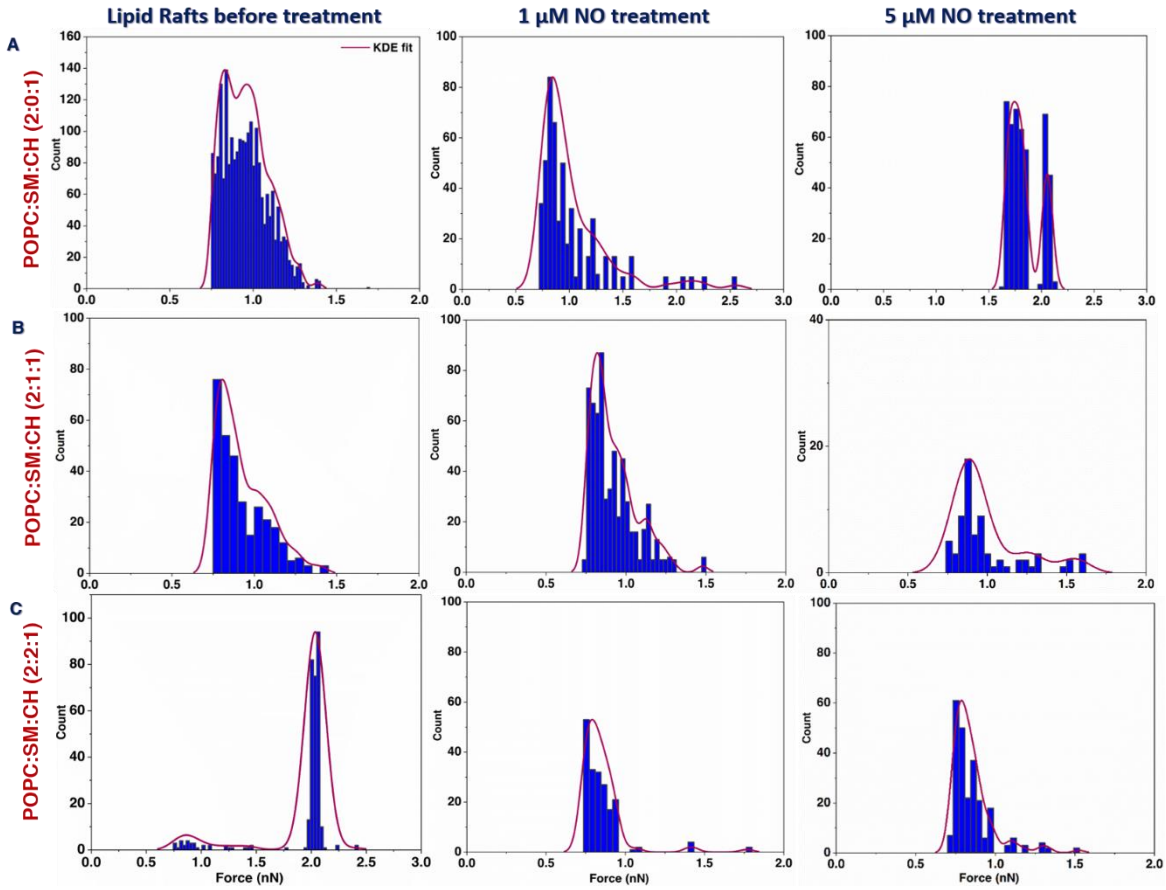

Figure 3. Histograms of tip-lipid bilayer pull-off forces of lipid rafts (LRs) with different SM concentration in dependence to NO treatment. Force data of untreated LRs (*left column*), LRs post 1 µM- (*middle column*) and post 5 µM NO treatment (*right column*) are shown. In each row, lipid rafts with the same composition are shown. Untreated LRs show increase in pull-off forces at the largest SM concentration (A, B, C, *left*) which indicates reduced membrane permeability. Addition of 1µM NO to 2:0:1 (POPC:SM:CH) ratio caused the force spectrum to broaden (A, *middle*) compared to control (A, *left*), with maxima forces at 0.85 nN and 1.21 nN. At 5 µM, the maxima forces increased further to 1.74 nN and 2.05 nN (A, *right*). For 2:1:1 (POPC:SM:CH) ratio, a competitive behavior is observed and after NO treatment (at 1 µM and 5 µM), the pull-off forces (B, *middle* and *right*) were similar to untreated 2:1:1 (POPC:SM:CH) ratio. This indicates presence of possible critical concentration in maintaining membrane integrity. At 2:2:1 (POPC:SM:CH) ratio, detrimental effect of NO is observed (C, *middle* and *right*) with decrease in pull-off forces compared to control (C, *left*) indicating membrane destruction. Histograms represent force data of only tip-membrane interactions; tip-mica forces being excluded.

NO modulates SM-dependent tip-membrane pull-off force

After describing the effect of inclusion of SM into bilayers, we now look into the action of NO on LRs. 1 µM and 5 µM concentrations of NO were used because they are found in cells (26, 27) at any given time and direct oxidation by NO is observed at lower concentrations. On treatment of LRs 2:0:1 (POPC:SM:CH) with 1 µM NO, we found that, with respect to control (in the absence of NO, Figure 3A, *left*), the force distribution became very broad and the forces ranged between 0.75 - 2.5 nN and maxima at 0.85 nN and 1.21 nN (a maximum with reduced intensity) were obtained (Figure 3A, *middle*). An increase in pull-off forces was visible with

increase in NO concentration to 5 µM with the force histogram ranged between 1.6 - 2.1 nN (Figure 3A, *right*) having peaks at 1.75 nN and 2.05 nN. These numbers collectively indicate that in case of LRs without SM, addition of NO caused reduction in tip-membrane permeability.

Upon addition of SM to the LRs i.e. in 2:1:1 (POPC:SM:CH) ratio, a competitive behavior was observed compared to 2:0:1 (POPC:SM:CH) ratio. When the bilayers were treated with 1 µM NO, the force range was similar as for the sample in absence of NO (Figure 3B, *left*) and the peak maxima were at 0.82 nN, 0.95 nN and 1.12 nN (Figure 3B, *middle*). However, treatment of the bilayer with 5 µM NO showed only one maximum at 0.89 nN, with forces ranging between 0.75-1.6 nN (Figure 3B, *right*). Although pull-off forces between 1 - 1.5 nN were captured for 2:1:1 (POPC:SM:CH) ratio, the number of events was too low for quantification. No significant shifts in the peaks or the force range were visible. At 2:2:1 (POPC:SM:CH) ratio, 1 µM NO treatment caused sufficient membrane damage, i.e. it increased tip-membrane permeability (opposite to previous ratios). The maximum force was obtained at 0.80 nN (Figure 3C, *middle*), while control (Figure 3C, *left*) showed pull-off forces at 2 nN. The increase in tip-membrane permeability continued for treatment with 5µM NO as well (Figure 3C, *right*) with peak at 0.78 nN (similar to 1 µM NO). These results confirm that as the concentration of SM is increased, membrane stability is significantly perturbed by NO radical. Also (in contrast to earlier observation), the results indicate that NO along with SM show a concentration dependence as expected for a regulatory molecule. To validate whether these observations correspond to any change in topological features, AFM imaging of the LRs was performed.

AFM imaging of LRs

At 2:0:1 (POPC:SM:CH) ratio, AFM imaging revealed a reduction in the height of bilayer on treatment with NO. 1 µM NO treated sample showed a reduced height of ~2 nm (Figure 4A, *middle*) when compared to control of ~4 nm (Figure 4A, *left*). This behaviour was persistent when NO concentration was increased to 5 µM with the height being reduced further to ~1.65 nm (Figure 4A, *right*). The decrease in the height profiles for 2:0:1 (POPC:SM:CH) ratio (showing membrane fluctuations) was in sharp contrast with the force data (where pull-off forces increased with NO addition). At 2:1:1 (POPC:SM:CH) ratio, we found that for 1 µM NO treatment, the height of the lipid bilayer remained unchanged and is similar to that of control i.e. ~4.5 nm (Figure 4B, *left and middle*). While this ratio definitely showed a shift in height profile when compared to the AFM images of 2:0:1 ratio, its behaviour was in accordance with the pull-off forces observed for 2:1:1 ratio. The correlation between AFM

images and force data confirms maintenance of membrane integrity (some sort of equilibrium) for this particular LRs composition. This equilibrium is however slightly disturbed when height of bilayers treated with 5 µM NO were reduced to ~4 nm (Figure 4B, *right*). Although, the obtained height is within the limits of a typical bilayer, its thickness is reduced partially compared to control (Figure 4B, *left*). This suggests that negligible changes in the height of bilayer do not necessarily mean that other physical parameters might not be influenced.

At 2:2:1 (POPC:SM:CH) ratio (Figure 4C), similar to 2:0:1 ratio, the height of bilayer is reduced from ~4 nm (control, Figure 4C, *left*) to ~3 nm (for 1 µM NO, Figure 4C, *middle*) and ~2.75 nm (for 5 µM NO, Figure 4C, *right*). Similar observations were made in the force data as well (i.e. decrease in the pull-off forces). This difference, when compared to 2:1:1 (POPC:SM:CH) ratio, underlines the change in the behaviour of bilayer and its dependency on lipid composition. These variations support our previous understanding that the action of NO becomes regulatory in presence of SM and is moving towards becoming increasingly pro-oxidant with increase in SM concentration.

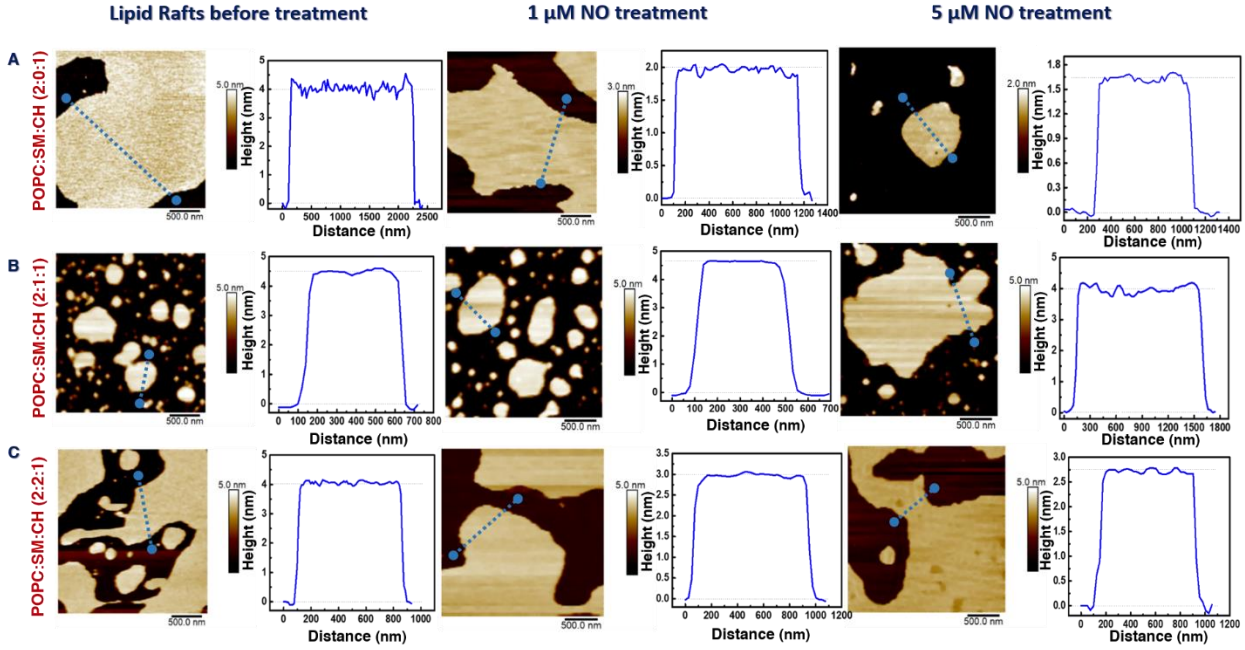

Figure 4. AFM images of lipid rafts (LRs) with changing SM concentration and NO treatment. Images of untreated LRs (*left column*), LRs post 1 µM- (*middle column*) and post 5 µM NO treatment (*right column*) are shown. The height profiles of each image are adjacent to it. At 2:0:1 (POPC:SM:CH) ratio, addition of NO showed decrease in the height of the lipid bilayer (A, *middle* and *right*) compared to control (A, *left*). At 2:1:1 (POPC:SM:CH) ratio, the height profile remained the same for both control and treated bilayer i.e. ~4.5 nm (B, *left* and *middle*) even after 1 µM NO treatment. This indicates membrane stability and negligible effect of NO. The height reduces partially for 5 µM NO treatment to ~4 nm (B, *right*). At 2:2:1 (POPC:SM:CH) ratio, change in height of lipid bilayer is observed (C, *middle* and *right*) indicating the role of NO as a pro-oxidant. Overall, a direct relation between membrane forces and bilayer height was obtained except for 2:0:1 ratio. Note the changed y-scale in the height profiles in (A) and (C).

Figure 5 summarizes the behaviour of tip-membrane permeability for all three LRs ratios at the investigated NO concentrations. In presence of NO (blue arrow), tip-membrane permeability of POPC:SM:CH (2:0:1) starts to decrease with addition of NO (i.e. the pull-off force increases). POPC:SM:CH (2:1:1) ratio showed mixed results i.e. at 1 µM NO, lipid rafts were stable and tip-membrane permeability was unaltered, while at 5 µM NO, lipid rafts became slightly unstable, but tip-membrane permeability was almost the same. These findings suggest the existence of a possible critical ratio (violet-dashed box) in natural cell membranes in response to change in redox conditions. POPC:SM:CH (2:2:1) ratio showed an increase in tip-membrane permeability with rising NO concentration.

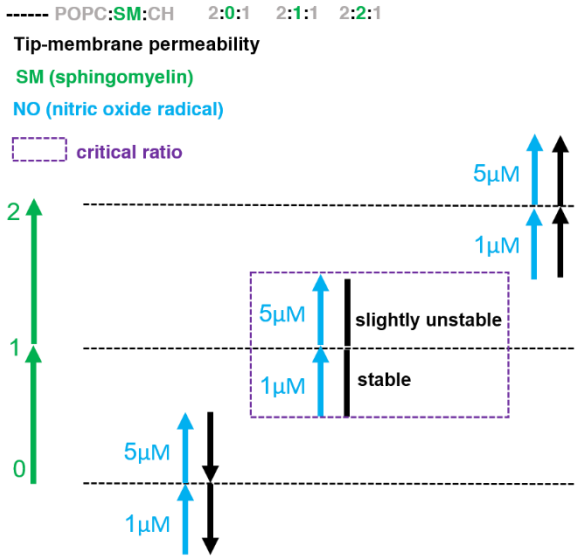

Figure 5. Interpretation of tip-membrane permeability of lipid rafts with changing sphingomyelin ratio and nitric oxide concentration. In the presence of NO (blue arrow), tip-membrane permeability (black arrow) of POPC:SM:CH (2:0:1) decreases with increase in NO concentration. With addition of sphingomyelin (green arrow) i.e. POPC:SM:CH (2:1:1) ratio, 1 µM NO shows stable lipid rafts and unaltered tip-membrane permeability. At 5 µM NO, the tip-membrane permeability was almost the same. This indicates existence of a critical ratio (violet-dashed box). POPC:SM:CH (2:2:1) ratio showed increase in tip-membrane permeability with increase in NO concentration.

Lipid composition-dependent physico-chemical modifications

A phospholipid undergoes modification when a radical attacks either the head group or tail group or both. We believe that in our setup the changes are restricted to the phospholipid tails because NO is a lipophilic molecule and has greater partition coefficient into the hydrophobic spaces of the membrane when compared to other solute molecules of similar size. This understanding is supported in literature both by experiments and simulations (17, 28, 29). With the presence of C=C bond in the phospholipid tail region, lipid peroxidation by NO is driven mainly by either nitration, nitroxidation, or both (30-32) unlike other radicals where one kind

of chemical reaction takes place (e.g. hydroxyl which causes only oxidative reaction and attacks the head group of phospholipid).

Although we cannot confirm on the exact type of chemical modifications undergone by the LRs, we performed peroxidation assay to detect in the system malondialdehyde (MDA), a product formed due to lipid modification mainly through oxidation and is a standard biomarker used for detection of oxidative stress in cells. We found that in LRs with 2:0:1 (POPC:SM:CH) ratio, ~ 0.6 nM of MDA for 1 µM NO and ~ 0.4 nM of MDA for 5 µM NO was formed. This amount increased to ~ 0.8 nM and ~ 0.75 nM (1 µM and 5 µM NO) for 2:1:1 (POPC:SM:CH) ratio and ~1.25 nM and ~ 1.4 nM (1 µM and 5 µM NO) for 2:2:1 (POPC:SM:CH) ratio (Figure 6).

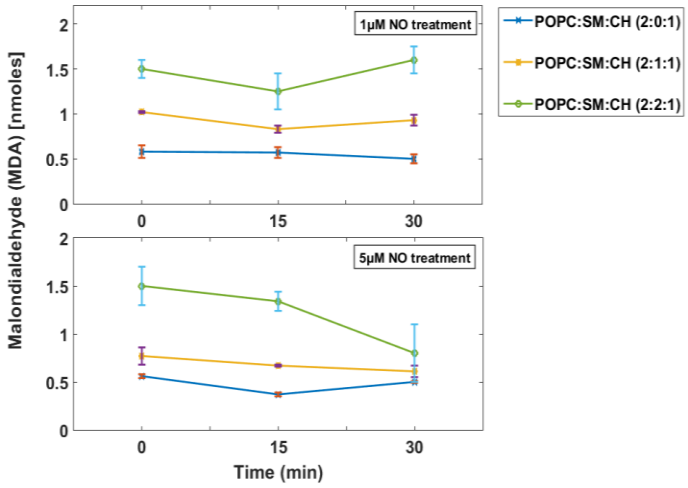

Figure 6. Lipid peroxidation assay to detect formation of MDA. With concentration of POPC being fixed, increasing SM supplemented to the amount of MDA (nM) formed. At 1µM NO treatment (above), LRs of 2:0:1 showed lower MDA concentration (~0.6 nM) compared to 2:1:1 (~0.8 nM) and 2:1:1 (POPC:SM:CH) showed lower MDA compared to 2:2:1 (POPC:SM:CH) ratio (~1.25 nM). The same behavior was observed at 5 µM NO concentration (below). Individual data points show that the formation of MDA is proportional to SM addition. The assay shows that while NO initiated the peroxidation, the concentration of produced MDA becomes constant over time, indicating that all available unsaturated lipids were either modified or subsequent arrested by NO as it can promote or inhibit lipid peroxidation. The absorbance values were obtained after subtraction of the blank as mentioned in the Materials and Methods section.

This increase in MDA clearly indicates that lipids underwent nitroxidation (i.e. oxidation by NO). By comparing the amount of MDA formed (Figure 6, *above* and *below)* for 1 µM and 5 µM NO treatment, we found that the difference between the obtained values is not significant, indicating that the MDA formation is independent of NO concentration or radical exposure time. Two possibilities arise here: i) all phospholipid molecules underwent initial chemical changes, and ii) NO radical itself underwent modification (as it is not a strong oxidant and no further increase in MDA was observed at 30 min).

Based on these results, we interpret that changes in the membrane mechanical properties (pull-off force and height) of LRs highly vary. This behaviour was absent when compared to simple

unsaturated phospholipid bilayers (e.g. POPC:POPS where radical attack showed a linear change in height and decrease in break-through forces, Supplementary Figure S2) or saturated bilayers (e.g. DMPC:DMPG where 1μM NO stabilized the membrane and 5μM NO increased tip-membrane permeability, Supplementary Figure S3). This was evident with other similar phospholipids as well (17, 33). In terms of lipid packing between unsaturated phospholipids (POPC) and sphingolipids (SM), the tail region of sphingolipids is elongated and contacts adjacent sphingolipid molecules thereby, increasing the van-der-Waals attraction forces between the tails (34-36). Such increased forces reduced the tip-membrane permeability as observed in bilayers with large SM concentration (Figure 3). As LRs also contains sterol (CH); this mixture underlines the possible interplay by SM and CH in the presence of NO. When looked individually, cholesterol is known to increase the thickness of lipid bilayer (37) by stretching its tails, but maintaining the chain volume (38) and causing close packing of lipid molecules (i.e. decreased molecular area). However, this does not occur in LRs of 2:0:1 (POPC:SM:CH) ratio in presence of NO because we observe a decrease in the bilayer thickness, but an increase in pull-off forces. If cholesterol had undergone nitroxidation, then it would be modified to oxysterols. There are many end products formed when cholesterol is chemically modified into oxysterols and they are primarily grouped as either tail-oxidized sterols or ring-oxidized sterols. Free radicals are known to cause mainly ring-oxidized sterols and these modified cholesterol molecules do not significantly change the membrane permeability (39, 40). However, possible change in the spatial orientations of these oxidized sterols cannot be overlooked (which could explain the reduction in the bilayer height). When SM was introduced i.e. in 2:1:1 (POPC:SM:CH) ratio, we reported that the membrane integrity was maintained at 1 μM NO and 5 μM NO exposure. In cell systems, there is evidence that SM sustains the redox homeostasis (41), but explicit information that a critical SM concentration is needed for sustainability, over which it starts to have deleterious effect is reported here for the first time. Available literature reports that based on the structure of sphingolipids (Supplementary Figure S2), they can participate in both inter- and intramolecular hydrogen bonding, which is not possible in glycerolipids. This assists in maintaining the membrane stability under stress (42), however it depends on the extent of oxidation undergone by the SM (43). This was clearly visible when the membrane characteristics of LRs 2:1:1 (POPC:SM:CH) ratio and 2:2:1 (POPC:SM:CH) ratio at two different NO concentrations were compared. Also, the presence of SM is known to inhibit oxidation of CH significantly (44), which might explain increase in MDA formation (due to increasing exposure of lipid unsaturation by SM and fixed POPC molecules), but not substantial variations in the heights

of bilayer. This leads to our understanding that upon NO addition, SM along with POPC starts to dominate in the interplay with CH in the final outcome of membrane modifications rather than each of the molecules when observed individually.

Nitration of phospholipids depends on radical environment

While we reported on nitroxidation (Figure 6), phospholipid nitration (i.e. modification to phospholipid by reactive nitrogen moiety) is another possible NO-induced modification of lipid bilayer. NO is a weak radical and usually not all the NO released by NOC-5 solution will cause direct membrane modification. It can easily be converted to other stable intermediates when reacted with other molecules depending on the surrounding environment (e.g. in presence of enzymes like glutathione peroxidase, radicals like hydroxyl or superoxide) (45, 46). One such molecule which is present in our system is molecular oxygen. By itself, molecular oxygen is hydrophobic in nature and can reside in the intermediate spaces of membrane similar to NO. Since force measurements and imaging experiments were carried out in aqueous aerobic solution for 15 min, we can easily assume that the time period was sufficient for NO to undergo reaction with oxygen. The stable products formed could be either nitrite (NO_2^-), nitrate (NO_3^-) or N_2O_3. Previously, we had reported on the formation of nitrite for the above used time duration (24). Hence, it is possible that these products can also constitute potential nitrosating agents and can cause nitro-fatty acid generation (47-49). A detailed chemical analysis is required to determine the influence of these products on lipid rafts.

Conclusion

In this study, combining biophysical and biochemical analyses, we show that nitric oxide radical can significantly alter the membrane characteristics and change the tip-membrane permeability and thickness of lipid rafts. The membrane modifications are dependent on the lipid composition and nitric oxide concentration. We found that in the absence of sphingomyelin in POPC:SM:CH lipid rafts (ratio 2:0:1), NO increased the pull-off forces and decreased the tip-membrane permeability and membrane thickness. At 2:1:1 (POPC:SM:CH) ratio, membrane integrity was maintained (when compared to control) even when exposed to 1 µM NO. Also, the thickness of lipid rafts remained unchanged. An interplay between sphingomyelin and cholesterol is believed to be involved in maintaining the stability where sphingomyelin seems to dominate along with POPC. Over 2:2:1 (POPC:SM:CH) ratio, the membrane thickness and stability were reduced, indicating regulatory role of sphingomyelin and NO. Peroxidation assay highlighted that lipids might have undergone nitroxidation and the

extent of lipid modification due to peroxidation depended on sphingomyelin concentration. In addition, the action of nitric oxide on the lipid rafts was instantaneous and independent of incubation time and radical concentration.

Author contributions

SK and AA contributed equally to this work. SK and MD are responsible for design and conceptualization. SK performed force-spectroscopy measurements, related data analysis and preparation of figures. AA performed AFM imaging. SK and AA jointly analyzed and finalized imaging figures. SK wrote the manuscript. SK, AA, CH and MD reviewed the manuscript.

Acknowledgements

We thank Deutsche Forschungsgemeinschaft (DFG, German Research Foundation) GRK 1947/3 - 231396381 for the financial support.

Conflict of Interest

The authors declare no competing financial interests regarding this work.

References

1. Anishkin, A., S. H. Loukin, J. Teng, and C. Kung. 2014. Feeling the hidden mechanical forces in lipid bilayer is an original sense. Proceedings of the National Academy of Sciences 111(22):7898-7905.
2. Diz-Muñoz, A., D. A. Fletcher, and O. D. Weiner. 2013. Use the force: membrane tension as an organizer of cell shape and motility. Trends in cell biology 23(2):47-53.
3. van Meer, G., and A. I. de Kroon. 2011. Lipid map of the mammalian cell. Journal of cell science 124(1):5-8.
4. Ayala, A., M. F. Muñoz, and S. Argüelles. 2014. Lipid peroxidation: production, metabolism, and signaling mechanisms of malondialdehyde and 4-hydroxy-2-nonenal. Oxidative medicine and cellular longevity 2014.
5. Crawford, G., and J. Earnshaw. 1987. Viscoelastic relaxation of bilayer lipid membranes. Frequency-dependent tension and membrane viscosity. Biophysical journal 52(1):87.
6. Espinosa, G., I. López-Montero, F. Monroy, and D. Langevin. 2011. Shear rheology of lipid monolayers and insights on membrane fluidity. Proceedings of the National Academy of Sciences 108(15):6008-6013.
7. Tyler, W. J. 2012. The mechanobiology of brain function. Nature Reviews Neuroscience 13(12):867-878.
8. Hogg, N., and B. Kalyanaraman. 1999. Nitric oxide and lipid peroxidation. Biochimica et Biophysica Acta (BBA)-Bioenergetics 1411(2-3):378-384.
9. Munro, S. 2003. Lipid rafts: elusive or illusive? Cell 115(4):377-388.
10. Calder, P. C., and P. Yaqoob. 2007. Lipid rafts—composition, characterization, and controversies. The Journal of nutrition 137(3):545-547.

11. Xiang, T.-X., and B. D. Anderson. 1998. Influence of chain ordering on the selectivity of dipalmitoylphosphatidylcholine bilayer membranes for permeant size and shape. Biophysical journal 75(6):2658-2671.
12. Thewalt, J. L., and M. Bloom. 1992. Phosphatidylcholine: cholesterol phase diagrams. Biophysical journal 63(4):1176-1181.
13. Owicki, J., and H. McConnell. 1980. Lateral diffusion in inhomogeneous membranes. Model membranes containing cholesterol. Biophysical journal 30(3):383-397.
14. Ohvo-Rekilä, H., B. Ramstedt, P. Leppimäki, and J. P. Slotte. 2002. Cholesterol interactions with phospholipids in membranes. Progress in lipid research 41(1):66-97.
15. Bodin, S., C. Soulet, H. Tronchère, P. Sié, C. Gachet, M. Plantavid, and B. Payrastre. 2005. Integrin-dependent interaction of lipid rafts with the actin cytoskeleton in activated human platelets. Journal of cell science 118(4):759-769.
16. Rabani, V. 2017. Lipid rafts of platelet membrane as therapeutic target: role of" Omics".
17. Yusupov, M., K. Wende, S. Kupsch, E. Neyts, S. Reuter, and A. Bogaerts. 2017. Effect of head group and lipid tail oxidation in the cell membrane revealed through integrated simulations and experiments. Scientific reports 7(1):1-14.
18. Roy, S., A. Dasgupta, U. Banerjee, P. Chowdhury, A. Mukhopadhyay, G. Saha, and O. Singh. 2016. Role of membrane cholesterol and lipid peroxidation in regulating the Na+/K+-ATPase activity in schizophrenia. Indian journal of psychiatry 58(3):317.
19. Jacob, R. F., and R. P. Mason. 2005. Lipid peroxidation induces cholesterol domain formation in model membranes. Journal of Biological Chemistry 280(47):39380-39387.
20. Van der Paal, J., E. C. Neyts, C. C. Verlackt, and A. Bogaerts. 2016. Effect of lipid peroxidation on membrane permeability of cancer and normal cells subjected to oxidative stress. Chemical science 7(1):489-498.
21. Koval, M., and R. E. Pagano. 1991. Intracellular transport and metabolism of sphingomyelin. Biochimica Et Biophysica Acta (BBA)-Lipids and Lipid Metabolism 1082(2):113-125.
22. Van Meer, G., D. R. Voelker, and G. W. Feigenson. 2008. Membrane lipids: where they are and how they behave. Nature reviews Molecular cell biology 9(2):112-124.
23. Casares, D., P. V. Escribá, and C. A. Rosselló. 2019. Membrane lipid composition: effect on membrane and organelle structure, function and compartmentalization and therapeutic avenues. International journal of molecular sciences 20(9):2167.
24. Karanth, S., and M. Delcea. 2020. Nitrosative stress affects the interaction of integrin alphaIIbbeta3 with its ligands. Biochimica et Biophysica Acta (BBA)-Biomembranes 1862(5):183198.
25. Franz, V., S. Loi, H. Müller, E. Bamberg, and H.-J. Butt. 2002. Tip penetration through lipid bilayers in atomic force microscopy. Colloids and Surfaces B: Biointerfaces 23(2-3):191-200.
26. Lancaster Jr, J. 1997. A tutorial on the diffusibility and reactivity of free nitric oxide. Nitric oxide 1(1):18-30.
27. Malinski, T., Z. Taha, S. Grunfeld, S. Patton, M. Kapturczak, and P. Tomboulian. 1993. Diffusion of nitric oxide in the aorta wall monitored in situ by porphyrinic microsensors. Biochemical and biophysical research communications 193(3):1076-1082.
28. Wennberg, C. L., D. Van Der Spoel, and J. S. Hub. 2012. Large influence of cholesterol on solute partitioning into lipid membranes. Journal of the American Chemical Society 134(11):5351-5361.

29. Möller, M., H. Botti, C. Batthyany, H. Rubbo, R. Radi, and A. Denicola. 2005. Direct measurement of nitric oxide and oxygen partitioning into liposomes and low density lipoprotein. Journal of Biological Chemistry 280(10):8850-8854.
30. Rubbo, H., R. Radi, M. Trujillo, R. Telleri, B. Kalyanaraman, S. Barnes, M. Kirk, and B. A. Freeman. 1994. Nitric oxide regulation of superoxide and peroxynitrite-dependent lipid peroxidation. Formation of novel nitrogen-containing oxidized lipid derivatives. Journal of Biological Chemistry 269(42):26066-26075.
31. Reis, A., and C. M. Spickett. 2012. Chemistry of phospholipid oxidation. Biochimica et Biophysica Acta (BBA)-Biomembranes 1818(10):2374-2387.
32. O'Donnell, V. B., J. P. Eiserich, P. H. Chumley, M. J. Jablonsky, N. R. Krishna, M. Kirk, S. Barnes, V. M. Darley-Usmar, and B. A. Freeman. 1999. Nitration of unsaturated fatty acids by nitric oxide-derived reactive nitrogen species peroxynitrite, nitrous acid, nitrogen dioxide, and nitronium ion. Chemical research in toxicology 12(1):83-92.
33. Riske, K. A., T. P. Sudbrack, N. L. Archilha, A. F. Uchoa, A. P. Schroder, C. M. Marques, M. S. Baptista, and R. Itri. 2009. Giant vesicles under oxidative stress induced by a membrane-anchored photosensitizer. Biophysical journal 97(5):1362-1370.
34. McIntosh, T. J., S. A. Simon, D. Needham, and C. H. Huang. 1992. Structure and cohesive properties of sphingomyelin/cholesterol bilayers. Biochemistry 31(7):2012-2020.
35. Demel, R. A., and B. De Kruyff. 1976. The function of sterols in membranes. Biochimica et Biophysica Acta (BBA)-Reviews on Biomembranes 457(2):109-132.
36. Brown, R. E. 1998. Sphingolipid organization in biomembranes: what physical studies of model membranes reveal. Journal of cell science 111(1):1-9.
37. Nezil, F. A., and M. Bloom. 1992. Combined influence of cholesterol and synthetic amphiphillic peptides upon bilayer thickness in model membranes. Biophysical journal 61(5):1176-1183.
38. Hung, W.-C., M.-T. Lee, F.-Y. Chen, and H. W. Huang. 2007. The condensing effect of cholesterol in lipid bilayers. Biophysical journal 92(11):3960-3967.
39. Kulig, W. T., H. Mikkolainen, A. Olzynska, P. Jurkiewicz, L. Cwiklik, T. Rog, M. Hof, I. Vattulainen, and P. Jungwirth. 2017. Oxidation of Cholesterol Changes the Permeability of Lipid Membranes. Biophysical Journal 112(3):377a.
40. Kulig, W., A. Olżyńska, P. Jurkiewicz, A. M. Kantola, S. Komulainen, M. Manna, M. Pourmousa, M. Vazdar, L. Cwiklik, and T. Rog. 2015. Cholesterol under oxidative stress—How lipid membranes sense oxidation as cholesterol is being replaced by oxysterols. Free radical biology and medicine 84:30-41.
41. Won, J.-S., and I. Singh. 2006. Sphingolipid signaling and redox regulation. Free Radical Biology and Medicine 40(11):1875-1888.
42. Pascher, I. 1976. Molecular arrangements in sphingolipids Conformation and hydrogen bonding of ceramide and their implication on membrane stability and permeability. Biochimica et Biophysica Acta (BBA)-Biomembranes 455(2):433-451.
43. Borchman, D., O. P. Lamba, S. Salmassi, M. Lou, and M. C. Yappert. 1992. The dual effect of oxidation on lipid bilayer structure. Lipids 27(4):261-265.
44. Sargis, R. M., and P. V. Subbaiah. 2006. Protection of membrane cholesterol by sphingomyelin against free radical-mediated oxidation. Free Radical Biology and Medicine 40(12):2092-2102.
45. Liu, X., M. J. Miller, M. S. Joshi, D. D. Thomas, and J. R. Lancaster. 1998. Accelerated reaction of nitric oxide with O2 within the hydrophobic interior of biological membranes. Proceedings of the National Academy of Sciences 95(5):2175-2179.

46. Violi, F., R. Marino, M. Milite, and L. Loffredo. 1999. Nitric oxide and its role in lipid peroxidation. Diabetes/metabolism research and reviews 15(4):283-288.
47. Bakan, E., S. Taysi, M. F. Polat, S. Dalga, Z. Umudum, N. Bakan, and M. Gumus. 2002. Nitric oxide levels and lipid peroxidation in plasma of patients with gastric cancer. Japanese journal of clinical oncology 32(5):162-166.
48. Freeman, B. A., P. R. Baker, F. J. Schopfer, S. R. Woodcock, A. Napolitano, and M. d'Ischia. 2008. Nitro-fatty acid formation and signaling. Journal of Biological Chemistry 283(23):15515-15519.
49. Jain, K., A. Siddam, A. Marathi, U. Roy, J. Falck, and M. Balazy. 2008. The mechanism of oleic acid nitration by• NO2. Free Radical Biology and Medicine 45(3):269-283.

Supplementary Information

Identification of a critical lipid ratio in lipid rafts exposed to nitric oxide: An AFM study

SK, AA, CAH and MD

Figure S1: Force histogram of tip-mica surface to determine non-specific interactions.

Figure S2: Force histogram, AFM images and height profiles of POPC:POPS bilayer treated with NO.

Figure S3: Force histogram, AFM images and height profiles of DMPC:DMPG bilayer treated with NO.

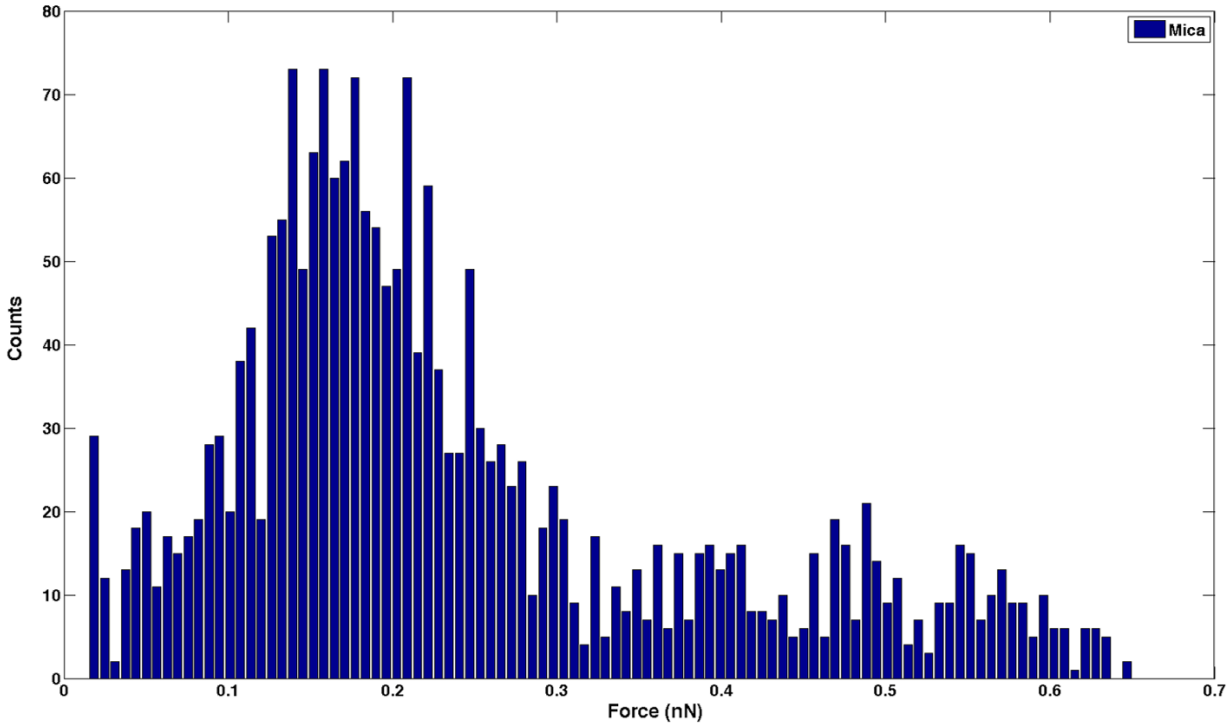

Figure S1. Force histogram of tip-mica surface to determine non-specific interactions. Forces ranging between 0.02 - 0.65 nN, with maximum forces at around 0.2 nN, are displayed.

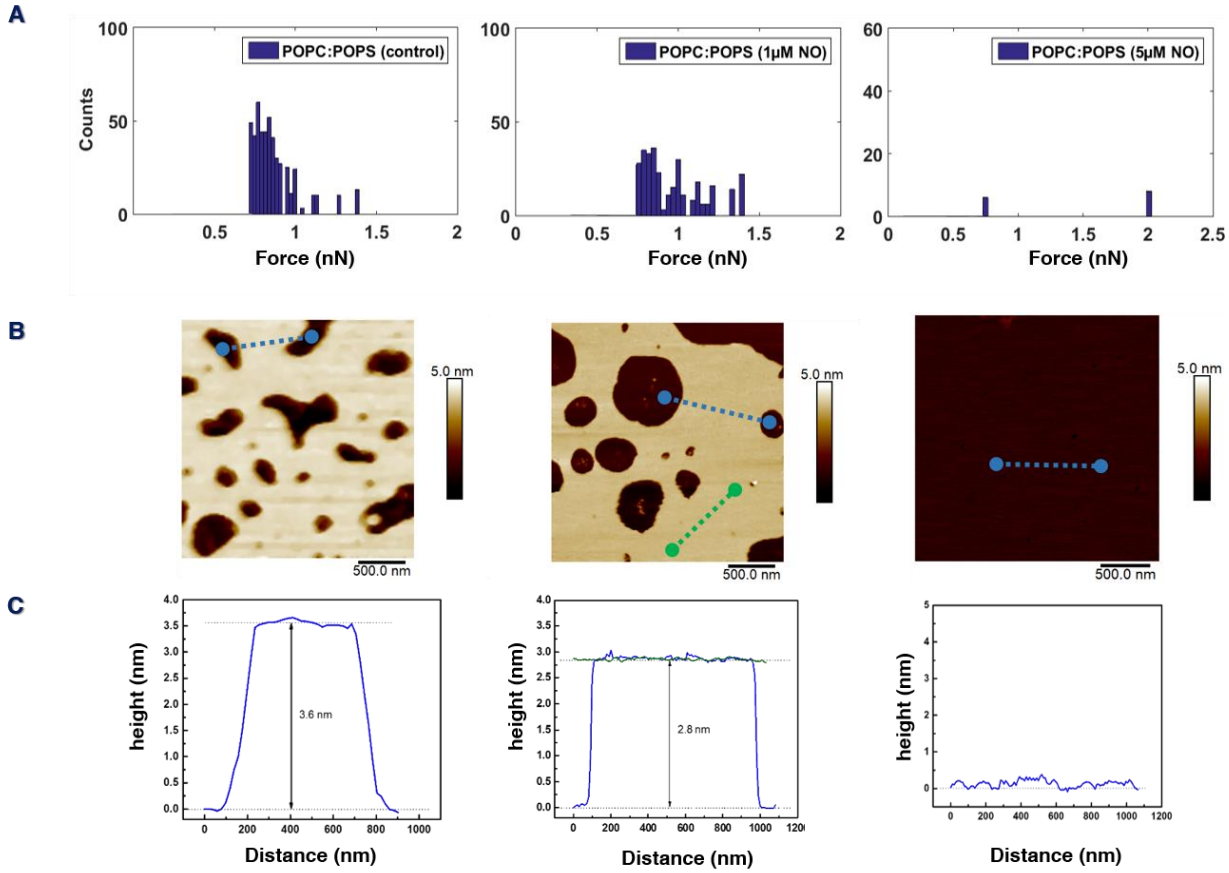

Figure S2. Force histogram (A) and AFM images (B) of POPC:POPS bilayer treated with 1 μM NO (*middle*) and 5 μM NO (*right*). Height profiles of respective images are also shown (C). POPC:POPS bilayer showed linear reduction in height of bilayer with increasing NO concentration. At 1 μM NO treatment, the maximum forces were similar to control (A, *left*), but complete membrane disruption was observed at 5 μM NO (A, *right*).

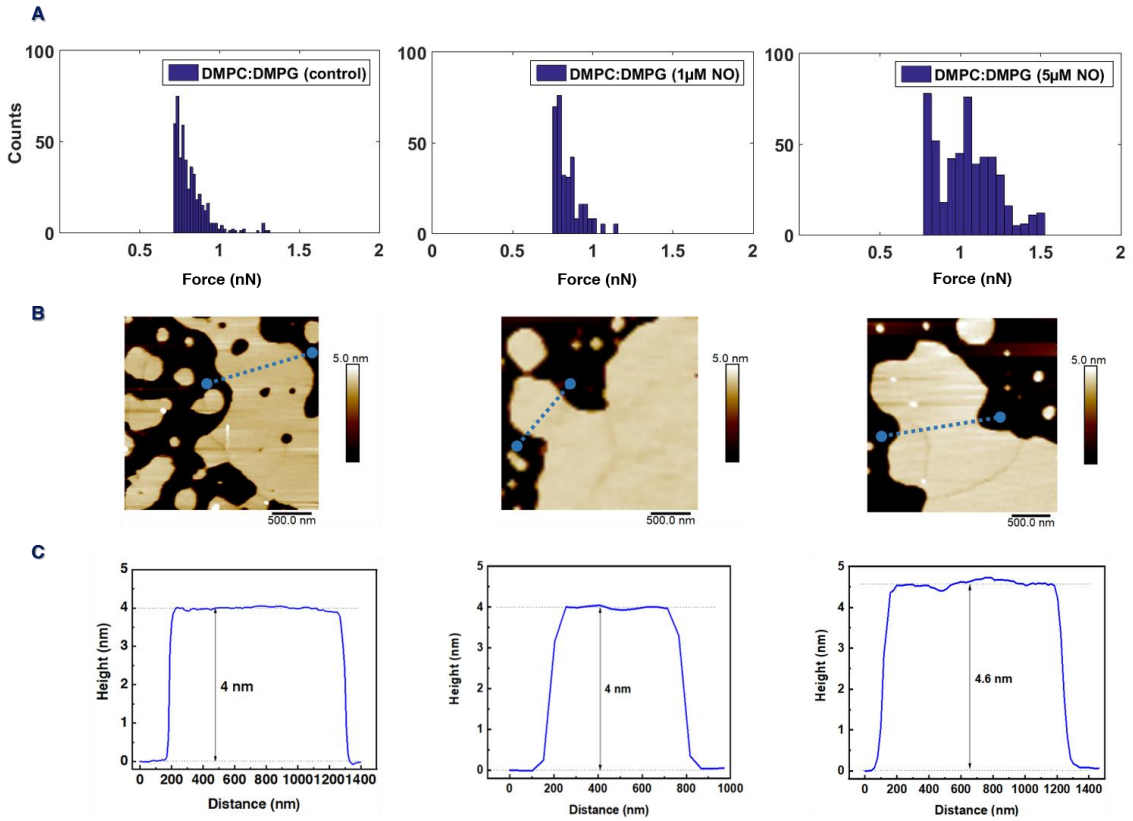

Figure S3. Force histogram (A) and AFM images (B) of DMPC:DMPG bilayer treated with 1 μM NO (middle) and 5 μM NO (right). Height profiles of respective images are also shown (C). DMPC: DMPG bilayer showed no changes in height or peak forces for 1 μM NO concentrations. At 5 μM NO, the maximum forces increased with increase in bilayer height, indicating NO dependent changes on saturated membranes.

II. Nitrosative stress affects the interaction of integrin alphaIIbbeta3 with its ligands

Sanjai Karanth and Mihaela Delcea

Biochimica et Biophysica Acta (BBA) - Biomembranes
Volume 1862, Issue 5,
1 May 2020, 183198
Available online: 17 January 2020

doi: 10.1016/j.bbamem.2020.183198

Published by Elsevier B.V.

BBA - Biomembranes 1862 (2020) 183198

Contents lists available at ScienceDirect

BBA - Biomembranes

journal homepage: www.elsevier.com/locate/bbamem

Nitrosative stress affects the interaction of integrin alphaIIbbeta3 with its ligands

Sanjai Karanth[a,b], Mihaela Delcea[a,b,c,*]

[a] Institute of Biochemistry, University of Greifswald, Felix-Hausdorff-Straße 4, 17489 Greifswald, Germany
[b] ZIK-HIKE, Zentrum für Innovationskompetenz "Humorale Immunreaktionen bei kardiovaskulären Erkrankungen", Fleischmannstraße 42, 17489 Greifswald, Germany
[c] DZHK (DeutschesZentrumfürHerz-Kreislauf-Forschung), Partnersite Greifswald, Germany

ARTICLE INFO

Keywords:
Integrin alphaIIbbeta 3
Nitric oxide
Nitrites
Nanodiscs
Atomic force microscopy imaging
Single molecule force spectroscopy

ABSTRACT

Binding of integrin alphaIIbbeta3 (αiibβ3) to its ligands is a highly restricted and regulated mechanism. Any modification of the protein structure yields a dysfunctional role, especially in a redox environment. Here, we examine the effect of nitrosative stress on the αiibβ3 reconstituted into nanodiscs. Using single molecule force spectroscopy, we measured the interaction between αiibβ3 and its ligand RGD and found that in the presence of exogenous nitric oxide (NO·) two force regimes are generated: a low force regime of ~100pN indicating the presence of integrin in a normal status, and a broad spectrum of high force regime (~210–450pN) suggesting the protein modification/aggregation. By high resolution atomic force microscopy imaging, we demonstrate that both NO· and nitrite (a stable product formed from NO·) are involved in destabilizing the transmembrane protein complex leading to release of αiibβ3 from the lipid bilayer and protein aggregation. Our experimental setup opens new ways for testing in a membrane environment the effect of radical species on integrins under clinically relevant conditions.

1. Introduction

Integrin alphaIIbbeta3 (αiibβ3) is a transmembrane protein belonging to a large family of integrin proteins. These proteins are heterodimers containing α- and β-subunits non-covalently linked to each other. They function as cell surface receptors and are found on platelets, mast cells, megakaryocytes to name a few [1]. αiibβ3 attaches itself to the extracellular matrix or ligands (e.g. fibrinogen, von Willebrand factor) inducing a signaling cascade to maintain hemostasis, a critical activity of platelets. This type of mechanism is referred to as *outside-in* signaling. The binding of integrin to its ligands occurs using specific tripeptide sequence RGD (Arg-Gly-Asp) [2]. αiibβ3 can also bind to molecules present in the cytosolic region (e.g. talin, kindlin) and cause *inside-out* signaling displaying a bidirectional operating behavior.

When platelets circulate in blood, αiibβ3 attains a bent-state conformation also referred to as *low affinity state*. However, on coming in contact with adhesion constituents (e.g. thrombin, ADP or the above mentioned ligands), αiibβ3 can modify itself to active state i.e. *high affinity state*. The active αiibβ3 proteins interact with neighboring integrins and cause spreading of platelets. Recent reports have suggested the presence of an intermediate state in the process of αiibβ3 activation [3–5].

Abnormality in the structure of protein was observed in patients suffering from Glanzmann thrombasthenia, a genetic disorder where αiibβ3 is not present or it is not properly expressed [6] leading to increased bleeding and reduced clot formation. Similar symptoms were also observed in immune thrombocytopenia purpura (ITP) patients, where the counts of circulating platelets in blood were found to be reduced [7].

Studies of integrin structure revealed that both subunits contain many cysteine residues (18 in α and 56 in β) which are mostly present in the ectodomain region. Most of cysteines have a structural role and few of them are involved in protein functionality [8–10] and therefore, any redox modifications can lead to irregularity. Reactive nitrogen species (RNS) are a potential source for protein structure modification. RNS belong to the class of free radicals which are generated by our cells. The endogenous production of radicals is balanced by the release of antioxidants. For example, nitric oxide (NO·) is a radical generated together with citrulline by the interaction between L-arginine and oxygen in the presence of nitric oxide synthase [11]. NO· has a small size and contains in its outer shell one free electron which causes its faster diffusion and reactivity. Lancaster et al. [12] revealed that at 37 °C, NO· can travel a distance of around 100–200 μm with a diffusion coefficient of 3300 $\mu m^2/s$.

* Corresponding author at: Institute of Biochemistry, University of Greifswald, Felix-Hausdorff-Straße 4, 17489 Greifswald, Germany.
E-mail address: delcea@uni-greifswald.de (M. Delcea).

https://doi.org/10.1016/j.bbamem.2020.183198
Received 25 October 2019; Received in revised form 13 January 2020; Accepted 15 January 2020
Available online 17 January 2020

Under physiological conditions, NO· functions as a signaling molecule, vasodilator and regulator of the immune response. Clinical reports have indicated that ITP patients have reduced levels of NO· [13]. Studies reported that endogenous production of radicals in platelets inhibits their activity [14]. The reactivity of NO· is highly influenced by the surrounding environment. In the presence of oxygen and thiol donors, s-nitrosothiols are formed. In addition, nitrosylation in the presence of heme-group is possible [15,16].

NO· being lipophilic in nature, can easily cross the lipid membranes. Concentration-dependent oxidation of unsaturated phospholipids by NO· makes this small molecule a potential target in generation of lipid peroxides [17,18]. Whereas most of the research studies focused on detecting endogenous NO·, the effect of exogenous NO· on the *outside-in* signaling was not much investigated.

Here, we use a membrane mimicking environment i.e. integrin reconstituted into nanometer-sized lipid bilayers (called nanodiscs) to investigate using single molecule force spectroscopy, atomic force microscopy imaging and dynamic light scattering the effect of NO· on αiibβ3. Tripeptide RGD was used as model binding ligand to αiibβ3. Nanodiscs are held together by an amphiphilic protein called membrane scaffold protein (MSP). A single integrin reconstituted per nanodisc is achieved through this system in comparison with multiple integrins reconstituted per liposome.

2. Material and methods

2.1. Reconstitution of single integrin alpha IIbbeta3 into nanodiscs

Reconstitution of integrin αiibβ3 into nanodiscs was carried out following a modified protocol described by Ye et al. [19]. Briefly, 1 μM integrin αiibβ3 (Enzyme Research labs, USA) and 40 μM membrane scaffold protein (MSP1D1, Cube Biotech, Germany) were dialyzed in Tris buffer (10 mM Tris with 100 mM NaCl, pH 7.4). Dimyristoyl phosphatidylcholine (DMPC) and dimyristoyl phosphatidylglycerol (DMPG) lipids (Avanti Polar Lipids Inc., USA) were first solubilized in solution containing chloroform (DMPC) and chloroform:methanol (DMPG), mixed well and dried first under a stream of nitrogen and later dried under vacuum overnight. The dried lipid film was resuspended in lipid buffer (10mMTris, 100 mM NaCl, 100 mM cholate, pH 7.4). Equal ratios of DMPC and DMPG solution were mixed with MSP1D1 (shortly MSP) and integrin αiibβ3 (referred as *integrin* in further text) to a final lipids:MSP:integrin molar ratio of 1525:17:1. 70 mg of biobeads (SM2 Biobeads, Bio-Rad, Germany) were pre-washed in methanol, water and Tris buffer saline (TBS) containing 20 mM Tris, 150 mM NaCl, pH 7.4. The washed beads were added to the above solution and incubated overnight with gentle agitation at 300 rpm and at room temperature (RT), above transition temperature of lipids. Supernatant was collected the next day and the nanodiscs with reconstituted protein were purified using size exclusion chromatography (SEC, Äkta Explorer, GE Life Sciences). A Superdex 200 Increase column (10/300) was first equilibrated with TBS. Next, 0.25 mL solution of the integrin nanodiscs (called here *proteonanodiscs*) was loaded into the column and the eluted fractions for every 0.5 mL were collected at a flow rate of 0.5 mL/min. The eluted samples were stored at −20 °C and used within one week.

2.2. Validation of proteonanodiscs

2.2.1. SDS-PAGE

Proteonanodiscs were loaded on 4–12% gradient Bis-Tris SDS gels and verified under reducing conditions to visualize the accurate reconstitution. The protein bands of individual subunits were detected using Pierce Silver Stain Kit (Thermo Fischer, Darmstadt, Germany).

2.2.2. Dynamic light scattering (DLS)

The size of proteonanodiscs was measured using DLS technique (Zetasizer Nano ZS Malvern Instruments, Herrenberg, Germany). Proteonanodiscs were diluted in Tris buffer (1:10) and measured at RT in 10 mm-path length acrylic cuvettes (Sarstedt, Germany) at a backward scattering angle of 173°. A refractive index of 1.45 (changing with wavelength) and an absorption of 0.001 were used. Hydrodynamic diameter data was analyzed with the Zetasizer software 7.11.

2.2.3. Atomic force microscopy (AFM) imaging

20 μl of 0.3 μM proteonanodiscs were spread on atomically flat muscovite mica sheet, used as substrate. Prior to spreading, the mica sheet was freshly cleaved. Samples were allowed to rest for 60 s and substrates were washed for 15 s in deionized water (Milli-Q, Millipore, Billerica, USA) and dried in a laminar flow box (ScanLaf Class 2, LaboGene, Lynge, Denmark). Air imaging was performed using a Nanoscope IIIa controller (Veeco/Digital Instruments, Santa Barbara, USA). Images were obtained in tapping mode using OMCL-AC160TS (Olympus Corporation, Japan) cantilevers with an approximate curvature radius of 10 nm and a spring constant of 42 Nm^{-1}.

2.2.4. AFM imaging data analysis

Data processing of the obtained AFM images was carried out using a home-written MATLAB (MathWorks, 2010b) script. The position of each proteonanodisc on the substrate was localized by determining the local maxima. To account only for the flatly adsorbed proteonanodiscs and to exclude contaminations such as lipid micelles and surface roughness, a threshold local maximum above 2.5 nm height was considered. The height threshold was determined in accordance to the theoretical height calculated for an empty individual nanodisc as reported by Hagn et al. [20]. Contour surrounding one particular local maximum (half of the maximum height) was defined as the lateral boundary, analogous to the full width at half maximum (FWHM) in peak analysis. The region encircled corresponds to the area of interest occupied by a particular nanodisc population. Cross-sections provided height profiles of individual nanodiscs.

2.3. Activation assay for proteonanodiscs

The functionality of the reconstituted protein was verified using a fluorescence assay. For this assay, αiibβ3 was reconstituted into His-tag MSP1D1-containing proteonanodiscs, which were added onto a Ni^{2+} coated 96-well plate (Thermo Fischer, Darmstadt, Germany). Activation of integrin by 1 mM $MnCl_2$ for 90 min at RT was tested using PAC-1, a well-established antibody which binds only to the active state of the protein. PAC-1 antibody contained the fluorophore dye FITC (Bio Legend, Germany) with a maximum emission at 520 nm. Post-incubation, the fluorescence signal intensity was measured and the activation was detected.

2.4. Detecting nanomolar (nM) concentration of NO· in solution

Commercially available amiNO sensor has been reported to detect the concentration of NO· in solution [21]. Here we use the amiNO-100 microsensor which contains gas selective permeable membrane through which NO· diffuses. The diffused gas molecule is oxidized on the sensor surface generating an electric current which indicates the concentration of NO· surrounding the membrane (recorded by *inNO* software provided by the company Innovative Instruments Inc., FL, USA). The sensor was calibrated before use, as per company instructions i.e. NO· was generated in-situ by adding nitrite solution to an acidified medium in the presence of potassium iodide, a reducing agent. Release of NO· occurs as shown in Eq. (1):

$$2NO^{-}_{2} + 2I^{-} + 4H^{+} \rightarrow 2NO^{\cdot} + I_2 + 2H_2O \quad (1)$$

Calibration curve was plotted and sensitivity of the electrode (defined as the number of current units (in pA) which can detect 1 nM concentration of NO·) was determined.

As mentioned earlier, NO· is highly unstable radical and in the

presence of molecular oxygen will form intermediate stable compounds (e.g. nitrites). The concentration of formed nitrites was detected using the standard Griess reagent assay (Promega Corporation, Germany) which generates diazotized nitrites whose absorbance is detected at 540 nm.

2.5. Single molecule force spectroscopy (SMFS)

2.5.1. Functionalization of AFM tip with RGD ligand

AFM cantilevers (OBL-10 having nominal spring constant of ~6pNnm^{-1}) were purchased from Bruker. The cantilevers were first UV-ozone treated for 30 min, then incubated with 1 mg/mL NHS-PEG-COOH (MW: 3400 Da, Nanocs, USA) for 2 h at RT and rinsed five times with deionized water. Equal volumes of amine coupling agents i.e. 0.4 M 1-ethyl-3-(3-dimethylaminopropyl) carbodiimide hydrochloride (EDC) and 0.1 M N-hydroxysuccinimide (NHS), both purchased from ThermoScientific, were added to activate the carboxyl group of PEG linkers. This was incubated for 1 h at RT. Cantilevers were then washed thoroughly with deionized water and incubated with 0.1 mg/mL RGD ligand (Abcam, Germany) for 1 h. To reduce non-specific binding, ethanolamine (BIO-RAD) was added and incubated for 30 min. The cantilevers were used on the same day of preparation, else stored at 4 °C and used the next day.

2.5.2. Measurement and analysis of force-distance curves

SMFS measurements were carried out in Tris buffer using JPK NanoWizard 3 (Berlin, Germany). To measure the rupture forces between integrin and RGD ligand (Fig. 1), His-MSP proteonanodiscs were used. The His-tag of the His-MSP protein attached covalently to Ni^{2+} ions on the mica sheet, thereby immobilizing the proteonanodiscs. This also reduced hindrance to the orientation of integrin protein (due to its bidirectional signaling) and minimized its activation due to attachment on the substrate.

To study NO· effect on proteonanodiscs, samples were incubated with varying concentrations of NO· donor, NOC-5 (Dojindo, Germany) for 10 min at RT. Following this, samples were immobilized on mica sheet and force measurements were carried out.

The rupture forces were processed with the JPK Data Processing software (version 5.0.91) and analyzed using a home-written MATLAB script. Data distribution was determined using Kernel density estimation (KDE). Gaussian kernel was applied and peak rupture forces were determined.

3. Results and discussion

3.1. Proteonanodiscs revealed specific physical characteristics

Validation of proteonanodiscs after their purification from empty nanodiscs (referred as *nanodiscs* in future text) and unincorporated integrin using SEC (Fig. S1) was carried out through various techniques. The SDS-PAGE gel in Fig. 2A shows the successful insertion of both alpha- and beta-subunits into nanodiscs as indicated by the presence of two corresponding bands with Mw of around 100 kDa and 90 kDa, respectively. A band corresponding to apolipoprotein MSP1D1 is also visible on the gel (Mw ~ 23 kDa). In contrast, integrin subunits are absent in nanodiscs (Fig. 2A) and only the apolipoprotein band is visible. The size of proteonanodiscs measured by DLS is shown in Fig. 2B. Proteonanodiscs show an increased size (18.5 ± 3.1 nm) (mean ± SD) than nanodiscs (11.7 ± 1.1 nm). The measured size of nanodiscs is in good agreement with theoretical value (~10.6 nm) calculated using the equation provided by Hagn et al. as given below:

$$D = (Naa * 0.15/\pi) + 1\ nm$$

whereD = Diameter of the nanodisc,Naa = number of amino acids in MSP protein (201 in our case).

To further validate the reconstitution of integrin into nanodiscs, we used atomic force microscopy (AFM) imaging. Initially, proteonanodiscs were imaged directly on plain mica and displayed two height profiles (data not shown). As proteonanodiscs formed a free floating system, the cytoplasmic tail of integrin getting sandwiched to the negatively charged mica was possible, causing a change of protein conformation. To overcome this and to achieve a single conformation of integrin (crucial in force spectroscopy measurements), the experimental setup was modified as per Fig. 1A i.e. MSP protein with His-tag. This setup was used for all future experiments. Fig. 3 shows the representative AFM images and the corresponding cross-sectional height profiles of nanodiscs (A) and proteonanodiscs (B). Nanodiscs showed a mean height of 4.6 ± 0.6 nm, while proteonanodiscs presented at 9.5 ± 1.9 nm (Fig. S2). The obtained height is in good agreement with the literature values [22,23]. This height refers to the bent state of integrin in nanodiscs as successfully indicated by Rosano et al. [24].

3.2. Preserved functionality of proteonanodiscs

Previously, our group has reported on the Mn^{2+}-induced activation of integrin reconstituted in liposomes using PAC-1 antibody which recognizes the active integrin [25]. Because the concentration of proteonanodiscs obtained after SEC procedure was very low (~50 nM), our existing protocol was modified so that proteonanodiscs with His-MSP can be bound to Ni^{2+}-coated microtiter plate. Upon activation with 1 mM $MnCl_2$, PAC-1 showed nearly five-fold increase in fluorescence intensity in proteonanodiscs when compared to nanodiscs (Fig. 4). In addition, the presence of both integrin subunits in proteonanodiscs was determined using commercially available CD41 and CD61 antibodies which bind specifically to alpha- and beta-subunits, respectively.

3.3. Effect of NO· on integrin reconstituted into nanodiscs

As mentioned previously, integrin binds to its ligands (e.g. fibrinogen) using recognition sequence R-G-D and undergoes structural changes. To examine whether NO· influences the adhesion between RGD ligand and integrin we measured rupture forces by carrying SMFS on mica substrates with surface area of 0.5 cm^2 such that only single protein interactions can be detected.

To eliminate non-specific interactions, threshold forces were first determined. As His-MSP protein contained six histidine residues (6×), its interaction with Ni^{2+} ions were known to generate forces around 500pN [26]. Hence forces above 450 pN were considered as upper limit and forces larger than 75pN were considered for analysis as determined from controls (i.e. RGD ligand interaction with Ni^{2+}-coated mica and on empty nanodiscs) (Fig. S3). Thus, 75 pN formed the lower limit. Less than 10% of the total force curves were detected for actual measurements. A typical force curve is represented in Fig. 1B.

3.4. Changes in the distribution of rupture forces in proteonanodiscs and Mn^{2+}-activated proteonanodiscs

While the force distribution of proteonanodiscs spanned over several hundreds of piconewtons (Fig. 5A), a substantial number of events were captured around 100pN. A small regime showed forces ranging between 200–300pN. The forces from proteonanodiscs were similar to those for immobilized pure integrin on mica (Fig. S4). When the proteonanodiscs were treated with 1 mM $MnCl_2$ for 90 min, the distribution of higher forces became long-ranged between 200–500pN (Fig. 5B). KDE was applied to extract the peaks of high force distribution (Fig. S6B) and it was found that proteonanodiscs showed large density curve with peaks at 210pN and few at 284pN. Mn^{2+}-activated proteonanodiscs showed larger density plots with Gaussian behavior at 188pN and 218pN and smaller density plots at 316pN, 387pN, 426pN and 458pN. Forces higher than 450pN were neglected to avoid collusion with His-tag-Ni^{2+} ions rupture forces. Also, the number of events at 100 pN increased close to two-fold in Mn^{2+}-activated

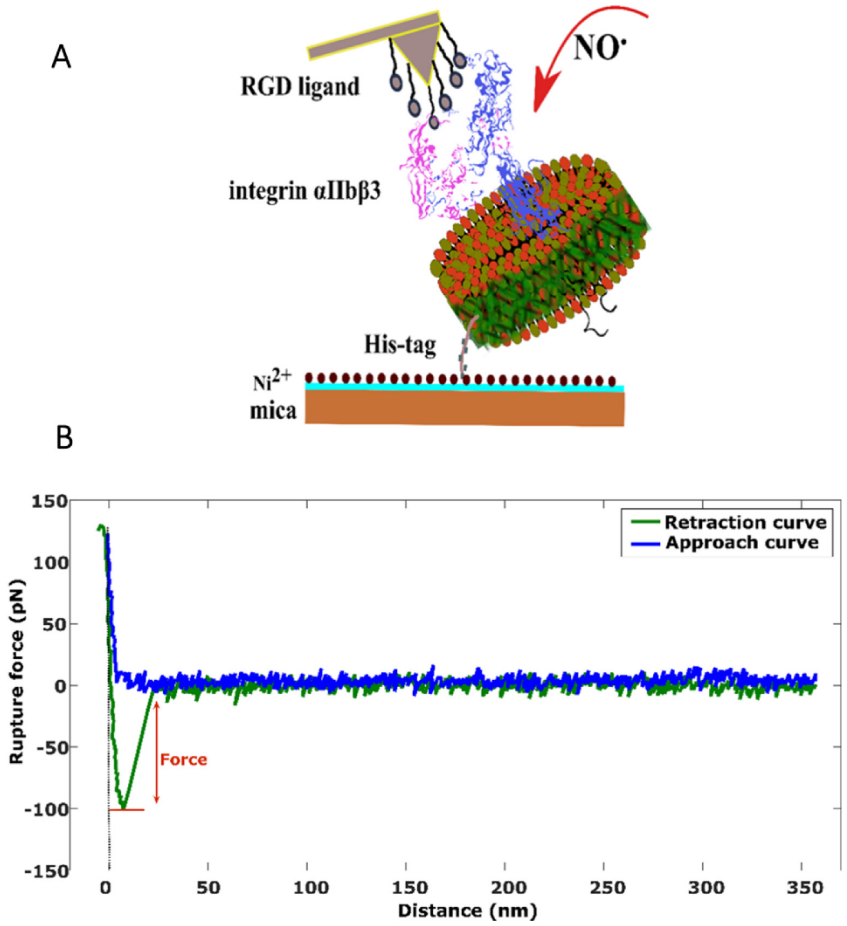

Fig. 1. Schematic representation of SMFS between integrin-RGD ligand. A) The AFM tip with attached RGD ligand is approaching the integrin leading to RGD-integrin interaction and upon separation allows to measure the rupture forces. The changes in the rupture forces over varying concentrations of NO· were recorded. Cartoon representation of integrin (α- subunit in pink and β-subunit in blue) from PDB structures (3FCS and 2K9J). B) Representation of a force curve obtained during experiment. Blue curve indicates the approach curve, where the RGD ligand coated tip comes in contact with the integrin protein and attaches itself. Green curve indicates the retraction curve when external force is applied on the cantilever tip to separate the interaction resulting in generation of rupture force. For force spectroscopy measurements, proteonanodiscs were immobilized on Ni^{2+}-coated mica sheets. This provided free orientation and reduced activation of protein due to its contact with the surface of the substrate.

proteonanodiscs when compared to untreated proteonanodiscs. This suggests that Mn^{2+} not only induces stronger adhesion of RGD ligand to integrin, but influences the overall conformational dynamics of protein to high affinity.

To understand the type of interaction occurring between RGD ligand and integrin, we analyzed the individual force curves. Each force curve generated a single rupture event indicating that only one bond is formed between the integrin and ligand. In our studies, it was difficult to determine the type of bond formed i.e. slip bond or catch bond. However, recent studies have confirmed that slip bond formation is predominant with RGD-integrin interaction. RGD inserts itself into the βTD and βA pocket of integrin, thereby causing the separation and

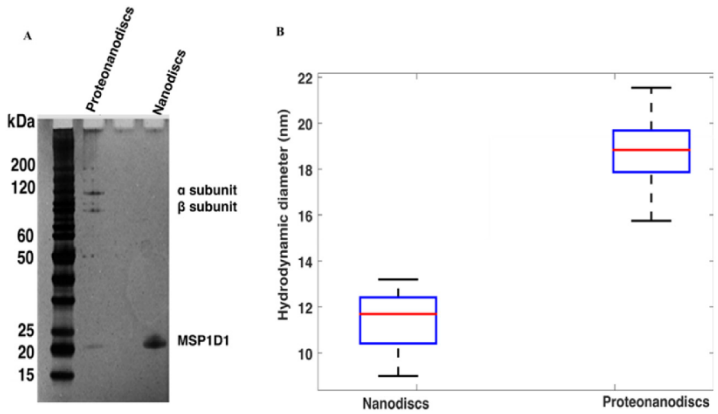

Fig. 2. Validation of proteonanodiscs formation. A) Reduced SDS-PAGE showing the presence of two bands corresponding to the integrin subunits in proteonanodiscs. The presence of MSP1D1 protein is evident for both nanodiscs and proteonanodiscs. B) Box and whisker plot indicating the hydrodynamic diameters obtained from DLS measurements carried out in Tris buffer, pH 7.4 at RT. Median is represented by red line. The lower and higher end of the box plot represents 25 and 75 percentiles, respectively.

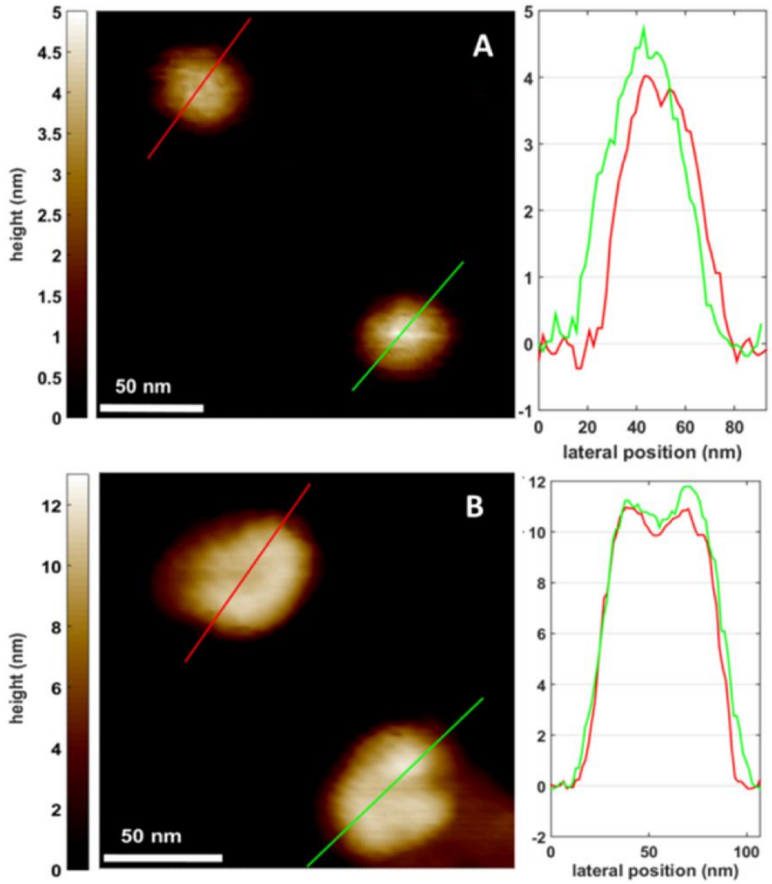

Fig. 3. Tapping mode AFM images on mica substrate. A) AFM image of empty nanodiscs indicating the formation of lipid bilayer and the corresponding cross-sectional profile showing heights of 4.6 ± 0.6 nm. B) AFM image of proteonanodiscs and the respective cross-sectional height profile of 9.5 ± 1.9 nm. Formation of an inverted bell shape in center with peaks on each side suggests the presence of the two subunits in the assembly. The cross-sectional heights are represented by the red and green lines and their corresponding peaks are on the right side.

rotation of transmembrane domains of the ß subunit [27]. As mentioned earlier, there are 18 cysteine residues in the α-subunit and 56 in the β-subunit. The cysteines in the β subunit are present in the ectodomain and this region is referred to as epidermal growth factor (EGF), which amounts to 31 residues. Although cysteines would be mostly present as disulfide bridges, studies have shown the presence of free thiols as well [9]. It was also reported that when cysteines in the EGF domain are present as disulfide bonds, they would maintain the inactive state of protein and even a single bond breakage would result in integrin activation [28]. However, further added evidence showed that

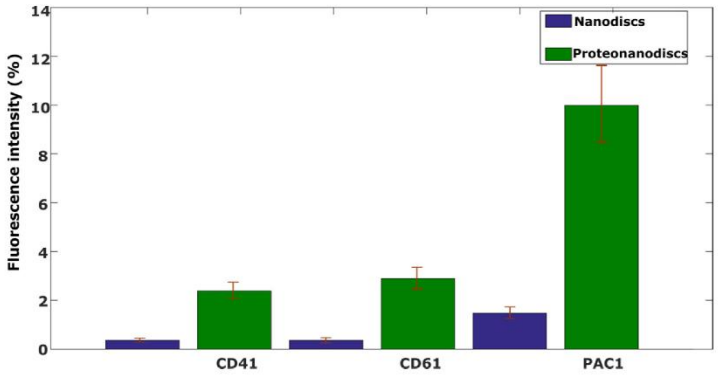

Fig. 4. Functionality of proteonanodiscs. Samples were tested for presence of integrin subunits and for its activity. The activation assay was performed using PAC-1 antibody (which binds to active integrin). Here, His-MSP proteonanodiscs coated on Ni^{2+}-coated microtiter plate were incubated with 1 mM $MnCl_2$ for 90 min and binding of FITC-labeled PAC-1 (5 μg/mL) was detected. The individual subunits were detected using FITC-CD41 and PE-CD61 (5 μg/mL each). The signal intensity was measured thrice and its standard deviation is represented. The background signals from buffer and nanodiscs were subtracted.

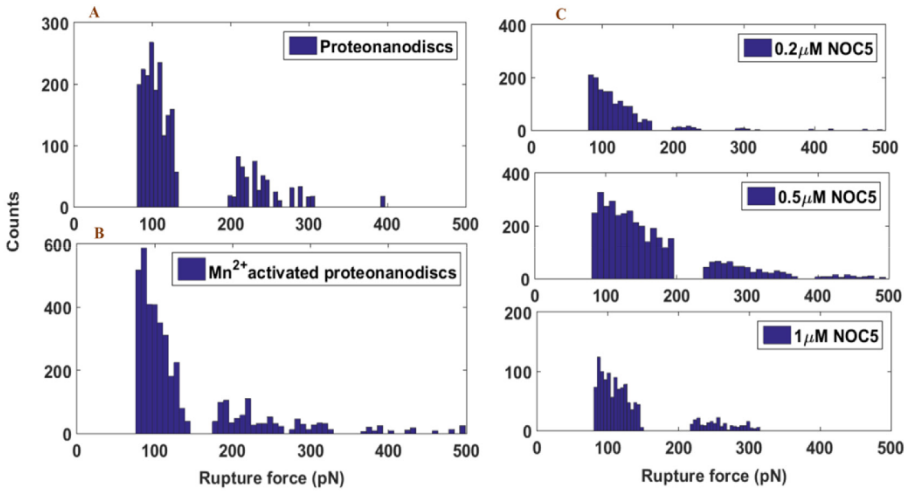

Fig. 5. Histogram of rupture forces at varying concentration of NOC-5. On treatment with 0.2 μM NOC-5, integrin showed relatively very low shifts in the high force distribution when compared with control i.e. *proteonanodiscs* (*A*). At high concentrations of NOC-5 (0.5 and 1 μM), forces greater than 250pN were generated. However, the distribution of these forces was not uniform as it was observed in the Mn^{2+} *activated proteonanodiscs* (*B*). These increased forces are due to the release of integrin from the lipid bilayer and aggregates of these integrins interacting with RGD ligand. Also the broadness of peak force curve at 100pN started to increase in NOC-5 treated samples compared to controls. NO· induced differential binding of RGD ligand changing structural dynamics. Note: All histograms were divided into equal bin width to observe changes in distribution.

even thiol-disulfide exchange induces integrin activation [29].

3.5. NO· treated proteonanodiscs generated forces similar to Mn^{2+}-activated proteonanodiscs

To further monitor the effect of NO· on the binding of integrin to RGD, NO· donor (i.e. NOC-5) at varying concentrations was incubated for 10 min with proteonanodiscs. NOC-5 instantly starts releasing NO· when it comes in contact with H^+ ions in solution. To reduce the degradation of the molecule, NOC-5 was prepared in 100 mM NaOH. Because OH^- can alter the pH of surrounding environment, as per company suggestions, the chemical was added such that volume ratio does not exceed 1/50 of total sample volume. Post-incubation, the sample was washed twice with Tris buffer to eliminate any possible pH effects. With increasing concentration of NOC-5, high range force distribution (> 130pN) was observed (Fig. 5C). 1 μM NOC-5 treated samples showed forces ranging between 210–320pN with density peaks at 224pN, 254pN and 298pN (Fig. S6A), while 0.5 μM NOC-5 treated samples showed a very broad distribution of high range forces between 230–370pN and 400–450pN. 0.2 μM NOC-5 samples showed similar high forces, but the density plots were very small with peaks observed at 223pN, 300pN, 400pN and 423pN. The distribution of forces for proteonanodiscs became broader with increasing NOC-5 concentration (visible for events captured at around 100 pN). While this indicates an increase in higher force regimes, the isolation of peak forces from these density plots became difficult. This was in strong contrast with the density plots obtained for Mn^{2+}-activated proteonanodiscs (as Mn^{2+} ions increases affinity of RGD-integrin interaction [30]). Also, recordings of single step rupture force with large lateral distances (~1% of total force curves) and few cases showing multiple rupture events were detected contradicting the type of interaction observed in proteonanodiscs and Mn^{2+}-activated proteonanodiscs. This divergent behavior in force curves was questioned.

3.6. NO· triggered release of integrin from lipid bilayer

Our initial understanding (from increased rupture forces) was that NO· is causing increased adhesion of RGD ligand to integrin. However, this contradicted the fact that decreased force events were captured during experiments (clearly visible in 1 μM NOC5-treated proteonanodiscs). To address this dilemma, we proceeded with AFM imaging. High resolution AFM imaging in air was performed to observe the topological changes in proteonanodiscs. As these proteonanodiscs contained His-MSP belt, mica was coated with Ni^{2+} [31]. Fig. 6 shows AFM images of NOC-5 treated proteonanodiscs.

At 0.2 μM NOC-5, both proteonanodiscs (Fig. 6A, green curve) and protein aggregates (Fig. 6A, red curve) were identified. With increase in NOC-5 concentration (Fig. 6B and C), disruption of proteonanodiscs was more predominant (disseminated structures with irregular heights). Cross-sectional heights of around 10 nm corresponding to height profiles of proteonanodiscs (for 0.5 and 1 μM concentrations) were not observed. In addition, heights of around 1 nm typical for integrin on mica [32] were found. These observations suggest the release of integrin from lipid bilayer.

To understand the reason for release, we studied possible protein-radical and lipid-protein interactions. We performed UV-spectroscopy on pure integrin (Fig. S5) and found that amide bonds peaked at 198 nm and 202 nm. Post-NO· treatment, shift in the peak was observed towards smaller wavelength and diminished peak at 202 nm. The peak at 202 nm corresponds to L-cysteine [33,34] and confirms the possible interaction of cysteine (in specific free thiols) with NO·. Oberprieler et al. [35] have also shown that NO· treated platelets have reduced platelet adhesion in a concentration-dependent manner. Also, s-nitrosylated integrin formed upon interaction with NO· was reported using Raman spectroscopy [36]. While we cannot indicate the exact type of protein modification, we can state that the reduced adhesion mentioned before can be due to structural rearrangement, wherein integrin is removed from the bilayer system. The long range high forces observed were from the interaction of RGD ligand with released aggregates.

To further confirm this observation, DLS measurements were carried out for nanodiscs and proteonanodiscs (Fig. S7). In NOC-5-treated proteonanodiscs, the average size continued to reduce, with sizes close to that of pure protein being observed.

Because NO· has higher affinity for membranes, topological changes in integrin can also be attributed to lipid-protein interactions.

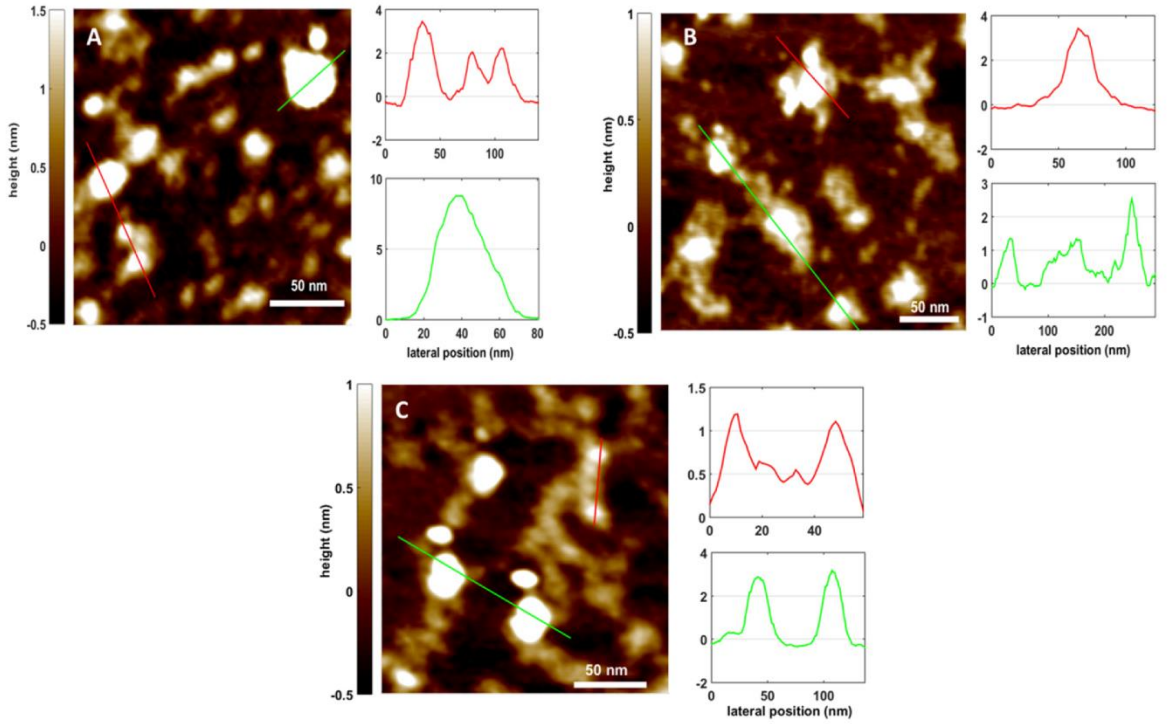

Fig. 6. AFM images of NOC-5 treated proteonanodiscs. A) 0.2 μM NOC-5 treated proteonanodiscs showed three types of population i.e. proteonanodiscs (green curve), empty nanodiscs (height of ~3.5 nm) and protein aggregates released from lipid system (indicated by red curve on the right). Samples treated with 0.5 μM (B) and 1 μM (C) NOC-5 only showed the presence of empty nanodiscs (very few in case of 1 μM NOC-5) and presence of protein aggregates. The height of the bilayer was essentially reduced to around 3.5 nm indicating the displacement of integrin from the bilayer.

Although the net charge on the nanodiscs was neutral (as DMPC is zwitterionic and DMPG is anionic lipid), it is well known that phospholipids rearrange themselves such that zwitterionic lipids are exposed to the outer leaflet of membrane, while anionic lipids to the inner region [37]. This contributes to the hydrophobic-electrostatic interactions between transmembrane (TM) domain of protein and lipid core. As DMPC and DMPG are saturated phospholipids, a potential site for radical attack in acyl chains was considered difficult. Electron paramagnetic resonance spectroscopy studies on DMPC have shown that radical activity depends on the diffusion-controlled concentration of NO· and its localization within the membrane to interact with protein residues [38]. Also, it is reported that NO· interaction is mostly with the choline group of the phospholipids thereby increasing the negative electron cloud on the head group and acting as protective layer [39]. DMPG, a negative surfactant was shown to inhibit production of nitric oxide both in vitro and in vivo [40]. We believe that, NO· causing destabilization of the lipid-TM complex is less predominant compared to protein-radical interaction.

3.7. Membrane integrity remained unaltered in DMPC/DMPG nanodiscs

As lipid bilayer is clasped with the help of MSP apolipoprotein (a high density lipoprotein), the next question we asked ourselves was whether NO· interaction is specific or unspecific in nature. With the concentrations selected close to physiological expectations and such that maximal effect from NO· is observed on integrin [41], we expected to see the presence of empty lipid bilayer in proteonanodiscs samples post NO·-treatment. All NOC-5-treated samples showed a characteristic height of ~3.5 nm (Fig. 6A–C). This reduced thickness in bilayer (in comparison to 4.5 ± 0.3 nm obtained from nanodiscs treated with NOC-5, Fig. S8) can be attributed to the exclusion of integrin from the bilayer, creating a void space exposed to hydrophilic environment which potentially changes the lipid-to-MSP ratio, very critical for stability of nanodiscs. While we cannot confirm on the modification of chain length of phospholipids due to radical exposure, a possible reorientation of phospholipids may have caused the MSP apolipoprotein belt to pack further, thereby reducing the diameter and thickness of bilayer.

3.8. NO· and its intermediates attack the integrin

NO· is a small, short lived molecule which diffuses well into the membranes with its reactivity depending on the environment (e.g. in the presence of superoxide ion it can form peroxynitrate, a potent oxidant causing lipid peroxidation). Having understood that NO· can modify integrin, we investigated the likelihood of this reaction because the exposure to NOC-5 is for only limited period (10 min). Under physiological conditions, direct interaction of NO· with protein thiols is slower and precursor agents such as NO^+ or N_2O_3 would be required first [42,43] for its detrimental effect. As, NO· is released in aqueous medium (contains oxygen), autoxidation of NO· becomes important here. NO· reacts with oxygen and forms NO_2 which can further react with other NO· molecules and form N_2O_3. In solution, N_2O_3 undergoes hydrolysis and forms nitrites. Due to plethora of possibilities, we investigated whether other stable products of NO· also affects the structural dynamics of integrin.

Direct NO· detection was carried out using an amperometric sensor, amiNO-100. The concentration was detected at the beginning and at the end of the incubation period of NOC-5 with proteonanodiscs (Table 1). Parallelly, Griess assay was carried out to detect the nitrite

Table 1
Determination of NO· production using amiNO-100 microsensor and nitrite production using Griess method. Direct NO· was detected using amiNO-100 microsensor. As compared to proteonanodiscs, the [NO·] in nanodiscs kept increasing with rise in NO· concentration. Proteonanodiscs samples showed decrease in concentration of nitrite over time indicating that both NO· and nitrite have been reacting with the integrin.

Sample	NOC-5 (μM)	Time (s)	NO· (nM)	Nitrite (nM)
Nanodiscs	0	0	20 ± 1	95 ± 3
		600	18 ± 1	95 ± 2
	0.2	0	29 ± 1	150 ± 1
		600	19 ± 2	~100
	0.5	0	88 ± 4	93 ± 3
		600	61 ± 2	~95
	1	0	243 ± 8	180 ± 50
		600	177 ± 7	1090 ± 90
Proteonanodiscs	0	0	20 ± 1	25 ± 2
		600	19 ± 1	23 ± 2
	0.2	0	65 ± 5	42 ± 2
		600	48 ± 3	40
	0.5	0	67 ± 4	123 ± 5
		600	60 ± 1	20 ± 2
	1	0	81 ± 6	120 ± 1
		600	62 ± 3	80 ± 2

concentration. Fig. S9 shows the standard curves used to determine the concentration of NO· and nitrite. NOC-5 is a slow degrading NO ··-amine molecule which exhibits exponential decay over time. One way to estimate whether its release is affected is to determine the half-life of the molecule. In nanodiscs treated with NOC-5, the half-life remained nearly constant for all NOC-5 concentrations with average of 19.5 ± 2 min. However, the rate was non-uniform and concentration-dependent in proteonanodiscs. 0.2 μM NOC-5-treated sample showed half-life of 22.8 min while 0.5 μM and 1 μM NOC-5 treated samples showed 66.4 min and 25.7 min, respectively. We speculated that nitrite concentration should increase with increasing NOC-5 concentration in both nanodiscs and proteonanodiscs. At 0.2 μM NOC-5, the release of nitrites in proteonanodiscs was very low and the values remained constant throughout. However, at 0.5 μM NOC-5, proteonanodiscs showed reduced nitrite concentration from 123 ± 5 nM (at t = 0 s) to 20 ± 2 nM (at t = 600 s). When compared to nanodiscs (control), the nitrite concentration was close to 95 nM. At 1 μM NOC-5 as well, proteonanodiscs showed nitrite concentration from 120 ± 1 nM to 80 ± 2 nM, while control showed increase from 180 ± 50 nM to 1090 ± 90 nM. These values point out that the interplay between NO· and nitrite are involved in subtle attack on integrin.

4. Conclusions

Here we showed by single molecule force spectroscopy studies combined with AFM imaging and NO.·/nitrites measurements that 0.5μM concentration of NOC-5 is a critical and limiting step above which the structure and functionality of integrin is essentially lost. AFM imaging confirmed the release of integrin from the proteonanodiscs and its further aggregation. The high forces obtained for the NOC-5 treated proteonanodiscs are predominantly due to interaction of released integrin with the RGD ligand.

For the first time, using nanodiscs we investigated with force spectroscopy the αiibβ3-NO.· interactions. We can confirm that NO.· not only modifies the αiibβ3, but also causes its release from the lipid bilayer. It is also shown that NO.· attacks αiibβ3 in both direct (as itself) and indirect (as nitrites) manner. Although NO.· is a short-lived molecule, its action is highly dependent on the surrounding environment. The multitude of NO.· steps significantly impacts the complex radical interactions and the adhesive forces formed between RGD-ligand and αiibβ3. While we were able to observe the existence of possible NO.·-αiibβ3 interactions, lipid-radical interactions aiding the release of integrin need to be explored. As the composition of biological membranes is more complex (containing glycolipids, saturated/unsaturated lipids etc.), reconstitution of αiibβ3 into similar biomimetic systems would help to investigate the impact of radical species on integrins under clinically relevant conditions. The observed changes in the physical properties of integrin can be further correlated with relevant biochemical assays to allow the understanding of the mechanism of integrin release from the lipid bilayer.

Funding

This work was funded by the Deutsche Forschungsgemeinschaft (DFG, German Research Foundation) 231396381/GRK1947.

Declaration of competing interests

The authors declare that they have no known competing financial interests or personal relationships that could have appeared to influence the work reported in this paper.

Acknowledgements

We would like to thank Una Janke for her help with the activation assay. Special thanks to Thi-Huong Ngyuyen for her valuable inputs during the design of force spectroscopy experiments. We thank Peter Nestler and Florian Gellert from the Institute of Physics for their support during MATLAB script preparation. Fruitful discussions with C.A. Helm, C.H. Lillig and RTG 1947 "BiOx" members are acknowledged. This work was funded by the Deutsche Forschungsgemeinschaft (DFG, German Research Foundation) 231396381/GRK1947.

Appendix A. Appendix A Supplementary data

Supplementary data to this article can be found online at https://doi.org/10.1016/j.bbamem.2020.183198.

References

[1] K. Bledzka, S.S. Smyth, E.F. Plow, Integrin αIIbβ3: from discovery to efficacious therapeutic target, Circulation research 112 (2013) 1189–1200.
[2] X. Du, E.F. Plow, A.L. Frelinger Iii, T.E. O'Toole, J.C. Loftus, M.H. Ginsberg, Ligands "activate" integrin αIIbβ3 (platelet GPIIb-IIIa), Cell 65 (1991) 409–416.
[3] I.D. Campbell, M.J. Humphries, Integrin structure, activation, and interactions, Cold Spring Harbor perspectives in biology 3 (2011) a004994.
[4] Y.-Q. Ma, J. Qin, E.F. Plow, Platelet integrin αIIbβ3: activation mechanisms, Journal of Thrombosis and Haemostasis 5 (2007) 1345–1352.
[5] T.N. Durrant, M.T. Bosch, I. Hers, Integrin αIIbβ3 outside-in signaling, Blood 130 (2017) 1607–1619.
[6] A.T. Nurden, Glanzmann thrombasthenia, Orphanet Journal of Rare Diseases 1 (2006) 10.
[7] G. Kistangari, K.R. McCrae, Immune thrombocytopenia, Hematology/Oncology Clinics 27 (2013) 495–520.
[8] J. Zhu, B.-H. Luo, T. Xiao, C. Zhang, N. Nishida, T.A. Springer, Structure of a complete integrin ectodomain in a physiologic resting state and activation and deactivation by applied forces, Molecular cell 32 (2008) 849–861.
[9] D.W. Essex, M. Li, Redox modification of platelet glycoproteins, Current drug targets 7 (2006) 1233–1241.
[10] R. Mor-Cohen, Disulfide bonds as regulators of integrin function in thrombosis and hemostasis, Antioxidants & redox signaling 24 (2016) 16–31.
[11] V. Dhawan, Reactive oxygen and nitrogen species: general considerations, Studies on Respiratory Disorders, Springer, 2014, pp. 27–47 (Place Published).
[12] J.R. Lancaster Jr, A tutorial on the diffusibility and reactivity of free nitric oxide, Nitric Oxide 1 (1997) 18–30.
[13] J. Thachil, Nitric oxide in immune thrombocytopenic purpura, Hematology 14 (2009) 59–62.
[14] J.E. Freedman, J. Loscalzo, M.R. Barnard, C. Alpert, J.F. Keaney, A.D. Michelson, Nitric oxide released from activated platelets inhibits platelet recruitment, The Journal of clinical investigation 100 (1997) 350–356.
[15] C.C. Winterbourn, M.B. Hampton, Thiol chemistry and specificity in redox signaling, Free Radical Biology and Medicine 45 (2008) 549–561.
[16] D.D. Murphy, E.C. Reddy, N. Moran, S. O'Neill, Regulation of platelet activity in a changing redox environment, Antioxidants & redox signaling 20 (2014) 2074–2089.
[17] N. Hogg, B. Kalyanaraman, Nitric oxide and lipid peroxidation, Biochimica et

Biophysica Acta (BBA)-Bioenergetics 1411 (1999) 378–384.
[18] F. Violi, R. Marino, M.T. Milite, L. Loffredo, Nitric oxide and its role in lipid peroxidation, Diabetes/metabolism research and reviews 15 (1999) 283–288.
[19] F. Ye, G. Hu, D. Taylor, B. Ratnikov, A.A. Bobkov, M.A. McLean, S.G. Sligar, K.A. Taylor, M.H. Ginsberg, Recreation of the terminal events in physiological integrin activation, The Journal of cell biology 188 (2010) 157–173.
[20] F. Hagn, M.L. Nasr, G. Wagner, Assembly of phospholipid nanodiscs of controlled size for structural studies of membrane proteins by NMR, Nature protocols 13 (2018) 79.
[21] F.A. Carvalho, J. Martins-Silva, C. Saldanha, Amperometric measurements of nitric oxide in erythrocytes, Biosensors and Bioelectronics 20 (2004) 505–508.
[22] M.A. Hussain, A. Agnihotri, C.A. Siedlecki, AFM imaging of ligand binding to platelet integrin αIIbβ3 receptors reconstituted into planar lipid bilayers, Langmuir 21 (2005) 6979–6986.
[23] F.T. Eng, B.J. Smagghe, T. Walz, T.A. Springer, Intact αIIbβ3 integrin is extended after activation as measured by solution X-ray scattering and electron microscopy, Journal of Biological Chemistry 286 (2011) 35218–35226.
[24] C. Rosano, M. Rocco, Solution properties of full-length integrin aIIbb3 refined models suggest environment-dependent induction of alternative bent/extended resting states, (2010).
[25] U. Janke, M. Kulke, I. Buchholz, N. Geist, W. Langel, M. Delcea, Drug-induced activation of integrin alpha IIb beta 3 leads to minor localized structural changes, PloS one 14 (2019) e0214969.
[26] V. Montana, W. Liu, U. Mohideen, V. Parpura, Single molecule probing of exocytotic protein interactions using force spectroscopy, Croatica Chemica Acta 81 (2008) 31–40.
[27] M. Mehrbod, S. Trisno, M.R.K. Mofrad, On the activation of integrin αIIbβ3: outside-in and inside-out pathways, Biophysical journal 105 (2013) 1304–1315.
[28] T. Kamata, A.M.B.O. Hironobu, W. Puzon-McLaughlin, K.K. Tieu, M. Handa, Y. Ikeda, Y. Takada, Critical cysteine residues for regulation of integrin alphaIIbbeta3 are clustered in the epidermal growth factor domains of the beta3 subunit, Biochemical Journal 378 (2004) 1079–1082.
[29] B. Yan, J.W. Smith, A redox site involved in integrin activation, Journal of Biological Chemistry 275 (2000) 39964–39972.
[30] D. Kirchhofer, J. Gailit, E. Ruoslahti, J. Grzesiak, M.D. Pierschbacher, Cation-Dependent Changes in the Binding Specificity of the Platelet Receptor GPIIb/IIIa, 265 (1990), pp. 18525–18530.
[31] T.-C. Tang, C.A. Amadei, N.H. Thomson, M. Chiesa, Ion exchange and DNA molecular dip sticks: studying the nanoscale surface wetting of muscovite mica, The Journal of Physical Chemistry C 118 (2014) 4695–4701.
[32] D. Nordin, L. Donlon, D.J.S.M. Frankel, Characterising Single Fibronectin–Integrin Complexes, 8 (2012), pp. 6151–6160.
[33] V.D. Nikolić, D.P. Ilić, L.B. Nikolić, M.Z. Stanković, L.P. Stanojević, I.M. Savić, I.M. Savić, The synthesis and structure characterization of deoxyalliin and alliin, Advan Technol 1 (2012) 38–46.
[34] J. Johnson, U V Atlas of Organic Compounds, Springer, 1971 (Place Published).
[35] N.G. Oberprieler, W. Roberts, A.M. Graham, S. Homer-Vanniasinkam, K.M. Naseem, cGMP-independent inhibition of integrin αIIbβ3-mediated platelet adhesion and outside-in signalling by nitric oxide, FEBS letters 581 (2007) 1529–1534.
[36] G.M. Walsh, D. Leane, N. Moran, T.E. Keyes, R.J. Forster, D. Kenny, S. O'Neill, S-nitrosylation of platelet αIIbβ3 as revealed by Raman spectroscopy, Biochemistry 46 (2007) 6429–6436.
[37] M. Bogdanov, J. Xie, W. Dowhan, Lipid-protein interactions drive membrane protein topogenesis in accordance with the positive inside rule, Journal of Biological Chemistry 284 (2009) 9637–9641.
[38] S. Nedelcianu, T. Páli, D. Marsh, Membrane penetration of nitric oxide and its donor S-nitroso-N-acetylpenicillamine: a spin-label electron paramagnetic resonance spectroscopic study, Biochimica et Biophysica Acta (BBA)-Biomembranes 1661 (2004) 135–143.
[39] M. Hermes, C. Czesnick, S. Stremlau, C. Stöhr, F. Scholz, Effect of NO on the adhesion–spreading of DMPC and DOPC liposomes on electrodes, and the partition of NO between an aqueous phase and DMPC liposomes, Journal of Electroanalytical Chemistry 671 (2012) 33–37.
[40] K. Kuronuma, H. Mitsuzawa, K. Takeda, C. Nishitani, F.D. Chan, Y. Kuroki, M. Nakamura, D.R. Voelker, Anionic pulmonary surfactant phospholipids inhibit inflammatory responses from alveolar macrophages and U937 cells by binding the lipopolysaccharide-interacting proteins CD14 and MD-2, Journal of Biological Chemistry 284 (2009) 25488–25500.
[41] D.A. Wink, J.B. Mitchell, Chemical biology of nitric oxide: insights into regulatory, cytotoxic, and cytoprotective mechanisms of nitric oxide, Free Radical Biology and Medicine 25 (1998) 434–456.
[42] L.K. Folkes, P. Wardman, Kinetics of the reaction between nitric oxide and glutathione: implications for thiol depletion in cells, Free Radical Biology and Medicine 37 (2004) 549–556.
[43] E. Ford, M.N. Hughes, P. Wardman, Kinetics of the reactions of nitrogen dioxide with glutathione, cysteine, and uric acid at physiological pH, Free Radical Biology and Medicine 32 (2002) 1314–1323.

Supplementary Information

Nitrosative stress affects the interaction of integrin alphaIIbbeta3 with its ligands

Sanjai Karanth[1,2] and Mihaela Delcea[1,2,3,*]

[1]Institute of Biochemistry, University of Greifswald, Felix-Hausdorff-Straße 4, 17489 Greifswald, Germany;
[2]ZIK-HIKE, Zentrum für Innovationskompetenz "Humorale Immunreaktionen bei kardiovaskulären Erkrankungen", Fleischmannstraße 42, 17489 Greifswald, Germany;
[3]DZHK (DeutschesZentrumfürHerz-Kreislauf-Forschung), partnersite Greifswald, Germany.

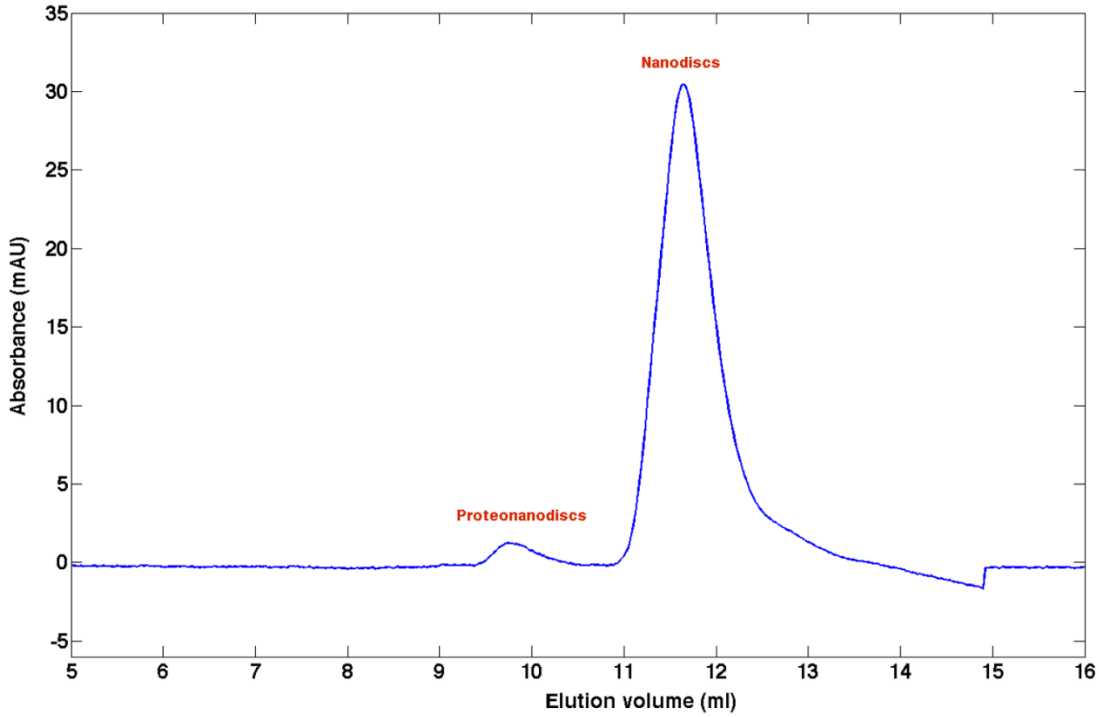

Figure S1. Purification of proteonanodiscs using size exclusion chromatography (SEC). SEC profile with peaks corresponding to proteonanodiscs and nanodiscs. Absorbance was detected at 280nm.

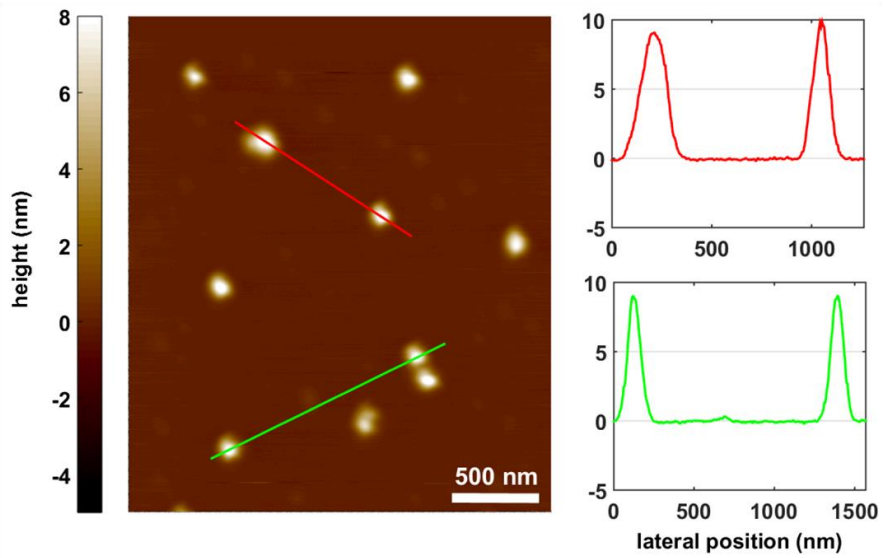

Figure S2. Height profile of proteonanodiscs immobilized through the His-MSP on Ni^{2+}-coated mica. The AFM image shows the presence of single integrin reconstituted into nanodiscs with one type of conformational state and orientation. The average height was found to be 9.5±1.9 nm.

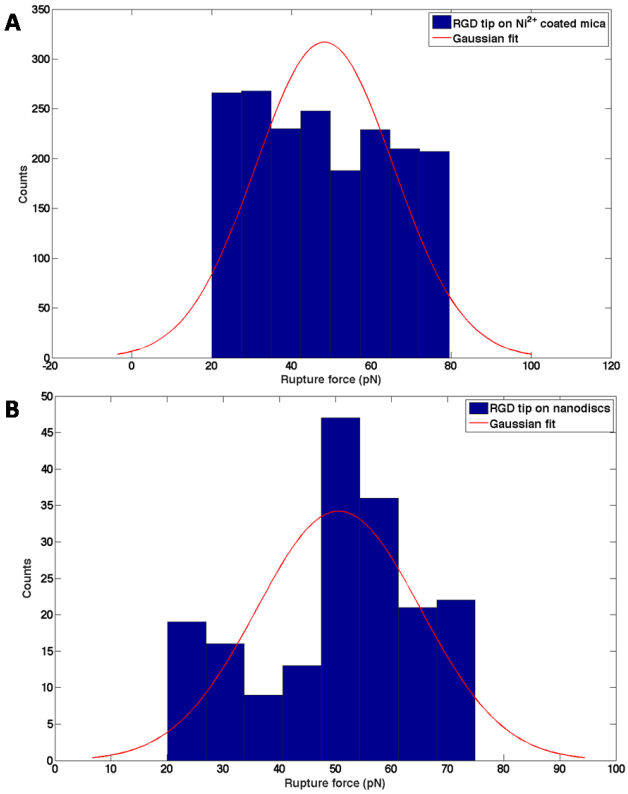

Figure S3. Determination of threshold rupture forces with RGD tip. Distribution of rupture forces between RGD ligand and Ni2+-coated mica (A) and empty nanodiscs (B).

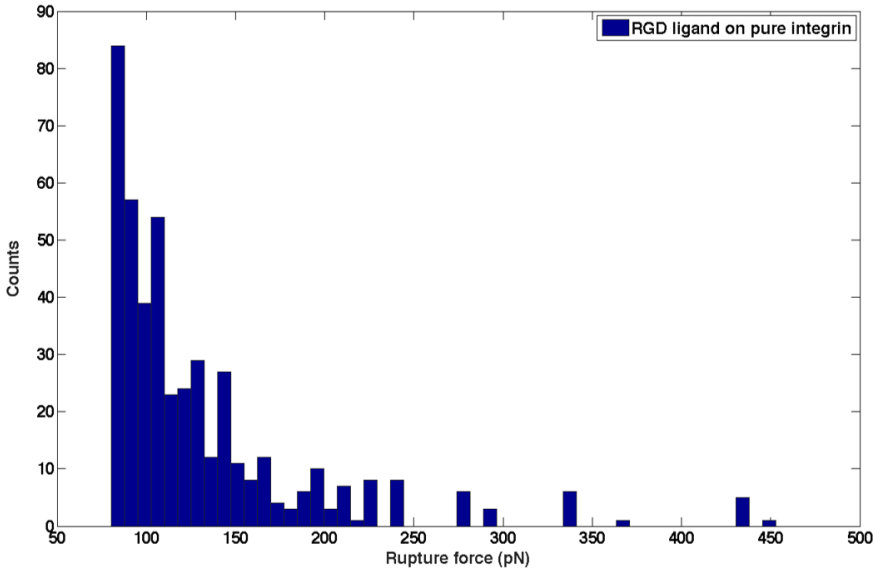

Figure S4. Rupture forces on interaction of RGD tip with immobilized pure integrin. Post-reconstitution, the force measurements were carried out to check the comparison of force curves between pure integrin and proteonanodiscs (Figure 5A). Overlap of histograms was observed as expected. Pure integrin immobilization was done by coating 1mg/ml of silane-PEG-COOH onto newly cleaved mica sheet. Using EDC/NHS chemistry, 0.3µM of integrin was added and incubated for 30 min. Ethanolamine was then added for 30 min and samples were then washed.

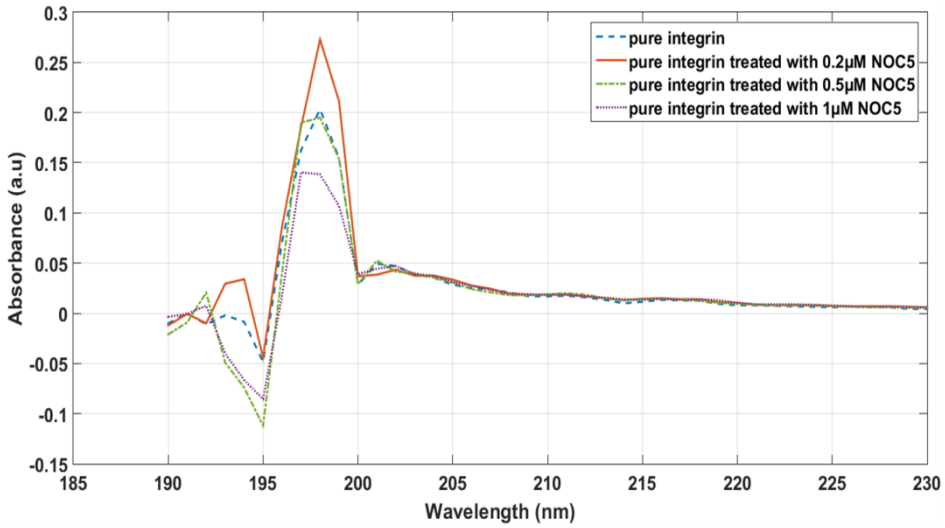

Figure S5. UV spectra of peptide bonds in pure integrin after NOC-5 treatment. Pure integrin shows peptide bond maxima at 198 nm and 202 nm. After exposure to 0.5µM and 1µM $NO^{\cdot}$, peaks of the peptide bonds shifted towards smaller wavelengths (visible below 198 nm and loss of peak at 202 nm).

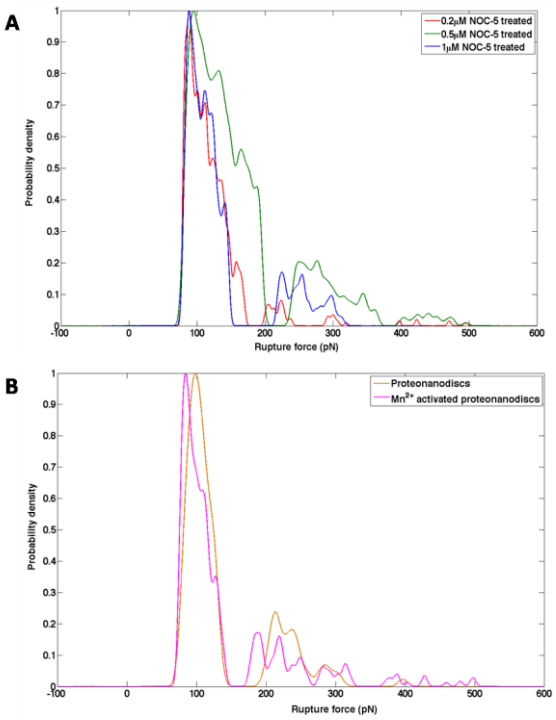

Figure S6. Kernel density estimation to determine peak forces. Using Gaussian kernel, the peak forces from data distribution was determined. The bandwidth of each curve (Table S1) represents the standard deviation taken into consideration for smoothing the data distribution. The area under the curve represents a peak force. The areas under the curves are broad and perfect peaks are not observed at forces greater than 200 pN for NOC-5 treated samples (A) when compared with proteonanodiscs and Mn2+-activated proteonanodiscs (B).

Table S1. Bandwidth of curves taken into consideration while calculating the peak forces for Gaussian kernel (Figure S6). Bandwidth represents the standard deviation of the data distribution. The bandwidth is used to obtain the smoothened curve highlighting peak forces. Optimal bandwidth was determined.

Sample	NOC-5 concentration(μM)	Bandwidth (pN)
Proteonanodiscs	n.a	6.8
Mn^{2+} activated proteonanodiscs	n.a.	3.8
Proteonanodiscs	0.2	2.6
	0.5	4.6
	1	3.3

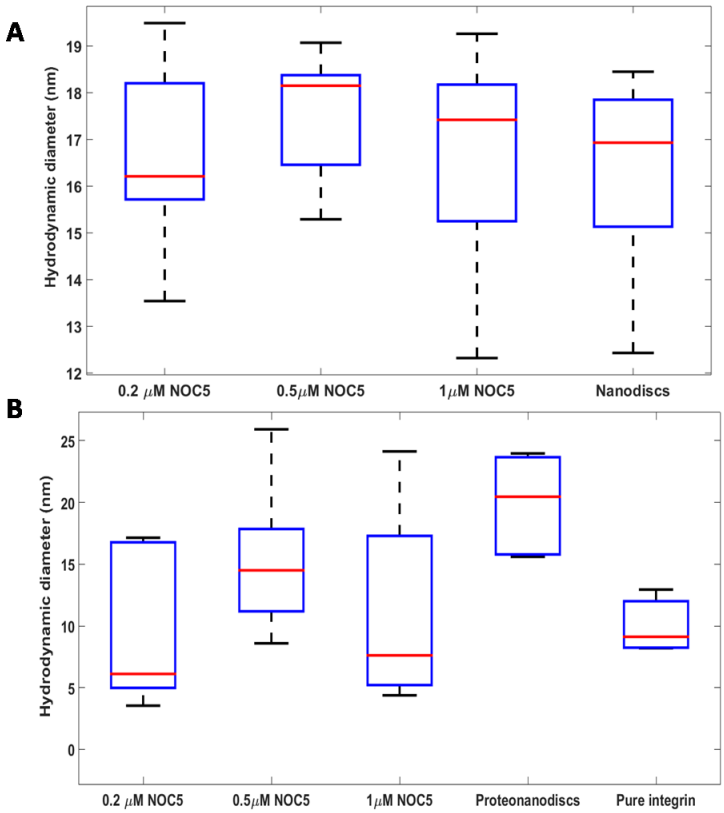

Figure S7. DLS data showing release of integrin from lipid system at varying NOC-5 concentration. A) The box and whisker plot showing the hydrodynamic diameter of empty nanodiscs formed using His-MSP belt. The diameters remain the same indicating no significant interaction of NOC-5 with either His-MSP or phospholipids in terms of the used concentrations in the experiment. B) In comparison to proteonanodiscs, there was considerable decrease in diameters with sizes matching that of the pure integrin. This indicates the release of integrin from the proteonanodiscs. Sizes correlating to that of empty nanodiscs were also measured.

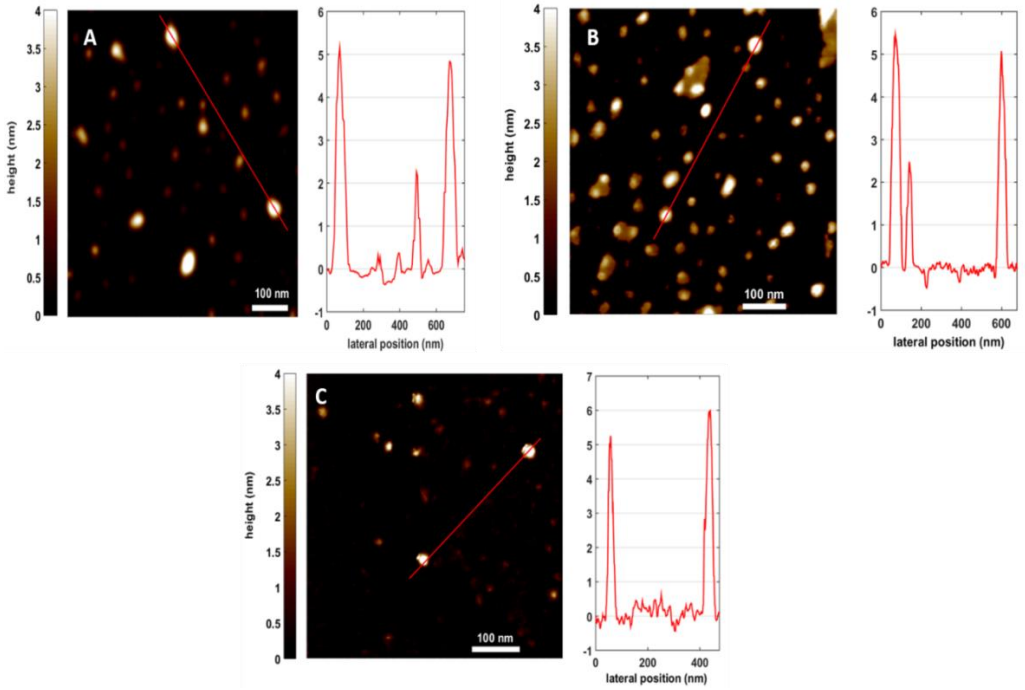

Figure S8. Membrane integrity of nanodiscs on exposure to NOC-5. AFM images (A, B & C) indicating that the there is little to no disruption to the bilayer on exposure to NOC-5. The average height of 4.5±0.3 nm was observed.

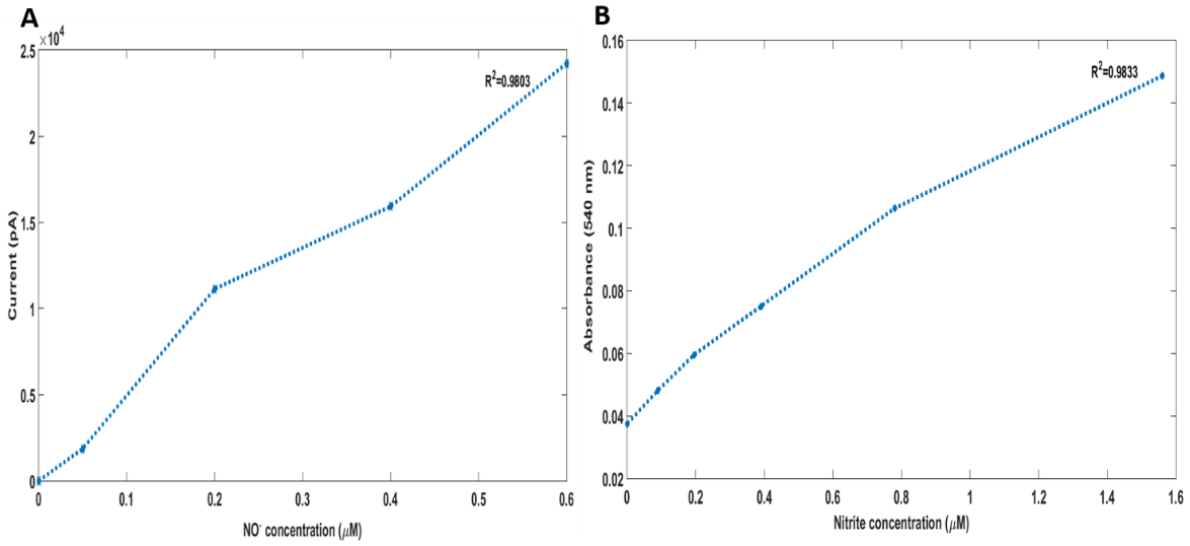

Figure S9. Standard plots to determine the NO· and nitrites concentration. (A) Calibration plot to determine the sensitivity of the amino-100 microsensor. The sensitivity was found to be 42pA/nM. This was used as input to determine concentration of NO· on surface of electrode. (B) Nitrite standard curve determined using Griess assay.

III. Changing surface properties of artificial lipid membranes at the interface with biopolymer coated gold nanoparticles under normal and redox conditions

Sanjai Karanth, Brahmaiah Meesaragandla and Mihaela Delcea

Biophysical Chemistry
Volume 267, December 2020, 106465

Available online: 1 September 2020

doi: 10.1016/j.bpc.2020.106465

Biophysical Chemistry 267 (2020) 106465

Contents lists available at ScienceDirect

Biophysical Chemistry

journal homepage: www.elsevier.com/locate/biophyschem

Changing surface properties of artificial lipid membranes at the interface with biopolymer coated gold nanoparticles under normal and redox conditions

Sanjai Karanth[a,b], Brahmaiah Meesaragandla[a,b], Mihaela Delcea[a,b,c,*]

[a] Institute of Biochemistry, University of Greifswald, Felix-Hausdorff-Straße 4, 17489 Greifswald, Germany
[b] ZIK-HIKE, Zentrum für Innovationskompetenz "Humorale Immunreaktionen bei kardiovaskulären Erkrankungen", Fleischmannstraße 42, 17489 Greifswald, Germany
[c] DZHK (DeutschesZentrumfürHerz-Kreislauf-Forschung), partner site, Greifswald, Germany

HIGHLIGHTS

- Changes in the interface dynamics of biopolymer-coated AuNPs and bilayers is crucial for effective drug delivery systems.
- Under flow and near physiological conditions, ChAuNPs disrupt lipid bilayer in a grazing manner as observed by QCM-D and AFM.
- Dextran-coated AuNPs followed a snorkeling approach to disrupt the bilayer.
- NO radical reduces the stability of ChAuNPs, but did not affect its functionality.

GRAPHICAL ABSTRACT

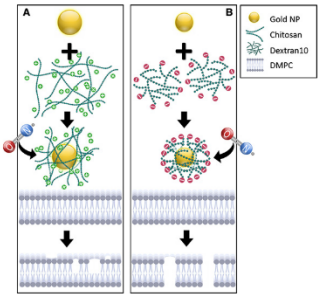

ARTICLE INFO

Keywords:
Chitosan
Dextran-10
Gold nanoparticles
DMPC
QCM-D
AFM
Nitric oxide

ABSTRACT

Gold nanoparticles (NPs) functionalized with biopolymers are increasingly effective in drug-delivery applications. Here, we investigated how chitosan coated NPs and dextran-10 coated NPs regulate their action on DMPC bilayer under normal and stress conditions. We found that chitosan-coated NPs interact with lipid membrane in an intermittent manner, causing lipid loss and partial membrane rupture, while dextran-10 coated NPs mostly induced complete rupture as observed by quartz crystal microbalance. *In-situ* atomic force microscopy imaging showed that chitosan-treated membranes have a higher surface roughness than those treated with dextran-10. Treatment with 1 μM nitric oxide (NO) radical caused the release of chitosan ligand from the surface of gold NPs (reduced stability) and its aggregation, but the functionality seemed less influenced. Dextran-10 ligand showed no such behavior, while its action was only delayed. Our findings give insights into possible challenges faced by NPs *in-situ* and show environment dependent effects of NPs on membranes.

1. Introduction

Biomolecular interactions at the interface of cell membranes are essential for determining the downstream activity of many cellular processes. Such interface studies are gaining high importance due to applications, especially in the field of drug delivery.

In recent years, gold nanoparticles (AuNPs) have been widely used in biomedical and pharmaceutical applications including diagnostic,

* Corresponding author at: Institute of Biochemistry, University of Greifswald, Felix-Hausdorff-Straße 4, 17489 Greifswald, Germany.
E-mail address: delceam@uni-greifswald.de (M. Delcea).

https://doi.org/10.1016/j.bpc.2020.106465
Received 19 July 2020; Received in revised form 25 August 2020; Accepted 25 August 2020
Available online 01 September 2020

photo thermal therapy, cellular imaging, tumor-cell targeting and drug delivery [1–6]. This is attributed mainly due to their small size, high surface-to-volume ratio and its distinctive optical and electronic properties. Moreover, AuNPs are inert nanoparticles (NPs) with easy synthesis and surface functionalization (*e.g.* with lipids, protein or peptides, and polymers) [6–10]. Functionalization of AuNPs with biopolymers is of high significance as these polymers are non-toxic, biocompatible and biodegradable, thereby, enhancing its therapeutic value. Also, when using functionalized NPs, the interaction is directly dependent on the coated material and independent on the NPs itself [11]. For a therapeutic use, permeation of NPs into the cell needs to be addressed as cell membrane (thickness of ~4–5 nm) forms the first barrier. Although such interactions are highly dynamic and complex, they are mainly governed by three constituents *i.e.* NPs, membrane composition and surrounding micro-environment. In case of NPs, interactions are mainly aided by the changes in the size, shape and its surface functionality [12–18]. While membrane composition influences the type of NPs uptake by the membrane [19–21], surrounding environment is also critical [22,23]. The environment takes precedence in scenarios where a toxic condition pre-exists to the proximity of target site for NPs (*e.g.* cancer induced inflammation) [24]. Commonly attributing factor in such conditions is the change in redox state. With NPs being observed as inducers or enhancers of radicals [25–27], significant physicochemical alteration to the membrane can be expected. One such biological phenomenon, where radicals have shown to alter the functionality is platelet aggregation; which occurs as a result of vascular injury. During aggregation, platelets come together and form a blood clot preventing further bleeding. Depending on the type of radical present in the environment, this process can be enhanced or reduced [28,29].

In our study, AuNPs were functionalized with two widely known and accepted biopolymers - chitosan and dextran-10, and their interactions with model membrane in normal and stress (redox) conditions were determined. Nitric oxide (NO) radical is used as a stress molecule here because in platelet-induced aggregation and inflammation, NO is one of the first chemical released [30]. Typically, concentrations ranging between 1 and 5 μM are present in blood [31]. Under normal conditions, NO functions as a signaling molecule, vasodilator and immune response regulator. However, its imbalance (due to increased release) can prove to be detrimental and act as a reactive nitrogen species agent [32,33].

Chitosan is a linear polysaccharide and can act as an antimicrobial agent [34]. In addition, existing literature reports on the role of chitosan in platelet aggregation [35–37] and wound healing. Dextran-10 is a branched polysaccharide and is known for its anti-thrombotic activity *i.e.* it inhibits platelet aggregation [38].

Along with wound healing abilities, research has shown that chitosan disrupts the lipid membranes causing cell death [39,40]. Such coexisting behavior of chitosan raises questions on the type of interaction it undergoes independently with phospholipids and proteins. These uncertainties lead our focus in understanding whether localization of chitosan determines its mode of action. Dextran-10 is used as a control biopolymer because it prevents interaction with extracellular components and undergoes easy permeation. However, to the best of our knowledge, the mechanism of interaction and the possible surface changes on the membrane have not been reported. In this study, selection of the type of phospholipid is crucial because composition-dependent changes in interactions are well known [41]. DMPC was chosen as model lipid in this work because platelet membranes contain around 40% phosphotidylcholines [42] of which 42% is contributed by saturated lipids [43]. As physical changes of DMPC (14,0) in presence of NO is well understood in our lab, it was ideal for this study. Also phosphotidylcholines form the outer leaflet of the lipid membrane, which undergoes substantial interaction with NPs.

Here, we have mimicked the environment of blood *i.e.* in-house synthesized polymer-coated gold nanoparticles (PcAuNPs) were allowed to flow at a constant flow rate to reach the cell site (here, supported lipid bilayers on surface). Further, the interaction between PcAuNPs and lipid bilayers was monitored using quartz crystal microbalance (QCM) and *in-situ* AFM imaging. For radical induced effect, PcAuNPs were pre-incubated with NO (depicting localized restrictions) and its effect on bilayer was analyzed.

2. Materials and methods

2.1. Preparation and characterization of biopolymer-coated gold nanoparticles (PcAuNPs)

2.1.1. Synthesis of chitosan coated gold nanoparticles (ChAuNPs)

Chitosan solution was prepared by dissolving 0.2 *w/v* % chitosan (Roth, Germany, Mw ~ 600 kDa) in 100 mL of 1% acetic acid (Sigma-Aldrich) under stirring for 30 min. To the above boiled solution 0.125 M aqueous solution of tetrachloroauric acid ($HAuCl_4$, Sigma-Aldrich, Germany) was added and continued the stirring for 30 min. Later, the mixture was allowed to cool to room temperature (RT) and centrifuged at 4 °C, 20 *g* for 30 min and the formed pellet was dispersed in 20 mL deionized water. The solution was washed three times with deionized water to remove unreacted chitosan molecules.

2.1.2. Synthesis of dextran-10 coated gold nanoparticles (Dn10AuNPs)

200 μl of 19 mM $HAuCl_4$ solution was added to 30 mL of 1 *w/v* % Dextran-10 (Sigma-Aldrich, Mw ~ 10 kDa) aqueous solution. The mixture was allowed to stir for 30 min at RT. For further reduction of gold, 1.5 mL of 0.05 M NaOH (Roth, Karlsruhe, Germany) was added to the above solution until colour changed from yellow to colorless. Then, the solution was boiled and kept for 30 min. Later, the mixture was allowed to cool to RT and centrifuged at 4 °C, 20 *g* for 30 min and the pellet was dispersed in 20 mL deionized water. The solution was washed three times with deionized water to remove any excess unreacted free dextran molecules.

2.2. UV–Vis absorption spectroscopy

UV–Vis spectra of prepared PcAuNPs were measured using NanoDrop 2000c spectrophotometer (Thermo Scientific, Germany) in 10 mm path length acrylic cuvettes (Sarstedt, Germany) at 25 °C. The spectra were recorded between 200 and 850 nm.

2.3. Dynamic light scattering (DLS)

A Zetasizer Nano-ZS (Malvern Instruments, Herrenberg, Germany) was employed to determine the hydrodynamic diameter (d_H) and the zeta potential for PcAuNPs. The prepared samples were first filtered through a 0.2 μm filter at 25 °C and then allowed to equilibrate for 5 min. Sample were run 12 times having run duration of 5 s per measurement. Average of the d_H of the samples were estimated from five independent measurements.

Disposal DTS1070 cuvettes (Malvern Instruments) were used to measure the zeta potential. The samples were first dispersed in deionized distilled water. Measurements were carried out at 50 V, 25 °C with 5 min equilibration between each measurement. Zeta potential data were acquired from 20 runs per measurement and the reported zeta potential is an average of five such independent measurements.

2.4. Transmission electron microscopy (TEM)

TEM analysis was performed using a negative staining procedure. PcAuNPs were allowed to adsorb onto a glow-discharged pioloform carbon-coated 400-mesh grid for 5 min. The grid was then transferred onto two droplets of deionized water, and finally onto a drop of 1% aqueous uranyl acetate for 30 s. After blotting with filter paper and air-drying, the samples were examined with a transmission electron

microscope LEO 906 (Carl Zeiss Microscopy GmbH) at an acceleration voltage of 80 kV. Afterwards, the micrographs were edited using Adobe Photoshop CS6.

2.5. Formation of DMPC small unilamellar vesicles (SUVs)

1 μM of dimyristoyl phosphatidylcholine (DMPC) lipid (Avanti Polar Lipids Inc., USA) were first solubilized in solution containing chloroform, mixed and dried under a stream of nitrogen. This was later kept under vacuum overnight. The dried lipid film was resuspended in Tris buffer (10 mM Tris, 100 mM NaCl, pH 7.4) at 24 °C (above the transition temperature of lipid). Next, the solution was sonicated (SoniPrep 150 Plus, MSE centrifuges, UK) with a probe tip sonicator until the solution turned milky to clear. The sonication was performed in the durations of one minute with intervals of 15 s. This solution was later centrifuged at 16200 *g* for 30 min to remove any titanium particles (deposited at the bottom) and the supernatant was collected (containing SUVs).

2.6. Monitoring the effect of PcAuNPs on the model membrane using quartz crystal microbalance with dissipation (QCM-D)

QCM-D is a label-free mass-adsorption technique at solid-liquid interface which can help to understand binding processes based on changes in the frequency [44]. Formation of lipid bilayer was confirmed using QCM-D technique (Biolin Scientific, Sweden). Here, 1 μM of DMPC SUVs were allowed to undergo surface adsorption onto SiO_2-coated quartz crystal (QSX 303) sensors to form a lipid bilayer. SUVs were injected into the QCM chamber at a flow rate of 100 μL/min using a peristaltic pump (Ismatec IPC-N4, Idex Health & Science GmbH, Wertheim-Mondfeld, Germany) at 37 °C. Formation of bilayer is indicated by change in frequency (depicting the deposition of mass on the sensor surface), PcAuNPs of 2 nM concentration were injected into the QCM chamber for 20 min and their influences on the membrane characteristics were determined.

Prior to SUVs deposition, cleaning of crystal sensors and its frequency calibration is mandatory. Crystals were first cleaned in 2% SDS solution for 30 min at RT followed by rinsing with deionized water. The crystals were then dried under N_2 stream and exposed to UV-ozone chamber (Pro Cleaner Plus, Bioforce Nanoscience, Ames, USA) for 20 min. Frequency calibration was performed by determining the resonant frequency (f_0) of the crystal at changing overtones. SiO_2-coated quartz crystal has a base frequency of 5 MHz. Changes in frequency (Δf) on the crystal post interaction are detected. Here, data for ninth overtone (45 MHz) are presented in the graphs.

2.7. In-situ atomic force microscopy (AFM) imaging

Post-interactions between PcAuNPs and DMPC lipid bilayers, QCM crystals were immediately removed and liquid imaging was performed using a Nanoscope IIIa controller (Veeco/Digital Instruments, Santa Barbara, USA). Images were obtained using OMCL-AC160TS (Olympus Corporation, Japan) cantilevers with a spring constant of 42 Nm^{-1}. If there was delay in imaging, samples were stored in Petri dishes at 37 °C under moist conditions to avoid any loss of water or any other possible changes.

2.8. Ex-situ AFM imaging

Due to increased background threshold and inconsistent structures on bare SiO_2 crystal, scanning at small areas is hindered. To overcome this problem, *ex-situ* imaging on mica was employed during PcAuNPs-DMPC studies under stress environment. Similar conditions used for QCM-D measurements were followed. 50 μl of 1 μM DMPC SUVs were spread on atomically flat muscovite mica sheet, which was used as substrate. Prior to spreading, mica sheets were freshly cleaved. Post addition of SUVs and after incubating 30 min at RT, samples were washed for 15 s in deionized water (Milli-Q, Millipore, Billerica, USA) to remove unbound vesicles. This time period is sufficient for the formation of bilayers on mica. Further, treated PcAuNPs were added to the formed lipid bilayer and allowed to interact. Later, samples were washed with deionized water and dried in a laminar flow box (ScanLaf Class 2, LaboGene, Lynge, Denmark). Air imaging was performed using a Nanoscope IIIa controller (Veeco/Digital Instruments, Santa Barbara, USA). Images were obtained in tapping mode using OMCL-AC160TS (Olympus Corporation, Japan) cantilevers.

2.9. AFM imaging data analysis

AFM images obtained from *in-situ* experiments were analyzed using a home-written MATLAB (Math Works, 2010b) script. To eliminate contaminations such as surface roughness and consider only flatly adsorbed samples, a threshold local maximum of 1.0 nm height was considered. The height threshold was considered by determining the RMS roughness of bare SiO_2 crystal. Contour surrounding a region of interest was determined and its local maximum (half of the maximum height) was defined. Cross-sections from each of these contours provided height profiles of the samples. For *ex-situ* experiments, analysis was performed as mentioned above with the surface roughness of mica (~ 0.3 nm) considered as threshold value.

2.10. PcAuNPs-DMPC membrane interaction under nitrosative stress

PcAuNPs were subjected to stress conditions (mimicking site of an injured cell) to observe the stability and efficacy of the NPs interaction with membrane. For this, PcAuNPs were first incubated with the NO donor 1-Hydroxy-2-oxo-3-(3-aminopropyl)-3-isopropyl-1-triazene called as NOC-5 (Dojindo, Germany) for 15 min at RT at 1 μM and 5 μM concentrations. NOC-5 instantly releases NO when it comes in contact with H^+ ions in solution. To reduce this effect, NOC-5 was prepared in 10 mM NaOH. As OH^- can alter the pH of surrounding environment, as per company suggestions, the chemical was added such that volume ratio does not exceed 1/50 of the total sample volume. This retained the sample pH in solution.

3. Results and discussion

In this study, we examined the changes in the surface properties of supported DMPC bilayers upon interaction with chitosan- and dextran-10 coated AuNPs using QCM-D and AFM techniques. Structurally, chitosan is a linear polysaccharide consisting of extended chain of glucosamine units and dextran-10 is a branched polysaccharide having repeating units of glucopyranosyl molecules (Fig. S1, B and C). The system is designed to run at near physiological conditions and under flow. Fig. 1 shows a schematic representation of the interaction between DMPC and biopolymer-coated AuNPs. Also, changes in the surface properties under stress environment (using NO radical) is reported.

3.1. Characterization of PcAuNPs

Synthesis and characterization of PcAuNPs were carried out as previously reported [45–48]. Formation of AuNPs was confirmed by the occurrence of surface plasmon resonance (SPR) bands at 528 nm. Fig. 2A shows the UV–Vis absorption spectra of AuNPs coated with dextran-10 and chitosan ligands. The size measurements of the PcAuNPs carried out using TEM (Fig. 2B and C) and AFM (Fig. S3) are presented in Table I.

DLS measurements showed that d_H were ~55 nm and ~37 nm for ChAuNPs and Dn10AuNPs, respectively (Fig. S2). Difference in the d_H of the PcAuNPs is due to the hydrated state of polymer (as the polymer undergoes expansion in aqueous condition). This hydration is dependent on the length and molecular weight of polymers (dextran-10 being

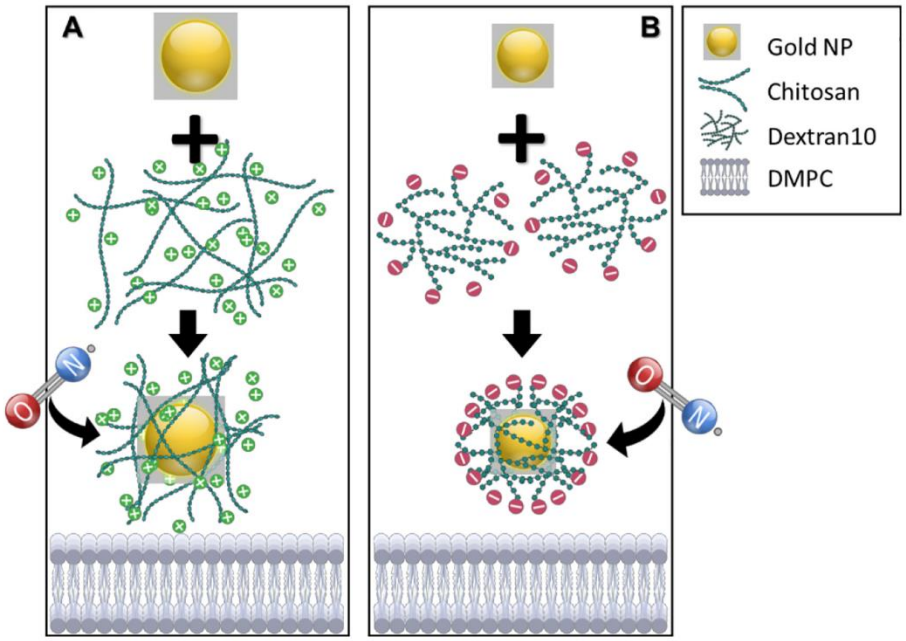

Fig. 1. Schematic representation of the interactions between DMPC bilayer and ChAuNPs (A) and Dn10AuNPs (B). Post-synthesis, 2 nM of PcAuNPs under flow (flow rate = 0.1 mL/min) were subjected to interact with DMPC membrane under normal and stress conditions (*i.e.* 1 μM NOC-5 treated PcAuNPs) at pH 7.4 and 37 °C for 20 min. Surface modifications undergone by the DMPC bilayer were observed and recorded.

a branched molecule and chitosan a linear molecule). For ChAuNPs and Dn10AuNPs, the measured zeta potential values were +30.1 mV and −33.6 mV, respectively. Water was used for measurements of surface charge.

The positive charge for ChAuNPs is due to the availability of -NH_3^+ groups at the surface, whereas the negative charge for the Dn10AuNPs is due to the presence of -OH groups at their surface.

3.2. Interaction of PcAuNPs with supported DMPC bilayers

Formation of supported lipid bilayers on the surface of SiO_2 was first proven by QCM technique (Fig. 3 (*top*) and Fig. 4 (*top*)). Initially, QCM crystals were washed with deionized water and Tris-HCl buffer (step A and B) to determine the baseline frequency of the oscillating crystal. On injection of SUVs (step C), deposition begins to occur on the sensor surface. Normally on deposition, SUVs will come together and undergo vesicle fusion reaching a threshold followed by their breakage and

Table 1
Summary of size and charge of PcAuNPs. The obtained zeta values indicate that the prepared PcAuNPs are quite stable.

Sample	Zeta potential (mV)	Size (nm)		
		TEM	AFM[a]	DLS[b]
ChAuNPs	30.1 ± 2.7	20.8 ± 3.4	18.3 ± 2.7	55.3 ± 1.0
Dn10AuNPs	−33.6 ± 0.6	10.9 ± 1.8	11.4 ± 3.5	37.0 ± 0.2

[a] Fig. S3 shows the sizes of PcAuNPs from AFM imaging on mica.
[b] Represents hydrodynamic diameter (d_H).

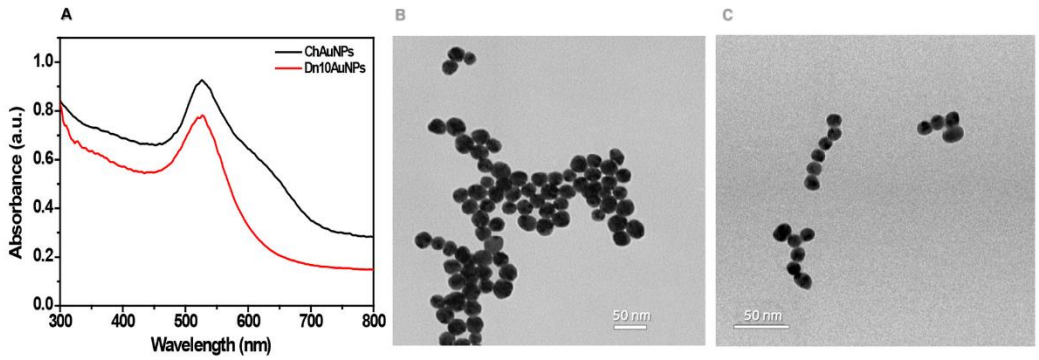

Fig. 2. Characterization of polymer-coated gold nanoparticles (PcAuNPs). A) UV–Vis spectra shows spectral band at 528 nm confirming the formation of gold nanoparticles (AuNPs). TEM images depict spherical morphology with ChAuNPs (B) having mean diameter of 20.8 ± 3.4 nm and Dn10AuNPs (C) of 10.9 ± 1.8 nm. Scale bar = 50 nm. (For interpretation of the references to colour in this figure legend, the reader is referred to the web version of this article.)

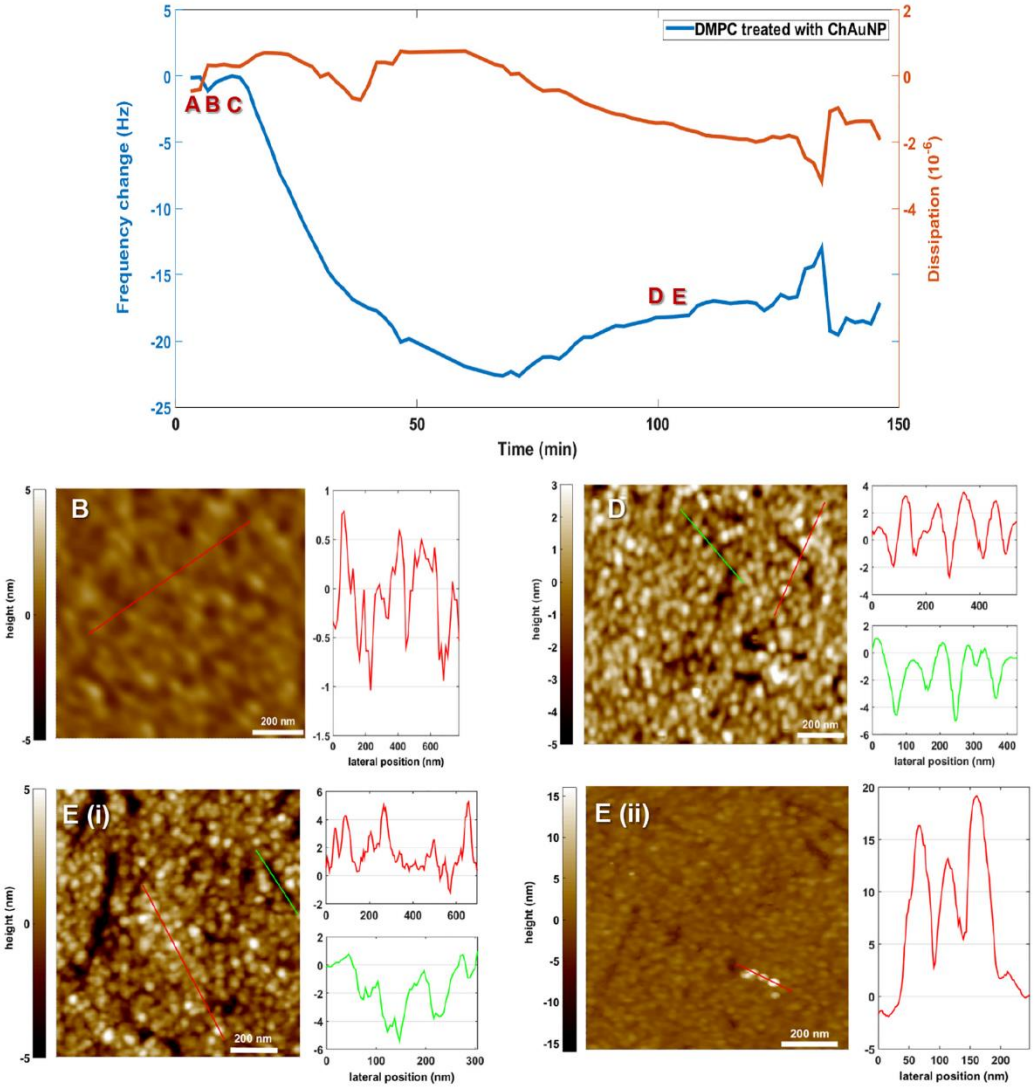

Fig. 3. Frequency changes in DMPC-ChAuNPs interaction (Top). QCM sensogram indicating the change in frequency (blue curve) and dissipation (brown curve). SiO_2 crystal subjected to deionized water flow (A), Tris-HCl buffer flow (B) and SUVs injection (C). Lipid bilayer was formed as indicated by a frequency shift of around −20 Hz (D). Later the crystal was washed with buffer for 5 min again and ChAuNPs were injected (E). Disruption in the formed lipid bilayer is visible with change in the increase in the frequency. (For interpretation of the references to colour in this figure legend, the reader is referred to the web version of this article.)
In-situ AFM imaging (Bottom). Alphabets in the inset of image represent respective steps in the QCM curve. AFM image of SiO_2 crystal washed with buffer (B) shows heights of ~1 nm. Post SUVs addition, height profiles of ~4 nm were obtained (D) indicating the formation of lipid bilayer (red cross section). In the image, the bilayer is visualized as white patches. Post-ChAuNPs injection, two types of height information were obtained. E (i) represents the disruption of bilayer (red-cross section showing heights of ~2 nm) and green section showing holes. When allowed to interact for longer than 20 min, deposition or aggregation of ChAuNPs was visible (E (ii)).

formation of a lipid bilayer. This is shown by the shift in the frequency to around −20 Hz (step D), characteristic for a lipid bilayer formation. This was consistent with previously reported QCM sensograms for DMPC phospholipids [49]. Post-bilayer formations, the crystal were washed with buffer for 5 min and PcAuNPs (both ChAuNPs and Dn10AuNPs) were injected (step E) and subjected for interaction with DMPC membrane.

In the case of DMPC-ChAuNPs interaction, we observed that on initial contact with the NPs, membrane removal begins to occur (increase in frequency), but the membrane desorption was less significant with small changes in the frequency proceeded by formation of saturation curve (Fig. 3, *top*). However, subsequently a rapid increase in the frequency and then a decrease in the frequency were observed. To understand such changes, parallel *in-situ* AFM imaging was performed (Fig. 3, *bottom*).

AFM images of each step in the QCM sensogram are shown with the alphabet in the inset of the image. AFM image of step B shows morphology of only bare SiO_2 crystal with height of around ~1 nm. AFM image of step D, *red curve* shows the formation of lipid bilayer depicted with height of ~4 nm. In the AFM image, it is visible as white patches.

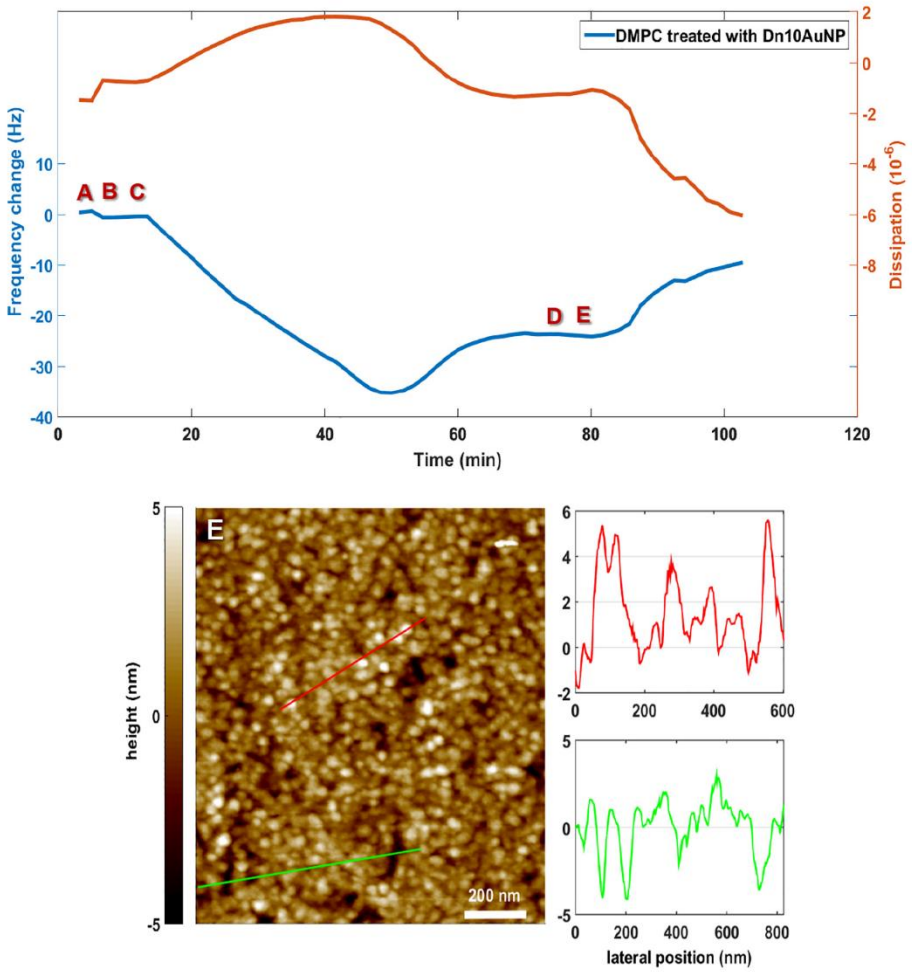

Fig. 4. Frequency changes in DMPC-Dn10AuNPs interaction (Top). QCM sensogram indicating change in frequency (blue curve) and dissipation (brown curve). SiO2 crystal subjected to deionized water flow (A), Tris-HCl buffer flow (B) and SUVs injection (C). Formation of lipid bilayer is observed at frequency of around −20 Hz (D). Later the crystal was washed with buffer for 5 min and Dn10AuNPs were injected (E). The disruption of bilayer started to occur within 5 min of Dn10AuNPs injection. (For interpretation of the references to colour in this figure legend, the reader is referred to the web version of this article.)
In-situ AFM imaging (Bottom). Alphabet in the inset of image indicate respective step of QCM curve. The image (E) shows complete disruption of lipid bilayer by Dn10AuNPs as indicated by holes (green cross section). Also reduction in the thickness of bilayer was also visible (red curve, of height ranging between 2 and 3 nm). Deposition of Dn10AuNPs on crystal was not observed. AFM images of steps B and D are similar as shown in Fig. 3, *bottom*.

Post ChAuNPs interaction, two distinct types of images were obtained. In Fig. 3, E (i), *red curve* shows the reduced height profiles around 2 nm along with heights of bilayer. The reduction in height is consistent with the loss of lipid mass as observed from the QCM curve. This indicates that DMPC underwent changes causing the loss of membrane structure and its integrity. When we prolonged the exposure of ChAuNPs, we observed that these nanoparticles started to deposit on the surface (AFM image, Fig. 3, E (ii)). While it is unclear whether the nanoparticles deposition was in the same region as that of lipid mass removal, aggregates were clearly visible. Deposition is consistent with the shift in frequency from around −12 to −17 Hz, indicating addition of mass on the sensor surface. This was also consistent with our observation that non-specific interactions between ChAuNPs and bare SiO_2 surface are possible (Fig. S4) under flow conditions. Hence a time limit of 20 min was set for the interactions.

In contrast to ChAuNPs, Dn10AuNPs started to interact with the membrane within 5 min of injection and there was a gradual removal of membrane from the sensor surface. In comparison to ChAuNPs, saturation step was not observed and the frequency shifted from around −23 Hz to −10 Hz (Fig. 4, *top*). *In-situ* AFM imaging showed that, unlike ChAuNPs, Dn10AuNPs caused full rupture of the membrane (Fig. 4, *bottom*). In QCM-D measurements, along with frequency we also detect energy dissipation. Generally, changes in the energy dissipation values indicate changes in the viscoelastic properties of a given system [50].

As it can be seen, dissipation values in the case of ChAuNPs were small and negative compared to Dn10AuNPs-treated membrane indicating enhanced changes by Dn10AuNPs when compared to ChAuNPs. However, we keep in mind that, even small changes in the bulk properties of solvent, results in increased change in the frequency and dissipation values. In our case, the contributing rheological factors would be the density and viscosity because for PcAuNPs, the solvent is

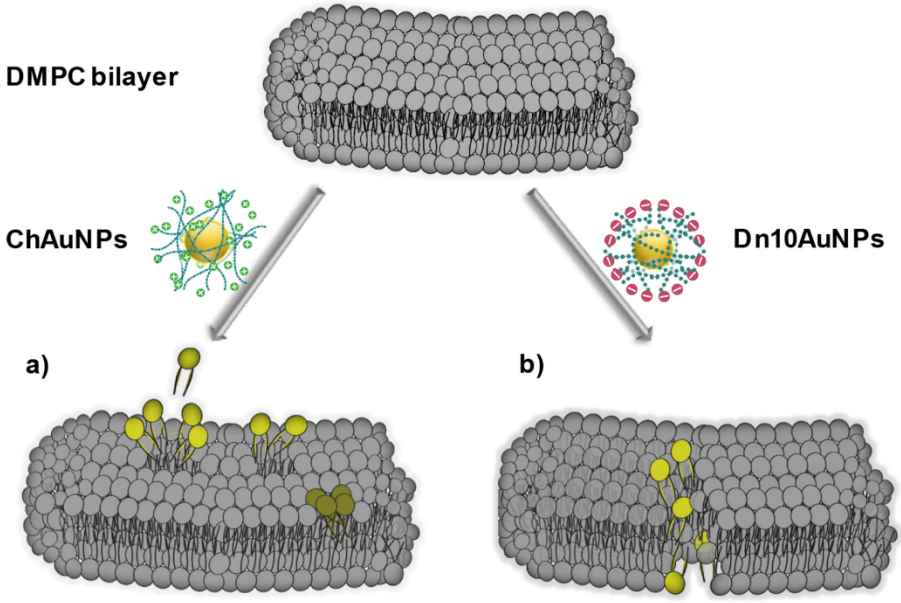

Fig. 5. Proposed interaction model. On coming in contact with membrane, ChAuNPs causes mainly surface changes (a). These changes can be associated to a partial membrane removal which in turn causes re-organization of lipid bilayer (green phospholipid heads) changing the overall stability and fluidity of membrane. The forces driving such modifications are mainly electrostatic and H-bonding and possible hydrophobicity. Dn10AuNPs causes complete membrane rupture (b) forming isolated patches of intact lipid bilayer. Possible re-orientation by the lipids at the periphery of interaction is possible to maintain the overall stability of membrane. These ruptures are due to electrostatic and H-bonding. Yellow phospholipids indicate the displacement from bilayer. (For interpretation of the references to colour in this figure legend, the reader is referred to the web version of this article.)

water, while for SUVs; Tris-HCL buffer was used. As the buffer contained only 100 mM NaCl and 10 mM Tris, we assumed viscosity and density of buffer to be similar to those of water and will have negligible effect on the PcAuNPs-membrane interactions. As ChAuNPs- and Dn10AuNPs treatment showed alterations on membrane surface, we asked ourselves the extent of internalization and the possible changes caused by the NPs. To understand this, we looked into the lipid spreading/reorganization as a parameter.

3.3. Change in surface heterogeneity of treated membrane

When the height sections of PcAuNPs treated DMPC were observed meticulously, it can be seen that there are differences in the smoothness of the plotted cross sections (AFM image 'E (i)', Fig. 3, *bottom* and AFM image 'E', Fig. 4, *bottom*). To understand these deviations, RMS roughness of each of the image was determined. Bare SiO_2 crystal has a roughness of 0.9 nm (Fig. S5, A) which increased to 1.13 nm on deposition of lipid bilayer (Fig. S5, B). On treatment with PcAuNPs, we expected that the roughness would range between above mentioned values. However, ChAuNPs-treated lipid surface had RMS value of 1.90 nm (Fig. S5, C), while RMS value of Dn10AuNPs treated surface was 1.60 nm (Fig. S5, D). These numbers indicate that PcAuNPs is inducing a significant change on the membrane surface. This perturbation was enhanced in case of chitosan. Depending on the type of molecular orientation by the chitosan, the perturbation can vary.

3.4. Self-diffusion of lipids versus PcAuNPs facilitated diffusion

Another distinct physical condition to be noted is the diffusion of phospholipids. It is well established that when DMPC bilayers are formed above the transition temperature (T_m ~ 23 °C), the lipids undergo self-diffusion [51] as shown in AFM image 'D', *green curve*, Fig. 3, *bottom*. The other factors which influence such self-diffusion are the ionic strength and the sugar molecules. It has been reported that, with increasing NaCl concentration, there is a decrease in the diffusion coefficient of lipids [52]. The same was reported when small sugars are present in the vicinity of membrane [53,54]. With environment parameters such as temperature (37 °C) and salt concentration (100 mM) being fixed in our experiments, sugar molecules of polysaccharides present on these biopolymers might have influenced the diffusion process. While we cannot standalone quantify its effect, the increased roughness accompanied by morphological and topological changes was unique for Dn10AuNPs (containing only –OH groups, similar to that present in sugars) and ChAuNPs (containing –OH and $–NH_2$ groups). On inspecting individual holes, one can observe that ChAuNPs treated holes showed visible peaks (AFM image 'E(i)', *green curve*, Fig. 3, *bottom*) and troughs indicating partial membrane rupture which was absent in the holes formed from Dn10AuNPs (only troughs, indicating complete rupture), as shown in AFM image 'E', *green curve*, Fig. 4, *bottom*. Also the number of holes formed was extensive in ChAuNPs treated surface when compared to Dn10AuNPs. This validates the reason for differences in surface roughness of the treated lipid membranes. Such visible differences also provide a conclusion that each of these polymers follows different modes of action on DMPC membrane.

3.5. Proposed-interaction model

Based on our results and evidences, we propose the following mechanism:

i) Initially, under given flow conditions (which is around 7% of blood flow rate [55]), ChAuNPs and Dn10AuNPs do not interact with the surface. The interaction energies seem to be negligible compared to rheological forces.

ii) On encountering a phospholipid surface, ChAuNPs can undergo

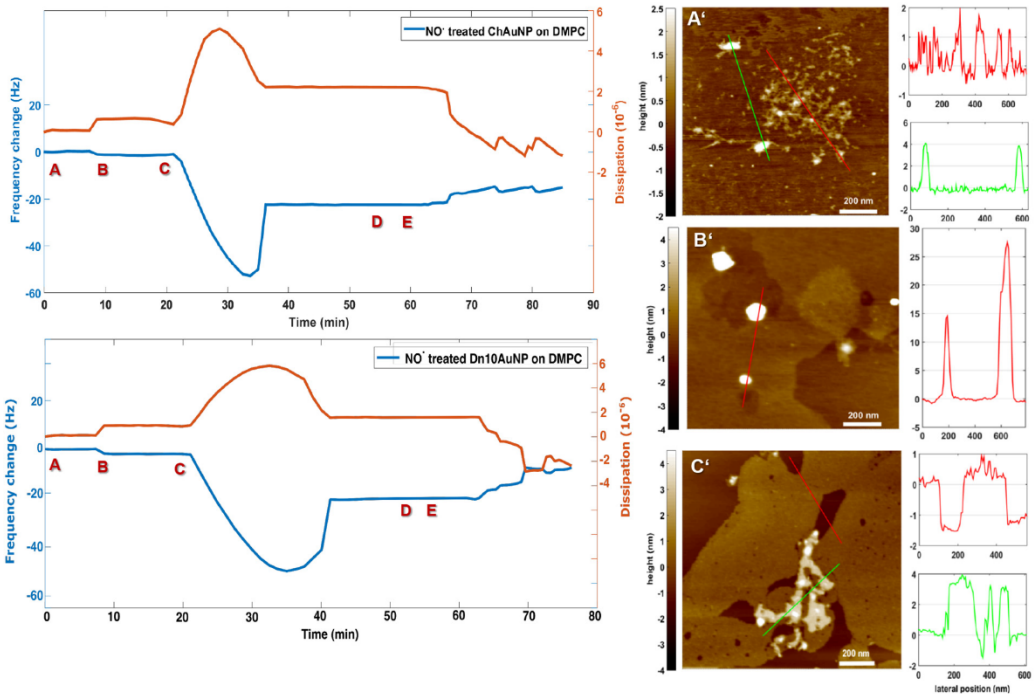

Fig. 6. QCM curves and AFM images of DMPC-NO treated PcAuNPs. Sensograms showing frequency and dissipation curves of NO treated PcAuNPs on DMPC **(Left)**. SiO_2 crystal subjected to deionized water flow (A), Tris-HCl buffer flow (B) and SUVs injection (C). Formation of bilayer corresponds to (D). Later the crystal was washed with buffer and treated PcAuNPs were injected (E). The treated ChAuNPs though was less stable; it showed similar action on membrane when compared to Fig. 3, *top*. On injection of treated Dn10AuNPs the membrane disruption was similar when compared to Fig. 4, *top*. However, the on-set of disruption was delayed by around 9 min.
Ex-situ AFM imaging on mica. (Right) (A') Image shows the release of chitosan ligand from the surface of AuNPs (red-cross section) and visible bilayers (green cross section). Also at the same time, very large heights (B') were observed. The increased heights could be due to released chitosan aggregates or nanoparticles themselves, but loss of stability is confirmed. (C') Dn10AuNPs did not show any loss of ligand but height profiles ranging between 1.5 and 2 nm was visible (red-cross section). Due to change in the imaging mode, it is difficult to contemplate on the disruption of lipid membrane.

either electrostatic or hydrogen bonding interactions between the head group of DMPC and the amine group present on the surface of chitosan. We believe that such interactions can effectively cause adsorption of ChAuNPs on the lipid surface for a short period of time causing displacement and disruption of membrane (Fig. 5a). The removal of very few lipids from the surface would be due to steric repulsion between the quaternary amine group on the DMPC head group (Fig. S1, A) and amine group of chitosan. This effectively reduces membrane modification mainly due to H-bonding. This partial removal can expose the hydrocarbon tail of the lower leaflet. In theory, the acetyl groups present on the chitosan should interact with the hydrocarbon tail of phospholipid *via* hydrophobic interactions. We believe that in our case, the hydrophobic forces are negligible and do not participate in membrane removal because only 15% of acetylation is present in the chitosan molecule (~85% degree of deacetylation). Another reason would be the quick re-orientation of the phospholipid molecules when hydrocarbon tail is exposed to solvent. This re-orientation occurs as membranes try to maintain their intrinsic thermodynamic stability resulting in change in the membrane packing (green colored lipid molecules, Fig. 5a) and area per molecule occupied by the phospholipids. This is reflected from AFM image where decreased bilayer thickness (~3 nm) was observed (AFM image, E(i) *red curve*, Fig. 3, *bottom*).

However, such adsorption based interactions are localized covering a small surface area of lipids, but occurring consistently until nanoparticles are washed away from the flow. Such type of surface modifications can be understood as grazing effect of ChAuNPs on membrane and believed to be concentration dependent [56]. This explains the increased RMS roughness measured (affecting fluidity) and presence of peaks and troughs in the holes (AFM image, E(i) *green curve*, Fig. 3, *bottom*). Membrane surface modifications with reduction in membrane thickness were previously reported for DMPC bilayer with anti-microbial peptide MSI-78 [57] and DMPA phospholipid with chitosan [58]. The above proposed model is in good agreement with the model of Pavinatto et al. [59] for pure chitosan-DPPC monolayers which explains changes in elasticity and expansion of monolayer determined from surface pressure-area and surface potential-area isotherms.

iii) Dn10AuNPs follows a snorkeling behavior on encountering the membrane. They undergo H-bonding interactions with the phospholipids due to the -OH group present on dextran-10 without any steric hindrances (as observed for ChAuNPs). These interactions were strong enough to cause complete disruptions and form sub-nano patches of intact membrane (Fig. 5b). The intrinsic thermodynamic stability of these nano patches is disturbed only when next set of Dn10AuNPs interact and remove them completely.

This is suggested by the values of RMS roughness of Dn10AuNPs treated membrane, indicating less heterogeneity (compared to ChAuNPs) post surface modifications. Along with above mentioned interactions, size also plays a crucial role. Few studies have reported that small nanoparticles (< 20 nm) tend to form holes inside a lipid bilayer [60–63] by permeation. If this is the case, then the possibility of direct penetration by Dn10AuNPs cannot be neglected on coming in contact with the membrane (AFM image, E, *green curve*, Fig. 4, *bottom*).

3.6. Exogenous nitrosative stress alters the stability of PcAuNPs

The above observations and model proposed holds good for normal conditions. However, the real application of PcAuNPs is to the site of injury surrounded by stress molecules. To mimic such an environment, nitric oxide was used. The action of NO molecule is dependent on concentration- and location. The concentrations of nitric oxide donor, NOC-5 were selected corresponding to the threshold limits present in the blood. Also at low concentrations, direct effect of nitric oxide is predominant (*i.e.* nitric oxide do not undergo oxidation). Initially, the effect of NOC-5 on control (*i.e.* only DMPC membrane) was observed. We found from QCM and AFM results that at 1 μM, nitric oxide stabilized the lipid membrane (Fig. S6, *top* and Fig. S7, *bottom*), while 5 μM caused membrane disruption indicating its regulatory role. This observation was in-line with our earlier reports [64,65]. Further experiments were done using 1 μM NOC-5, such that action of nitric oxide on PcAuNPs was estimated independent of lipid bilayer.

Frequency values obtained for the QCM sensogram of NO treated ChAuNPs showed a gradual change in frequency from −21 to −18 Hz indicating removal of lipid mass (Fig. 6, *left*). While this indicated relatively no loss in the activity of chitosan (compared to normal *i.e.* Fig. 3), AFM imaging showed that the stability of ChAuNPs was reduced significantly and chitosan was released from the surface of nanoparticles (Fig. 6A', *red curve*). This might be due to the -NH_2 groups present in the chitosan molecules which change to N=N bonds after interacting with NO radicals, thereby changing the binding of chitosan with NPs. Zeta potential of the treated ChAuNPs was determined and it was found that the surface charge reduced from ~30 mV (control) to ~23.1 mV (Table S1). The reduction in the surface charge after interacting with NO radicals indicates a change in the charge of NPs surface. Moreover, it has been reported that nitric oxide causes depolymerization of polysaccharides [66,67]. This occurs due to the intermediate nitrosonium ion (NO^+) formation which interacts with the primary amine of chitosan. This leads to potential loss of the nitrogen moiety from the chitosan and changing it overall structure [68]. This could explain the loss of stability and progressive aggregation (Fig. 6 B'). While the obtained results indicate that the surrounding microenvironment is crucial for NPs stability and functionality, the integrity of Dn10AuNPs seemed to be intact under action of NO. Unlike ChAuNPs, AFM imaging of Dn10AuNPs did not show any ligand loss (Fig. 6C').

Rather a height distribution ranging between 1.5 and 2 nm was observed which could be due the height of disrupted membrane but cannot be contemplated truly due to change in the imaging mode.

The QCM sensogram for NO treated Dn10AuNPs on membrane were similar to that of normal (Fig. 4), however the difference is that under normal conditions, the action of Dn10AuNPs on membrane started within 5 min of NPs injection, while it took 12 min in presence of NO. The zeta potential increased from ~ − 33 mV to ~ − 41 mV (Table S1) for Dn10AuNPs which might indicate that NO surrounded the polysaccharides without any interaction. As dextran-10 contains secondary alcohol groups on its surface, any chemical modification to its structure requires the use of a catalyst [69]. With dextran-10 also being a polyanion, presence of NO does not seem to change the overall electrostatics of the biopolymer. However, further experiment is needed to confirm on the possible interactions between NO with Dn10AuNPs.

4. Conclusion

In this study, combining QCM-D and AFM imaging, we show that under near physiological conditions, AuNPs coated with the biopolymers chitosan- and dextran-10 interact with model lipid membranes significantly. The interactions on the membrane are much localized. Each of these coated nanoparticles disrupts the lipid membrane and has different modes of action. A model has been proposed where we suggest that chitosan-coated gold nanoparticles rupture the membrane in a grazing manner, whereas dextran-10 coated gold nanoparticles follow a snorkeling approach. Under stress conditions *i.e.* in presence of nitric oxide radical, the stability of chitosan coated gold nanoparticles is influenced causing chitosan to get released from the gold surface. However, the functionality of the chitosan seemed to be less affected.

On the other hand, dextran-10 coated nanoparticles were inert in the presence of nitric oxide and neither its stability, nor functionality was altered. While these results supplement on possible membrane modifications by polymer coated gold nanoparticles under different conditions, it also highlights the fact that biological membranes are in fact more complex in their structure and organization. With the presence of membrane proteins on the surface and anchored by varying composition of phospholipids, questions such as membrane crowding effect on the action of the coated gold nanoparticles needs to be ascertained. As cells are a continuum rather than isolated systems, targeting an injured cell is a priority.

Conflicts of interest

There are no conflicts to declare.

Declaration of Competing Interest

The authors declare that they have no known competing financial interests or personal relationships that could have appeared to influence the work reported in this paper.

Acknowledgements

This work was funded by the Deutsche Forschungsgemeinschaft (DFG, German Research Foundation) 231396381/GRK1947 and the German Federal Ministry of Education and Research (BMBF) within the project NanoImmun (FKZ03Z22C51).

Appendix A. Supplementary data

Supplementary data to this article can be found online at https://doi.org/10.1016/j.bpc.2020.106465.

References

[1] E.C. Wang, A.Z. Wang, Nanoparticles and their applications in cell and molecular biology, Integr. Biol. 6 (1) (2014) 9–26.
[2] D.K. Kirui, D.A. Rey, C.A. Batt, Gold hybrid nanoparticles for targeted phototherapy and cancer imaging, Nanotechnology 21 (10) (2010) 105105.
[3] D.A. Giljohann, D.S. Seferos, W.L. Daniel, M.D. Massich, P.C. Patel, C.A. Mirkin, Gold nanoparticles for biology and medicine, Angew. Chem. Int. Ed. 49 (19) (2010) 3280–3294.
[4] P. Ghosh, G. Han, M. De, C.K. Kim, V.M. Rotello, Gold nanoparticles in delivery applications, Adv. Drug Deliv. Rev. 60 (11) (2008) 1307–1315.
[5] W.-T. Liu, Nanoparticles and their biological and environmental applications, J. Biosci. Bioeng. 102 (1) (2006) 1–7.
[6] S. Drescher, G. Graf, G. Hause, B. Dobner, A. Meister, Amino-functionalized single-chain bolalipids: Synthesis and aggregation behavior of new basic building blocks, Biophys. Chem. 150 (1–3) (2010) 136–143.
[7] L. Dykman, N.J.C.S.R. Khlebtsov, Gold nanoparticles in biomedical applications: Recent advances and perspectives, Chem. Soc. Rev. 41 (6) (2012) 2256–2282.
[8] P.M. Tiwari, K. Vig, V.A. Dennis, S.R.J.N. Singh, Functionalized gold nanoparticles and their biomedical applications, Nanomaterials (Basel) 1 (1) (2011) 31–63.
[9] A. Luchini, G. D'Errico, S. Leone, Z. Vaezi, A. Bortolotti, L. Stella, G. Vitiello, L. Paduano, Structural organization of lipid-functionalized-Au nanoparticles, Colloids Surf. B: Biointerfaces 168 (2018) 2–9.
[10] M. Kumar, W. Tegge, N. Wangoo, R. Jain, R.K. Sharma, Insights into cell penetrating peptide conjugated gold nanoparticles for internalization into bacterial cells, Biophys. Chem. 237 (2018) 38–46.
[11] C.M. Bailey, E. Kamaloo, K.L. Waterman, K.F. Wang, R. Nagarajan, T.A. Camesano, Size dependence of gold nanoparticle interactions with a supported lipid bilayer: A QCM-D study, Biophys. Chem. 203 (2015) 51–61.
[12] S. Nangia, R. Sureshkumar, Effects of nanoparticle charge and shape anisotropy on translocation through cell membranes, Langmuir 28 (51) (2012) 17666–17671.
[13] B.Y. Moghadam, W.-C. Hou, C. Corredor, P. Westerhoff, J.D. Posner, Role of nanoparticle surface functionality in the disruption of model cell membranes, Langmuir 28 (47) (2012) 16318–16326.

[14] A. Albanese, P.S. Tang, W.C. Chan, The effect of nanoparticle size, shape, and surface chemistry on biological systems, Annu. Rev. Biomed. Eng. 14 (2012) 1–16.
[15] A. Verma, F. Stellacci, Effect of surface properties on nanoparticle–cell interactions, Small 6 (1) (2010) 12–21.
[16] R.R. Arvizo, O.R. Miranda, M.A. Thompson, C.M. Pabelick, R. Bhattacharya, J.D. Robertson, V.M. Rotello, Y. Prakash, P. Mukherjee, Effect of nanoparticle surface charge at the plasma membrane and beyond, Nano Lett. 10 (7) (2010) 2543–2548.
[17] M. Schulz, A. Olubummo, W.H. Binder, Beyond the lipid-bilayer: interaction of polymers and nanoparticles with membranes, Soft Matter 8 (18) (2012) 4849–4864.
[18] L. Shang, K. Nienhaus, G.U. Nienhaus, Engineered nanoparticles interacting with cells: Size matters, J. Nanobiotechnol. 12 (1) (2014) 5.
[19] H. Abumanhal-Masarweh, D. da Silva, M. Poley, A. Zinger, E. Goldman, N. Krinsky, R. Kleiner, G. Shenbach, J.E. Schroeder, J. Shklover, Tailoring the lipid composition of nanoparticles modulates their cellular uptake and affects the viability of triple negative breast cancer cells, J. Control. Release 307 (2019) 331–341.
[20] S. Wang, H. Guo, Y. Li, X. Li, Penetration of nanoparticles across a lipid bilayer: Effects of particle stiffness and surface hydrophobicity, Nanoscale 11 (9) (2019) 4025–4034.
[21] A. Lesniak, A. Salvati, M.J. Santos-Martinez, M.W. Radomski, K.A. Dawson, C. Åberg, Nanoparticle adhesion to the cell membrane and its effect on nanoparticle uptake efficiency, J. Am. Chem. Soc. 135 (4) (2013) 1438–1444.
[22] C. Contini, M. Schneemilch, S. Gaisford, N. Quirke, Nanoparticle–membrane interactions, J. Exp. Nanosci. 13 (1) (2018) 62–81.
[23] F. Lolicato, L. Joly, H. Martinez-Seara, G. Fragneto, F. Scoppola, F. Baldelli Bombelli, I. Vattulainen, J. Akola, M. Maccarini, The role of temperature and lipid charge on intake/uptake of cationic gold nanoparticles into lipid bilayers, Small 15 (23) (2019) 1805046.
[24] P.A. Thompson, M. Khatami, C.J. Baglole, J. Sun, S.A. Harris, E.-Y. Moon, F. Al-Mulla, R. Al-Temaimi, D.G. Brown, A.M. Colacci, Environmental immune disruptors, inflammation and cancer risk, Carcinogenesis 36 (Suppl_1) (2015) S232–S253.
[25] R. Foldbjerg, P. Olesen, M. Hougaard, D.A. Dang, H.J. Hoffmann, H. Autrup, PVP-coated silver nanoparticles and silver ions induce reactive oxygen species, apoptosis and necrosis in THP-1 monocytes, Toxicol. Lett. 190 (2) (2009) 156–162.
[26] P.P. Fu, Q. Xia, H.-M. Hwang, P.C. Ray, H. Yu, Mechanisms of nanotoxicity: Generation of reactive oxygen species, J. Food Drug Anal. 22 (1) (2014) 64–75.
[27] V. Kumar, N. Sharma, S. Maitra, In vitro and in vivo toxicity assessment of nanoparticles, Int. Nano Lett. 7 (4) (2017) 243–256.
[28] D. Caccese, D. Praticò, A. Ghiselli, S. Natoli, P. Pignatelli, V. Sanguigni, L. Iuliano, F. Violi, Superoxide anion and hydroxyl radical release by collagen-induced platelet aggregation-role of arachidonic acid metabolism, Thromb. Haemost. 83 (3) (2000) 485–490.
[29] J. Loscalzo, Nitric oxide insufficiency, platelet activation, and arterial thrombosis, Circ. Res. 88 (8) (2001) 756–762.
[30] D.R. Riddell, J.S. Owen, Nitric Oxide and Platelet Aggregation, Vitamins & Hormones, Elsevier, 1997, pp. 25–48.
[31] J.J. Lancaster Jr., A tutorial on the diffusibility and reactivity of free nitric oxide, Nitric Oxide 1 (1) (1997) 18–30.
[32] D.A. Wink, J.B. Mitchell, Medicine, Chemical biology of nitric oxide: Insights into regulatory, cytotoxic, and cytoprotective mechanisms of nitric oxide, Free Radic Biol Med 25 (4–5) (1998) 434–456.
[33] V.R. de Lima, M.P. Morfim, A. Teixeira, T.B. Creczynski-Pasa, Relationship between the action of reactive oxygen and nitrogen species on bilayer membranes and antioxidants, Chem. Phys. Lipids 132 (2) (2004) 197–208.
[34] M.A. Matica, F.L. Aachmann, A. Tøndervik, H. Sletta, V. Ostafe, Chitosan as a wound dressing starting material: Antimicrobial properties and mode of action, Int J Mol Sci 20 (23) (2019) 5889.
[35] T. Dai, M. Tanaka, Y.-Y. Huang, M.R. Hamblin, Chitosan preparations for wounds and burns: Antimicrobial and wound-healing effects, Expert Rev Anti Infect Ther 9 (7) (2011) 857–879.
[36] R. Nadesh, D. Narayanan, S. Vadakumpully, U. Mony, M. Koyakkutty, S.V. Nair, D. Menon, Hematotoxicological analysis of surface-modified and-unmodified chitosan nanoparticles, J Biomed Mater Res A 101 (10) (2013) 2957–2966.
[37] H. Hattori, M. Ishihara, Changes in blood aggregation with differences in molecular weight and degree of deacetylation of chitosan, Biomed Mater 10 (1) (2015) 015014.
[38] G. Sun, J.J. Mao, Engineering dextran-based scaffolds for drug delivery and tissue repair, Nanomedicine 7 (11) (2012) 1771–1784.
[39] N. Fang, V. Chan, H.-Q. Mao, K.W. Leong, Interactions of phospholipid bilayer with chitosan: effect of molecular weight and pH, Biomacromolecules 2 (4) (2001) 1161–1168.
[40] A.C. Martínez-Torres, D.G. Zarate-Triviño, I.L.Y. Lorenzo-Anota, A. Ávila-Ávila, C. Rodríguez-Abrego, C. Rodríguez-Padilla, Chitosan gold nanoparticles induce cell death in HeLa and MCF-7 cells through reactive oxygen species production, Int J Nanomedicine 13 (2018) 3235.
[41] R.L.C.G. da Silva, H.F.O. da Silva, L.H. da Silva Gasparotto, L. Caseli, Lipopolysaccharides and peptidoglycans modulating the interaction of Au nanoparticles with cell membranes models at the air-water interface, Biophys. Chem. 238 (2018) 22–29.
[42] V.B. O'Donnell, R.C. Murphy, S.P. Watson, Platelet lipidomics: modern day perspective on lipid discovery and characterization in platelets, Circ Res 114 (7) (2014) 1185–1203.
[43] P. Cohen, A. Derksen, Comparison of phospholipid and fatty acid composition of human erythrocytes and platelets, Br. J. Haematol. 17 (4) (1969) 359–371.
[44] D. Behn, S. Bosk, H. Hoffmeister, A. Janshoff, R. Witzgall, C. Steinem, Quantifying the interaction of the C-terminal regions of polycystin-2 and polycystin-1 attached to a lipid bilayer by means of QCM, Biophys. Chem. 150 (1–3) (2010) 47–53.
[45] D.R. Bhumkar, H.M. Joshi, M. Sastry, V.B. Pokharkar, Chitosan reduced gold nanoparticles as novel carriers for transmucosal delivery of insulin, Pharm. Res. 24 (8) (2007) 1415–1426.
[46] Y. Wang, L. Zhan, C.Z. Huang, One-pot preparation of dextran-capped gold nanoparticles at room temperature and colorimetric detection of dihydralazine sulfate in uric samples, Anal. Methods 2 (12) (2010) 1982–1988.
[47] S. Nath, C. Kaittanis, A. Tinkham, J.M. Perez, Dextran-coated gold nanoparticles for the assessment of antimicrobial susceptibility, Anal. Chem. 80 (4) (2008) 1033–1038.
[48] M. Delcea, B. Meesaragandla, S. Karanth, U. Janke, Biopolymer-coated gold nanoparticles inhibit human insulin amyloid fibrillation, Sci. Rep. 10 (1) (2020) 7862.
[49] M. Shahmiri, M. Enciso, A. Mechler, Controls and constrains of the membrane disrupting action of Aurein 1.2, Sci Rep 5 (2015) 16378.
[50] S. Pandidan, A. Mechler, Membrane morphology effects in quartz crystal microbalance characterization of antimicrobial peptide activity, Biophys. Chem. (2020) 106381.
[51] L.K. Tamm, H.M. McConnell, Supported phospholipid bilayers, Biophys J. 47 (1) (1985) 105–113.
[52] R. Vácha, S.W. Siu, M. Petrov, R.A. Böckmann, J. Barucha-Kraszewska, P. Jurkiewicz, M. Hof, M.L. Berkowitz, P. Jungwirth, Effects of alkali cations and halide anions on the DOPC lipid membrane, J. Phys. Chem. A 113 (26) (2009) 7235–7243.
[53] A.K. Sum, R. Faller, J.J. de Pablo, Molecular simulation study of phospholipid bilayers and insights of the interactions with disaccharides, Biophys J. 85 (5) (2003) 2830–2844.
[54] G. Van Den Bogaart, N. Hermans, V. Krasnikov, A.H. de Vries, B. Poolman, On the decrease in lateral mobility of phospholipids by sugars, Biophys J 92 (5) (2007) 1598–1605.
[55] M. Klarhöfer, B. Csapo, C. Balassy, J. Szeles, E. Moser, High-resolution blood flow velocity measurements in the human finger, Magnetic Resonance in Medicine 45 (4) (2001) 716–719.
[56] F. Yang, X. Cui, X. Yang, Interaction of low-molecular-weight chitosan with mimic membrane studied by electrochemical methods and surface plasmon resonance, Biophys. Chem. 99 (1) (2002) 99–106.
[57] A. Mecke, D.-K. Lee, A. Ramamoorthy, B.G. Orr, M.M.B. Holl, Membrane thinning due to antimicrobial peptide binding: An atomic force microscopy study of MSI-78 in lipid bilayers, Biophys. J. 89 (6) (2005) 4043–4050.
[58] F.J. Pavinatto, L. Caseli, A. Pavinatto, D.S. dos Santos, T.M. Nobre, M.E. Zaniquelli, H.S. Silva, P.B. Miranda, O.N. de Oliveira, Probing chitosan and phospholipid interactions using Langmuir and Langmuir – Blodgett films as cell membrane models, Langmuir 23 (14) (2007) 7666–7671.
[59] F.J. Pavinatto, A. Pavinatto, L. Caseli, D.S. dos Santos, T.M. Nobre, M.E. Zaniquelli, O.N. Oliveira, Interaction of chitosan with cell membrane models at the air – water interface, Biomacromolecules 8 (5) (2007) 1633–1640.
[60] M.R. de Planque, S. Aghdaei, T. Roose, H. Morgan, Electrophysiological characterization of membrane disruption by nanoparticles, ACS Nano 5 (5) (2011) 3599–3606.
[61] V.V. Ginzburg, S. Balijepalli, Modeling the thermodynamics of the interaction of nanoparticles with cell membranes, Nano Lett 7 (12) (2007) 3716–3722.
[62] Y. Roiter, M. Ornatska, A.R. Rammohan, J. Balakrishnan, D.R. Heine, S. Minko, Interaction of nanoparticles with lipid membrane, Nano Lett 8 (3) (2008) 941–944.
[63] W.-C. Hou, B.Y. Moghadam, C. Corredor, P. Westerhoff, J.D. Posner, Distribution of functionalized gold nanoparticles between water and lipid bilayers as model cell membranes, Environ. Sci. Technol. 46 (3) (2012) 1869–1876.
[64] M. Hermes, C. Czesnick, S. Stremlau, C. Stöhr, F. Scholz, Effect of NO on the adhesion–spreading of DMPC and DOPC liposomes on electrodes, and the partition of NO between an aqueous phase and DMPC liposomes, Journal of Electroanalytical Chemistry 671 (2012) 33–37.
[65] S. Karanth, M. Delcea, Nitrosative stress affects the interaction of integrin alphaIIbbeta3 with its ligands, Biochim. Biophys. Acta (BBA)-Biomemb. (2020) 183198.
[66] M.S. Hassan, M.M. Mileva, H.S. Dweck, L. Rosenfeld, Nitric oxide products degrade chondroitin sulfates, Nitric Oxide 2 (5) (1998) 360–365.
[67] J.E. Shively, H.E. Conrad, Formation of anhydrosugars in the chemical depolymerization of heparin, Biochemistry 15 (18) (1976) 3932–3942.
[68] J. Duan, D.L. Kasper, Oxidative depolymerization of polysaccharides by reactive oxygen/nitrogen species, Glycobiology 21 (4) (2010) 401–409.
[69] S.t. Možina, J. Iskra, Aerobic oxidation of secondary alcohols with nitric acid and iron (III) chloride as catalysts in fluorinated alcohol, J. Org. Chem. 84 (22) (2019) 14579–14586.

Supplementary Information

Changing surface properties of artificial lipid membranes at the interface with biopolymer coated gold nanoparticles under normal and redox conditions

Sanjai Karanth,[1,2] Brahmaiah Meesaragandla[1,2] and Mihaela Delcea[1,2,3*]

[1]Institute of Biochemistry, University of Greifswald, Felix-Hausdorff-Straße 4, 17489 Greifswald, Germany;
[2]ZIK-HIKE, Zentrum für Innovationskompetenz "Humorale Immunreaktionen bei kardiovaskulären Erkrankungen", Fleischmannstraße 42, 17489 Greifswald, Germany;
[3]DZHK (DeutschesZentrumfürHerz-Kreislauf-Forschung), partner site Greifswald, Germany.

*Corresponding author: Mihaela Delcea: Institute of Biochemistry, University of Greifswald, Felix-Hausdorff-Straße 4, 17489 Greifswald; delceam@uni-greifswald.de; Tel. +4938344204423; Fax. +4938344204377

Figure S1: Chemical structure of (A) DMPC phospholipid, (B) Chitosan and (C) dextran-10.

Figure S2: Hydrodynamic diameter of PcAuNPs obtained from DLS.

Figure S3: AFM images of PcAuNPs in air.

Figure S4: QCM graph indicating interactions between PcAuNPs and bare SiO_2 crystal.

Figure S5: Surface modifications observed from RMS roughness.

Figure S6: QCM graph showing effect of nitric oxide on DMPC membrane.

Figure S7: *Ex-situ* AFM imaging of DMPC bilayer and effect of nitric oxide.

Table S1: Nitric oxide effect on the zeta potential of PcAuNPs.

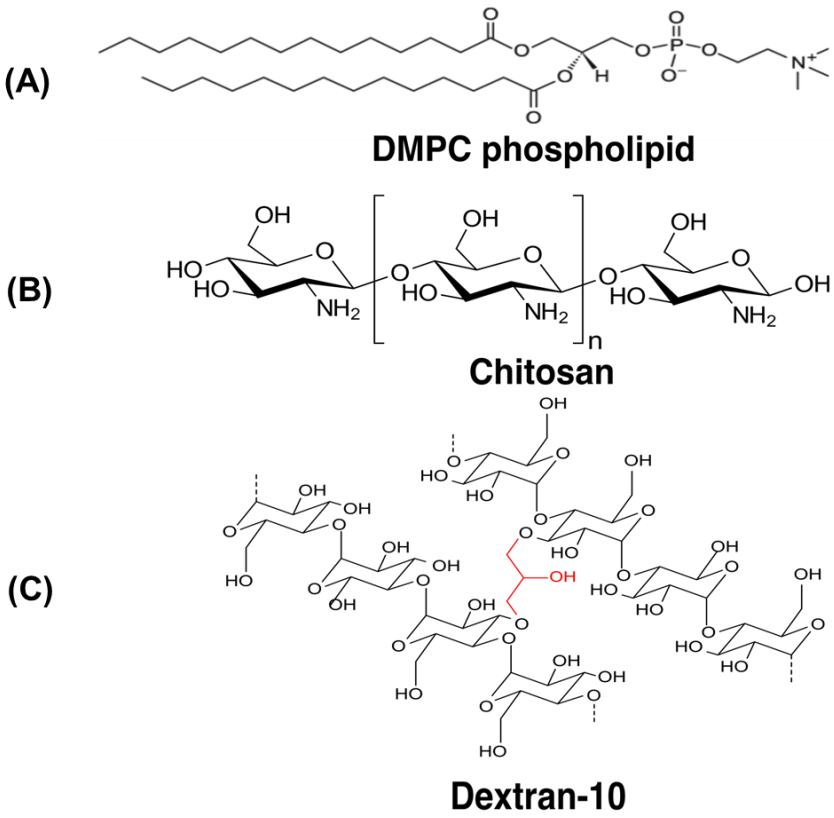

Figure S1: Chemical structure of (A) DMPC phospholipid, (B) Chitosan and (C) dextran-10.

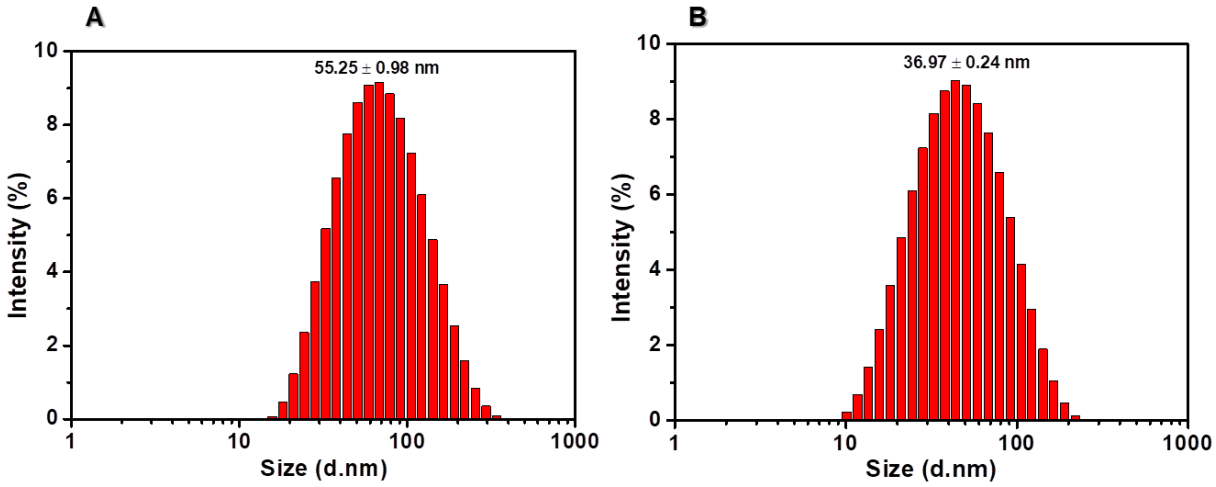

Figure S2: Hydrodynamic diameter of PcAuNPs obtained from DLS. Distributions showing mean diameters of ChAuNPs (A) and Dn10AuNPs (B). The average sizes are indicated in the representative plots.

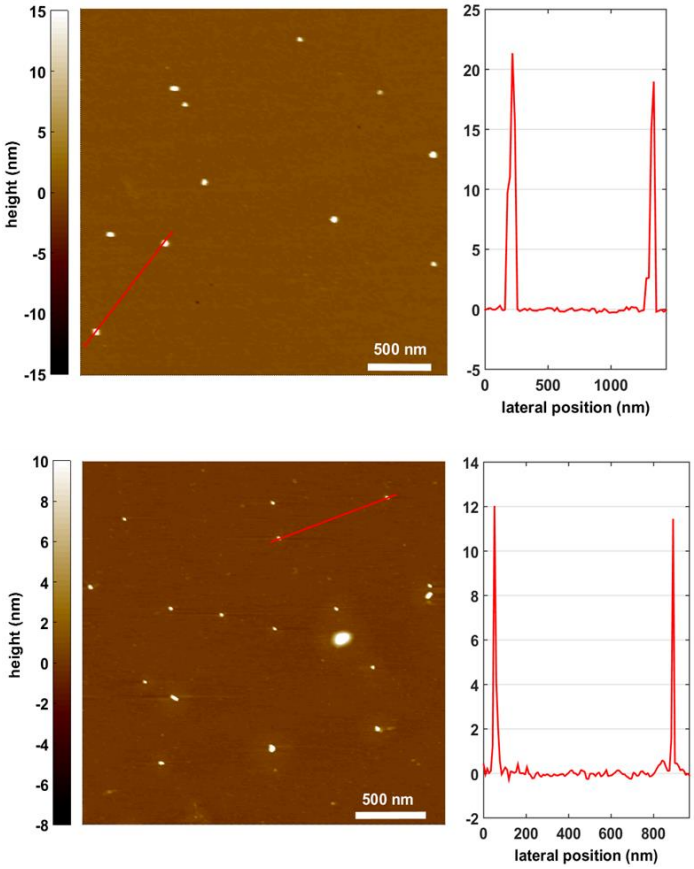

Figure S3: AFM images of PcAuNPs in air. **(Top)** Pure ChAuNPs when allowed to deposit on mica showed height profiles ranging between 15-20 nm. **(Bottom)** Pure Dn10AuNPs formed heights ranging between 9-12 nm. These particles showed spherical morphology and is in good agreement with the TEM images (Figure 2B, C).

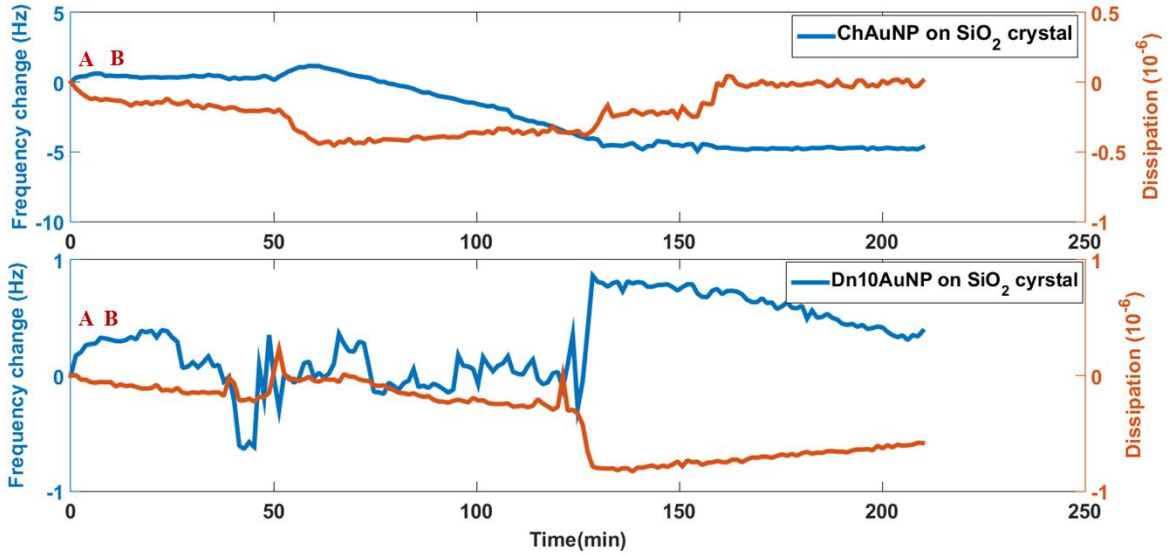

Figure S4: QCM graph indicating interactions between PcAuNPs and bare SiO_2 crystal. **(Top)** ChAuNPs have shown to interact with bare crystal after long time of exposure. Deposition of NPs and increase in mass is indicated by change in frequency (blue curve) shifts from around 0 Hz to -6 Hz. **(Bottom)** Dn10AuNPs do not interact with bare crystal as the frequency is around 0-1 Hz. Steps in QCM: The crystal was washed with deionized water (A) followed by PcAuNPs addition (B).

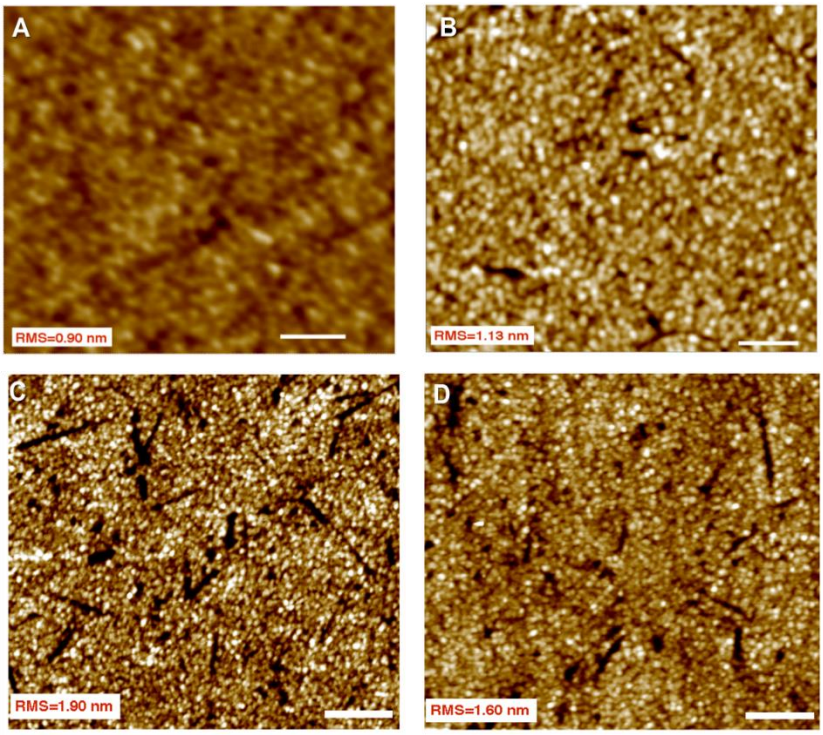

Figure S5: Surface modifications observed from RMS roughness. Bare SiO_2 crystal (A) showed RMS roughness of 0.90 nm. On formation of lipid bilayers (B) on the surface, the roughness was 1.13 nm. Post nanoparticles interaction, the heterogeneity in the surface structures increased considerably for ChAuNPs treated membrane (C) compared to Dn10AuNPs treated membrane (D). This heterogeneity represents the morphological changes undergone by the membrane. Holes formed by ChAuNPs predominantly showed structures containing crests and troughs indicating severe surface perturbations while Dn10AuNPs showed only troughs indicating complete rupture of membrane. These images when looked in combination with AFM heights (from Figure 3, *bottom* and Figure 4, *bottom*) provides a better overview. Scale bar =500 nm.

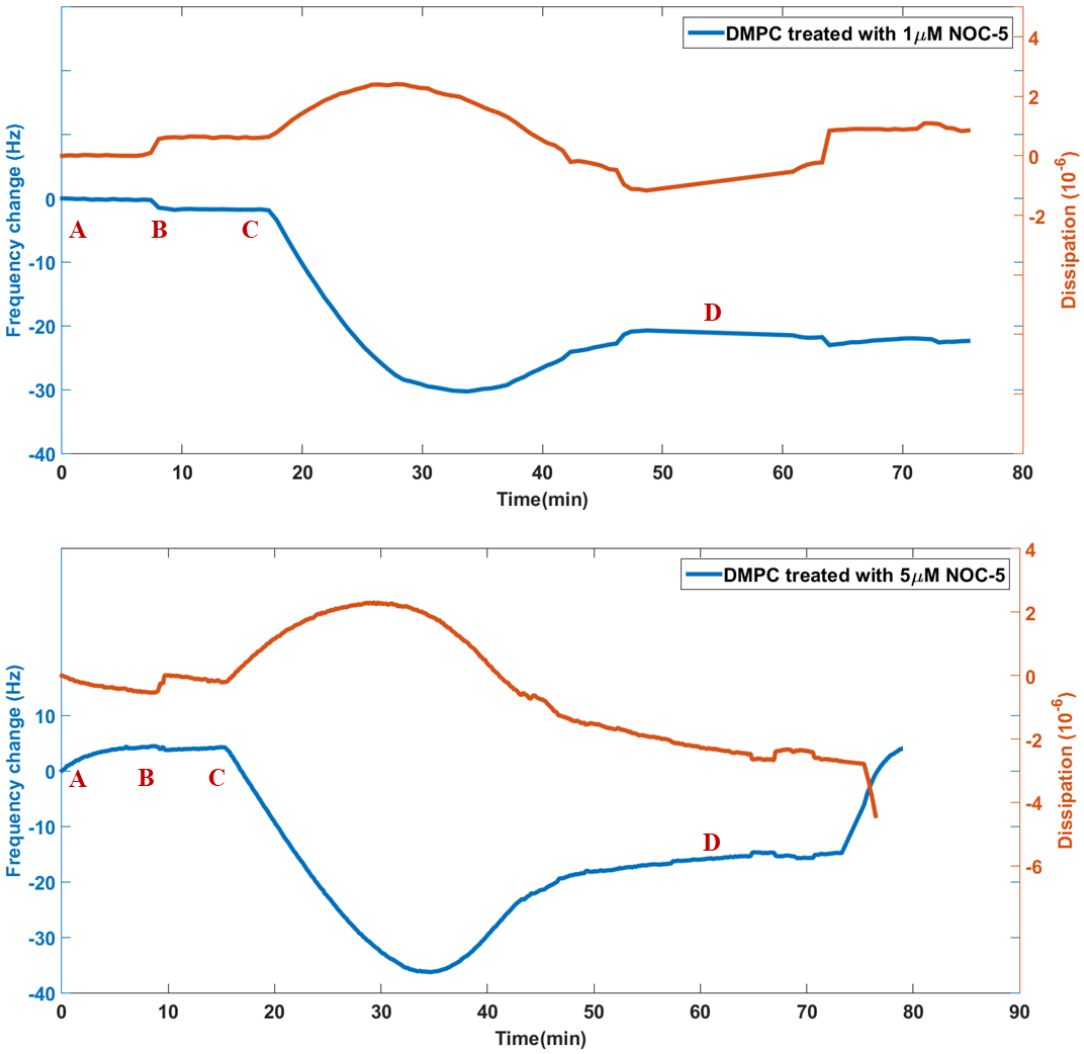

Figure S6: QCM graph showing effect of nitric oxide on DMPC membrane. When formed DMPC lipid bilayer was allowed to interact with 1µM NOC-5, we observed stabilization of lipid membrane by the nitric oxide (*top*), while 5 µM started to disrupt the membrane after 10 min (*bottom*). Steps in QCM: The crystal was washed with deionized water (A), Tris-HCl buffer (B) and SUVs were injected (C). After lipid bilayer formation 1µM (*top*) and 5µM NOC-5 (*bottom*) was added.

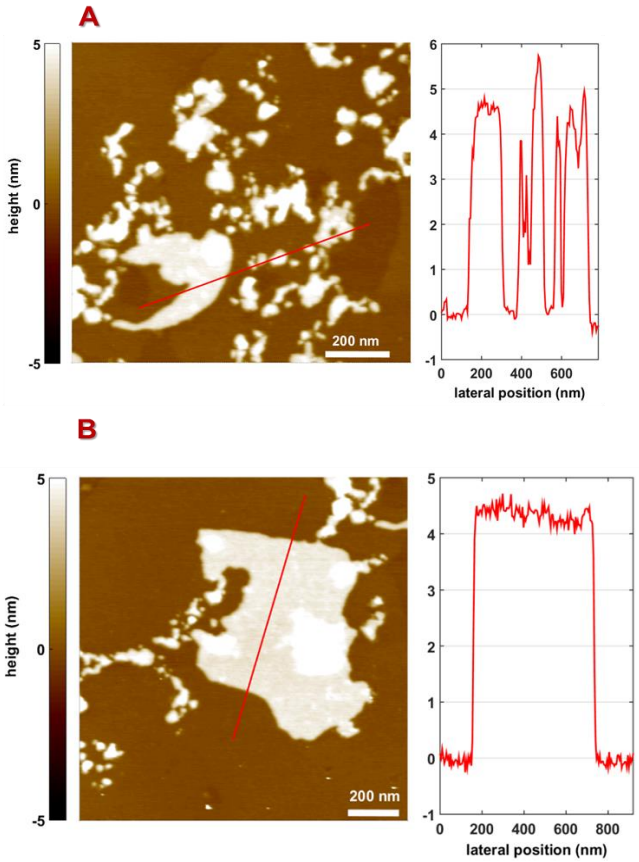

Figure S7: *Ex-situ* AFM imaging of DMPC bilayer and effect of nitric oxide. A) AFM image showing the height profiles (red curve) of DMPC bilayer formed on mica surface. The height obtained (ranging between 4-5 nm) are typical for a bilayer. B) Under the influence of 1µM NOC-5, most of the lipid patches were found to come together and form a continuous bilayer (red curve) compared to control. This shows membrane stabilization by NOC-5 at 1µM. These results are consistent with QCM sensogram (Figure S6, *top*).

Sample	Zeta values (mV)	
	Control	Treatment with 1µM NOC5
ChAuNP	30.1±2.7	23.1±1.3
Dn10AuNP	-33.6±0.6	-41.3±1.0
DMPC	2.3±1.1	-3.4±0.3

Table S1: Nitric oxide effect on the zeta potential of PcAuNPs. Post treatment with 1µM NOC-5, reduction in zeta potential of ChAuNPs indicates loss of positive charge from the amino group of chitosan, thereby its modification and decrease in its stability. In dextran-10 no such interaction is possible as it only contained –OH groups. We believe the change in zeta values of DMPC is due to cumulative effect of phosphate ions and nitric oxide (changing the net charge to negative).

IV. Biopolymer-coated gold nanoparticles inhibit human insulin amyloid fibrillation

Brahmaiah Meesaragandla, **Sanjai Karanth**, Una Janke and Mihaela Delcea

Scientific Reports, Volume 10
Article number: 7862 (2020)

Published: 12 May 2020

doi: 10.1038/s41598-020-64010-7

www.nature.com/scientificreports

SCIENTIFIC REPORTS
nature research

OPEN

Biopolymer-coated gold nanoparticles inhibit human insulin amyloid fibrillation

Brahmaiah Meesaragandla[1,2], Sanjai Karanth[1,2], Una Janke[1,2] & Mihaela Delcea[1,2,3]✉

Deposits of protein misfolding and/or aggregates are a pathological hallmark of amyloid-related diseases. For instance, insulin amyloid fibril deposits have been observed in patients with insulin-dependent diabetes mellitus after insulin administration. Here, we report on the use of AuNPs functionalized with linear- (i.e. dextrin and chitosan) and branched- (i.e. dextran-40 and dextran-10) biopolymers as potential agents to inhibit insulin fibril formation. Our dynamic light scattering analyses showed a size decrease of the amyloid fibrils in the presence of functionalized AuNPs. Circular dichroism spectroscopy as well as enzyme-linked immunosorbent assay data demonstrated that the secondary structural transition from α-helix to β-sheet (which is characteristic for insulin amyloid fibril formation) was significantly suppressed by all biopolymer-coated AuNPs, and in particular, by those functionalized with linear biopolymers. Both transmission electron microscopy and atomic force microscopy analyses showed that the long thick amyloid fibrils formed by insulin alone become shorter, thinner or cluster when incubated with biopolymer-coated AuNPs. Dextrin- and chitosan-coated AuNPs were found to be the best inhibitors of the fibril formation. Based on these results, we propose a mechanism for the inhibition of insulin amyloid fibrils: biopolymer-coated AuNPsstrongly interact with the insulin monomers and inhibit the oligomer formation as well as elongation of the protofibrils.Moreover, cytotoxicity experiments showed that AuNP-insulin amyloid fibrils are less toxic compared to insulin amyloid fibrils alone. Our results suggest that both dextrin- and chitosan-AuNPs could be used as therapeutic agents for the treatment of amyloid-related disorders.

Deposition of insoluble protein aggregates referred as amyloids has been observed as a common feature of various degenerative diseases (e.g. Alzheimer's, type II diabetes, Parkinson's, and Huntington's disease)[1–5]. Almost 20 different human proteins have been identified to form amyloid deposits and aggregates in intracellular and extracellular matrix of the brain[6]. Amyloid fibrils have been recognized as highly-ordered aggregates, rich in cross β-sheet secondary structures with unbranched filamentous morphology[7]. Generally, amyloid fibril formation involves several steps including oligomers, protofibrils, and fibrils[8,9]. Each of these forms has distinctive molecular conformations and different degrees of toxicity to the neuronal cells[10].

One of the human proteins where amyloid fibril formation is considered a major problem is insulin. It is a 51-residue polypeptide hormone involved in regulating the blood glucose level and is used for the treatment of diabetes. It consists of an A-chain (21-residues) and B-chain (30-residues) which are connected by a pair of inter-chain disulfide bonds[11]. Furthermore, it has been shown to exhibit an *in vitro* amyloid fibril-forming tendency at certain destabilizing conditions (e.g., low pH, elevated temperature, increased ionic strength, and stirring)[12]. Moreover, insulin amyloid fibril deposits have been observed in patients with insulin-dependent diabetes mellitus after insulin infusion as well as repeated injection at subcutaneous site (injection localized amyloidosis)[13–15]. Insulin amyloid fibrillation is a major concern during insulin manufacture, long-term storage, as well as delivery of the protein and any degree of amyloid fibril formation leads to reduced efficacy of insulin administration[16].

Currently, there is no approved therapeutic agent available for the treatment of amyloid-related diseases. Recently, there has been an increasing interest in developing nanoparticles (NPs) as therapeutic agents to prevent and treat protein-amyloid related diseases due to their distinctive properties such as: small size, high surface/

[1]Institute of Biochemistry, University of Greifswald, Felix-Hausdorff-Straße 4, 17489, Greifswald, Germany. [2]ZIK HIKE - Zentrum für Innovationskompetenz, Humorale Immunreaktionen bei kardiovaskulären Erkrankungen", Fleischmannstraße 42, 17489, Greifswald, Germany. [3]DZHK (Deutsches Zentrum für Herz-Kreislauf-Forschung), partner site, Greifswald, Germany. ✉e-mail: delceam@uni-greifswald.de

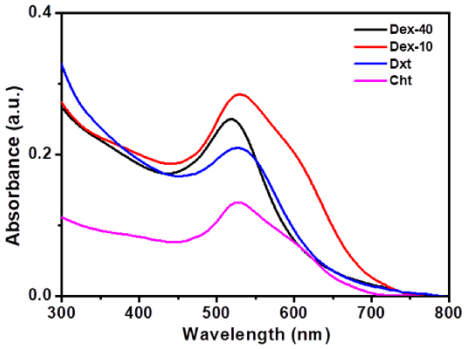

Figure 1. (**A**) UV-Vis absorption spectra of AuNPs coated with Dex-40 (black), Dex-10 (red), Dxt (blue) and Cht (magenta) ligands (AuNPs concentration = 100 nM).

volume ratio, composition and biocompatibility. It has been shown that NPs may either promote or suppress the amyloid fibrillogenesis. Various copolymer particles such as CeO_2, TiO_2, carbon nanotubes, and quantum dots have been reported to promote the rate of amyloid fibril formation *in vitro* depending on the amount and surface of the particles[17]. In contrast, a significant suppression of amyloid fibrillogenesis was observed for hydrophobic teflon and fluorinated NPs[18].

Gold nanoparticles (AuNPs) have been widely used in biomedical applications as they are chemically inert, readily synthesized, easily functionalized and show excellent biocompatibility[19,20]. However, only very few studies have focused on the influence of AuNPs on amyloid fibril formation of proteins/peptides. Sardar *et al.* have shown that AuNPs inhibit the amyloid fibrillogenesis of β-lactoglobulin in a dose-dependent manner[21]. In another study, Moore *et al.* have studied the effect of AuNPs properties on inhibition of Aβ (beta amyloid) aggregation[22]. They have shown that both surface chemistry and size of NPs can influence the extent of fibril inhibition, whereas the electric charge defines the ability of NPs to alter aggregate morphology. In another study, Guanbin and coworkers have described the distinct size effect of AuNPs and Au nanocrystals (AuNCs) on Aβ fibrillation[23]. In addition, it was found that large AuNPs accelerate Aβ fibrillation, whereas small AuNPs significantly suppress the inhibition process. Esmail *et al.* have used AuNPs to detect the formation of A3 amyloid fibrils and oligomers[24]. They have demonstrated that the surface plasmon resonance (SPR) band intensity of the AuNPs is sensitive to the presence of oligomers of both A340 and an A340 mutant. In addition, the change in the SPR band intensity can be used to monitor the kinetics of the stable oligomer formation of the A340 mutant.

In this work, we combine spectroscopic and microscopic techniques as well as biological assays to investigate how linear- or branched polymeric ligands at the AuNPs surface influence the insulin amyloid fibril formation. Small-sized AuNPs coated with various biopolymers (dextran-40 (Dex-40), dextran-10 (Dex-10), dextrin (Dxt), and chitosan (Cht)) were used to investigate their effect on insulin amyloid suppression and/or inhibition. The biocompatibility of AuNP-insulin amyloid fibrils was also assessed on human pancreatic and embryonic kidney cell lines.

Results and discussion

Synthesis and characterization of biopolymer-coated AuNPs. Biopolymer-coated small-sized AuNPs were prepared using a previously reported protocol[25,26] with a slight modification. The chosen biopolymers Dex-40, Dex-10, Dxt and Cht as capping ligands present low toxicity, higher dispersibility, availability of functional groups, and robust chemical and thermal stability. Both Dex-40 and Dex-10 molecules are highly branched, whereas Dxt and Cht molecules are linear in nature (see Fig. S1). The branching order is as follows: Dex-40 > Dex-10 > Dxt ≈ Cht.

The formation of biopolymer-coated AuNPs was confirmed by the occurrence of SPR bands near 519–528 nm. Figure 1 shows the UV-Vis absorption spectra of AuNPs coated with Dex-40 (black), Dex-10 (red), Dxt (blue) and Cht (magenta) ligands. Highly branched Dex-40-AuNPs showed the SPR band at 519 nm, whereas AuNPs coated with other ligands showed the SPR band at approx. 528 nm. The broadening of SPR band indicates the formation of small particles.

TEM images shown in Fig. 2 demonstrate that all biopolymer-coated AuNPs have spherical morphology with an average size about 5–15 nm with the exception ofCht-AuNPs which show an average size of about 23.6 ± 5.8 nm.

The hydrodynamic diameters (d_H) of biopolymer-coated AuNPs measured by DLS was determined to be ~20, ~53, ~40 and ~55 nm for Dex-40-AuNPs, Dex-10-AuNPs, Dxt-AuNPs and Cht-AuNPs, respectively (Fig. S2A). The overall increase in d_H is due to the hydrated expansion of the polymer layer in aqueous state which further varies with length and molecular weight of polymers. Both Dex-10 and Cht-AuNPs show similar d_H, even though the core size was different as shown in TEM images. This could be due to the multilayer adsorption of polymers on AuNPs surface[27,28]. Among all the biopolymer-coated AuNPs, a large increment in the d_H was observed for the Dxt-AuNPs, which is due to the multilayer linear adsorption of Dxt molecules. Moreover, all the biopolymer

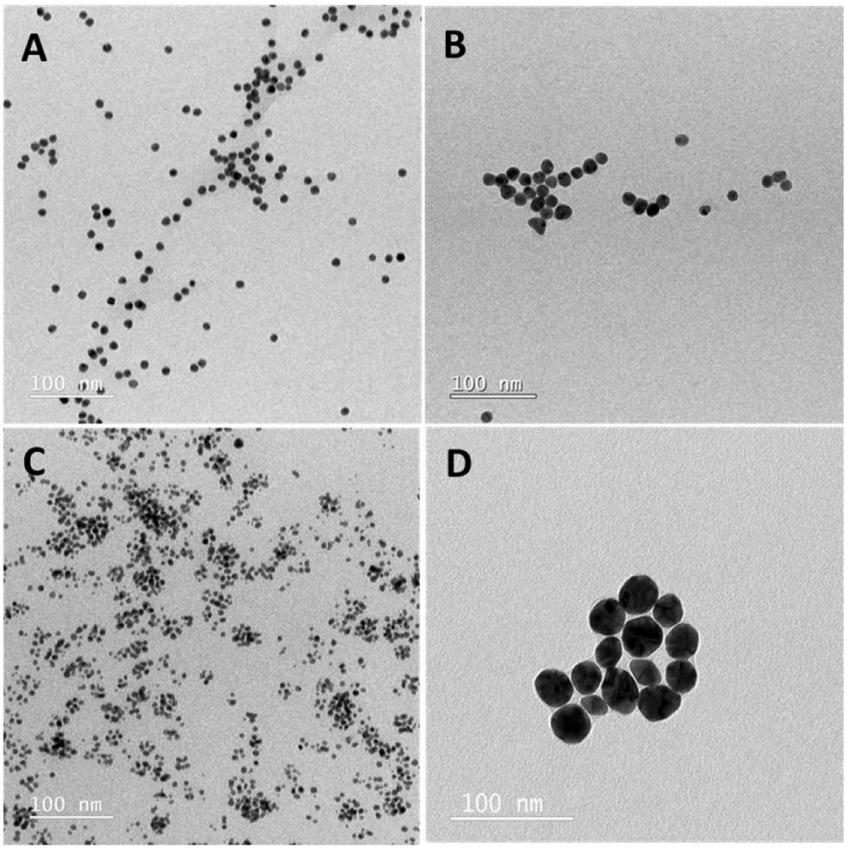

Figure 2. TEM images of AuNPs coated with Dex-40 (**A**), Dex-10 (**B**), Dxt (**C**) and Cht (**D**) ligands.

coatings keep the refractive index of the medium around AuNPs similar as they contain –OH groups at their surface, which may retain the SPR band unaltered[29]. These results indicate that except Dex-40-AuNPs, all the other biopolymer-coated AuNPs exhibits similar SPR band, irrespective of their sizes (see Table S1)."

It has been well distinguished that the maximum wavelength of SPR band for AuNPs strongly depends on size, shape,dielectric environment and space between NPs. Zeta potential data showed positively charged Cht-AuNPs due to the availability of-NH_2 groups at the surface, whereas all other coated-AuNPs were negatively charged due to the presence of -OH groups at the surface (Fig. S2B).

Characterization of biopolymer-coated AuNPs at acidic pH and high temperature. In order to understand the effect of both temperature and pH on the stability of biopolymer-coated AuNPs, we have incubated the biopolymer-coated AuNPs in glycine buffer at 65 °C for 3 h. Figure S3 shows the UV-Vis absorption spectra of biopolymer-coated AuNPs in glycine buffer at pH 2 before and after incubation at 65 °C. Both Dex-40 and Dex-10-AuNPs after immediate dispersion in glycine buffer shows a significant change in the SPR band position at longer wavelength in the region of 550–700 nm. However, no detectable change in the SPR band was observed for Dxt-AuNPs, whereas Cht-AuNPs showed an additional peak at 650 nm along with main peak. The appearance of a second peak for Cht-AuNPs is attributed mainly to the bimodal size distribution or aggregation of few particles by decreasing the interspacing between AuNPs.Remarkably, except for Dxt-AuNPs, the SPR band for all biopolymer-coated AuNPs shifted to longer wavelength with decreased intensity after 3 h incubation. Dxt-AuNPs shift the SPR band from 528 to 533 nm without affecting the intensity suggesting aggregation of few particles. The decreased intensity of the SPR band indicates the aggregation of biopolymer-coated AuNPs in acidic medium and at higher temperature. The instability of biopolymer-coated AuNPs in glycine buffer is due to: 1) biopolymer molecules which bind to the AuNPs through weak -OH/-NH_2 groups; and 2) high ionic strength in the solution which would reduce the electrostatic repulsive forces between AuNPs and further accelerate the aggregation behaviour. In contrast, a small shift (5 nm) in the SPR band for Dxt-AuNPs might be due tothe formation of few aggregates or a slight change in the microenvironment around the NPs as Dxt is thermally stable. The

AuNPs	d_H (nm)	Zeta potential (mV)
Dex-40-AuNPs	715.4 ± 64.6	10.7 ± 2.5
Dex-10-AuNPs	566 + 75.3	18.6 + 2.3
Dxt-AuNPs	1866 ⊥ 56.9	1.3 ⊥ 0.3
Cht-AuNPs	439.8 ± 39.6	25.4 ± 0.5

Table 1. DLS and Zeta potential results of the biopolymer-coated AuNPs in glycine buffer (pH 2) after 3 h incubation at 65 °C.

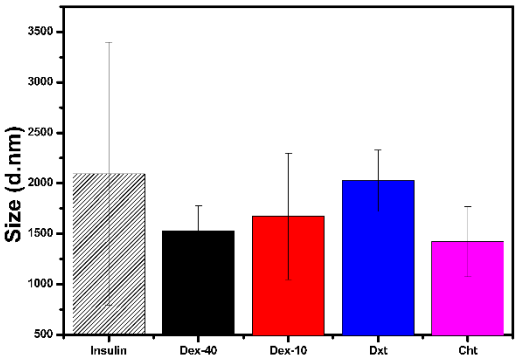

Figure 3. DLS data of pure insulin amyloid fibrils and the same in presence of biopolymer-coated AuNPs in glycine buffer after 3 h incubation at 65 °C (100 nM AuNPs).

aggregation behavior of the AuNPs was further supported by the increased d_H of thebiopolymer-coated AuNPs in DLS measurements (Table 1).As listed in Table 1, the d_H of Dex-40-AuNPs, Dex-10-AuNPs, Dxt-AuNPs and Cht-AuNPs after 3 h incubation at 65 °C were determined to be ~715, ~566, ~1866 and 439 nm, respectively. Interestigly, among all the biopolymer-coated AuNPs, Dxt-AuNPs showed a huge increment in d_H after 3 h incubation. Contradictorily, a very small shift (~5 nm)in the SPR band was observed for Dxt-AuNPs even after 3 h incubation (see Fig. S3B). This indicates that the increase in d_H for Dxt-AuNPs isdue to either the binding of NPs to the both edges of the linear Dxt molecule or to the formation of the chain-like structures with the NPs. Xing *et al.* showed an increment in the d_H of AuNPs after adsorption of siRNA-cathepsin K and a further increase after layering of chitosan and gelatin molecules on the AuNPs surface[30]. According to the zeta potential results shown in Table 1, all biopolymer-coated AuNPs were found to be positively charged at pH 2.0, which could be due to the protonation of -OH groups and availability of $-NH^{3+}$ groups under the acidic condition.

Interaction of human insulin amyloid fibrils with biopolymer-coated AuNPs. Preparation of insulin fibrils at acidic pH and high temperature has been previously described[31]. To study the interaction of biopolymer-coated AuNPs with insulin amyloid fibrils, fibrils were prepared in the presence of biopolymer-coated AuNPs with varying concentrationas described in the experimental section. Initially, DLS analyses were performed to detect the changes in the size distribution of amyloid fibrils in the presence of biopolymer-coated AuNPs. Figure 3 shows the DLS data of insulin solutions incubated in the presence and in the absence of biopolymer-coated AuNPs. Interestingly, insulin alone incubated for 3 h at 65 °C has a d_H about 2200 nm, suggesting the formation of long mature insulin amyloid fibrils. The d_H of the insulin monomers before heating was about 3.4 nm (Fig. S4) and consistent with previously reported data[32].

In the presence of biopolymer-coated AuNPs, the d_H of insulin amyloid fibrils (ranging from 1500 to 2000 nm) decreased compared to the pure insulin amyloid fibrils. This suggests either formation of oligomers or shortening of mature fibrils caused by the interaction of biopolymer-coated AuNPs with insulin monomers during the fibril formation.

To evaluate the effect of biopolymer-coated AuNPson insulin amyloid fibrils, UV-Vis analyses were carried out for biopolymer-coated AuNPs-insulin amyloid fibril solution (final AuNP concentration 100 nM). As shown in Fig. 4, the SPR band position of the biopolymer-coated AuNPs exhibits a change after insulin amyloid fibrils formation. After 3 h incubation, a significant change in the SPR band position was observed for Dex-40 (519 to 590 nm) and Dex-10-AuNPs (528 to 630 nm), whereas no detectable changes were observed for both Dxt- and Cht-AuNPs in the insulin amyloid fibrils.The existence of the SPR band after fibrillation in the presence of insulin indicates the formation of protein corona around the AuNPs, whereas except Dxt-AuNPs, such band (longer wavelength with decreased intensity) was not observed in the absence of insulin (see Fig. S3B). Branched polymers (Dex-40/Dex-10) bind weakly to the AuNPs surface and further, insulin molecules can bind either direct to the AuNPs surface or can intercalate on the AuNPs surface forming protein corona aggregates. Instead, linear

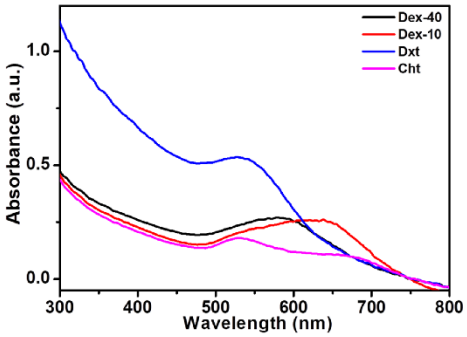

Figure 4. UV-Vis spectra of insulin amyloid fibrils with biopolymer-coated AuNPs in glycine buffer after 3 h incubation at 65 °C (100 nM AuNPs).

molecules (Dxt/Cht) cover the entire AuNPs surface and allow strong binding to the AuNPs. Therefore, insulin can adsorb on the linear polymer coated AuNPs forming a stable AuNP-protein corona.These results indicate that both branched molecules Dex-40 and Dex-10-AuNPs undergo aggregation, whereas the linear molecules Dxt- and Cht-AuNPs are rather stable even after fibril formation. This observation shows that the nature of the biopolymer-coated AuNPs (stable particles or aggregates) has a strong influence on the inhibition of insulin amyloid fibril formation through either strong or weak interaction. The existence of a SPR band for Dxt- and Cht-AuNPs in the presence of amyloid fibrils indicates the stability of AuNPs which can strongly interact with insulin monomers, whereas aggregated AuNPs (Dex-10/Dex-40-AuNPs) can participate in weak interaction with insulin monomers. In the view of stability, both Dxt- and Cht-AuNPs may lead to strong inhibition of insulin amyloid fibrils as they strongly interact with insulin monomers.

We have compared the SPR band position before and after fibril formation to understand the sensitivity of AuNPs during fibril formation. Interestingly, after fibril formation, both Dxt- and Cht-AuNPs resulted in increased intensity of absorption band compared to the Dex-40/Dex-10-AuNPs (see Fig. S5). This suggests that insulin amyloid fibrils make both Dxt- and Cht-AuNPsrelatively stable compared to Dex-40/Dex-10-AuNPs. This could be due to the strong interaction of biopolymer-coated AuNPswith insulin monomers during fibril formation. Moreover, the intact SPR band position before and after fibril formation indicates that the inhibition of fibril formation is purely dependenton the interaction between surface of the biopolymer-coated AuNPsand the insulin monomers. Therefore, AuNPs can be used as a tool to detect the amount of amyloid fibril formation as they exhibit change in the SPR band position and intensity with the fibril formation.

To further understand the effect of biopolymer-coated AuNPconcentration on the insulin amyloid fibril formation, we have performed the absorption measurements for the amyloid fibrils in presence of biopolymer-coated AuNPs at various concentrations. Data showed in Fig. 5 indicates no further shift in the SPR band position upon increasing concentrations. The increase in the intensity of absorption band of biopolymer-coated AuNPs in the insulin amyloid fibrils was purely due to the different concentrations of biopolymer-coated AuNPs.

We have carried out control experiments with bare AuNPs to understand the difference between functionalized and non-functionalized AuNPs interacting with insulin fibrils. We have chosen 10 nm bare AuNPs, which exhibit SPR band at 515 nm (Fig. S6A). Figure S6B shows the UV-Vis spectra of bare AuNPs in the presence of insulin amyloid fibrils before and after 3 h incubation at 65 °C. After immediate dispersion of bare AuNPs to the insulin in glycine buffer, the SPR band shifts towards longer wavelength (542 nm), which is due to the formation of AuNP-insulin protein corona aggregates. This is expected because of the availability of bare AuNPs surface to bind to free -SH, and/or $-NH_2$ or -COOH groups of the insulin monomers. This results in the change in the dielectric environment around the AuNPs surface, which allows a shift in the SPR band position. However, a further shift in the absorption band was observed to a longer wavelength (565 nm) after 3 h incubation at 65 °C. This could be due to the aggregation of AuNPs induced by the formed soft corona, which changes their binding sites during fibril formation. There was no further shift in the SPR band position after incubation with biopolymer-coated AuNPs (see Fig. S5). This clearly indicates that inhibition of insulin amyloid fibrils is purely due to the interaction of biopolymers with the insulin monomers. In addition, no further shift in the absorption band was observed for various concentration of bare AuNPs (see Fig. S6C)."

Figures 6 and S7 show the CD spectra of insulin alone and co-incubated with the biopolymer-coated AuNPs with varying concentrations before and after 3 h incubation at 65 °C, respectively. All samples at the beginning of incubation exhibita common spectrum with two negative minima at ~208 and ~222 nm, and a pronounced positive peak at ~195 nm which corresponds to an α-helix-rich secondary structure (Fig. S7). Such peaks were not observed for biopolymer-coated AuNPs alone (see Fig. S8). However, after 3 h incubation, the same samples exhibit typical negative band at 220–225 nm and a positive band at 201–203 nm which corresponds to the mature insulin amyloid fibrils with 3-sheet structures (Fig. 6).

The structural changes from α-helix rich to β-sheet structures in CD measurements demonstrated the formation of insulin amyloid fibrils[33]. The intensity and shape of CD spectra were found to be dependent on the type and concentration of AuNPs used during the insulin amyloid fibril formation. The secondary structural transition

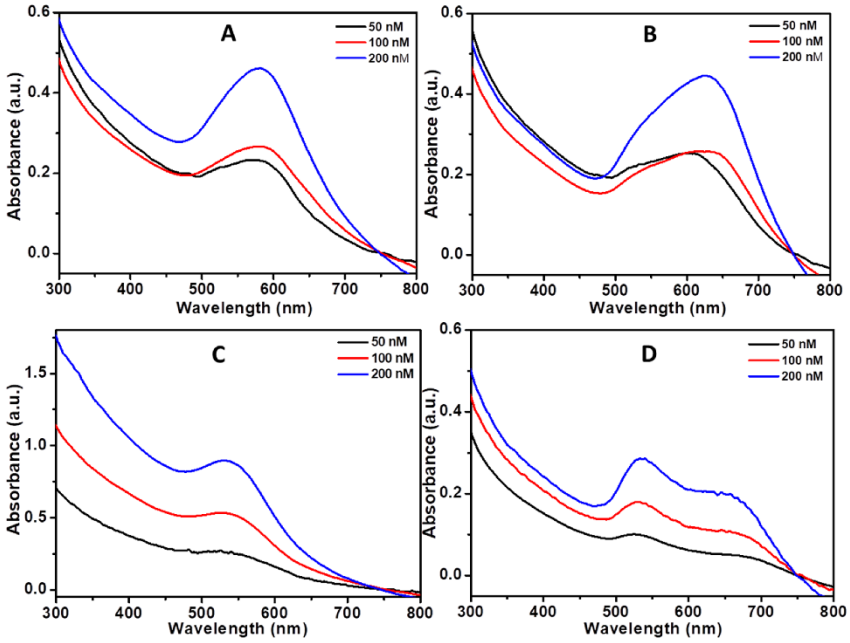

Figure 5. UV-Vis spectra of insulin amyloid fibrils in the presence of biopolymer-coated AuNPs with various concentrations after 3 h incubation at 65 °C in glycine buffer. (**A**) Dex-40, (**B**) Dex-10, (**C**) Dxt, and (**D**) Cht-AuNPs. (AuNPs concentration = 50, 100, 200 nM).

from α-helix to β-sheet was significantly suppressed by all biopolymer-coated AuNPs. The results indicate that all biopolymer-coated AuNPs diminished the insulin fibril formation in a dose-dependent manner. In particular, both Dxt- and Cht-AuNPs completely inhibit α-to-3 transition. Especially, a small amount of Cht-AuNPs inhibit the rich α-helix to β-sheet formation. In contrast, both Dex-40 and Dex-10-AuNPs inhibit moderately β-sheet formation. These results indicate that Dxt- and Cht-AuNPs are more efficient than Dex-40 and Dex-10-AuNPs in inhibiting insulin amyloid fibrillation.

To further confirm the CD data showing the structural change of insulin after fibril formation in presence of different polymer-coated AuNPs, we have established an ELISA in our laboratory. We have chosen three antibodies (anti-insulin 1, anti-insulin 2 or anti-amyloid beta) to study the interaction with antigens (pure insulin, insulin amyloid fibrils alone and AuNPs-insulin amyloid fibrils). Anti-insulin 1 is the antibody against the insulin receptor binding region, anti-insulin 2 is the antibody against the internal region C-peptide and anti-amyloid beta is the antibody against amyloids in the brain. Figure 7 shows the ELISA measurements of insulin alone before and after fibrillation as well as insulin amyloid fibrils in presence of different polymer-coated AuNPs incubated with anti-insulin 1, anti-insulin 2 or anti-amyloid beta antibodies. It can be seen that anti-insulin 1 antibody binds to all samples (insulin, insulin amyloid fibrils and AuNP-insulin amyloid fibrils) in a similar way. Hardly any change in the binding was observed for all the samples. However, both anti-insulin 2 and anti-amyloid beta antibodies showed difference in the binding with insulin, insulin amyloid fibrils and AuNPs-insulin amyloid fibrils. Anti-insulin 2 antibody binds more strongly to the insulin amyloid fibrils as well as pure insulin, whereas binding has decreased for AuNP-insulin amyloid fibrils. In a similar way anti-amyloid antibody also shows less binding to the biopolymer-coated AuNP-insulin amyloid fibrils than insulin amyloid fibrils alone. Overall, both antibodies showed very less binding to biopolymer-coated AuNP-insulin amyloid fibrils compared to insulin amyloid fibrils alone.

Interestingly, all types of biopolymer-coated AuNPs, regardless of the nature of the attached polymer induced similar binding efficiency of the antibodies. The decrease in the binding efficiency compared to insulin alone might be due to changes in the conformation of insulin from α-helix to β-sheet in the presence of biopolymer-coated AuNPs. However, antibody binding sites might be hidden due to insulin-nanoparticle binding.

From this data it can be proposed that biopolymer-coated AuNPs inhibit the structural changes from α-helix rich to β-sheet structures as indicated by CD data.

In order to visualize the fibril morphology, TEM analyses were performed on the insulin amyloid fibrils and the same treated with biopolymer-coated AuNPs. Figure 8 shows the TEM micrographs of all insulin samples (in the absence or in the presence of Dex-40, Dex-10, Dxt and Cht-AuNPs) obtained after 3 h of incubation at

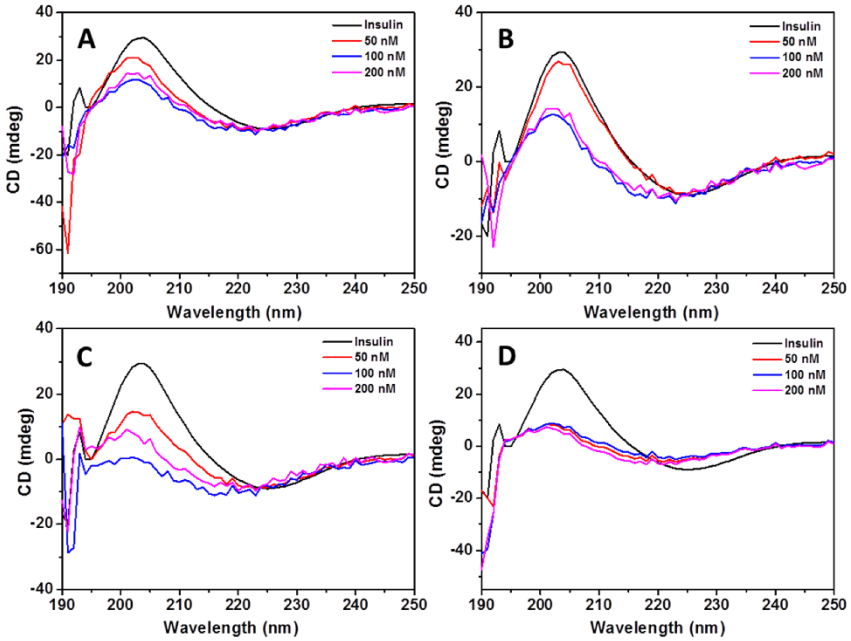

Figure 6. CD spectra of insulin amyloid fibrils in the presence of various concentrations of biopolymer-coated AuNPs after 3 h incubation at 65 °C. (**A**) Dex-40-AuNPs, (**B**) Dex-10-AuNPs, (**C**) Dxt-AuNPs, and (**D**) Cht-AuNPs.

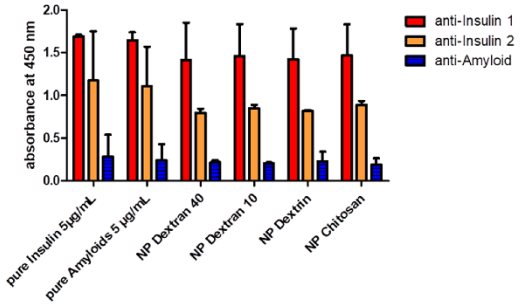

Figure 7. ELISA measurements for insulin, insulin amyloid fibril and AuNP-insulin amyloid fibrils with 10 µg/mL antibodies (anti-Insulin 1, anti-Insulin 2 and anti-amyloid beta antibodies). The bars represent average values of the maxima of the optical density (OD) values. Error bars correspond to the standard deviation.

65 °C. As expected, high density of thick long fibril aggregates of 10–20 nm in diameter and several µm in length were observed for insulin amyloid fibrils (control), whereas reduced amount of amyloid fibrils with thin and shorter species were observed in the presence of biopolymer-coated AuNPs. However, the level of fibrillogenesis was found to be associated with the type of biopolymer-coated AuNPs. For example, both Dxt and Cht-AuNPs strongly inhibit the amyloid fibril formation compared to Dex-10 and Dex-40-AuNPs. The difference in the fibrillogenesis is due to the interaction of biopolymer-coated AuNPs with the insulin monomers during amyloid fibril formation. In the case of branched polymer-coated AuNPs (Dex-40, Dex-10-AuNPs), the AuNPs undergo self-aggregation which may reduce the interaction with the insulin monomers. This self-aggregationbehaviour was already shown above in the UV-Vis spectra (Fig. 4) and is further confirmed by the aggregation of particles in the TEM images. However, the interaction is different in the case of linear polymer-coated AuNPi.eDxt- and Cht-AuNPs, because both the Dxt- and Cht-AuNPs are rather stable and are attachedon the side of the amyloid

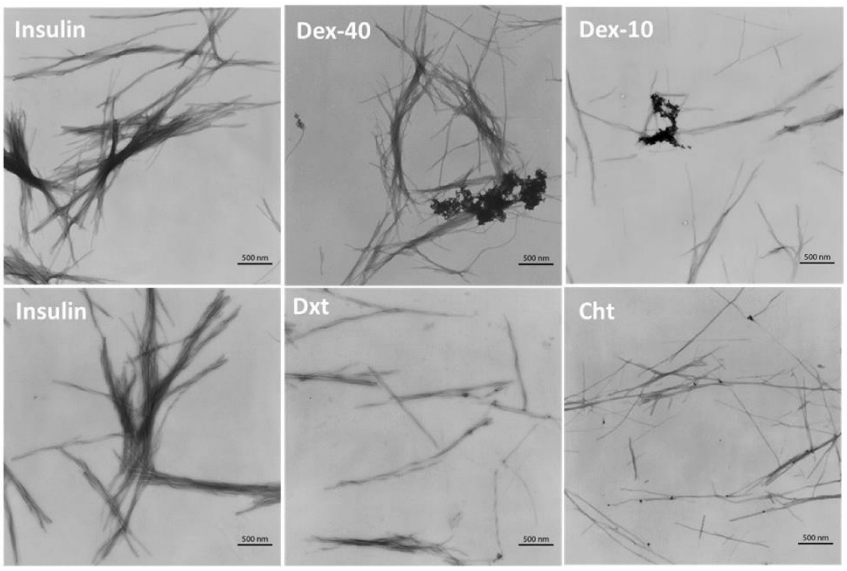

Figure 8. TEM micrographs of insulin sample alone and insulin samples in the presence of Dex-40, Dex-10, Dxt and Cht-AuNPs after 3 h incubation at 65 °C. (AuNPs concentration — 100 nM).

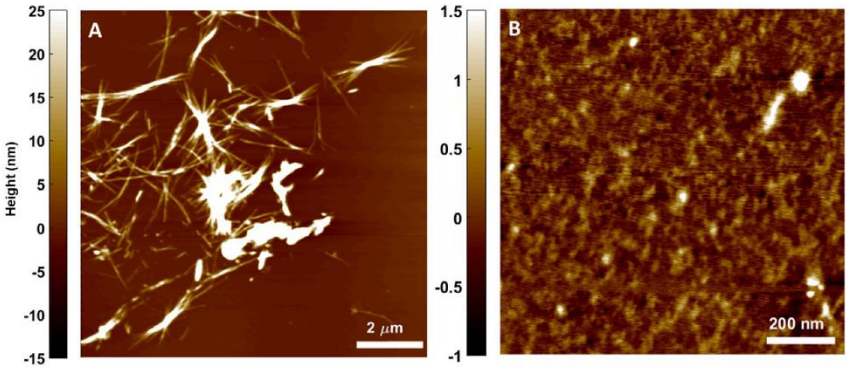

Figure 9. AFM images showing the formation of insulin fibrils (**A**) when subjected to 3 h incubation at 65 °C. Very few oligomers were present (**B**) post fibril formation. The color bar indicates the heights (in nm) of insulin fibrils.

fibrils asit can be seen in the TEM images. Therefore, only amorphous insulin amyloid fibril aggregates are formed in the presence of Dex-40 and Dex-10-AuNPs, whereas some short and thin fibrils are observed in the presence of Dxt- and Cht-AuNPs. TEM observations along with CD results clearly demonstrated that AuNPs induce an inhibitory activity towards amyloid fibril formation of insulin.

While it was clear from TEM images that fibril thickness was getting reduced, we investigated the faith of disintegrated fibrils and the way their growth was being restricted by biopolymer-coated AuNPs. To understand this, AFM images were taken for the insulin fibrils in the absence and in the presence of biopolymer-coated AuNPs after 3 h incubation at 65 °C. Figure 9 and Fig. S9 show the AFM images of pure insulin before and after 3 h incubation at 65 °C. Insulin monomers before incubation are spherical with height ranging between 0.4 to 0.5 nm (Fig. S9). After 3 h incubation under experimental conditions (pH 2 and 65 °C), the monomers of insulin converted to insulin amyloid fibrils with typical amyloid morphology– long, thick, and unbranched fibrils (Fig. 9A) as well as formation of very few oligomers were observed (Fig. 9B). When observed at smaller scan range, similar

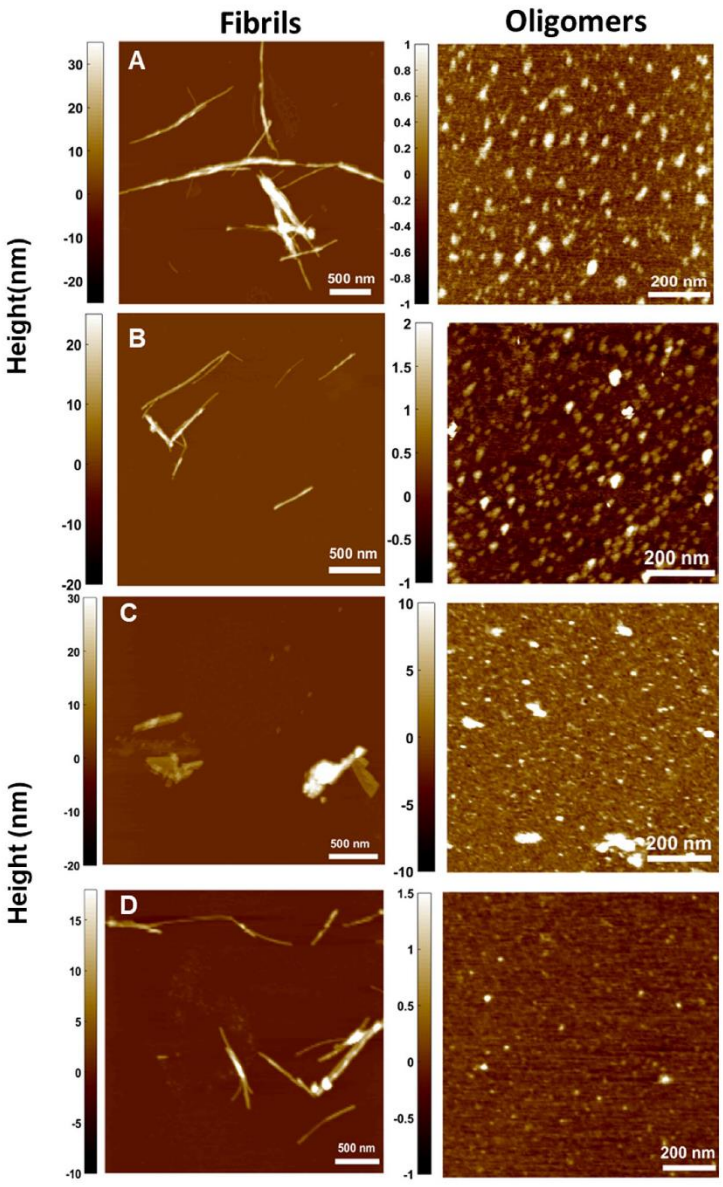

Figure 10. AFM images showing fibrils (left) and oligomers (right) of the insulin samples in the presence of (**A**) Dex-40, (**B**) Dex-10, (**C**) Dxt and (**D**) Cht-AuNPs after 3 h incubation at 65 °C (AuNPs concentration = 100 nM). The color scale on the right represents the height information in nm.

height range comparable to that of monomers were visible, but structurally changed to rather strand-like indicating opening of insulin monomers (Fig. 9B).

Figure 10 shows AFM images of insulin amyloid fibrils in the presence of biopolymer-coated AuNPs. In the presence of both Dex-40/Dex-10-AuNPs, the insulin fibrils were less prominent and became partially shorter and thinner compared to structures observed for insulin alone after 3 h (Fig. 10A,B). Furthermore, a number of oligomers and globular aggregates with an average height ranging between 0.5–2 nm were observed in the presence of Dex-40/Dex-10-AuNPs (Fig. 10A,B), whereas a very few of such oligomers were formed in the case of

insulin amyloid fibrils alone. Interestingly, in the presence of Dxt-AuNPs, very few short and thick fibrils as well as aggregates were found (Fig. 10C).

From the AFM images it can be understood that the effect on fibrils in presence of Dxt-coated AuNPs is less predominant when compared to the same prepared with both Dex-40orDex-10-coated AuNPs. Remarkably, Cht-AuNPs induce thin and short fibrils with a very less amount of oligomers (Fig. 10D). This similar behaviour was also observed in TEM analysis. As depicted in the AFM images, following incubation of insulin with biopolymer-coated AuNPs the height of the fibrils became smaller compared to fibrils formed in the absence of biopolymer-coated AuNPs. The height of insulin fibrils was between 15–20 nm and 10–15 nm in the absence and presence of biopolymer-coated AuNPs, respectively (heights of multiple overlapping fibrils were not considered). The amount of insulin fibril aggregates was significantly predominantly reduced for Dxt/Cht-AuNPs compared to that observed for Dex-40/Dex-10-AuNPs.Overall, biopolymer-coated AuNPs induce shorter fibrillar species, and non-fibrillar aggregates in the insulin sample solutions as compared to the pure insulin fibrils. The obtained results indicate that the surface of biopolymer-coated AuNPs is the main driving factor on insulin amyloid fibrillogenesis.

Proposed model for the inhibition of insulin amyloid fibrils by biopolymer-coated AuNPs. The amyloid fibrils formation is a multi-step process, involving nucleation, growth and proliferation steps[34]. In general, protein monomers in the nucleation period form oligomers/protofilaments first and further undergo protofibril formation followed by elongation to form mature fibrils. The inhibitory activity of biopolymer-coated AuNPs in the insulin amyloid fibril formation is attributed to the interactions between the surface of the AuNPs and insulin monomers during the nucleation period. The basic structure of all amyloid fibrils involves the polypeptide as main chain and is predominantly stabilized by hydrogen bonds. Moreover, it has been shown that the fibril surface is strongly heterogeneous, and their surface is equally distributed with carboxyl, amino and imino groups[35]. We believe that both functional groups and structural properties of the biopolymers (Dex-40/Dex-10/Dxt/Cht) can inhibit amyloid fibril formation. All dextran family molecules (Dex-40/Dex-10/Dxt) are rich in -OH groups, whereas chitosan molecules have both -OH and -NH_2 groups. Moreover, Dex-40 and Dex-10 molecules are branched in nature and Dxt and Cht molecules are linear in nature. Having realised that both biopolymer-coated AuNPs and insulin molecules distribute positive charges over their surface at acidic pH, we suggest that electrostatic repulsion and hydrogen bonding are likely to be responsible for the interactions between insulin and biopolymer-coated AuNPs. Generally, proteins fold into a globular structure in which polypeptide chain and the hydrophobic residues are hidden in the core of the protein. When insulin molecules are exposed to certain denaturing conditions (low pH and high temperature), the peptide backbone is not accessible to form the interchain hydrogen bonds which results in the unfolded structure. At that stage, the surface of the biopolymer-coated AuNPs interacts with the insulin monomers and repels their folded structure to completely unfolded structure. Most probably, at the nucleation stage, both Dxt and Cht-AuNPs strongly interact with the insulin monomers *via* their respective -OH and -NH_2 groups and inhibit the oligomer formation as well as elongation of the protofibrilsand thus,lead to formation of thin and short fibrils. This was supported by the observation of oligomers in the AFM analysis. Moreover, increased intensity of absorption band after fibril formation indicates that both Dxt and Cht-AuNPs particles are quite stable and allow strong interaction with insulin monomers. In another case, Dex-40 and Dex-10-AuNPs undergo self-aggregation which reduces the interaction with insulin monomers and allows the formation of a higher number of oligomers and protofibrils than mature fibrils. This is supported by the aggregation of biopolymer-coated AuNPs in TEM images as well as shift in the absorption band after fibril formation. Although all dextran family molecules have -OH groups, Dxt-AuNPs inhibit insulin amyloid fibrils stronger than Dex-40/Dex10-AuNPs. This could be due to differences in the interaction between biopolymer-coated AuNPs and insulin monomers as they are different in structure (linear and branched). In addition, during the fibrillation process, both Dex-40 and Dex-10-AuNP aggregates interact weakly with insulin monomers as the availability of reactant sites of AuNP aggregates to insulin is lower, whereas the reactant sites for Dxt-AuNPs are higher, leading to inhibition of amyloid fibrillation. When comparing branched-coated AuNPs, Dex-10-AuNPs inhibit insulin amyloid fibrils formation slightly more than Dex-40-AuNPs. This was supported by a higher decrease in the CD signal for Dex-10-AuNPs compared to Dex-40-AuNPs and a slight variation in the fibrils in microscopic imaging analysis. Our results suggest that inhibition of amyloid fibrillation increases as the branching of the polymers decreases.

Scheme 1 shows our proposed interaction mechanism of biopolymer-coated AuNPs in the inhibition of insulin amyloid fibrils.

Cytotoxicity of biopolymer-coatedAuNPs-insulin amyloid fibrils. Proceeding further, we also investigated the toxicity of insulin amyloid fibrils and biopolymer-coated AuNPs-insulin amyloid fibrils on pancreatic (PaTu-T and PaTu-S) and HEK293 cell lines. Figure 11 shows the cell viability after treatment with different biopolymer-coatedAuNPs, insulin amyloid fibrils and AuNP-insulin amyloid fibrils for PaTu-T and PaTu-S cells. Compared to pure insulin amyloid fibrils, all other types of biopolymer-coated AuNPs and AuNP-insulin amyloid fibrils present a lower cytotoxicity. Stronger luminescence signal indicates higher amounts of vital cells. The increased viability for AuNP-insulin amyloid fibrils compared to the insulin amyloid fibrils is due to the formation of fragmented fibrils or filaments which are less toxic to the pancreatic cells than mature fibrils. Similar behaviour was also observed for HEK293 cells (see Fig. S10). Additionally, to avoid any unspecific interactions of fetal bovine serum (FBS) with biopolymer-coated AuNPs, cells were incubated with media without FBS. However, cells incubated without FBS are growing less than those incubated with FBS, most probably due to missing growth factors and other metabolic requirements.

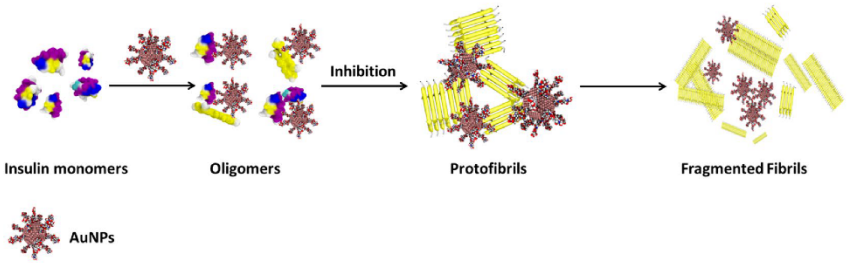

Scheme 1. Schematic representation of inhibition of insulin amyloid fibrils in presence of biopolymer-coated AuNPs.

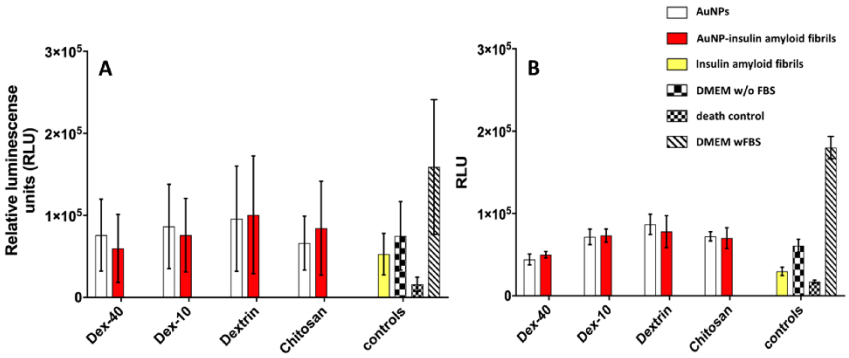

Figure 11. Cytotoxicity results of insulin amyloid fibrils (1 nM, yellow), AuNP (white) and AuNP-insulin amyloid fibrils (red) with PaTu-S (**A**) and PaTu-T (**B**) cells. Error bars correspond to the standard deviation.

Conclusion

We have described the effect of biopolymer-coated AuNPs on the inhibition of insulin amyloid fibrils. Small-sizedAuNPs were prepared using branched and linear biodegradable polymers (Dextran-40, Dextran-10, Dextrin and Chitosan) as stabilizing ligands. We found that the inhibition of insulin fibril formation was dependent on both surface and concentration of biopolymer-coated AuNPs,irrespective of their core sizes. DLS analysis showed a decrease in the diameter of the fibrils in the presence of AuNPs compared to pure insulin amyloid fibrils. UV-Vis analysis indicated the interaction of AuNPs with insulin molecules. Furthermore, CD results demonstrated that the AuNPs strongly inhibit structural changes from α-helix rich to β-sheet structures in a dose-dependent manner, which was further confirmed by ELISA. Shorter and fewer fibrils observed in TEM and AFM images also support the fact that AuNPs inhibit the insulin fibrillation from monomers or oligomers to mature fibrils. Cell cytotoxicity results showed that AuNP-insulin amyloid fibrils are less toxic to pancreatic cells as well as HEK cells compared to treatment with insulin amyloid fibrils alone. Also, a mechanism for the inhibitory activity of AuNPs on the insulin amyloid fibrillation process has been proposed. Overall, linear molecules Dxt- and Cht-AuNPs showed the best inhibitory activity compared to branched Dex-40/Dex-10-AuNPs on insulin amyloid fibrils formation, indicating that the inhibitory activity of AuNPs largely depends on the structure of the ligands as well as functional groups at the surface. Our results suggest that both Dxt- and Cht-AuNPs may be used as therapeutic delivery agents to target the insulin association/aggregation.

Experimental Sections

Materials. Human insulin (molecular weight 5700 Da), 10 nm bare gold NPs, tetrachloroauric acid ($HAuCl_4$), glycine, NaN_3 and dextrin were purchased from Sigma-Aldrich (Taufkirchen, Germany). Chitosan, dextran-40, dextran-10, EtOH, HCl, and NaOH were purchased from Roth (Karlsruhe, Germany). The concentration of insulin was measured spectrophotometrically using a molar extinction coefficient of 5734 $mol^{-1}cm^{-1}$ at 280 nm. All the chemicals were used as received. The water used was purified through an ultrapure water system, Millipore system and Sartorius Stedim Biotech (Göttingen, Germany).

Synthesis of AuNPs functionalized with Dex-40, Dext−10 and Dxt ligands. 200 µl of 19 mM $HAuCl_4$ solution was added to 30 mL of 1 w/v % Dex-40 aqueous solution and the mixture was allowed to stir for 30 min at room temperature (RT). Next, 1.5 mL of 0.05 M NaOH was added to the above solution until colour

changed from yellow to colourless. Then, the solution was heated up to 95–99 °C and kept for 30 min at that temperature. Further, the mixture was allowed to cool to RT and it was then centrifuged at 4 °C, 20 × g for 30 min and the pellet was redispersed in 20 mL deionized water. The AuNPs were washed three times with deionized water to remove any excess of free ligands in the solution. Same protocol was used to coat AuNPs with Dex-10 and Dxt. In the case of Dxt-coated AuNPs, Dxt solution was first heated up to 60 °C to dissolve the ligand and then cooled to RT and the above mentioned synthetic protocol was performed to make the Dxt-AuNPs.

Synthesis of Cht-AuNPs. First, 100 mL of 0.2 w/v % Cht solution was prepared in 1% acetic acid and stirred for 30 min to completely dissolve the Cht molecules. Next, 0.125 M $HAuCl_4$ aqueous solution was added to the above boiling solution and kept stirring for 30 min. After 15 min, the colour of the solution changed from colourless to ruby red. This indicated the formation of the Cht-AuNPs. Afterwards, the mixture was allowed to cool to RT and centrifuged at 4 °C, 20 × g for 30 min and redispersed in 20 mL deionized water. The AuNPs were washed three times with deionized water to remove unbound ligands in solution.

Insulin amyloid fibril formation. Insulin amyloid fibrils were prepared by mixing the solution of human insulin (0.1 mg/mL) with various amounts of biopolymer-coated AuNPs to make different concentrations of AuNPs (50, 100, 200 nM) in the glycine buffer (pH 2.0; 100 mM glycine, 100 mMNaCl, and 1.54 mM NaN_3). Next, the mixtures of insulin-AuNPs sample solutions were incubated for 3 h at 65 °C with a constant stirring at 300 rpm on a stirring plate (Thermo scientific). In order to reduce the possible formation of fibril nuclei in the solution, all insulin samples were freshly prepared prior to each experiment.

UV-Vis absorption spectroscopy. UV-Vis spectra of biopolymer-coated AuNPs and insulin amyloid fibrils with AuNPs were measured using NanoDrop 2000c spectrophotometer (Thermo Scientific, Germany) in a 10 mm path length cuvette (Brand UV cuvettes, Germany) at 25 °C. The spectra were recorded between 200 to 850 nm.

Dynamic light scattering (DLS) and zeta potential measurements. The hydrodynamic diameter (d_H) and the zeta potential for biopolymer-coated AuNPs and insulin amyloid fibrils with the AuNPs were measured using a Zetasizer Nano-ZS (Malvern Instruments, Herrenberg, Germany). Samples were prepared as described above and filtered through a 0.2 µm (for AuNPs) filter followed by equilibration (typically 5 min) at 25 °C. Measurements were taken at detector angle of 173° using a refractive index of 1.45 and absorption about 0.001 for water. Five independent measurements (12 runs per measurement with a run duration of 5 s) were carried out to estimate d_H of the samples, with measurement uncertainty indicated as standard deviation. The zeta potential measurements were carried out at 25 °C with 5 min equilibration between each measurement and a voltage of 50 V using disposal DTS1070 cuvettes using sample dispersions in deionized distilled water (biopolymer-coated AuNPs). The reported zeta potential is an average of five independent measurements of 20 runs (each with duration of 5 s).

Circular Dichroism (CD) spectroscopy measurements. A Chirascan spectrophotometer (Applied Photophysics, Leatherhead, UK) equipped with a thermostatically controlled cell holder (Quantum Northwest, Liberty Lake, USA) was used for CD measurements which were carried out in the region 190 to 260 nm with a bandwidth of 1.0 nm at 25 °C with a speed scan of 15 nm min^{-1} using a 5 mm path length cuvette (Hellma Analytics, Müllheim, Germany). Each CD spectrum represents an average of 5 scans. Each sample, including the insulin alone and samples with insulin and biopolymer-coated AuNPs, was first diluted five times with deionized water, and then subjected to the CD measurement. The final spectra were obtained by subtracting the corresponding AuNPs without insulin contribution from the original spectra.

Enzyme-linked immunosorbent assay (ELISA). Microtiter plates (Capitol Scientific, Austin, USA) were coated with 5 µg/µL of insulin or insulin amyloid fibrils or AuNP-insulin amyloid fibrils (1:10) in a coating buffer (15 mM sodium hydrogen carbonate, pH 9.5 [Merck KGaA, Darmstadt, Germany]) and incubated at 4 °C for 12 h, then washed with washing buffer containing PBS (Merck) with 0.05% Tween 20 (AppliChem, Darmstadt, Germany). After blocking for 2 h with 5% milk powder (Safeway, Calgary, Canada) in PBS at 37 °C, the plate was washed five times with washing buffer and 10 µg/mL of antibodies (mouse anti-Insulin 1 and anti-Insulin 2 [antibodies-online GmbH, Aachen, Germany]) were incubated for 1 h at RT. Plates were washed again five times with washing buffer and 70 ng/mL of the specific peroxidase-coupled antibody (anti-rabbit IgG-HRP and anti-mouse IgG-HRP [Jackson immunoresearch laboratories, West Grove, USA]) was incubated at RT for 45 min. After 5 times washing, the plate was incubated with TMB substrate reagent (3,3′, 5,5′Tetramethylbenzidine; BDBioscience, Heidelberg, Germany) for 5 min at RT. The reaction was stopped by 100 µL 0.5 M H_2SO_4 (CarlRoth, Karlsruhe, Germany) and optical density (OD) was measured at 450 nm with a Tecan (Tecan group, Männedorf, Switzerland) infinite 200 absorbance reader. For evaluation, the values of a blank control, without primary antibodies, were subtracted from the samples.

Transmission electron microscopy (TEM). TEM analysis of AuNPs or AuNP-insulin amyloid fibrils was performed using a negative staining procedure. Samples were allowed to adsorb for 5 min onto a glow-discharged Pioloform carbon-coated 400-mesh grid, which was then transferred onto two droplets of deionized water, and finally for 30 s onto a drop of 1% aqueous uranyl acetate. After blotting with filter paper and air-drying, samples were examined using a transmission electron microscope LEO 906 (Carl Zeiss Microscopy GmbH) at an acceleration voltage of 80 kV. Adobe Photoshop CS6 was used to edit the micrographs.

Atomic force microscopy (AFM). AuNP-insulin amyloid fibrils (20 µl, 2.5 µM) samples were spread on atomically flat muscovite mica sheet (Science Services, Germany,used as substrate) having RMS of ~0.1 nm and was allowed to rest for 60 seconds. Then, the substrate was washed for 15 seconds with deionized water and dried in a laminar flow box (ScanLaf Class 2, LaboGene, Lynge, Denmark). Air imaging was performed using NanoscopeIIIa controller (Veeco/Digital Instruments, Santa Barbara, USA). Images were captured in tapping mode using OMCL-AC160TS (Olympus Corporation, Japan) cantilevers having an approximate curvature radius of 10 nm and a spring constant of 42 N m^{-1}. Data processing of the obtained AFM images were carried out using a home-written MATLAB (The MathWorks, 2010b, Natick, USA) script.

Cytotoxicity assay. The determination of cell viability was performed by the CellTiter-Glo 2.0 assay from Promega (Madison, USA) following manufacturer's instructions. Briefly, 5×10^4 cells/mL were seeded in DMEM media without fetal bovine serum (FBS), to exclude albumin binding to the biopolymer-coated AuNP, and sedimented for 2 h in an opaque walled 96-well plate. After aspiration of media, 1 nM of biopolymer-coated AuNPssolution was added and incubated for 24 h at 37 °C and 5% CO_2. Further, 100 µl of CellTiter-Glo 2.0 was added to the wells and 10 min after incubation, the luminescence signal was measured in a SpectraMax Paradigm (Molecular Devices, San Jose, USA).

Received: 15 February 2020; Accepted: 6 April 2020;
Published online: 12 May 2020

References

1. Dobson, C. M. Protein folding and misfolding. *Nature* **426**, 884–890 (2003).
2. Lansbury, P. T. Jr & Rochet, J. C. Amyloid fibrillogenesis: themes and variations. *Curr. Opin. Struct. Biol.* **10**, 60–68 (2000).
3. Chiti, F. & Dobson, C. M. Protein misfolding, functional amyloid, and human disease. *Annu. Rev. Biochem.* **75**, 333–366 (2006).
4. Dobson, C. M. The Structural Basis of Protein Folding and its Links with Human Disease. *Philos. Trans. R. Soc. Lond. B. Biol. Sci.* **356**, 133–145 (2001).
5. Eisenberg, D. & Jucker, M. The amyloid state of proteins in human diseases. *Cell* **148**, 1188–1203 (2012).
6. Ross, C. A. & Poirier, M. A. Protein aggregation and neurodegenerative disease. *Nat. Med.* **10**, S10–S17 (2004).
7. Dobson, C. M. Principles of protein folding, misfolding and aggregation. *Semin. Cell Dev. Biol.* **15**, 3–16 (2004).
8. Akkermans, C. *et al.* Shear pulses nucleate fibril aggregation. *Food Biophys.* **1**, 144–150 (2006).
9. Giri, K., Bhattacharyya, N. P. & Basak, S. pH-dependent self-assembly of polyalanine peptides. *Biophys. J.* **92**, 293–302 (2007).
10. Lee, G. *et al.* Self-assembled amyloid fibrils with controllable conformational heterogeneity. *Sci Rep* **5**, 16220 (2015).
11. Bowsher, R. R. *et al.* Sensitive RIA for the Specific determination of insulin lispro. *Clin. Chem.* **45**, 104–110 (1999).
12. Brange, J., Andersen, L., Laursen, E. D., Meyn, G. & Rasmussen, E. Toward understanding insulin fibrillation. *J. Pharm. Sci.* **86**, 517–525 (1997).
13. Shikama, Y. *et al.* Localized Amyloidosis at the Site of Repeated Insulin Injection in a Diabetic Patient. *Inter Med.* **49**, 397–401 (2010).
14. Yashdeep, G., Gaurav, S. & Rajiv, S. Insulin-derived amyloidosis. *Indian J. Endocrinol Metab.* **19**, 174–177 (2015).
15. Zraika, S. *et al.* Toxic oligomers and islet beta cell death: guilty by association or convicted by circumstantial evidence? *Diabetologia* **53**, 1046–1056 (2010).
16. Woods, R. J., Alarcon, J., McVey, E. & Pettis, R. J. Intrinsic fibrillation of fast-acting insulin analogs. *J. Diabetes Sci. Technol.* **6**, 265–276 (2012).
17. Linse, S. *et al.* Nucleation of protein fibrillation by nanoparticles. *Proc. Natl. Acad. Sci. USA* **104**, 8691–8696 (2007).
18. Rocha, S. *et al.* Influence of fluorinated and hydrogenated nanoparticles on the structure and fibrillogenesis of amyloid beta-peptide. *Biophys. Chem.* **137**, 35–42 (2008).
19. Murphy, C. J. *et al.* Gold nanoparticles in biology: Beyond toxicity to cellular imaging. *Acc Chem Res.* **41**, 1721–1730 (2008).
20. Tiwari, P. M., Vig, K., Dennis, V. A. & Singh, S. R. Functionalized Gold Nanoparticles and Their Biomedical Applications. *Nanomaterials* **1**, 31–63 (2011).
21. Sardar, S., Pal, S., Maity, S., Chakraborty, J. & Halder, U. C. Amyloid fibril formation by beta-lactoglobulin is inhibited by gold nanoparticles. *Int. J. Biol. Macromol.* **69**, 137–145 (2014).
22. Moore, K. A. *et al.* Influence of gold nanoparticle surface chemistry and diameter upon Alzheimer's disease amyloid-β protein aggregation. *J. Biol. Eng.* **11**, 5 (2017).
23. Gao, G. *et al.* The size-effect of gold nanoparticles and nanoclusters in the inhibition of amyloid-β fibrillation. *Nanoscale* **9**, 4107–4113 (2017).
24. Elbassal, E. A. *et al.* Gold Nanoparticles as a Probe for Amyloid-β Oligomer and Amyloid Formation. *J. Phys. Chem. C.* **121**, 20007–20015 (2017).
25. Wang, Y., Zhan, L. & Huang, C. Z. One-pot preparation of dextran-capped gold nanoparticles at room temperature and colorimetric detection of dihydralazine sulfate in uric samples. *Anal. Methods.* **2**, 1982–1988 (2010).
26. Bhumkar, D. R., Joshi, H. M., Sastry, M. & Pokharkar, V. B. Chitosan Reduced Gold Nanoparticles as Novel Carriers for Transmucosal Delivery of Insulin. *Pharm Res.* **24**, 1415–1426 (2007).
27. Meesaragandla, B. *et al.* H-Bonding-mediated binding and charge reorganization of proteins on gold nanoparticles. *Phys. Chem. Chem. Phys.* **22**, 4490–4500 (2020).
28. Sotnikov, D. V., Berlina, A. N., Ivanov, V. S., Zherdev, A. V. & Dzantiev, B. B. Adsorption of proteins on gold nanoparticles: One or more layers? *Colloids Surf. B: Biointerfaces* **173**, 557–563 (2019).
29. Underwood, S. & Mulvaney, P. Effect of the solution refractive-index on the color of gold colloids. *Langmuir* **10**, 3427–3430 (1994).
30. Xing, H. *et al.* Hierarchical Assembly of Nanostructured Coating for siRNA-Based Dual Therapy of Bone Regeneration and Revascularization. *Biomaterials* **235**, 119784 (2020).
31. Lu, N. H. *et al.* Examining the effects of dextran-based polymer-coated nanoparticles on amyloid fibrillogenesis of human insulin. *Colloids Surf B Biointerfaces.* **172**, 674–683 (2018).
32. Nie, R. Z., Zhu, W., Peng, J. M., Ge, Z. Z. & Li, C. M. A-type dimeric epigallocatechin-3-gallate (EGCG) is a more potent inhibitor against the formation of insulin amyloid fibril than EGCG monomer. *Biochimie.* **125**, 204–212 (2016).
33. Wang, S. S. S., Liu, K. N. & Han, T. C. Amyloid fibrillation and cytotoxicity of insulin are inhibited by the amphiphilic surfactants. *Biochimica et Biophysica Acta* **1802**, 519–530 (2010).
34. Buell, A. K. The growth of amyloid fibrils: rates and mechanisms. *Biochemical Journal* **476**, 2677–2703 (2019).
35. Kurouski, D., Gaudig, T. D., Deckert, V. & Lednev, I. K. Structure and composition of insulin fibril surfaces probed by TERS. *J. Am. Chem. Soc.* **134**, 13323–13329 (2012).

Acknowledgements

We acknowledge Dr. Rabea Schlüter (University of Greifswald) and Dr. Isabel García (CIC biomaGUNE) for TEM analyses and Dr. Ulrich Weiß (University Medicine Greifswald) for providing the human cell lines. We thank Norman Geist for creating Scheme 1. This work was financially supported by the German Federal Ministry of Education and Research (BMBF) within the project NanoImmun (FKZ03Z22C51).

Author contributions

B.M. designed and carried out most of the experiments. S.K. carried out AFM measurements, AFM data analysis and prepared AFM figures. U.J. carried out ELISA and cytotoxicity experiments, data analysis and prepared figures summarising the ELISA and cytotoxicity results. B.M. and M.D. designed the study and wrote the main manuscript text. All authors reviewed the manuscript.

Competing interests

The authors declare no competing interests.

Additional information

Supplementary information is available for this paper at https://doi.org/10.1038/s41598-020-64010-7.

Correspondence and requests for materials should be addressed to M.D.

Reprints and permissions information is available at www.nature.com/reprints.

Publisher's note Springer Nature remains neutral with regard to jurisdictional claims in published maps and institutional affiliations.

Supplementary Information

Biopolymer-coated gold nanoparticles inhibit human insulin amyloid fibrillation

Brahmaiah Meesaragandla,[1,2] Sanjai Karanth,[1,2] Una Janke,[1,2] and Mihaela Delcea[1,2,3]*

[1]*Institute of Biochemistry, University of Greifswald, Felix-Hausdorff-Straße 4, 17489 Greifswald, Germany*

[2]*ZIK HIKE - Zentrum für Innovationskompetenz „Humorale Immunreaktionen bei kardiovaskulären Erkrankungen", Fleischmannstraße 42, 17489 Greifswald, Germany*

[3]*DZHK (Deutsches Zentrum für Herz-Kreislauf-Forschung), partner site Greifswald, Germany*

*Corresponding author, delceam@uni-greifswald.de

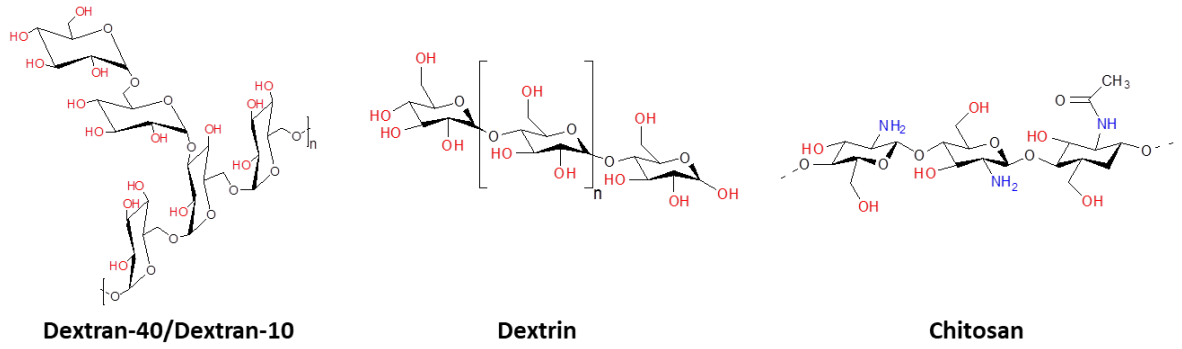

Figure S1. Chemical structures of Dex-40, Dex-10, Dxt and Cht molecules.

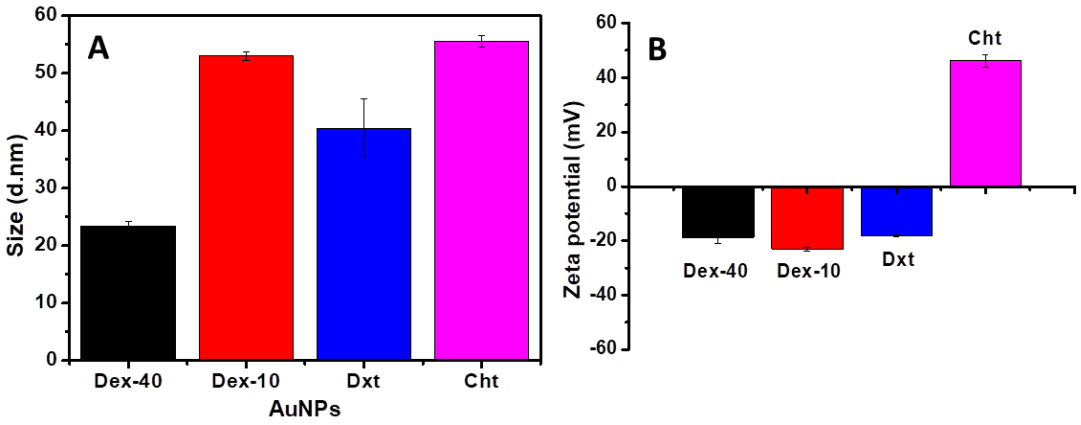

Figure S2. DLS (A) and zeta potential (B) data of AuNPs coated with Dex-40 (black), Dex-10 (red), Dxt (blue) and Cht (magenta) ligands.

Table S1. Surface plasmon resonance (SPR) peak position and size from TEM analysis for AuNPs coated with different ligands.

AuNPs	SPR (nm)	TEM (nm)
Dex-40	519	8.7 ± 0.6
Dex-10	528	13.5 ± 2.0
Dxt	527	6.3 ± 2.1
Cht	528	23.6 ± 5.8

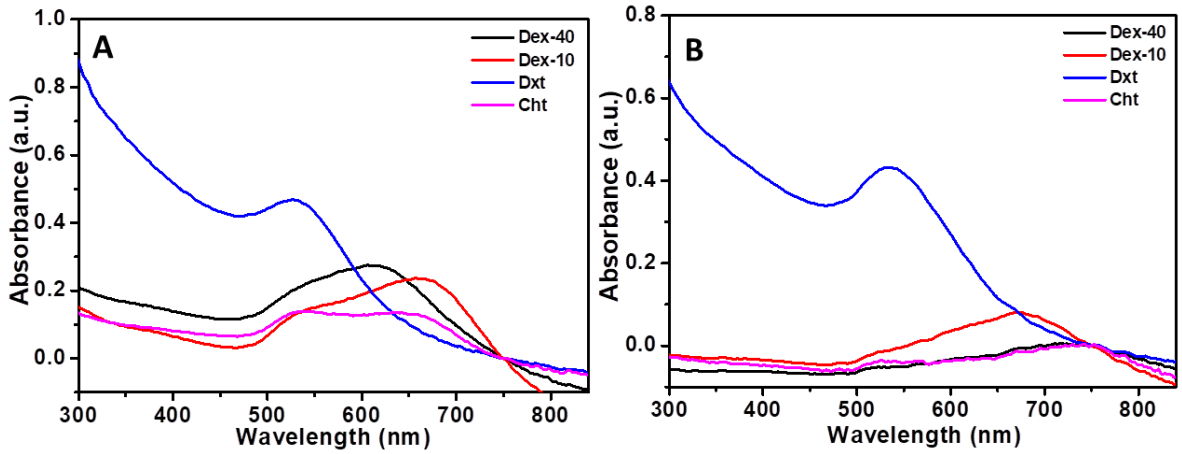

Figure S3. UV-Vis spectra of different biopolymer-coated AuNPs in glycine buffer A) before and B) after 3 h incubation at 65 °C (100 nM AuNPs).

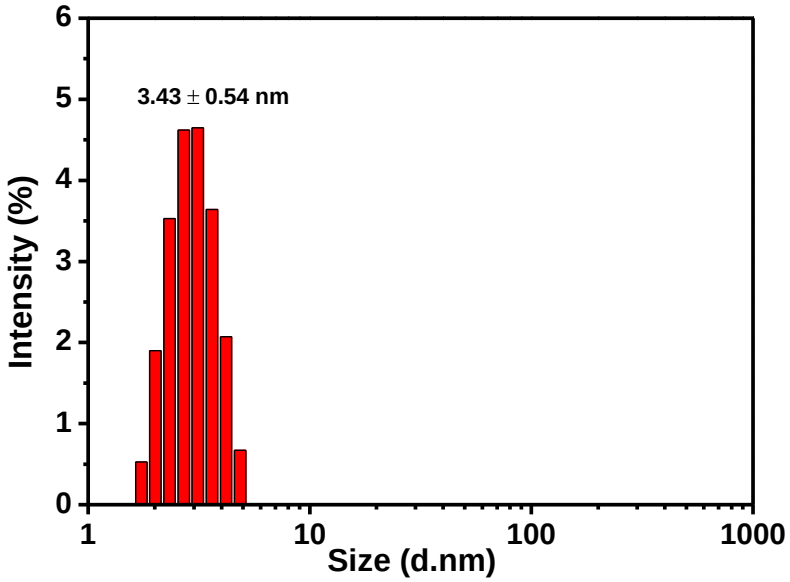

Figure S4. DLS data showing the size of pure insulin in glycine buffer before incubation at 65 °C.

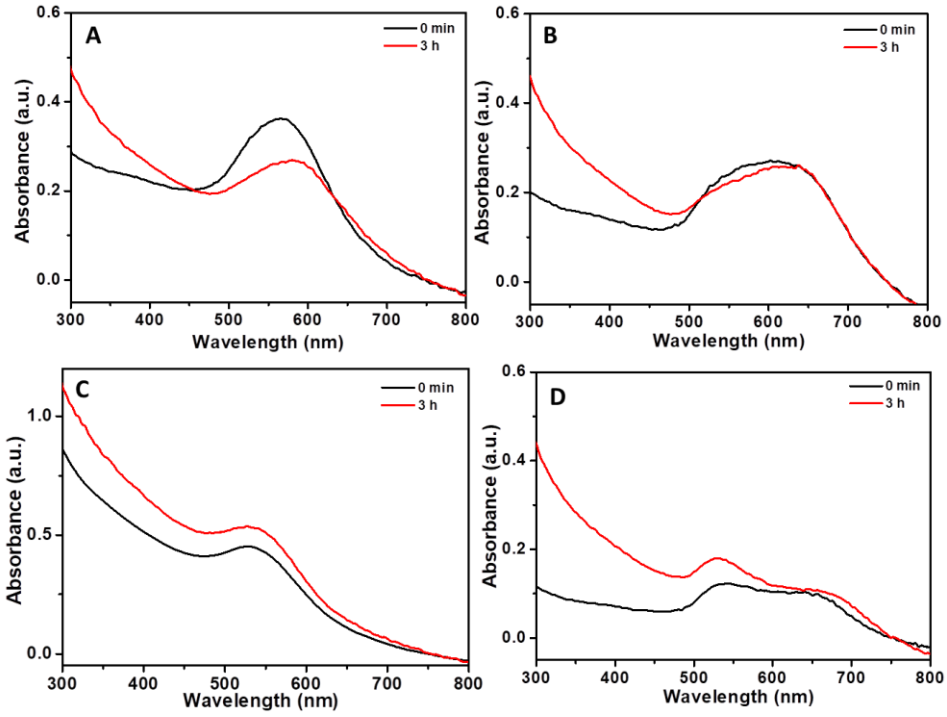

Figure S5. UV-Vis spectra of insulin amyloid fibrils in presence of A) Dex-40, B) Dex-10, C) Dxt, and D) Cht-AuNPs in glycine buffer before and after incubation at 65 °C for 3h (100 nM AuNPs).

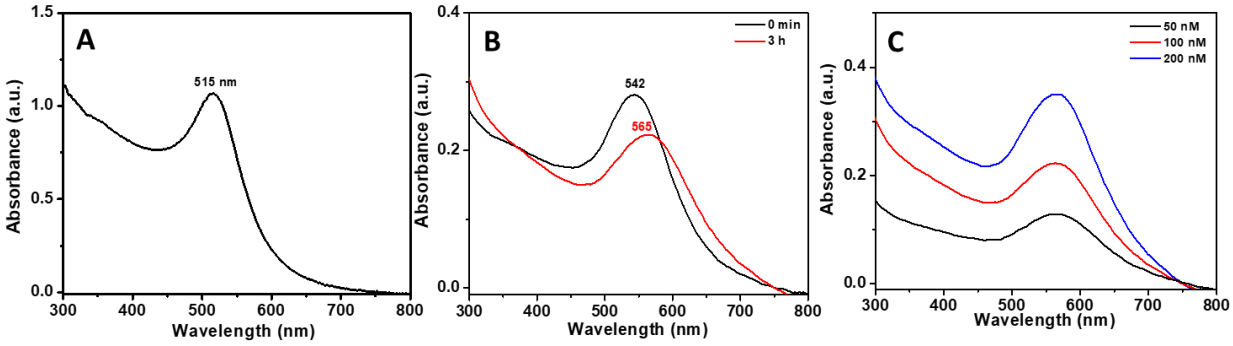

Figure S6: UV-Vis spectra of (A) bare AuNPs, (B) AuNPs (100 nM) in the presence of insulin amyloid fibrils, (C) AuNPs (50, 100, 200 nM) in the presence of insulin amyloid fibrils after 3 h incubation at 65 °C.

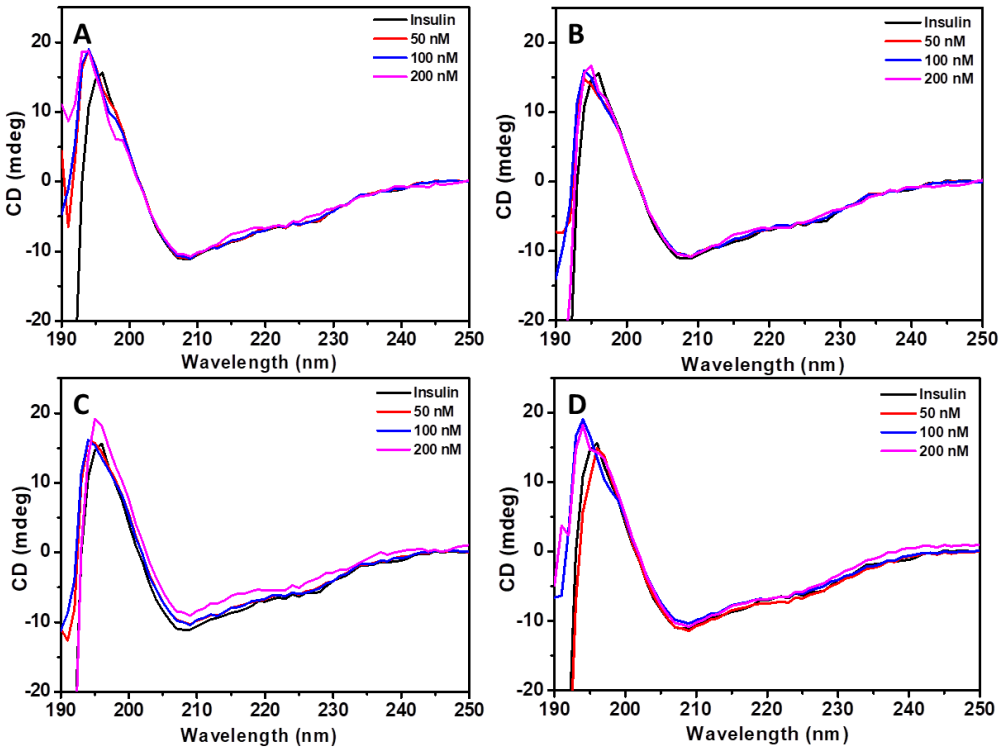

Figure S7: CD spectra of pure insulin and same in the presence of different polymer-coated AuNPs with various concentrations before incubation. A) Dex-40-AuNPs, B) Dex-10-AuNPs, C) Dxt-AuNPs and D) Cht-AuNPs.

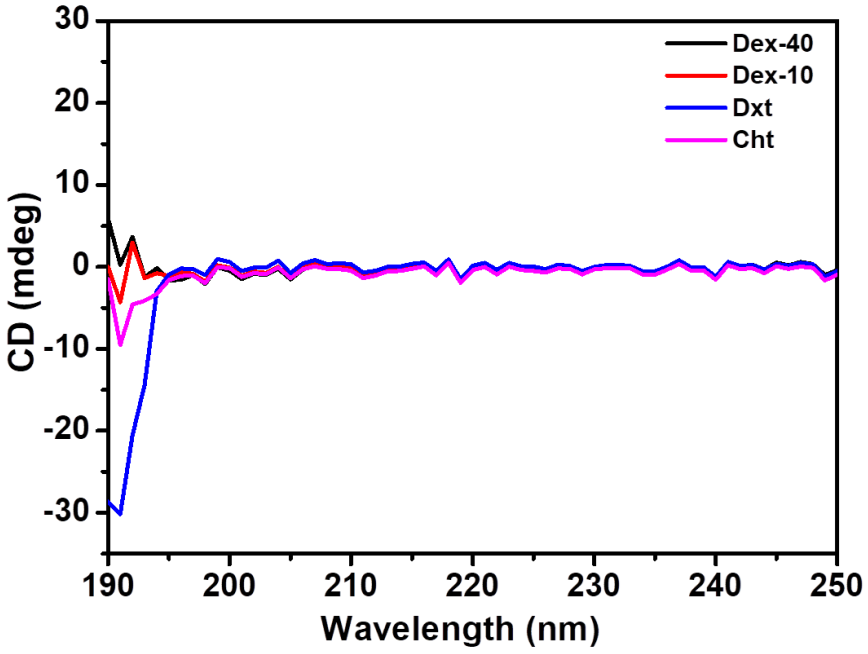

Figure S8: CD spectra of different polymer-coated AuNPs.

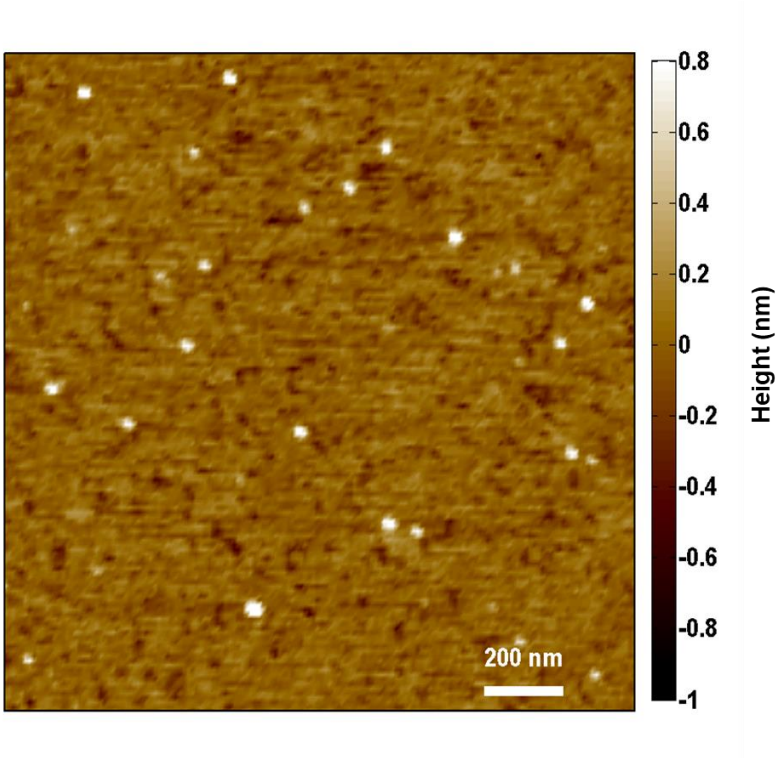

Figure S9. AFM image of pure insulin monomers before incubation.

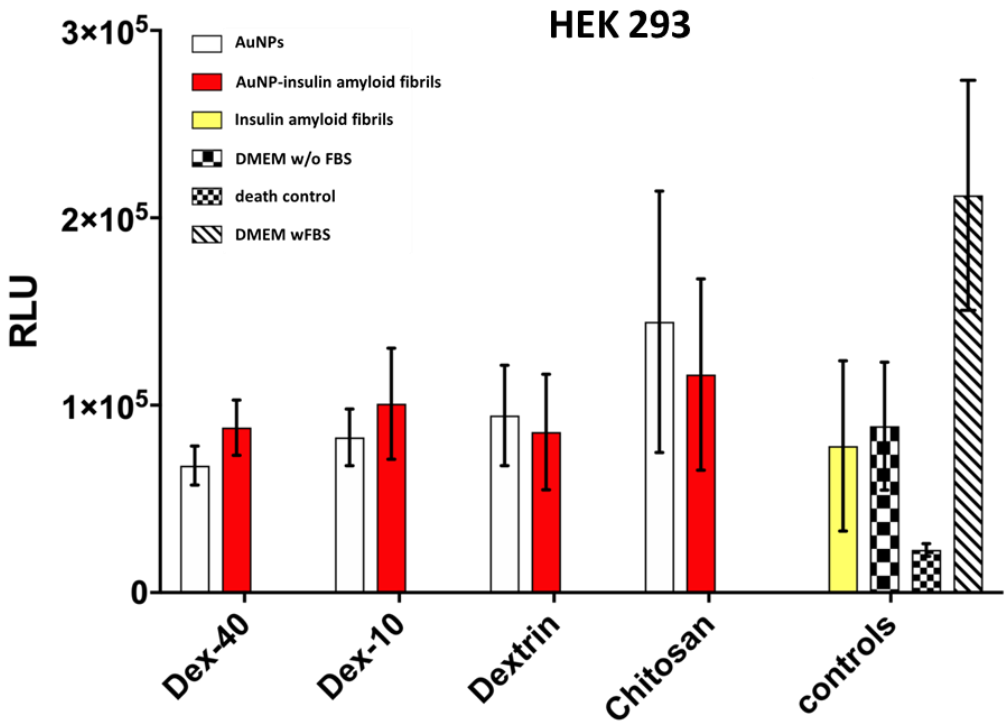

Figure S10: Cytotoxicity effect of different coated AuNPs, insulin amyloid fibrils, and AuNP-insulin amyloid fibrils on HEK293 cells. Error bars correspond to the standard deviation.

7. Appendix

7.1 MATLAB scripts

Script in ***Section 1*** was written by Sanjai Karanth.

Scripts in ***Section 2*** was originally written by Dr. Peter Nestler, University of Greifswald. Parts of the script were modified as per requirements.

Section 1: Determination of peak rupture forces

```
clear all;
clc;
```

Combining all text files and obtaining rupture forces in single column

```
pwd= cd('E:\Measurements\AFM\JPK\NDs_NO\smFS\20190723\RGD_itg_NDs\processed');
txtfiles=dir('*.tsv'); %List all text files in directory
S_name='Proteonanodiscs_20190723';

force=[];
for k=1:length(txtfiles)
    fname=txtfiles(k,1).name;
    fid = fopen(fname,'r');
    data{k} = textscan(fid, '%s%f%f%f%f%s%f%f%f%f%f%f%f','HeaderLines',1);
    for i=1:k
      data_temp{i}=data{1,i}{1,10};
    end
    for i=1:k
      force=[force; data_temp{i}];

    end
    fclose(fid);
end


rupture_force=force(force >= 80.0e-12 & force <= 500.0e-12); % threshold force levels determined by accounting the background values including control. Maximum value indicates the force required to break a covalent bond
```

Kernel density estimation (KDE) and Cumulative density function(CDF)

```
nbins = 100; % for histogram
[bandwidth,density,xmesh,cdf] = kde(rupture_force); %Calling function
k_density=density/max(density);

% Data output
figure;
```

```
[n,h] = hist(rupture_force,nbins); % 'n' refers to counts and 'h' refers to centers
%bar(h,n/sum(n)/abs(h(2)-h(1)),'b','EdgeColor','k')
hold on
plot(xmesh,k_density,'r','LineWidth',1.5);
ylabel('Probability density', 'FontSize', 18);
xlabel('Rupture force (N)', 'FontSize', 18);
legend('Proteonanodiscs','Fontsize',14);
set (gca,'Fontsize',16);

% figure; %% Plotting CDF (OPTIONAL)
%
% subplot(1,2, 1);
% bar(h,n);
% legend('Histogram','FontSize', 14);
% ylabel('Counts', 'FontSize', 18);
% xlabel('Rupture force (N)', 'FontSize', 18);
% set (gca,'Fontsize',16);
%
% hold on
% subplot(1,2, 2);
% plot(xmesh,cdf,'g','LineWidth',1.5);
% legend('Proteonanodiscs','FontSize', 14);
% ylabel('Percentage rupture force', 'FontSize', 18);
% xlabel('Rupture force (N)', 'FontSize', 18);
% set (gca,'Fontsize',16);
```

Saving data

```
save(S_name,'rupture_force','xmesh','density','cdf');
```

```
function [bandwidth,density,xmesh,cdf]=kde(rupture_force,n,MIN,MAX)
%       Gaussian kernel is assumed and the bandwidth is chosen automatically;
% OUTPUTS:
%   bandwidth - the optimal bandwidth (Gaussian kernel assumed);
%     density - column vector of length 'n' with the values of the density
%               estimate at the grid points;
%     xmesh   - the grid over which the density estimate is computed;
%             - If no output is requested, then the code automatically   plots a graph of the density
estimate.
%       cdf  - column vector of length 'n' with the values of the cdf
%  Reference:
% Kernel density estimation via diffusion
% Z. I. Botev, J. F. Grotowski, and D. P. Kroese (2010)
% Annals of Statistics, Volume 38, Number 5, pages 2916-2957.

rupture_force=rupture_force(:); %make data a column vector
if nargin<2 % if n is not supplied switch to the default
```

```
    n=2^14;
end
n=2^ceil(log2(n)); % round up n to the next power of 2;
if nargin<4 %define the default  interval [MIN,MAX]
    minimum=min(rupture_force); maximum=max(rupture_force);
    Range=maximum-minimum;
    MIN=minimum-Range/2; MAX=maximum+Range/2;
end
% set up the grid over which the density estimate is computed;
R=MAX-MIN; dx=R/(n-1); xmesh=MIN+[0:dx:R]; N=length(unique(rupture_force));
%bin the data uniformly using the grid defined above;
initial_data=histc(rupture_force,xmesh)/N;  initial_data=initial_data/sum(initial_data);
a=dct1d(initial_data); % discrete cosine transform of initial data
% now compute the optimal bandwidth^2 using the referenced method
I=[1:n-1]'.^2; a2=(a(2:end)/2).^2;
% use  fzero to solve the equation t=zeta*gamma^[5](t)
t_star=root(@(t)fixed_point(t,N,I,a2),N);
% smooth the discrete cosine transform of initial data using t_star
a_t=a.*exp(-[0:n-1]'.^2*pi^2*t_star/2);
% now apply the inverse discrete cosine transform
if (nargout>1)|(nargout==0)
    density=idct1d(a_t)/R;
end
% take the rescaling of the data into account
bandwidth=sqrt(t_star)*R;
density(density<0)=eps; % remove negatives due to round-off error
if nargout==0
    figure(1), plot(xmesh,density)
end
% for cdf estimation
if nargout>3
    f=2*pi^2*sum(I.*a2.*exp(-I*pi^2*t_star));
    t_cdf=(sqrt(pi)*f*N)^(-2/3);
    % now get values of cdf on grid points using IDCT and cumsum function
    a_cdf=a.*exp(-[0:n-1]'.^2*pi^2*t_cdf/2);
    cdf=cumsum(idct1d(a_cdf))*(dx/R);
    % take the rescaling into account if the bandwidth value is required
    bandwidth_cdf=sqrt(t_cdf)*R;
end

end
%###################################################################
function  out=fixed_point(t,N,I,a2)
% this implements the function t-zeta*gamma^[l](t)
l=7;
f=2*pi^(2*l)*sum(I.^l.*a2.*exp(-I*pi^2*t));
for s=l-1:-1:2
    K0=prod([1:2:2*s-1])/sqrt(2*pi);  const=(1+(1/2)^(s+1/2))/3;
    time=(2*const*K0/N/f)^(2/(3+2*s));
    f=2*pi^(2*s)*sum(I.^s.*a2.*exp(-I*pi^2*time));
```

```
end
out=t-(2*N*sqrt(pi)*f)^(-2/5);
end
%###################################################################
function out = idct1d(rupture_force)
% computes the inverse discrete cosine transform
[nrows,ncols]=size(rupture_force);
% Compute weights
weights = nrows*exp(i*(0:nrows-1)*pi/(2*nrows)).';
% Compute x tilde using equation (5.93) in Jain
rupture_force = real(ifft(weights.*rupture_force));
% Re-order elements of each column according to equations (5.93) and
% (5.94) in Jain
out = zeros(nrows,1);
out(1:2:nrows) = rupture_force(1:nrows/2);
out(2:2:nrows) = rupture_force(nrows:-1:nrows/2+1);
%   Reference:
%      A. K. Jain, "Fundamentals of Digital Image
%      Processing", pp. 150-153.
end
%###################################################################
function rupture_force=dct1d(rupture_force)
% computes the discrete cosine transform of the column vector data
[nrows,ncols]= size(rupture_force);
% Compute weights to multiply DFT coefficients
weight = [1;2*(exp(-i*(1:nrows-1)*pi/(2*nrows))).'];
% Re-order the elements of the columns of x
rupture_force = [ rupture_force(1:2:end,:); rupture_force(end:-2:2,:) ];
% Multiply FFT by weights:
rupture_force= real(weight.* fft(rupture_force));
end

function t=root(f,N)
% try to find smallest root whenever there is more than one
N=50*(N<=50)+1050*(N>=1050)+N*((N<1050)&(N>50));
tol=10^-12+0.01*(N-50)/1000;
flag=0;
while flag==0
   try
      t=fzero(f,[0,tol]);
      flag=1;
   catch
      tol=min(tol*2,.1); % double search interval
   end
   if tol==.1 % if all else fails
      t=fminbnd(@(x)abs(f(x)),0,.1); flag=1;
   end
end
end
```

Section 2: Determining height profiles from AFM images

```
clear all
close all
```

Importing text files from Nanoscope IIIa controller machine

```
DirName  = 'E:\Measurements\AFM\JPK\20181011\processed';
FileName = 'sk181011_nanodisc.001';
[AFMdata_Ch1 , AFMdata_Ch2 , N , ScanSize , ScanDate , ScanRate , CaptureDirection] =
ModReadVeeco(DirName,FileName);
close
MinMaxPlot = [-4.0 5.0];
afm_topo = AFMdata_Ch1;
```

Data levelling and background substitution. Use of below options varies for every image and are used accordingly.

```
PlanePara  = [];
[afm_topo,PlanePara] = ModPlanefit(DirName,FileName,afm_topo,PlanePara,MinMaxPlot);
%Plane fit the image
close

LineMedian = [];
[afm_topo,LineMedian]                                                    =
ModLineMedian(DirName,FileName,afm_topo,LineMedian,MinMaxPlot); %Median based
subtraction
close

MinMaxFlatten = [NaN 2]; %Image flattening
PolyDegree = 2;
PolyPara = [];
[afm_topo,PolyPara]                                                      =
ModFlatten(DirName,FileName,afm_topo,PolyDegree,PolyPara,MinMaxFlatten,MinMaxPlo
t);
close

ScarLine = [];
[afm_topo,ScarLine]                                                      =
ModExludeScars(DirName,FileName,afm_topo,MinMaxPlot,ScarLine); %remove any lines
obtained due to change in drive amplitude etc.
close

ROI    =    [3391.89189189189,3545.04504504505,1594.59459459460,1441.44144144144];
%Values in pixels
[afm_topo,N,ScanSize,ROI]                                                =
ModSelectROI(DirName,FileName,afm_topo,ROI,MinMaxPlot);    %selecting    region    of
interest for highlighting specific onservations
close
```

```
RMS = sqrt(mean(mean( ( afm_topo - mean(mean(afm_topo)) ).^2 )));   % Surface roughness of the image
```

Obtaining height profiles

```
NumberSections = 1;  % To highlight the cross-sections in the image. Can be either 1, 2 or 3.
SectionVector = [1229.50000000000,433.300000000000;1468.20000000000,91.9000000000000];     %Values in pixels
[SectionData,SectionVector] = ModPlotSection(DirName,FileName,afm_topo,NumberSections,MinMaxPlot,SectionVector);
```

Used only if the background image is very uneven depending on the substrate (Optional)

```
Iterations = 1;                % Number of smoothing iterations
[afm_topo_Smooth] = ModSmooth3x3(DirName,FileName,afm_topo,MinMaxPlot,Iterations);
close;
```

Statistical analysis from image (optional)

```
Threshold = 2.5;       % determined by the surface roughness or from the control images to differentiate heterogenous samples. Values in nm.
GridSize  = 3;       % scan afm_topo with sqaure matrix. Values in pixels
[MaximaPosition,MaximaNumber] = ModLocateMaxima(DirName,FileName,afm_topo_Smooth,Threshold,GridSize,MinMaxPlot);
height_sort=sort(MaximaPosition(:,5));
lpd_bi_ht=height_sort(height_sort >= 3.75 & height_sort <= 6.0); %height of DMPC lipid bilayer (nm) as per Enders et al 2004 & Charrier et al 2005
mean_lpd_bi_ht=mean(lpd_bi_ht); SD_lpd_bi_ht=std(lpd_bi_ht);

ModPrint(DirName,FileName);
```

```
function [afm_topo,PlanePara] = ModPlanefit(DirName,FileName,afm_topo,PlanePara,MinMaxPlot);
N = load(strcat(DirName,'\',FileName,'.mat'),'N');
N = getfield(N,'N');

ScanSize = load(strcat(DirName,'\',FileName,'.mat'),'ScanSize');
ScanSize = getfield(ScanSize,'ScanSize');

if and( length(PlanePara) == 3 , sum(isnan(PlanePara)) == 0 )          % pr?ft, ob PanePara bereits vorgegeben ist
   isPlanePara = 1;
else
   isPlanePara = 0;
```

```
end
TopoFlatten = [];

if isPlanePara

   for laufvar = 1:N(2)
      TopoFlatten(laufvar,:) = afm_topo(laufvar,:) - polyval( [PlanePara(1) 0] , [1:N(1)] );
   end

   for laufvar = 1:N(1)
      TopoFlatten(:,laufvar) = TopoFlatten(:,laufvar) - polyval( [PlanePara(2) 0] , (1:N(2))' );
   end;

   TopoFlatten  = TopoFlatten - PlanePara(3);                    % Substrat als H?he Null
definieren

% Histogramm erstellen; Maximum des Histogramms als Offset subtrahieren

   MinTopo = min(min(TopoFlatten));
   MaxTopo = max(max(TopoFlatten));
   HistIndex = linspace(floor(MinTopo*10)/10,ceil(MaxTopo*10)/10,100);     % 100 Bins zw.
minamalem & maximalem H?henwert (auf- bzw. abgerunded auf 0.2 nm)
   HistData = histc(reshape(TopoFlatten,1,[]) , HistIndex);

else

% mittlere xy-Ebene von afm_topo subtrahieren

   PolyPara = [];

   for laufvar = 1:N(2)
      IndexNumLine = find( ~isnan(afm_topo(laufvar,:)) );                    % Ignoriert
NaN-Werte
      PolyPara(laufvar,:) = polyfit( IndexNumLine , afm_topo(laufvar,IndexNumLine) , 1 );
   end

   for laufvar = 1:N(2)
      TopoFlatten(laufvar,:) = afm_topo(laufvar,:) - polyval( [median(PolyPara(:,1)) 0] ,
[1:N(1)] );
   end

   PlanePara(1) = median(PolyPara(:,1));

   PolyPara = [];

   for laufvar = 1:N(1)
      IndexNumLine = find( ~isnan(afm_topo(:,laufvar)) );
      PolyPara(laufvar,:) = polyfit( IndexNumLine , afm_topo(IndexNumLine,laufvar) , 1 );
   end
```

```
   for laufvar = 1:N(1)
      TopoFlatten(:,laufvar) = TopoFlatten(:,laufvar) - polyval( [median(PolyPara(:,1)) 0] , (1:N(2))' );
   end;

   PlanePara(2) = median(PolyPara(:,1));

% Histogramm erstellen; Maximum des Histogramms als Offset subtrahieren

   MinTopo = min(min(TopoFlatten));
   MaxTopo = max(max(TopoFlatten));
   HistIndex = linspace(floor(MinTopo*10)/10,ceil(MaxTopo*10)/10,100);     % 100 Bins zw. minamalem & maximalem H?henwert (auf- bzw. abgerunded auf 0.2 nm)

   HistData = histc(reshape(TopoFlatten,1,[]) , HistIndex);

   [maxValue, maxIndex] = max(HistData);
   SubstratShift = HistIndex(maxIndex);                    % Substratoberfl?che = Max. im Histogramm

   HistIndex     = HistIndex - SubstratShift;                    % Substrat als H?he Null definieren
   TopoFlatten  = TopoFlatten - SubstratShift;                    % Substrat als H?he Null definieren

   PlanePara(3) = SubstratShift;

end

afm_topo = TopoFlatten;
figure('unit','normalized','outerposition',[0.1,0.02,0.82,0.82])
fig1 = subplot(1,3,[1 2]);
hold on

surf( (0:N(1)-1)/N(1)*ScanSize(1) , (0:N(2)-1)/N(2)*ScanSize(2) , afm_topo);

plot(                [0:N(1)-1]*ScanSize(1)/N(1)                ,                0*ones(N(1),1) ,'k.','MarkerSize',2,'ZData',0*ones(N(1),1));    % schwarze Linie an unterer Kante
plot(                0*ones(N(2),1)                ,                [0:N(2)-1]*ScanSize(2)/N(2) ,'k.','MarkerSize',2,'ZData',0*ones(N(2),1));    % schwarze Linie an linker Kante

hold off

axis([0 ScanSize(1) 0 ScanSize(2)]);
xlabel('X distance [nm]','FontSize',14);
ylabel('Y distance [nm]','FontSize',14);
set(gcf,'Color',[1 1 1])

shading interp;
% colormap('gray');
```

```
load('ColormapRust','CmapRust')
set(gcf,'Colormap',CmapRust)

ChildFig  = get(gcf,'Children');
AxisLimit = get(ChildFig(1),'CLim');
IsMinMaxPlot = whos('MinMaxPlot');
if ~isempty(IsMinMaxPlot); if ~isnan(MinMaxPlot(1)); AxisLimit(1) = MinMaxPlot(1); end;
end
if ~isempty(IsMinMaxPlot); if ~isnan(MinMaxPlot(2)); AxisLimit(2) = MinMaxPlot(2); end;
end
set(ChildFig(1),'CLim',[min(AxisLimit) max(AxisLimit)])
CBarHandle = colorbar;
CBarHandle = ylabel(CBarHandle,'Height [nm]','FontSize',14,'Rotation',270);
CBarPos = get(CBarHandle,'Position');
set(CBarHandle,'Position',[1.5*CBarPos(1) CBarPos(2) CBarPos(3)]);
clear('CBarHandle','CBarPos')
pbaspect([ScanSize(1) ScanSize(2) 1])                    % L□nge von x- und y-Achse dem
gescannten Bildbereich anpassen
set(fig1,'FontSize',14);
box on
view(0,90);

fig2 = subplot(1,3,3);
hold on
bar( HistIndex , log10(HistData) ,'b')
hold off

ChildFig  = get(gcf,'Children');
AxisLimitY = get(ChildFig(1),'YLim');

hold on
plot([min(AxisLimit),min(AxisLimit)],[0 max(AxisLimitY)],'g-')
plot([max(AxisLimit),max(AxisLimit)],[0 max(AxisLimitY)],'g-')
hold off


% set(ChildFig(1),'XLim',[min(AxisLimit) max(AxisLimit)])
axis([min(HistIndex) max(HistIndex) 0 max(AxisLimitY)]);
% axis 'auto y'
xlabel('Height [nm]','FontSize',14);
ylabel('log( Counts )','FontSize',14);
box on
set(fig2,'FontSize',14);
set(fig2,'LineWidth',1.2);
```

Output Parameter-Data saving: afm_topo

```
SaveData = struct('afm_topo',afm_topo,'PlanePara',PlanePara);
save(strcat(DirName,'\',FileName,'.mat'),'-struct','SaveData','-append');
end
```

```
function [afm_topo,LineMedian] =
ModLineMedian(DirName,FileName,afm_topo,LineMedian,MinMaxPlot);
N = load(strcat(DirName,'\',FileName,'.mat'),'N');
N = getfield(N,'N');

ScanSize = load(strcat(DirName,'\',FileName,'.mat'),'ScanSize');
ScanSize = getfield(ScanSize,'ScanSize');

if and( size(LineMedian,1) == N(2) , sum(isnan(LineMedian)) == 0 )  % pr?ft, ob
LineMedian bereits vorgegeben ist
   isLineMedian = 1;
else
   isLineMedian = 0;
end
if isLineMedian

   for laufvar = 1:N(2)
      TopoLineMedian(laufvar,:) = afm_topo(laufvar,:) - LineMedian(laufvar);
   end

else

% von jeder Linie den Median bestimmen und als Offset von der Linie substrahieren

   for laufvar = 1:N(2)
      IndexNumLine = find( ~isnan(afm_topo(laufvar,:)) );  % Ignoriert
NaN-Werte
      LineMedian(laufvar) = median( afm_topo(laufvar,IndexNumLine) );
      TopoLineMedian(laufvar,:) = afm_topo(laufvar,:) - LineMedian(laufvar);
   end

   LineMedian = LineMedian';  % Spaltenvektor

end


MinTopo = min(min(TopoLineMedian));
MaxTopo = max(max(TopoLineMedian));
HistIndex = linspace(floor(MinTopo*10)/10,ceil(MaxTopo*10)/10,100);  % 100 Bins zw.
minamalem & maximalem H?henwert (auf- bzw. abgerunded auf 0.2 nm)

HistData = histc(reshape(TopoLineMedian,1,[]) , HistIndex);

afm_topo = TopoLineMedian;
figure('unit','normalized','outerposition',[0.1,0.02,0.82,0.82])
fig1 = subplot(1,3,[1 2]);
hold on

surf( (0:N(1)-1)/N(1)*ScanSize(1) , (0:N(2)-1)/N(2)*ScanSize(2) , afm_topo);
```

```
plot(                [0:N(1)-1]*ScanSize(1)/N(1)                ,                0*ones(N(1),1)
,'k.','MarkerSize',2,'ZData',0*ones(N(1),1));   % schwarze Linie an unterer Kante
plot(                0*ones(N(2),1)                ,                [0:N(2)-1]*ScanSize(2)/N(2)
,'k.','MarkerSize',2,'ZData',0*ones(N(2),1));   % schwarze Linie an linker Kante

hold off

axis([0 ScanSize(1) 0 ScanSize(2)]);
xlabel('X distance [nm]','FontSize',14);
ylabel('Y distance [nm]','FontSize',14);
set(gcf,'Color',[1 1 1])

shading interp;
% colormap('gray');
load('ColormapRust','CmapRust')
set(gcf,'Colormap',CmapRust)

ChildFig  = get(gcf,'Children');
AxisLimit = get(ChildFig(1),'CLim');
IsMinMaxPlot = whos('MinMaxPlot');
if ~isempty(IsMinMaxPlot); if ~isnan(MinMaxPlot(1)); AxisLimit(1) = MinMaxPlot(1); end;
end
if ~isempty(IsMinMaxPlot); if ~isnan(MinMaxPlot(2)); AxisLimit(2) = MinMaxPlot(2); end;
end
set(ChildFig(1),'CLim',[min(AxisLimit) max(AxisLimit)])
CBarHandle = colorbar;
CBarHandle = ylabel(CBarHandle,'Height [nm]','FontSize',14,'Rotation',270);
CBarPos = get(CBarHandle,'Position');
set(CBarHandle,'Position',[1.5*CBarPos(1) CBarPos(2) CBarPos(3)]);
clear('CBarHandle','CBarPos')
pbaspect([ScanSize(1) ScanSize(2) 1])                    % L□nge von x- und y-Achse dem
gescannten Bildbereich anpassen
set(fig1,'FontSize',14);
box on
view(0,90);

fig2 = subplot(1,3,3);
hold on
bar( HistIndex , log10(HistData) ,'b')
hold off

ChildFig  = get(gcf,'Children');
AxisLimitY = get(ChildFig(1),'YLim');

hold on
plot([min(AxisLimit),min(AxisLimit)],[0 max(AxisLimitY)],'g-')
plot([max(AxisLimit),max(AxisLimit)],[0 max(AxisLimitY)],'g-')
hold off
```

```
% set(ChildFig(1),'XLim',[min(AxisLimit) max(AxisLimit)])
axis([min(HistIndex) max(HistIndex) 0 max(AxisLimitY)]);
% axis 'auto y'
xlabel('Height [nm]','FontSize',14);
ylabel('log( Counts )','FontSize',14);
box on
set(fig2,'FontSize',14);
set(fig2,'LineWidth',1.2);
```

Output Parameter-Data saving: afm_topo

```
SaveData = struct('afm_topo',afm_topo,'LineMedian',LineMedian);
save(strcat(DirName,'\',FileName,'.mat'),'-struct','SaveData','-append');
end
```

```
function [afm_topo,ScarLine] =
ModExludeScars(DirName,FileName,afm_topo,MinMaxPlot,ScarLine);
N = load(strcat(DirName,'\',FileName,'.mat'),'N');
N = getfield(N,'N');

ScanSize = load(strcat(DirName,'\',FileName,'.mat'),'ScanSize');
ScanSize = getfield(ScanSize,'ScanSize');
```

Figure of afm_topo before procedure

```
figure('unit','normalized','outerposition',[0.01,0.02,0.98,0.82])
fig1 = subplot(1,2,1);
hold on

surf( [0:N(1)-1]*ScanSize(1)/N(1) , [0:N(2)-1]*ScanSize(2)/N(2) , afm_topo);

plot( [0:N(1)-1]*ScanSize(1)/N(1) , 0*ones(N(1),1)
,'k.','MarkerSize',2,'ZData',0*ones(N(1),1)); % schwarze Linie an unterer Kante
plot( 0*ones(N(2),1) , [0:N(2)-1]*ScanSize(2)/N(2)
,'k.','MarkerSize',2,'ZData',0*ones(N(2),1)); % schwarze Linie an linker Kante

hold off

axis([0 ScanSize(1) 0 ScanSize(2)]);
xlabel('X-distance [nm]','FontSize',14);
ylabel('Y-distance [nm]','FontSize',14);
set(gcf,'Color',[1 1 1])
shading interp;

load('ColormapRust','CmapRust')
set(gcf,'Colormap',CmapRust)
```

```
ChildFig  = get(gcf,'Children');
AxisLimit = get(ChildFig(1),'CLim');
if ~isnan(MinMaxPlot(1)); AxisLimit(1) = MinMaxPlot(1); end
if ~isnan(MinMaxPlot(2)); AxisLimit(2) = MinMaxPlot(2); end
set(ChildFig(1),'CLim',[min(AxisLimit) max(AxisLimit)])
CBarHandle = colorbar;
CBarHandle = ylabel(CBarHandle,'Height [nm]','FontSize',14,'Rotation',270);
CBarPos = get(CBarHandle,'Position');
set(CBarHandle,'Position',[1.5*CBarPos(1) CBarPos(2) CBarPos(3)]);
clear('CBarHandle','CBarPos')
pbaspect([ScanSize(1) ScanSize(2) 1])                    % L□nge von x- und y-Achse dem
gescannten Bildbereich anpassen
set(fig1,'FontSize',14);
box on
view(0,90);
if isempty(ScarLine)                                     % pr□ft, ob Linien mit Scars bereits
vorgegeben sind
   [ ~ , ScarPos , Button] = ginput(1);                  % erste ScarLine manuell angeben

   if ~or( Button == 1 , Button == 3 )                   % pr□ft, ob Mausklick durchgef□hrt
wurde
      return
   end

   ScarLine = [ScarLine round(ScarPos*N(2)/ScanSize(2))+1];          % Nr. der Linie, die
entfernt wird (gez□hlt von unten)

   ScarLine(ScarLine == 1) = [];              % Algorithmus funktioniert nicht in der ersten und
letzten Linie
   ScarLine(ScarLine == N(2)) = [];

   afm_topo_NoScar = afm_topo;
   if ~isempty(ScarLine)
      afm_topo_NoScar(ScarLine,:) = mean(afm_topo([ScarLine-1 ScarLine+1],:));    % Linie
mit Scar gegen den Mittelwert aus Vorg□nger- und Nachfolgerlinie ersetzen
   end

   fig1 = subplot(1,2,1);                % Figure of afm_topo_NoScar
   hold on
   if ~isempty(ScarLine)
      PlotHandle1 = plot( [0.1*ScanSize(1) ScanSize(1)] , (ScarLine-
1)/N(2)*ScanSize(2)*ones(1,2) ,'g-','LineWidth',1,'ZData',max(max(afm_topo))*ones(1,2));
      PlotHandle2 = text( 0 , ScarLine*ScanSize(2)/N(2) , max(max(afm_topo)) ,
sprintf('%1.0f',ScarLine) ,'FontSize',14,'Color',[0 1 0]);
   else
      PlotHandle1 = []; PlotHandle2 = [];
   end
   hold off
```

```
   fig2 = subplot(1,2,2);
   hold on
   PlotHandle3 = surf( [0:N(1)-1]/N(1)*ScanSize(1) , [0:N(2)-1]/N(2)*ScanSize(2) , afm_topo_NoScar );
   hold off

   axis([0 ScanSize(1) 0 ScanSize(2)]);
   xlabel('X-distance [nm]','FontSize',14);
   ylabel('Y-distance [nm]','FontSize',14);
   set(gcf,'Color',[1 1 1])

   shading interp;
   load('ColormapRust','CmapRust')
   set(gcf,'Colormap',CmapRust)

   ChildFig  = get(gcf,'Children');
   AxisLimit = get(ChildFig(1),'CLim');
   if ~isnan(MinMaxPlot(1)); AxisLimit(1) = MinMaxPlot(1); end
   if ~isnan(MinMaxPlot(2)); AxisLimit(2) = MinMaxPlot(2); end
   set(ChildFig(1),'CLim',[min(AxisLimit) max(AxisLimit)])
   CBarHandle = colorbar;
   CBarHandle = ylabel(CBarHandle,'Height [nm]','FontSize',14,'Rotation',270);
   CBarPos = get(CBarHandle,'Position');
   set(CBarHandle,'Position',[1.5*CBarPos(1) CBarPos(2) CBarPos(3)]);
   clear('CBarHandle','CBarPos')
   pbaspect([ScanSize(1) ScanSize(2) 1])                % L□nge von x- und y-Achse dem gescannten Bildbereich anpassen
   set(fig2,'FontSize',14);
   box on
   view(0,90);
   while or( Button == 1 , Button == 3 )
   [ ~ , ScarPos , Button] = ginput(1);                 % weitere ScarLinen manuell angeben

   ScarLine = [ScarLine round(ScarPos*N(2)/ScanSize(2))+1];          % Nr. der Linie, die entfernt wird (gez□hlt von unten)

   if length(ScarLine) >= 2                             % pr□ft, ob mehr als 1 ScarLine vorliegt
      [DiffLine,IndexLine] = min(abs(ScarLine(1:end-1)-ScarLine(end)));    % kleinster Abstand zw. zuletztgew□hlte ScarLine und zuvor gew□hlen ScarLines
      if DiffLine == 1                                  % pr□ft, ob zuletztgew□hlte ScarLine Nachbar einer zuvor gew□hlen ScarLine ist
         ScarLine(IndexLine) = [];                      % entfernt die □ltere der beiden benachbarten ScarLines
      elseif DiffLine == 0                              % pr□ft, ob zuletztgew□hlte ScarLine gleich einer zuvor gew□hlen ScarLine ist
         ScarLine(IndexLine) = [];                      % entfernt zuletztgew□hlte ScarLine und deren Zwilling
         ScarLine(end) = [];
      end
```

```
    end

    ScarLine = sort(ScarLine);
    ScarLine(ScarLine == 1) = [];                % Algorithmus funktioniert nicht in der ersten und
letzten Linie
    ScarLine(ScarLine == N(2)) = [];

    afm_topo_NoScar = afm_topo;
    for laufvar = 1:length(ScarLine)
        afm_topo_NoScar(ScarLine(laufvar),:)        =        mean(afm_topo([ScarLine(laufvar)-1
ScarLine(laufvar)+1],:));      % Linien mit Scar gegen den Mittelwert aus Vorg?nger- und
Nachfolgerlinie ersetzen
    end

    delete(PlotHandle1); clear('PlotHandle1')
    delete(PlotHandle2); clear('PlotHandle2')
    delete(PlotHandle3); clear('PlotHandle3')

    fig1 = subplot(1,2,1);                % Figure of afm_topo after procedure
    hold on
    for laufvar = 1:length(ScarLine)
        PlotHandle1(laufvar) = plot( [0.1*ScanSize(1) ScanSize(1)] , (ScarLine(laufvar)-
1)/N(2)*ScanSize(2)*ones(1,2) ,'g-','LineWidth',1,'ZData',max(max(afm_topo))*ones(1,2));
        PlotHandle2(laufvar)     =     text(     0     ,     ScarLine(laufvar)*ScanSize(2)/N(2)     ,
max(max(afm_topo)) , sprintf('%1.0f',ScarLine(laufvar)) ,'FontSize',14,'Color',[0 1 0]);
    end
    hold off

    fig2 = subplot(1,2,2);
    hold on
    PlotHandle3     =     surf(     [0:N(1)-1]/N(1)*ScanSize(1)     ,     [0:N(2)-1]/N(2)*ScanSize(2)     ,
afm_topo_NoScar );
    hold off

    shading interp;
    end

    afm_topo = afm_topo_NoScar;
else

    ScarLine(ScarLine == 1) = [];                % Algorithmus funktioniert nicht in der ersten und
letzten Linie
    ScarLine(ScarLine == N(2)) = [];

    for laufvar = 1:length(ScarLine)
        afm_topo(ScarLine(laufvar),:)              =              mean(afm_topo([ScarLine(laufvar)-1
ScarLine(laufvar)+1],:));      % Linien mit Scar gegen den Mittelwert aus Vorg?nger- und
Nachfolgerlinie ersetzen
    end
```

```
   fig1 = subplot(1,2,1);                % Figure of afm_topo after procedure
   hold on
   if ~isempty(ScarLine)
      for laufvar = 1:length(ScarLine)
         plot( [0.1*ScanSize(1) ScanSize(1)] , (ScarLine(laufvar)-
1)/N(2)*ScanSize(2)*ones(1,2) ,'g-','LineWidth',1,'ZData',max(max(afm_topo))*ones(1,2));
         text( 0 , ScarLine(laufvar)*ScanSize(2)/N(2) , max(max(afm_topo)) ,
sprintf('%1.0f',ScarLine(laufvar)) ,'FontSize',14,'Color',[0 1 0])
      end
   end
   hold off

   fig2 = subplot(1,2,2);
   hold on

   surf( [0:N(1)-1]/N(1)*ScanSize(1) , [0:N(2)-1]/N(2)*ScanSize(2) , afm_topo );

   hold off

   axis([0 ScanSize(1) 0 ScanSize(2)]);
   xlabel('X-distance [nm]','FontSize',14);
   ylabel('Y-distance [nm]','FontSize',14);
   set(gcf,'Color',[1 1 1])

   shading interp;
   load('ColormapRust','CmapRust')
   set(gcf,'Colormap',CmapRust)

   ChildFig  = get(gcf,'Children');
   AxisLimit = get(ChildFig(1),'CLim');
   if ~isnan(MinMaxPlot(1)); AxisLimit(1) = MinMaxPlot(1); end
   if ~isnan(MinMaxPlot(2)); AxisLimit(2) = MinMaxPlot(2); end
   set(ChildFig(1),'CLim',[min(AxisLimit) max(AxisLimit)])
   CBarHandle = colorbar;
   CBarHandle = ylabel(CBarHandle,'Height [nm]','FontSize',14,'Rotation',270);
   CBarPos = get(CBarHandle,'Position');
   set(CBarHandle,'Position',[1.5*CBarPos(1) CBarPos(2) CBarPos(3)]);
   clear('CBarHandle','CBarPos')
   pbaspect([ScanSize(1) ScanSize(2) 1])                % L□nge von x- und y-Achse dem
gescannten Bildbereich anpassen
   set(fig2,'FontSize',14);
   box on
   view(0,90);

end
```

Output Parameter-Data saving: afm_topo

```
SaveData = struct('afm_topo',afm_topo,'ScarLine',ScarLine);
save(strcat(DirName,'\',FileName,'.mat'),'-struct','SaveData','-append');
```

```
end
```

```
function [afm_topo,PolyPara] = ModFlatten(DirName,FileName,afm_topo,PolyDegree,PolyPara,MinMaxFlatten,MinMaxPlot);
N = load(strcat(DirName,'\',FileName,'.mat'),'N');
N = getfield(N,'N');
ScanSize = load(strcat(DirName,'\',FileName,'.mat'),'ScanSize');
ScanSize = getfield(ScanSize,'ScanSize');

if isnan(MinMaxFlatten(1)); MinMaxFlatten(1) = -inf; end
if isnan(MinMaxFlatten(2)); MinMaxFlatten(2) =  inf; end
TopoFlatten = NaN*ones(size(afm_topo));
if size(PolyPara,1) == N(2)
   isPolyPara = 1;
else
   isPolyPara = 0;
end
if isPolyPara
   for laufvarX = 1:N(2)
      PolyData = polyval( PolyPara(laufvarX,:) , [0:N(1)-1] , [] , [mean([0:N(1)-1]);std([0:N(1)-1])] );
      TopoFlatten(laufvarX,:) = afm_topo(laufvarX,:) - PolyData;
   end
else

   for laufvarX = 1:N(2)

      TopoLine = [];
      TopoLine = afm_topo(laufvarX,:);
      IndexFlatten = find(and( TopoLine <= max(MinMaxFlatten) , TopoLine >= min(MinMaxFlatten) ));
      TopoLine = TopoLine(IndexFlatten);                    % Werte ignorieren, welche au◆erhalb von MinMaxFlatten sind

      [PolyParaLine , PolyParaStruct , PolyParaMu] = polyfit( IndexFlatten-1 , TopoLine , PolyDegree );
      PolyPara(laufvarX,:) = PolyParaLine;
      PolyData = polyval(PolyPara(laufvarX,:),[0:N(1)-1],[],PolyParaMu);
   %     PolyPara(laufvarX,:) = polyfit(IndexFlatten-1,TopoLine,PolyDegree);
   %     PolyData = polyval(PolyPara(laufvarX,:),[0:N(1)-1]);
      TopoFlatten(laufvarX,:) = afm_topo(laufvarX,:) - PolyData;

   end
end
clear('IndexFlatten')
```

```
[IndexMaxX,IndexMaxY] = find( afm_topo > max(MinMaxFlatten) );
[IndexMinX,IndexMinY] = find( afm_topo < min(MinMaxFlatten) );

figure ('unit','normalized','outerposition',[0.05,0.2,0.9,0.65])

figure('unit','normalized','outerposition',[0.01,0.02,0.98,0.82])
fig1 = subplot(1,2,1);
hold on

surf( [0:N(1)-1]*ScanSize(1)/N(1) , [0:N(2)-1]*ScanSize(2)/N(2) , afm_topo);

if ~isPolyPara
plot(              (IndexMaxY-1)*ScanSize(1)/N(1)              ,(IndexMaxX-1)*ScanSize(2)/N(2)
,'g.','MarkerSize',2,'ZData',max(max(afm_topo))*ones(1,length(IndexMaxX)));
plot(              (IndexMinY-1)*ScanSize(1)/N(1)              ,(IndexMinX-1)*ScanSize(2)/N(2)
,'m.','MarkerSize',2,'ZData',max(max(afm_topo))*ones(1,length(IndexMinX)));
end

plot(                  [0:N(1)-1]*ScanSize(1)/N(1)                  ,                  0*ones(N(1),1)
,'k.','MarkerSize',2,'ZData',0*ones(N(1),1));   % schwarze Linie an unterer Kante
plot(                  0*ones(N(2),1)                  ,                  [0:N(2)-1]*ScanSize(2)/N(2)
,'k.','MarkerSize',2,'ZData',0*ones(N(2),1));   % schwarze Linie an linker Kante

hold off

axis([0 ScanSize(1) 0 ScanSize(2)]);
xlabel('X-distance [nm]','FontSize',14);
ylabel('Y-distance [nm]','FontSize',14);
set(gcf,'Color',[1 1 1])
shading interp;

load('ColormapRust','CmapRust')
set(gcf,'Colormap',CmapRust)
% colormap(gray)

ChildFig  = get(gcf,'Children');
AxisLimit = get(ChildFig(1),'CLim');
if ~isnan(MinMaxPlot(1)); AxisLimit(1) = MinMaxPlot(1); end
if ~isnan(MinMaxPlot(2)); AxisLimit(2) = MinMaxPlot(2); end
set(ChildFig(1),'CLim',[min(AxisLimit) max(AxisLimit)])
CBarHandle = colorbar;
CBarHandle = ylabel(CBarHandle,'Height [nm]','FontSize',14,'Rotation',270);
CBarPos = get(CBarHandle,'Position');
set(CBarHandle,'Position',[1.5*CBarPos(1) CBarPos(2) CBarPos(3)]);
clear('CBarHandle','CBarPos')
pbaspect([ScanSize(1) ScanSize(2) 1])                  % L□nge von x- und y-Achse dem
gescannten Bildbereich anpassen
set(fig1,'FontSize',14);
box on
view(0,90);
```

```
fig2 = subplot(1,2,2);
hold on
surf( [0:N(1)-1]/N(1)*ScanSize(1) , [0:N(2)-1]/N(2)*ScanSize(2) , TopoFlatten );
hold off

axis([0 ScanSize(1) 0 ScanSize(2)]);
xlabel('X-distance [nm]','FontSize',14);
ylabel('Y-distance [nm]','FontSize',14);
set(gcf,'Color',[1 1 1])

shading interp;
load('ColormapRust','CmapRust')
set(gcf,'Colormap',CmapRust)
% colormap(gray)

ChildFig  = get(gcf,'Children');
AxisLimit = get(ChildFig(1),'CLim');
if ~isnan(MinMaxPlot(1)); AxisLimit(1) = MinMaxPlot(1); end
if ~isnan(MinMaxPlot(2)); AxisLimit(2) = MinMaxPlot(2); end
set(ChildFig(1),'CLim',[min(AxisLimit) max(AxisLimit)])
CBarHandle = colorbar;
CBarHandle = ylabel(CBarHandle,'Height [nm]','FontSize',14,'Rotation',270);
CBarPos = get(CBarHandle,'Position');
set(CBarHandle,'Position',[1.5*CBarPos(1) CBarPos(2) CBarPos(3)]);
clear('CBarHandle','CBarPos')
pbaspect([ScanSize(1) ScanSize(2) 1])                    % L□nge von x- und y-Achse dem
gescannten Bildbereich anpassen
set(fig2,'FontSize',14);
box on
view(0,90);
afm_topo = TopoFlatten;
```

Output Parameter-Data saving: afm_topo

```
SaveData = struct('afm_topo',afm_topo,'PolyPara',PolyPara);
save(strcat(DirName,'\',FileName,'.mat'),'-struct','SaveData','-append');
end
```

```
function                              [SectionData,SectionVector]                              =
ModPlotSection(DirName,FileName,afm_topo,NumberSections,MinMaxPlot,SectionVector)
;
if nargin < 6;
   SectionVector = [];
end
N = load(strcat(DirName,'\',FileName,'.mat'),'N');
N = getfield(N,'N');
```

```
ScanSize = load(strcat(DirName,'\',FileName,'.mat'),'ScanSize');
ScanSize = getfield(ScanSize,'ScanSize');

LateralUnit = load(strcat(DirName,'\',FileName,'.mat'),'LateralUnit');
LateralUnit = getfield(LateralUnit,'LateralUnit');
```

Prüfen ob SectionVector schon vorgeben ist oder per ginput bestimmt wird

```
ManualInput = 1;

if and( size(SectionVector,2) == 2 , sum(sum(isnan(SectionVector))) == 0 )
   switch size(SectionVector,1)
      case 2
         Section1Vector = SectionVector;
         NumberSections = 1;
         ManualInput = 0;
      case 4
         Section1Vector = SectionVector(1:2,:);
         Section2Vector = SectionVector(3:4,:);
         NumberSections = 2;
         ManualInput = 0;
      case 6
         Section1Vector = SectionVector(1:2,:);
         Section2Vector = SectionVector(3:4,:);
         Section3Vector = SectionVector(5:6,:);
         NumberSections = 3;
         ManualInput = 0;
      otherwise
         ManualInput = 1;
   end
end
SectionData   = [];

figure('unit','normalized','outerposition',[0.01,0.02,0.98,0.82])
set(gcf,'Color',[1 1 1])

switch NumberSections
  case 1
   fig1 = subplot(1,3,[1 2]);
   hold on
   surf( (0:N(1)-1)/N(1)*ScanSize(1) , (0:N(2)-1)/N(2)*ScanSize(2) , afm_topo);

   plot(                [0:N(1)-1]*ScanSize(1)/N(1)                ,                0*ones(N(1),1)
,'k.','MarkerSize',2,'ZData',0*ones(N(1),1));    % schwarze Linie an unterer Kante
   plot(                0*ones(N(2),1)                ,                [0:N(2)-1]*ScanSize(2)/N(2)
,'k.','MarkerSize',2,'ZData',0*ones(N(2),1));    % schwarze Linie an linker Kante

   hold off
```

```
    axis([0 ScanSize(1) 0 ScanSize(2)]);

    switch LateralUnit
      case '?m'
        xlabel('X distance [?m]','FontSize',14);
        ylabel('Y distance [?m]','FontSize',14);
      case 'nm'
        xlabel('X distance [nm]','FontSize',14);
        ylabel('Y distance [nm]','FontSize',14);
      case 'cm'
        xlabel('X distance [cm]','FontSize',14);
        ylabel('Y distance [cm]','FontSize',14);
      otherwise
        xlabel('X distance [a.u.]','FontSize',14);
        ylabel('Y distance [a.u.]','FontSize',14);
    end
%     xlabel('X distance [nm]','FontSize',14);
%     ylabel('Y distance [nm]','FontSize',14);
    shading interp;
    load('ColormapRust','CmapRust')
    set(gcf,'Colormap',CmapRust)
    title(fig1,'Section ausw?hlen','FontSize',14)

    ChildFig  = get(gcf,'Children');
    AxisLimit = get(ChildFig(1),'CLim');
    if ~isnan(MinMaxPlot(1)); AxisLimit(1) = MinMaxPlot(1); end
    if ~isnan(MinMaxPlot(2)); AxisLimit(2) = MinMaxPlot(2); end
    set(ChildFig(1),'CLim',[min(AxisLimit) max(AxisLimit)])

    PlotHandle3 = colorbar; ylabel(PlotHandle3,'height [nm]','FontSize',14,'Rotation',270);
    ChildFig  = get(gcf,'Children');
    LabelPos = get(get(ChildFig(1),'YLabel'),'Position');
    set(get(ChildFig(1),'YLabel'),'Position',[8 LabelPos(2) LabelPos(3)]);

    pbaspect([ScanSize(1) ScanSize(2) 1])                    % L?nge von x- und y-Achse dem
gescannten Bildbereich anpassen
    set(fig1,'FontSize',14);
    box on
    view(0,90);

    fig2 = subplot(1,3,3);
    switch LateralUnit
      case '?m'
        xlabel('lateral position [?m]','FontSize',14);
      case 'nm'
        xlabel('lateral position [nm]','FontSize',14);
      case 'cm'
        xlabel('lateral position [cm]','FontSize',14);
      otherwise
        xlabel('lateral position [a.u.]','FontSize',14);
```

```
    end
%     xlabel('lateral position [nm]','FontSize',14);
    ylabel('height [nm]','FontSize',14);
    box on
    set(fig2,'FontSize',14);
    set(fig2,'LineWidth',1.2);
    set(fig2,'YGrid','on');

  case 2
    fig1 = subplot(2,3,[1 2 4 5]);
    hold on

    surf( (0:N(1)-1)/N(1)*ScanSize(1) , (0:N(2)-1)/N(2)*ScanSize(2) , afm_topo);

    plot(                [0:N(1)-1]*ScanSize(1)/N(1)                ,                0*ones(N(1),1)
,'k.','MarkerSize',2,'ZData',0*ones(N(1),1));    % schwarze Linie an unterer Kante
    plot(                0*ones(N(2),1)                ,                [0:N(2)-1]*ScanSize(2)/N(2)
,'k.','MarkerSize',2,'ZData',0*ones(N(2),1));    % schwarze Linie an linker Kante

    hold off

    axis([0 ScanSize(1) 0 ScanSize(2)]);

    switch LateralUnit
      case '?m'
        xlabel('X distance [?m]','FontSize',14);
        ylabel('Y distance [?m]','FontSize',14);
      case 'nm'
        xlabel('X distance [nm]','FontSize',14);
        ylabel('Y distance [nm]','FontSize',14);
      case 'cm'
        xlabel('X distance [cm]','FontSize',14);
        ylabel('Y distance [cm]','FontSize',14);
      otherwise
        xlabel('X distance [a.u.]','FontSize',14);
        ylabel('Y distance [a.u.]','FontSize',14);
    end
%     xlabel('X distance [nm]','FontSize',14);
%     ylabel('Y distance [nm]','FontSize',14);
    shading interp;
    load('ColormapRust','CmapRust')
    set(gcf,'Colormap',CmapRust)
    title(fig1,'Select first section','FontSize',14)

    ChildFig  = get(gcf,'Children');
    AxisLimit = get(ChildFig(1),'CLim');
    if ~isnan(MinMaxPlot(1)); AxisLimit(1) = MinMaxPlot(1); end
    if ~isnan(MinMaxPlot(2)); AxisLimit(2) = MinMaxPlot(2); end
    set(ChildFig(1),'CLim',[min(AxisLimit) max(AxisLimit)])
```

```
   PlotHandle3 = colorbar; ylabel(PlotHandle3,'height [nm]','FontSize',14,'Rotation',270);
   ChildFig  = get(gcf,'Children');
   LabelPos = get(get(ChildFig(1),'YLabel'),'Position');
   set(get(ChildFig(1),'YLabel'),'Position',[8 LabelPos(2) LabelPos(3)]);

   pbaspect([ScanSize(1) ScanSize(2) 1])                    % L?nge von x- und y-Achse dem
gescannten Bildbereich anpassen
   set(fig1,'FontSize',14);
   box on
   view(0,90);

   fig2 = subplot(2,3,3);
   switch LateralUnit
     case '?m'
       xlabel('lateral position [?m]','FontSize',14);
     case 'nm'
       xlabel('lateral position [nm]','FontSize',14);
     case 'cm'
       xlabel('lateral position [cm]','FontSize',14);
     otherwise
       xlabel('lateral position [a.u.]','FontSize',14);
   end
%     xlabel('lateral position [nm]','FontSize',14);
   ylabel('height [nm]','FontSize',14);
   box on
   set(fig2,'FontSize',14);
   set(fig2,'LineWidth',1.2);
   set(fig2,'YGrid','on');

   fig3 = subplot(2,3,6);
   switch LateralUnit
     case '?m'
       xlabel('lateral position [?m]','FontSize',14);
     case 'nm'
       xlabel('lateral position [nm]','FontSize',14);
     case 'cm'
       xlabel('lateral position [cm]','FontSize',14);
     otherwise
       xlabel('lateral position [a.u.]','FontSize',14);
   end
%     xlabel('lateral position [nm]','FontSize',14);
   ylabel('height [nm]','FontSize',14);
   box on
   set(fig3,'FontSize',14);
   set(fig3,'LineWidth',1.2);
   set(fig3,'YGrid','on');

 case 3
   fig1 = subplot(3,3,[1 2 4 5 7 8]);
   hold on
```

```
   surf( (0:N(1)-1)/N(1)*ScanSize(1) , (0:N(2)-1)/N(2)*ScanSize(2) , afm_topo);

   plot(                [0:N(1)-1]*ScanSize(1)/N(1)                ,                0*ones(N(1),1)
,'k.','MarkerSize',2,'ZData',0*ones(N(1),1));    % schwarze Linie an unterer Kante
   plot(                0*ones(N(2),1)                ,                [0:N(2)-1]*ScanSize(2)/N(2)
,'k.','MarkerSize',2,'ZData',0*ones(N(2),1));    % schwarze Linie an linker Kante

   hold off

   axis([0 ScanSize(1) 0 ScanSize(2)]);

   switch LateralUnit
     case '?m'
       xlabel('X distance [?m]','FontSize',14);
       ylabel('Y distance [?m]','FontSize',14);
     case 'nm'
       xlabel('X distance [nm]','FontSize',14);
       ylabel('Y distance [nm]','FontSize',14);
     case 'cm'
       xlabel('X distance [cm]','FontSize',14);
       ylabel('Y distance [cm]','FontSize',14);
     otherwise
       xlabel('X distance [a.u.]','FontSize',14);
       ylabel('Y distance [a.u.]','FontSize',14);
   end
%     xlabel('X distance [nm]','FontSize',14);
%     ylabel('Y distance [nm]','FontSize',14);
   shading interp;
   load('ColormapRust','CmapRust')
   set(gcf,'Colormap',CmapRust)
   title(fig1,'Erste Section ausw?hlen','FontSize',14)

   ChildFig  = get(gcf,'Children');
   AxisLimit = get(ChildFig(1),'CLim');
   if ~isnan(MinMaxPlot(1)); AxisLimit(1) = MinMaxPlot(1); end
   if ~isnan(MinMaxPlot(2)); AxisLimit(2) = MinMaxPlot(2); end
   set(ChildFig(1),'CLim',[min(AxisLimit) max(AxisLimit)])

   PlotHandle3 = colorbar; ylabel(PlotHandle3,'height [nm]','FontSize',14,'Rotation',270);
   ChildFig  = get(gcf,'Children');
   LabelPos = get(get(ChildFig(1),'YLabel'),'Position');
   set(get(ChildFig(1),'YLabel'),'Position',[8 LabelPos(2) LabelPos(3)]);

   pbaspect([ScanSize(1) ScanSize(2) 1])                    % L?nge von x- und y-Achse dem
gescannten Bildbereich anpassen
   set(fig1,'FontSize',14);
   box on
   view(0,90);
```

```
    fig2 = subplot(3,3,3);
    switch LateralUnit
      case '?m'
        xlabel('lateral position [?m]','FontSize',14);
      case 'nm'
        xlabel('lateral position [nm]','FontSize',14);
      case 'cm'
        xlabel('lateral position [cm]','FontSize',14);
      otherwise
        xlabel('lateral position [a.u.]','FontSize',14);
    end
%     xlabel('lateral position [nm]','FontSize',14);
    ylabel('height [nm]','FontSize',14);
    box on
    set(fig2,'FontSize',14);
    set(fig2,'LineWidth',1.2);
    set(fig2,'YGrid','on');

    fig3 = subplot(3,3,6);
    switch LateralUnit
      case '?m'
        xlabel('lateral position [?m]','FontSize',14);
      case 'nm'
        xlabel('lateral position [nm]','FontSize',14);
      case 'cm'
        xlabel('lateral position [cm]','FontSize',14);
      otherwise
        xlabel('lateral position [a.u.]','FontSize',14);
    end
%     xlabel('lateral position [nm]','FontSize',14);
    ylabel('height [nm]','FontSize',14);
    box on
    set(fig3,'FontSize',14);
    set(fig3,'LineWidth',1.2);
    set(fig3,'YGrid','on');

    fig4 = subplot(3,3,9);
    switch LateralUnit
      case '?m'
        xlabel('lateral position [?m]','FontSize',14);
      case 'nm'
        xlabel('lateral position [nm]','FontSize',14);
      case 'cm'
        xlabel('lateral position [cm]','FontSize',14);
      otherwise
        xlabel('lateral position [a.u.]','FontSize',14);
    end
%     xlabel('lateral position [nm]','FontSize',14);
    ylabel('height [nm]','FontSize',14);
    box on
```

```
    set(fig4,'FontSize',14);
    set(fig4,'LineWidth',1.2);
    set(fig4,'YGrid','on');

  otherwise
    fig1 = subplot(1,3,[1 2]);
    hold on

    surf( (0:N(1)-1)/N(1)*ScanSize(1) , (0:N(2)-1)/N(2)*ScanSize(2) , afm_topo);

    plot(                [0:N(1)-1]*ScanSize(1)/N(1)                ,                0*ones(N(1),1)
,'k.','MarkerSize',2,'ZData',0*ones(N(1),1));    % schwarze Linie an unterer Kante
    plot(                0*ones(N(2),1)                ,                [0:N(2)-1]*ScanSize(2)/N(2)
,'k.','MarkerSize',2,'ZData',0*ones(N(2),1));    % schwarze Linie an linker Kante

    hold off

    axis([0 ScanSize(1) 0 ScanSize(2)]);
    switch LateralUnit
      case '?m'
        xlabel('lateral position [?m]','FontSize',14);
      case 'nm'
        xlabel('lateral position [nm]','FontSize',14);
      case 'cm'
        xlabel('lateral position [cm]','FontSize',14);
      otherwise
        xlabel('lateral position [a.u.]','FontSize',14);
    end
%     xlabel('lateral position [nm]','FontSize',14);
    ylabel('height [nm]','FontSize',14);
    shading interp;
    load('ColormapRust','CmapRust')
    set(gcf,'Colormap',CmapRust)

    ChildFig  = get(gcf,'Children');
    AxisLimit = get(ChildFig(1),'CLim');
    if ~isnan(MinMaxPlot(1)); AxisLimit(1) = MinMaxPlot(1); end
    if ~isnan(MinMaxPlot(2)); AxisLimit(2) = MinMaxPlot(2); end
    set(ChildFig(1),'CLim',[min(AxisLimit) max(AxisLimit)])
    colorbar;
    pbaspect([ScanSize(1) ScanSize(2) 1])                    % L?nge von x- und y-Achse dem
gescannten Bildbereich anpassen
    set(fig1,'FontSize',14);
    box on
    view(0,90);
end
```

Erste Section auswählen; Start- und Endpunkt in afm_topo darstellen; Section darstellen

```
 title(fig1,'Select first section')
```

```
if isempty(find( strcmp( who ,'Section1Vector') ))          % Pr?fen, ob Section1Vector schon existiert
   [SectionX , SectionY ] = ginput(2);
   SectionX = max(SectionX,0*ones(size(SectionX)));                % begrenzt SectionX, falls au?erhalb des linken Randes von afm_topo geklickt wurde
   SectionX = min(SectionX,ScanSize(1)*ones(size(SectionX)));    % begrenzt SectionX, falls au?erhalb des rechten Randes von afm_topo geklickt wurde
   SectionY = max(SectionY,0*ones(size(SectionY)));                % begrenzt SectionY, falls au?erhalb des unteren Randes von afm_topo geklickt wurde
   SectionY = min(SectionY,ScanSize(2)*ones(size(SectionY)));    % begrenzt SectionY, falls au?erhalb des oberen Randes von afm_topo geklickt wurde
   Section1Vector = [SectionX SectionY];
else
   SectionX = Section1Vector(:,1);
   SectionX = max(SectionX,0*ones(size(SectionX)));                % begrenzt SectionX, falls au?erhalb des linken Randes von afm_topo geklickt wurde
   SectionX = min(SectionX,ScanSize(1)*ones(size(SectionX)));    % begrenzt SectionX, falls au?erhalb des rechten Randes von afm_topo geklickt wurde

   SectionY = Section1Vector(:,2);
   SectionY = max(SectionY,0*ones(size(SectionY)));                % begrenzt SectionY, falls au?erhalb des unteren Randes von afm_topo geklickt wurde
   SectionY = min(SectionY,ScanSize(2)*ones(size(SectionY)));    % begrenzt SectionY, falls au?erhalb des oberen Randes von afm_topo geklickt wurde
end

NumberPixels = round( sqrt( (diff(SectionX)*N(1)/ScanSize(1)).^2 + (diff(SectionY)*N(2)/ScanSize(2)).^2 ));

SectionIndexX = round( linspace( SectionX(1) , SectionX(2) , NumberPixels )*N(1)/ScanSize(1) );
SectionIndexX = max(SectionIndexX,1*ones(size(SectionIndexX)));          % begrenzt SectionIndexX, falls au?erhalb des linken Randes von afm_topo geklickt wurde
SectionIndexX = min(SectionIndexX,N(1)*ones(size(SectionIndexX)));       % begrenzt SectionIndexX, falls au?erhalb des rechten Randes von afm_topo geklickt wurde

SectionIndexY = round( linspace( SectionY(1) , SectionY(2) , NumberPixels )*N(2)/ScanSize(2) );
SectionIndexY = max(SectionIndexY,1*ones(size(SectionIndexY)));          % begrenzt SectionIndexY, falls au?erhalb des unteren Randes von afm_topo geklickt wurde
SectionIndexY = min(SectionIndexY,N(2)*ones(size(SectionIndexY)));       % begrenzt SectionIndexY, falls au?erhalb des oberen Randes von afm_topo geklickt wurde

Section1Data = linspace( 0 , sqrt( diff(SectionX).^2 + diff(SectionY).^2 ) , NumberPixels )';
Section1Data = [Section1Data , diag(afm_topo(SectionIndexY,SectionIndexX))];

switch NumberSections
  case 1
     fig1 = subplot(1,3,[1 2]);
```

```
    hold on
    PlotHandle1 = plot( SectionX , SectionY ,'r-
','LineWidth',2,'ZData',max(max(afm_topo))*ones(1,2));
    hold off

    fig2 = subplot(1,3,3);
    hold on
    PlotHandle2 = plot( Section1Data(:,1) , Section1Data(:,2) ,'r-','LineWidth',2);
    hold off
    axis([min(Section1Data(:,1)) max(Section1Data(:,1)) 0 1])
    axis 'auto y'

 case 2
    fig1 = subplot(2,3,[1 2 4 5]);
    hold on
    PlotHandle1 = plot( SectionX , SectionY ,'r-
','LineWidth',2,'ZData',max(max(afm_topo))*ones(1,2));
    hold off

    fig2 = subplot(2,3,3);
    hold on
    PlotHandle2 = plot( Section1Data(:,1) , Section1Data(:,2) ,'r-','LineWidth',2);
    hold off
    axis([min(Section1Data(:,1)) max(Section1Data(:,1)) 0 1])
    axis 'auto y'

  case 3
    fig1 = subplot(3,3,[1 2 4 5 7 8]);
    hold on
    PlotHandle1 = plot( SectionX , SectionY ,'r-
','LineWidth',2,'ZData',max(max(afm_topo))*ones(1,2));
    hold off

    fig2 = subplot(3,3,3);
    hold on
    PlotHandle2 = plot( Section1Data(:,1) , Section1Data(:,2) ,'r-','LineWidth',2);
    hold off
    axis([min(Section1Data(:,1)) max(Section1Data(:,1)) 0 1])
    axis 'auto y'
  otherwise
end
if ManualInput == 0
   StartEnd = 0;                    % Abbruchbedingung
else
   [ X , Y , StartEnd] = ginput(1);
   StartEnd = [ 1 ; 3 ; StartEnd ];
end

while or( StartEnd(end) == 1 , StartEnd(end) == 3 )
```

```
   SectionX = [ SectionX ; X ];
   SectionX = max(SectionX,0*ones(size(SectionX)));                % begrenzt SectionX, falls au?erhalb des linken Randes von afm_topo geklickt wurde
   SectionX = min(SectionX,ScanSize(1)*ones(size(SectionX)));   % begrenzt SectionX, falls au?erhalb des rechten Randes von afm_topo geklickt wurde

   SectionY = [ SectionY ; Y ];
   SectionY = max(SectionY,0*ones(size(SectionY)));                % begrenzt SectionY, falls au?erhalb des unteren Randes von afm_topo geklickt wurde
   SectionY = min(SectionY,ScanSize(2)*ones(size(SectionY)));   % begrenzt SectionY, falls au?erhalb des oberen Randes von afm_topo geklickt wurde

   IndexStart = find(StartEnd == 1);
   IndexEnd   = find(StartEnd == 3);

   NumberPixels = round( sqrt( ( (SectionX(IndexEnd(end))-SectionX(IndexStart(end)))*N(1)/ScanSize(1) )^2 + ( (SectionY(IndexEnd(end))-SectionY(IndexStart(end)))*N(2)/ScanSize(2) )^2 ) );

   SectionIndexX = round( linspace( SectionX(IndexStart(end)) , SectionX(IndexEnd(end)) , NumberPixels )*N(1)/ScanSize(1) );
   SectionIndexX = max(SectionIndexX,1*ones(size(SectionIndexX)));          % begrenzt SectionIndexX, falls au?erhalb des linken Randes von afm_topo geklickt wurde
   SectionIndexX = min(SectionIndexX,N(1)*ones(size(SectionIndexX)));       % begrenzt SectionIndexX, falls au?erhalb des rechten Randes von afm_topo geklickt wurde

   SectionIndexY = round( linspace( SectionY(IndexStart(end)) , SectionY(IndexEnd(end)) , NumberPixels )*N(2)/ScanSize(2) );
   SectionIndexY = max(SectionIndexY,1*ones(size(SectionIndexY)));          % begrenzt SectionIndexY, falls au?erhalb des unteren Randes von afm_topo geklickt wurde
   SectionIndexY = min(SectionIndexY,N(2)*ones(size(SectionIndexY)));       % begrenzt SectionIndexY, falls au?erhalb des oberen Randes von afm_topo geklickt wurde

   clear('Section1Data')
   Section1Data = linspace( 0 , sqrt( ( SectionX(IndexEnd(end))-SectionX(IndexStart(end)) )^2 + ( SectionY(IndexEnd(end))-SectionY(IndexStart(end)) )^2 ) , NumberPixels )';
   Section1Data = [Section1Data , diag(afm_topo(SectionIndexY,SectionIndexX))];

   Section1Vector = [SectionX(IndexStart(end)) SectionY(IndexStart(end)) ; SectionX(IndexEnd(end)) SectionY(IndexEnd(end))];

   delete(PlotHandle1)
   delete(PlotHandle2)

   switch NumberSections
    case 1
       fig1 = subplot(1,3,[1 2]);
       hold on
```

```
        PlotHandle1 = plot( [SectionX(IndexStart(end)) SectionX(IndexEnd(end))] ,
[SectionY(IndexStart(end)) SectionY(IndexEnd(end))] ,'r-
','LineWidth',2,'ZData',max(max(afm_topo))*ones(1,2));
        hold off

        fig2 = subplot(1,3,3);
        hold on
        PlotHandle2 = plot( Section1Data(:,1) , Section1Data(:,2) ,'r-','LineWidth',2);
        hold off
        axis([min(Section1Data(:,1)) max(Section1Data(:,1)) 0 1])
        axis 'auto y'

    case 2
        fig1 = subplot(2,3,[1 2 4 5]);
        hold on
        PlotHandle1 = plot( [SectionX(IndexStart(end)) SectionX(IndexEnd(end))] ,
[SectionY(IndexStart(end)) SectionY(IndexEnd(end))] ,'r-
','LineWidth',2,'ZData',max(max(afm_topo))*ones(1,2));
        hold off

        fig2 = subplot(2,3,3);
        hold on
        PlotHandle2 = plot( Section1Data(:,1) , Section1Data(:,2) ,'r-','LineWidth',2);
        hold off
        axis([min(Section1Data(:,1)) max(Section1Data(:,1)) 0 1])
        axis 'auto y'

    case 3
        fig1 = subplot(3,3,[1 2 4 5 7 8]);
        hold on
        PlotHandle1 = plot( [SectionX(IndexStart(end)) SectionX(IndexEnd(end))] ,
[SectionY(IndexStart(end)) SectionY(IndexEnd(end))] ,'r-
','LineWidth',2,'ZData',max(max(afm_topo))*ones(1,2));
        hold off

        fig2 = subplot(3,3,3);
        hold on
        PlotHandle2 = plot( Section1Data(:,1) , Section1Data(:,2) ,'r-','LineWidth',2);
        hold off
        axis([min(Section1Data(:,1)) max(Section1Data(:,1)) 0 1])
        axis 'auto y'

    otherwise
        Section1Data = [];
  end

  [X , Y , Button] = ginput(1);
  StartEnd = [StartEnd ; Button];

end
```

```
SectionData   = Section1Data;
SectionVector = round(Section1Vector*10)/10;
% VectorString = strcat('SectionVector = [ ',sprintf('%0.1f %0.1f',Section1Vector(1,:)),' ; ',sprintf('%0.1f %0.1f',Section1Vector(2,:)),' ];');

clear('X','Y','IndexStart','IndexEnd','StartEnd','Button','SectionIndexX','SectionIndexY','NumberPixels','SectionX','SectionY')
```

Zweite Section auswählen; Start- und Endpunkt in afm_topo darstellen; Section darstellen

```
if or(NumberSections == 2,NumberSections == 3)

   title(fig1,'Select second section')

   if isempty(find( strcmp( who ,'Section2Vector') ))        % Pr?fen, ov Section2Vector schon existiert
      [SectionX , SectionY ] = ginput(2);
      SectionX = max(SectionX,0*ones(size(SectionX)));              % begrenzt SectionX, falls au?erhalb des linken Randes von afm_topo geklickt wurde
      SectionX = min(SectionX,ScanSize(1)*ones(size(SectionX)));    % begrenzt SectionX, falls au?erhalb des rechten Randes von afm_topo geklickt wurde
      SectionY = max(SectionY,0*ones(size(SectionY)));              % begrenzt SectionY, falls au?erhalb des unteren Randes von afm_topo geklickt wurde
      SectionY = min(SectionY,ScanSize(2)*ones(size(SectionY)));    % begrenzt SectionY, falls au?erhalb des oberen Randes von afm_topo geklickt wurde
      Section2Vector = [SectionX SectionY];
   else
      SectionX = Section2Vector(:,1);
      SectionX = max(SectionX,0*ones(size(SectionX)));              % begrenzt SectionX, falls au?erhalb des linken Randes von afm_topo geklickt wurde
      SectionX = min(SectionX,ScanSize(1)*ones(size(SectionX)));    % begrenzt SectionX, falls au?erhalb des rechten Randes von afm_topo geklickt wurde

      SectionY = Section2Vector(:,2);
      SectionY = max(SectionY,0*ones(size(SectionY)));              % begrenzt SectionY, falls au?erhalb des unteren Randes von afm_topo geklickt wurde
      SectionY = min(SectionY,ScanSize(2)*ones(size(SectionY)));    % begrenzt SectionY, falls au?erhalb des oberen Randes von afm_topo geklickt wurde
   end

   NumberPixels = round( sqrt( (diff(SectionX)*N(1)/ScanSize(1)).^2 + (diff(SectionY)*N(2)/ScanSize(2)).^2 ));

   SectionIndexX = round( linspace( SectionX(1) , SectionX(2) , NumberPixels )*N(1)/ScanSize(1) );
   SectionIndexX = max(SectionIndexX,1*ones(size(SectionIndexX)));          % begrenzt SectionIndexX, falls au?erhalb des linken Randes von afm_topo geklickt wurde
```

```
   SectionIndexX = min(SectionIndexX,N(1)*ones(size(SectionIndexX)));          % begrenzt SectionIndexX, falls au?erhalb des rechten Randes von afm_topo geklickt wurde

   SectionIndexY = round( linspace( SectionY(1) , SectionY(2) , NumberPixels )*N(2)/ScanSize(2) );
   SectionIndexY = max(SectionIndexY,1*ones(size(SectionIndexY)));             % begrenzt SectionIndexY, falls au?erhalb des unteren Randes von afm_topo geklickt wurde
   SectionIndexY = min(SectionIndexY,N(2)*ones(size(SectionIndexY)));          % begrenzt SectionIndexY, falls au?erhalb des oberen Randes von afm_topo geklickt wurde

   Section2Data = linspace( 0 , sqrt( diff(SectionX).^2 + diff(SectionY).^2 ) , NumberPixels )';
   Section2Data = [Section2Data , diag(afm_topo(SectionIndexY,SectionIndexX))];

   switch NumberSections
    case 2
       fig1 = subplot(2,3,[1 2 4 5]);
       hold on
       PlotHandle1 = plot( SectionX , SectionY ,'g-','LineWidth',2,'ZData',max(max(afm_topo))*ones(1,2));
       hold off

       fig3 = subplot(2,3,6);
       hold on
       PlotHandle2 = plot( Section2Data(:,1) , Section2Data(:,2) ,'g-','LineWidth',2);
       hold off
       axis([min(Section2Data(:,1)) max(Section2Data(:,1)) 0 1])
       axis 'auto y'

      case 3
       fig1 = subplot(3,3,[1 2 4 5 7 8]);
       hold on
       PlotHandle1 = plot( SectionX , SectionY ,'g-','LineWidth',2,'ZData',max(max(afm_topo))*ones(1,2));
       hold off

       fig3 = subplot(3,3,6);
       hold on
       PlotHandle2 = plot( Section2Data(:,1) , Section2Data(:,2) ,'g-','LineWidth',2);
       hold off
       axis([min(Section2Data(:,1)) max(Section2Data(:,1)) 0 1])
       axis 'auto y'
      otherwise
   end


   if ManualInput == 0
      StartEnd = 0;                    % Abbruchbedingung
   else
      [ X , Y , StartEnd] = ginput(1);
      StartEnd = [ 1 ; 3 ; StartEnd ];
```

```
    end


    while or( StartEnd(end) == 1 , StartEnd(end) == 3 )

        SectionX = [ SectionX ; X ];
        SectionX = max(SectionX,0*ones(size(SectionX)));              % begrenzt SectionX, falls au?erhalb des linken Randes von afm_topo geklickt wurde
        SectionX = min(SectionX,ScanSize(1)*ones(size(SectionX)));    % begrenzt SectionX, falls au?erhalb des rechten Randes von afm_topo geklickt wurde

        SectionY = [ SectionY ; Y ];
        SectionY = max(SectionY,0*ones(size(SectionY)));              % begrenzt SectionY, falls au?erhalb des unteren Randes von afm_topo geklickt wurde
        SectionY = min(SectionY,ScanSize(2)*ones(size(SectionY)));    % begrenzt SectionY, falls au?erhalb des oberen Randes von afm_topo geklickt wurde

        IndexStart = find(StartEnd == 1);
        IndexEnd   = find(StartEnd == 3);

        NumberPixels = round( sqrt( ( (SectionX(IndexEnd(end))-SectionX(IndexStart(end)))*N(1)/ScanSize(1) )^2 + ( (SectionY(IndexEnd(end))-SectionY(IndexStart(end)))*N(2)/ScanSize(2) )^2 ) );

        SectionIndexX = round( linspace( SectionX(IndexStart(end)) , SectionX(IndexEnd(end)) , NumberPixels )*N(1)/ScanSize(1) );
        SectionIndexX = max(SectionIndexX,1*ones(size(SectionIndexX)));          % begrenzt SectionIndexX, falls au?erhalb des linken Randes von afm_topo geklickt wurde
        SectionIndexX = min(SectionIndexX,N(1)*ones(size(SectionIndexX)));       % begrenzt SectionIndexX, falls au?erhalb des rechten Randes von afm_topo geklickt wurde

        SectionIndexY = round( linspace( SectionY(IndexStart(end)) , SectionY(IndexEnd(end)) , NumberPixels )*N(2)/ScanSize(2) );
        SectionIndexY = max(SectionIndexY,1*ones(size(SectionIndexY)));          % begrenzt SectionIndexY, falls au?erhalb des unteren Randes von afm_topo geklickt wurde
        SectionIndexY = min(SectionIndexY,N(2)*ones(size(SectionIndexY)));       % begrenzt SectionIndexY, falls au?erhalb des oberen Randes von afm_topo geklickt wurde

        clear('Section2Data')
        Section2Data = linspace( 0 , sqrt( ( SectionX(IndexEnd(end))-SectionX(IndexStart(end)) )^2 + ( SectionY(IndexEnd(end))-SectionY(IndexStart(end)) )^2 ) , NumberPixels )';
        Section2Data = [Section2Data , diag(afm_topo(SectionIndexY,SectionIndexX))];

        Section2Vector = [SectionX(IndexStart(end)) SectionY(IndexStart(end)) ; SectionX(IndexEnd(end)) SectionY(IndexEnd(end))];

        delete(PlotHandle1)
        delete(PlotHandle2)

        switch NumberSections
```

```
        case 2
            fig1 = subplot(2,3,[1 2 4 5]);
            hold on
            PlotHandle1 = plot( [SectionX(IndexStart(end)) SectionX(IndexEnd(end))] , [SectionY(IndexStart(end)) SectionY(IndexEnd(end))] ,'g-','LineWidth',2,'ZData',max(max(afm_topo))*ones(1,2));
            hold off

            fig2 = subplot(2,3,6);
            hold on
            PlotHandle2 = plot( Section2Data(:,1) , Section2Data(:,2) ,'g-','LineWidth',2);
            hold off
            axis([min(Section2Data(:,1)) max(Section2Data(:,1)) 0 1])
            axis 'auto y'

        case 3
            fig1 = subplot(3,3,[1 2 4 5 7 8]);
            hold on
            PlotHandle1 = plot( [SectionX(IndexStart(end)) SectionX(IndexEnd(end))] , [SectionY(IndexStart(end)) SectionY(IndexEnd(end))] ,'g-','LineWidth',2,'ZData',max(max(afm_topo))*ones(1,2));
            hold off

            fig2 = subplot(3,3,6);
            hold on
            PlotHandle2 = plot( Section2Data(:,1) , Section2Data(:,2) ,'g-','LineWidth',2);
            hold off
            axis([min(Section2Data(:,1)) max(Section2Data(:,1)) 0 1])
            axis 'auto y'

         otherwise
            Section2Data = [];
       end

       [X , Y , Button] = ginput(1);
       StartEnd = [StartEnd ; Button];

   end

   SectionData = NaN*ones(max([size(Section1Data,1),size(Section2Data,1)]),4);
   SectionData(1:size(Section1Data,1),[1 2]) = Section1Data;
   SectionData(1:size(Section2Data,1),[3 4]) = Section2Data;

   SectionVector = [SectionVector ; round(Section2Vector*10)/10];


clear('X','Y','IndexStart','IndexEnd','StartEnd','Button','SectionIndexX','SectionIndexY','NumberPixels','SectionX','SectionY')
end
```

Dritte Section auswählen; Start- und Endpunkt in afm_topo darstellen; Section darstellen

```
if NumberSections == 3

   Section3Data = [];
   title(fig1,'Select third section')

   if isempty(find( strcmp( who ,'Section3Vector') ))        % Pr?fen, ov Section3Vector schon existiert
      [SectionX , SectionY ] = ginput(2);
      SectionX = max(SectionX,0*ones(size(SectionX)));              % begrenzt SectionX, falls au?erhalb des linken Randes von afm_topo geklickt wurde
      SectionX = min(SectionX,ScanSize(1)*ones(size(SectionX)));    % begrenzt SectionX, falls au?erhalb des rechten Randes von afm_topo geklickt wurde
      SectionY = max(SectionY,0*ones(size(SectionY)));              % begrenzt SectionY, falls au?erhalb des unteren Randes von afm_topo geklickt wurde
      SectionY = min(SectionY,ScanSize(2)*ones(size(SectionY)));    % begrenzt SectionY, falls au?erhalb des oberen Randes von afm_topo geklickt wurde
      Section3Vector = [SectionX SectionY];
   else
      SectionX = Section3Vector(:,1);
      SectionX = max(SectionX,0*ones(size(SectionX)));              % begrenzt SectionX, falls au?erhalb des linken Randes von afm_topo geklickt wurde
      SectionX = min(SectionX,ScanSize(1)*ones(size(SectionX)));    % begrenzt SectionX, falls au?erhalb des rechten Randes von afm_topo geklickt wurde

      SectionY = Section3Vector(:,2);
      SectionY = max(SectionY,0*ones(size(SectionY)));              % begrenzt SectionY, falls au?erhalb des unteren Randes von afm_topo geklickt wurde
      SectionY = min(SectionY,ScanSize(2)*ones(size(SectionY)));    % begrenzt SectionY, falls au?erhalb des oberen Randes von afm_topo geklickt wurde
   end

   NumberPixels = round( sqrt( (diff(SectionX)*N(1)/ScanSize(1)).^2 + (diff(SectionY)*N(2)/ScanSize(2)).^2 ));

   SectionIndexX = round( linspace( SectionX(1) , SectionX(2) , NumberPixels )*N(1)/ScanSize(1) );
   SectionIndexX = max(SectionIndexX,1*ones(size(SectionIndexX)));          % begrenzt SectionIndexX, falls au?erhalb des linken Randes von afm_topo geklickt wurde
   SectionIndexX = min(SectionIndexX,N(1)*ones(size(SectionIndexX)));       % begrenzt SectionIndexX, falls au?erhalb des rechten Randes von afm_topo geklickt wurde

   SectionIndexY = round( linspace( SectionY(1) , SectionY(2) , NumberPixels )*N(2)/ScanSize(2) );
   SectionIndexY = max(SectionIndexY,1*ones(size(SectionIndexY)));          % begrenzt SectionIndexY, falls au?erhalb des unteren Randes von afm_topo geklickt wurde
   SectionIndexY = min(SectionIndexY,N(2)*ones(size(SectionIndexY)));       % begrenzt SectionIndexY, falls au?erhalb des oberen Randes von afm_topo geklickt wurde
```

```
   Section3Data = linspace( 0 , sqrt( diff(SectionX).^2 + diff(SectionY).^2 ) , NumberPixels )';
   Section3Data = [Section3Data , diag(afm_topo(SectionIndexY,SectionIndexX))];


   fig1 = subplot(3,3,[1 2 4 5 7 8]);
   hold on
   PlotHandle1 = plot( SectionX , SectionY ,'b-','LineWidth',2,'ZData',max(max(afm_topo))*ones(1,2));
   hold off

   fig4 = subplot(3,3,9);
   hold on
   PlotHandle2 = plot( Section3Data(:,1) , Section3Data(:,2) ,'b-','LineWidth',2);
   hold off
   axis([min(Section3Data(:,1)) max(Section3Data(:,1)) 0 1])
   axis 'auto y'


   if ManualInput == 0
      StartEnd = 0;                    % Abbruchbedingung
   else
      [ X , Y , StartEnd] = ginput(1);
      StartEnd = [ 1 ; 3 ; StartEnd ];
   end


   while or( StartEnd(end) == 1 , StartEnd(end) == 3 )

      SectionX = [ SectionX ; X ];
      SectionX = max(SectionX,0*ones(size(SectionX)));          % begrenzt SectionX, falls au?erhalb des linken Randes von afm_topo geklickt wurde
      SectionX = min(SectionX,ScanSize(1)*ones(size(SectionX)));   % begrenzt SectionX, falls au?erhalb des rechten Randes von afm_topo geklickt wurde

      SectionY = [ SectionY ; Y ];
      SectionY = max(SectionY,0*ones(size(SectionY)));          % begrenzt SectionY, falls au?erhalb des unteren Randes von afm_topo geklickt wurde
      SectionY = min(SectionY,ScanSize(2)*ones(size(SectionY)));   % begrenzt SectionY, falls au?erhalb des oberen Randes von afm_topo geklickt wurde

      IndexStart = find(StartEnd == 1);
      IndexEnd   = find(StartEnd == 3);

      NumberPixels = round( sqrt( ( (SectionX(IndexEnd(end))-SectionX(IndexStart(end)))*N(1)/ScanSize(1) )^2 + ( (SectionY(IndexEnd(end))-SectionY(IndexStart(end)))*N(2)/ScanSize(2) )^2 ) );

      SectionIndexX = round( linspace( SectionX(IndexStart(end)) , SectionX(IndexEnd(end)) , NumberPixels )*N(1)/ScanSize(1) );
```

```
        SectionIndexX = max(SectionIndexX,1*ones(size(SectionIndexX)));          % begrenzt SectionIndexX, falls au?erhalb des linken Randes von afm_topo geklickt wurde
        SectionIndexX = min(SectionIndexX,N(1)*ones(size(SectionIndexX)));       % begrenzt SectionIndexX, falls au?erhalb des rechten Randes von afm_topo geklickt wurde

        SectionIndexY = round( linspace( SectionY(IndexStart(end)) , SectionY(IndexEnd(end)) , NumberPixels )*N(2)/ScanSize(2) );
        SectionIndexY = max(SectionIndexY,1*ones(size(SectionIndexY)));          % begrenzt SectionIndexY, falls au?erhalb des unteren Randes von afm_topo geklickt wurde
        SectionIndexY = min(SectionIndexY,N(2)*ones(size(SectionIndexY)));       % begrenzt SectionIndexY, falls au?erhalb des oberen Randes von afm_topo geklickt wurde

        clear('Section3Data')
        Section3Data = linspace( 0 , sqrt( ( SectionX(IndexEnd(end))-SectionX(IndexStart(end)) )^2 + ( SectionY(IndexEnd(end))-SectionY(IndexStart(end)) )^2 ) , NumberPixels )';
        Section3Data = [Section3Data , diag(afm_topo(SectionIndexY,SectionIndexX))];

        Section3Vector = [SectionX(IndexStart(end)) SectionY(IndexStart(end)) ; SectionX(IndexEnd(end)) SectionY(IndexEnd(end))];

        delete(PlotHandle1)
        delete(PlotHandle2)

        fig1 = subplot(3,3,[1 2 4 5 7 8]);
        hold on
        PlotHandle1 = plot( [SectionX(IndexStart(end)) SectionX(IndexEnd(end))] , [SectionY(IndexStart(end)) SectionY(IndexEnd(end))] ,'b-','LineWidth',2,'ZData',max(max(afm_topo))*ones(1,2));
        hold off

        fig3 = subplot(3,3,9);
        hold on
        PlotHandle2 = plot( Section3Data(:,1) , Section3Data(:,2) ,'b-','LineWidth',2);
        hold off
        axis([min(Section3Data(:,1)) max(Section3Data(:,1)) 0 1])
        axis 'auto y'

        [X , Y , Button] = ginput(1);
        StartEnd = [StartEnd ; Button];

    end

    SectionData = NaN*ones(max([size(Section1Data,1),size(Section2Data,1),size(Section3Data,1)]),6);
    SectionData(1:size(Section1Data,1),[1 2]) = Section1Data;
    SectionData(1:size(Section2Data,1),[3 4]) = Section2Data;
    SectionData(1:size(Section3Data,1),[5 6]) = Section3Data;

    SectionVector = [SectionVector ; round(Section3Vector*10)/10];
```

```
clear('X','Y','IndexStart','IndexEnd','StartEnd','Button','SectionIndexX','SectionIndexY','Numb
erPixels','SectionX','SectionY')
end

title(fig1,'')
```

Output in Parameter-Data Saving: SectionData und SectionVector

```
SaveData = struct('SectionData',SectionData,'SectionVector',SectionVector);
save(strcat(DirName,'\',FileName,'.mat'),'-struct','SaveData','-append');
end
```

```
function [afm_topo,N,ScanSize,ROI] =
ModSelectROI(DirName,FileName,afm_topo,ROI,MinMaxPlot);
N = load(strcat(DirName,'\',FileName,'.mat'),'N');
N = getfield(N,'N');

ScanSize = load(strcat(DirName,'\',FileName,'.mat'),'ScanSize');
ScanSize = getfield(ScanSize,'ScanSize');

LateralUnit = load(strcat(DirName,'\',FileName,'.mat'),'LateralUnit');
LateralUnit = getfield(LateralUnit,'LateralUnit');


if and( length(ROI) == 4 , sum(isnan(ROI)) == 0 )

   RangeIndexX(1) = min(max(round( ROI(1)*N(1)/ScanSize(1)),1),N(1));
   RangeIndexX(2) = min(max(round((ROI(1)+ROI(3))*N(1)/ScanSize(1)),1),N(1));
   RangeIndexY(1) = min(max(round( ROI(2)*N(2)/ScanSize(2)),1),N(2));
   RangeIndexY(2) = min(max(round((ROI(2)+ROI(4))*N(2)/ScanSize(2)),1),N(2));

   if abs(diff(RangeIndexX)) == 0
      RangeIndexX(1) = min(max(RangeIndexX(1)-2,1),N(1));
      RangeIndexX(2) = min(max(RangeIndexX(2)+2,1),N(1));
   end

   if abs(diff(RangeIndexY)) == 0
      RangeIndexY(1) = min(max(RangeIndexY(1)-2,1),N(2));
      RangeIndexY(2) = min(max(RangeIndexY(2)+2,1),N(2));
   end

   AFMtopoROI = afm_topo( min(RangeIndexY):max(RangeIndexY) ,
min(RangeIndexX):max(RangeIndexX) );
   figure('unit','normalized','outerposition',[0.01,0.02,0.98,0.82])

   fig1 = subplot(2,2,[1 3]);
   hold on
```

```
   surf( (0:N(1)-1)/N(1)*ScanSize(1) , (0:N(2)-1)/N(2)*ScanSize(2) , afm_topo);
   plot( [ ROI(1),ROI(1),ROI(1)+ROI(3),ROI(1)+ROI(3),ROI(1) ] , [
ROI(2),ROI(2)+ROI(4),ROI(2)+ROI(4),ROI(2),ROI(2) ] ,'g-
','LineWidth',1,'ZData',max(max(afm_topo))*ones(1,5));

   plot( [0:N(1)-1]*ScanSize(1)/N(1) , 0*ones(N(1),1)
,'k.','MarkerSize',2,'ZData',0*ones(N(1),1));    % schwarze Linie an unterer Kante
   plot( 0*ones(N(2),1) , [0:N(2)-1]*ScanSize(2)/N(2)
,'k.','MarkerSize',2,'ZData',0*ones(N(2),1));    % schwarze Linie an linker Kante

   hold off

   axis([min(0,ROI(1)) max(ScanSize(1),ROI(1)+ROI(3)) min(0,ROI(2))
max(ScanSize(2),ROI(2)+ROI(4))]);
      switch LateralUnit
    case '�m'
      xlabel('X distance [�m]','FontSize',14);
      ylabel('Y distance [�m]','FontSize',14);
    case 'nm'
      xlabel('X distance [nm]','FontSize',14);
      ylabel('Y distance [nm]','FontSize',14);
    case 'cm'
      xlabel('X distance [cm]','FontSize',14);
      ylabel('Y distance [cm]','FontSize',14);
    otherwise
      xlabel('X distance [a.u.]','FontSize',14);
      ylabel('Y distance [a.u.]','FontSize',14);
   end
%    xlabel('X distance [nm]','FontSize',14);
%    ylabel('Y distance [nm]','FontSize',14);
   set(gcf,'Color',[1 1 1])
   shading interp;
   load('ColormapRust','CmapRust'); set(gcf,'Colormap',CmapRust);
   ChildFig  = get(gcf,'Children');
   AxisLimit = get(ChildFig(1),'CLim');
   if ~isnan(MinMaxPlot(1)); AxisLimit(1) = MinMaxPlot(1); end
   if ~isnan(MinMaxPlot(2)); AxisLimit(2) = MinMaxPlot(2); end
   set(ChildFig(1),'CLim',[min(AxisLimit) max(AxisLimit)])
   CBarHandle = colorbar;
   CBarHandle = ylabel(CBarHandle,'Height [nm]','FontSize',14,'Rotation',270);
   CBarPos = get(CBarHandle,'Position');
   set(CBarHandle,'Position',[1.5*CBarPos(1) CBarPos(2) CBarPos(3)]);
   clear('CBarHandle','CBarPos')
   pbaspect([ScanSize(1) ScanSize(2) 1])                % L�nge von x- und y-Achse dem
gescannten Bildbereich anpassen
   view(0,90);
   box on
   set(fig1,'FontSize',14);
   set(fig1,'LineWidth',1.2);
```

```
   fig2 = subplot(2,2,[2 4]);
   hold on

   surf(      (0:size(AFMtopoROI,2)-1)/N(1)*ScanSize(1)      ,      (0:size(AFMtopoROI,1)-
1)/N(2)*ScanSize(2) , AFMtopoROI);

   hold off

   axis([0 ROI(3) 0 ROI(4)]);
      switch LateralUnit
    case '�m'
      xlabel('X distance [�m]','FontSize',14);
      ylabel('Y distance [�m]','FontSize',14);
    case 'nm'
      xlabel('X distance [nm]','FontSize',14);
      ylabel('Y distance [nm]','FontSize',14);
    case 'cm'
      xlabel('X distance [cm]','FontSize',14);
      ylabel('Y distance [cm]','FontSize',14);
    otherwise
      xlabel('X distance [a.u.]','FontSize',14);
      ylabel('Y distance [a.u.]','FontSize',14);
   end
%     xlabel('X distance [nm]','FontSize',14);
%     ylabel('Y distance [nm]','FontSize',14);
   set(gcf,'Color',[1 1 1])

   shading interp;
%     colormap('gray')
   load('ColormapRust','CmapRust'); set(gcf,'Colormap',CmapRust);
   ChildFig  = get(gcf,'Children');
   AxisLimit = get(ChildFig(1),'CLim');
   if ~isnan(MinMaxPlot(1)); AxisLimit(1) = MinMaxPlot(1); end
   if ~isnan(MinMaxPlot(2)); AxisLimit(2) = MinMaxPlot(2); end
   set(ChildFig(1),'CLim',[min(AxisLimit) max(AxisLimit)])
   pbaspect([ROI(3) ROI(4) 1])                  % L�nge von x- und y-Achse dem gescannten
Bildbereich anpassen
   CBarHandle = colorbar;
   CBarHandle = ylabel(CBarHandle,'Height [nm]','FontSize',14,'Rotation',270);
   CBarPos = get(CBarHandle,'Position');
   set(CBarHandle,'Position',[1.5*CBarPos(1) CBarPos(2) CBarPos(3)]);
   clear('CBarHandle','CBarPos')
   view(0,90);
   box on
   set(fig2,'FontSize',14);
   set(fig2,'LineWidth',1.2);

   afm_topo = AFMtopoROI;
   ScanSize = [ROI(3) ROI(4)];
   N = [abs(diff(RangeIndexX))+1 abs(diff(RangeIndexY))+1];
```

```
else
   figure('unit','normalized','outerposition',[0.01,0.02,0.98,0.82])

   fig1 = subplot(2,2,[1 3]);
   hold on

   surf( (0:N(1)-1)/N(1)*ScanSize(1) , (0:N(2)-1)/N(2)*ScanSize(2) , afm_topo);

   plot( [0:N(1)-1]*ScanSize(1)/N(1) , 0*ones(N(1),1) ,'k.','MarkerSize',2,'ZData',0*ones(N(1),1));  % schwarze Linie an unterer Kante
   plot( 0*ones(N(2),1) , [0:N(2)-1]*ScanSize(2)/N(2) ,'k.','MarkerSize',2,'ZData',0*ones(N(2),1));  % schwarze Linie an linker Kante

   hold off

   axis([0 ScanSize(1) 0 ScanSize(2)]);
   xlabel('X distance [nm]','FontSize',14);
   ylabel('Y distance [nm]','FontSize',14);
   set(gcf,'Color',[1 1 1])

   shading interp;
   load('ColormapRust','CmapRust'); set(gcf,'Colormap',CmapRust);
   ChildFig  = get(gcf,'Children');
   AxisLimit = get(ChildFig(1),'CLim');
   if ~isnan(MinMaxPlot(1)); AxisLimit(1) = MinMaxPlot(1); end
   if ~isnan(MinMaxPlot(2)); AxisLimit(2) = MinMaxPlot(2); end
   set(ChildFig(1),'CLim',[min(AxisLimit) max(AxisLimit)])
   CBarHandle = colorbar;
   CBarHandle = ylabel(CBarHandle,'Height [nm]','FontSize',14,'Rotation',270);
   CBarPos = get(CBarHandle,'Position');
   set(CBarHandle,'Position',[1.5*CBarPos(1) CBarPos(2) CBarPos(3)]);
   clear('CBarHandle','CBarPos')
   pbaspect([ScanSize(1) ScanSize(2) 1])                % L□nge von x- und y-Achse dem gescannten Bildbereich anpassen
   view(0,90);
   box on
   set(fig1,'FontSize',14);
   set(fig1,'LineWidth',1.2);
   PlotHandle0 = title('Bildbereich ausw□hlen')

   % Bildbereich ausw□hlen und darstellen

   [Range1X , Range1Y] = ginput(1);
   Range1X = min(max(Range1X,0),ScanSize(1));          % Range auf den x- und y-Bereich von afm_topo beschr□nken
   Range1Y = min(max(Range1Y,0),ScanSize(2));

   fig1 = subplot(2,2,[1 3]);
   hold on
```

```
   PlotHandle1 = plot( [0 ScanSize(1)] , [Range1Y Range1Y] ,'g-','LineWidth',1,'ZData',max(max(afm_topo))*ones(1,2));
   PlotHandle2 = plot( [Range1X Range1X] , [0 ScanSize(2)] ,'g-','LineWidth',1,'ZData',max(max(afm_topo))*ones(1,2));
   hold off

   [Range2X , Range2Y] = ginput(1);
   Range2X = min(max(Range2X,0),ScanSize(1));          % Range auf den x- und y-Bereich von afm_topo beschr◆nken
   Range2Y = min(max(Range2Y,0),ScanSize(2));

   ROI(1) = min(Range1X,Range2X);
   ROI(2) = min(Range1Y,Range2Y);
   ROI(3) = abs(diff([Range1X,Range2X]));
   ROI(4) = abs(diff([Range1Y,Range2Y]));

   RangeIndexX(1) = min(max(round( ROI(1)*N(1)/ScanSize(1)),1),N(1));
   RangeIndexX(2) = min(max(round((ROI(1)+ROI(3))*N(1)/ScanSize(1)),1),N(1));
   RangeIndexY(1) = min(max(round( ROI(2)*N(2)/ScanSize(2)),1),N(2));
   RangeIndexY(2) = min(max(round((ROI(2)+ROI(4))*N(2)/ScanSize(2)),1),N(2));

   AFMtopoROI = afm_topo( min(RangeIndexY):max(RangeIndexY) , min(RangeIndexX):max(RangeIndexX) );

   fig1 = subplot(2,2,[1 3]);
   hold on
   plot( [ ROI(1),ROI(1),ROI(1)+ROI(3),ROI(1)+ROI(3),ROI(1) ] , [ ROI(2),ROI(2)+ROI(4),ROI(2)+ROI(4),ROI(2),ROI(2) ] ,'g-','LineWidth',1,'ZData',max(max(afm_topo))*ones(1,5));
   hold off

   delete(PlotHandle0)
   delete(PlotHandle1)
   delete(PlotHandle2)
   % AFMtopoROI darstellen

   fig2 = subplot(2,2,[2 4]);
   hold on

   surf( (0:size(AFMtopoROI,2)-1)/N(1)*ScanSize(1) , (0:size(AFMtopoROI,1)-1)/N(2)*ScanSize(2) , AFMtopoROI);

   hold off

   axis([0 ROI(3) 0 ROI(4)]);
   xlabel('X distance [nm]','FontSize',14);
   ylabel('Y distance [nm]','FontSize',14);
   set(gcf,'Color',[1 1 1])

   shading interp;
```

```
    load('ColormapRust','CmapRust'); set(gcf,'Colormap',CmapRust);
    ChildFig  = get(gcf,'Children');
    AxisLimit = get(ChildFig(1),'CLim');
    if ~isnan(MinMaxPlot(1)); AxisLimit(1) = MinMaxPlot(1); end
    if ~isnan(MinMaxPlot(2)); AxisLimit(2) = MinMaxPlot(2); end
    set(ChildFig(1),'CLim',[min(AxisLimit) max(AxisLimit)])
    pbaspect([ROI(3) ROI(4) 1])                    % L?nge von x- und y-Achse dem gescannten
Bildbereich anpassen
    CBarHandle = colorbar;
    CBarHandle = ylabel(CBarHandle,'Height [nm]','FontSize',14,'Rotation',270);
    CBarPos = get(CBarHandle,'Position');
    set(CBarHandle,'Position',[1.5*CBarPos(1) CBarPos(2) CBarPos(3)]);
    clear('CBarHandle','CBarPos')
    view(0,90);
    box on
    set(fig2,'FontSize',14);
    set(fig2,'LineWidth',1.2);

    afm_topo = AFMtopoROI;
    ScanSize = [ROI(3) ROI(4)];
    N = [abs(diff(RangeIndexX))+1 abs(diff(RangeIndexY))+1];
end
```

Output in Parameter-Data Saving: afm_topo

```
SaveData = struct('afm_topo',afm_topo,'N',N,'ScanSize',ScanSize,'ROI',ROI);
save(strcat(DirName,'\',FileName,'.mat'),'-struct','SaveData','-append');
end
```

7.2 Curriculum Vitae